Thermoelectric transport in two-dimensional materials: Impacts of structure, composition, and strain

Himanshu Murari

Roll No. : 206121014

under the supervison of

Prof. Subhradip Ghosh

Department of Physics
Indian Institute of Technology Guwahati
Guwahati-781039, Assam, India

Thermoelectric transport in two-dimensional materials: Impacts of structure, composition, and strain

A thesis submitted by

Himanshu Murari

to

Department of Physics
Indian Institute of Technology Guwahati
In partial fulfillment of the requirements
for the award of the degree of
Doctor of Philosophy in Physics

Department of Physics
Indian Institute of Technology Guwahati
Guwahati-781039, Assam, India

Statement

The work contained in the thesis entitled **" Thermoelectric transport in two-dimensional materials: Impacts of structure, composition, and strain "** has been carried out at the Department of Physics, Indian Institute of Technology Guwahati, India, by me under the supervision of Prof. Subhradip Ghosh. The material of this thesis has not been submitted elsewhere for any other degree. Works presented in the thesis are all my own unless referenced to the contrary in the text.

Himanshu Murari
Roll No. - 206121014
Department of Physics
Indian Institute of Technology Guwahati
Guwahati-781039, Assam, India

Date: 25/08/2025

Disclaimer

The bibliography included in this thesis is, by no means, complete, but it contains the ones that I have consulted thoroughly. I apologize for inadvertently missing out on some of the research papers, review articles, and other scientific documents pertaining to the focus of this thesis, which should also have been cited. For illustration purposes, some of the figures in this thesis are taken from other sources and properly cited.

Certificate

It is certified that the work contained in the thesis entitled **"Thermoelectric transport in two-dimensional materials: Impacts of structure, composition, and strain"** by Himanshu Murari, a Ph.D. student of the Department of Physics, Indian Institute of Technology Guwahati is carried out under my supervision, and has not been submitted elsewhere for the award of any other degree.

Prof. Subhradip Ghosh
Department of Physics
Indian Institute of Technology Guwahati
Guwahati-781039, Assam, India

Date: 25/08/2025

Dedicated to my family

Acknowledgement

First of all, I express my sincere gratitude to my thesis supervisor, Prof. Subhradip Ghosh, for his continuous support during my PhD programme. I have always been motivated by his expert supervision and dedication to work. I am also thankful to him for giving me the opportunity to be involved in different types of problems and collaborations that enriched my knowledge and experience. Beyond academics, I am grateful to him for shaping me into a better human being, and I truly enjoyed our political discussions.

I would like to thank my collaborators, Dr. Biplab Sanyal, Dr. Ashis Kundu, Prof. Mukul Kabir, and Prof. P. K. Giri. I have learned many theoretical and experimental aspects of the subject from them.

I would also like to acknowledge my doctoral committee members, Prof. P. K. Giri, Dr. Pankaj Mishra, and Prof. Sandip Paul, for their valuable suggestions during the yearly assessments of my research work. I thank all the HODs (Prof. Subhradip Ghosh, Prof. Perumal Alagarsamy, Prof. Bosanta R. Boruah) during my Ph.D. tenure. I am grateful to the technical assistants and the academic as well as non-academic staff of the department who helped me in various ways during my research. I especially thank Basab-da for his constant support in cluster-related issues. I am grateful to IIT Guwahati for the financial support during my Ph.D. tenure. I am thankful to Param Ishan and Param Kamrupa, IIT Guwahati, for the supercomputing facility. I also thank the Department of Physics, IIT Guwahati, India, for allowing me to utilize the Newton cluster, funded under the FIST programme by DST, India. I am thankful to Anusandhan National Research Foundation (ANRF) for providing international travel support that enabled me to present my work at the ICT 2025 conference in Sendai, Japan.

I would like to thank my past and present group members, Dr. Ashis Kundu, Dr. Sheuly Ghosh, Dr. Mandira Das, Himangshu Sekhar Sarmah, Madhumita Kundu, Swati Shaw, Arvind Rajbhar, and Dr. Mayuri Bora, for research discussions. I am particularly grateful to Dr. Mandira Das and Swati Shaw for collaborating on two projects and for the valuable discussions during those works. I am especially grateful to Dr. Ashis Kundu for his invaluable guidance and numerous discussions, which helped me tackle research problems and build intuitive thinking.

I feel fortunate to have had a wonderful circle of seniors, friends, and juniors, without whom PhD life would not have been the same. Among seniors, I would like to thank Ashirbad Padhan, Dipankar Pradhan, Swarup Kanti Sarkar, Lipika Kolay, Seshadri Majumder, and Gargi Sen. I am equally grateful to my fellow batch of 2020. I would also like to thank my friends Sirsendu, Debraj, Sanju, Soumya, Bhagwat, Sanu, Madan, Dinesh, Shilpi, and Swati, who were always there during my ups and downs. My heartfelt thanks go to my Kameng hostel friends, Adri, Gurinder, Nabojyoti, Bansal, Manish, Sukhjeet, and Ravi Vashist, for creating a family-like environment. Special thanks to my Badminton group, Charu Sir, Ravi Kiran Dokala, Rahul, Devendra Bodh, and Anterdipan, for keeping life balanced and enjoyable. I am deeply grateful to Deepanwita Basu Ma'am, whose kindness, warmth, and hospitality have always made me feel welcome. I also wish to acknowledge and thank my school and graduation friends, Kushal, Mansi, Mohit, Anshu, Tanya, Paras, Prakash, Mayank, Souvik, Umesh, Devvrat, and Pranay Da, for their encouragement and support.

Special thanks to all my teachers from school through graduation for their constant guidance and encouragement. I am particularly grateful to Adhikari Sir, Gupta Sir, Mishra Sir, and Dr. Gali Hemchandra for their support during my early academic years. I would also like to extend my heartfelt gratitude to Dr. Poorva Singh, who first introduced me to the concepts of Density Functional Theory (DFT) during my Master's. Her teaching and guidance played a pivotal role in shaping my research direction.

Finally, I would like to thank my parents and family members for their unconditional love and support, which has always encouraged me to aim higher. I would also like to give my heartfelt thanks to Nisha Pandey for her love, care, and constant support throughout this journey.

Abstract

Thermoelectric materials that efficiently convert waste heat to electricity (and vice versa) are crucial for sustainable energy. Traditional bulk thermoelectrics have seen improvement in thermoelectric performance by engineering materials through various strategies. However, expected gains in performances are often constrained by intrinsically linked transport properties. Two-dimensional (2D) materials, with quantum confinement and high surface-to-volume ratios, offer new opportunities to overcome these limitations. This thesis investigates these scopes by computations of the thermoelectric behavior of diverse 2D materials using first-principles density functional theory (DFT) and Boltzmann transport theory for electrons and phonons. The goal is to identify design strategies for enhancing the thermoelectric figure of merit (ZT) by tailoring structural features, surface aspects, strain, and composition. We find that structural arrangement can significantly influence electron and phonon transport: for example, hexagonal Si-X monolayers (X = N, P, As, Sb, Bi) show modified band structures and phonon dispersions that boost ZT. The improvements in thermoelectric parameters by surface modifications and strain engineering are examined in compounds belonging to the MXene family, where surface modifications lead to breaking of symmetry. The formation of Janus compounds $MM'CO_2$ by replacing one M atom in conventional MXene M_2CO_2 by a different transition metal M′ is considered as the example in the present thesis. This increases lattice anharmonicity and alters band edges, thus reducing lattice thermal conductivity and raising ZT. Strain engineering further amplifies these effects. Tensile strain lengthens bonds and induces phonon bunching, lowering κ_l, while also tuning orbital hybridization (e.g., driving a semi-metallic to semiconductor transition) to optimize electrical transport. In a similar way, Janus monochalcogenides (M_2XY and $MM'X_2$; M, M′ = Ge, Sn; X, Y = S, Se, Te) which possess puckered anisotropic lattices and unconventional electronic structures, featuring "pudding-mold" band shapes, high density of states near the band edges, and multi-valley characteristics have been investigated with regard to their thermoelectric performances over the conventional M_2X_2 counterparts. We find that these attributes yield large, anisotropic power factors ($S^2\sigma$) and improved ZT. Finally, we demonstrate the critical role of higher-order phonon processes in monolayer h-NbN, where, despite absence of mirror symmetry selection rules, strong four-phonon scattering (attributed to flexural modes, a large acoustic-optical gap, and non-dispersive acoustic branches) substantially lowers lattice thermal conductivity. Incorporating four-phonon scattering in calculations increases ZT by 2-3 fold. This material emerges as a promising thermoelectric with ZT $\approx$ 1 at elevated temperatures. In a nutshell, this thesis provides fundamental insight into how composition, structural asymmetry, and strain can be effective routes to enhance thermoelectric performance in 2D materials.

Contents

List of Figures

List of Tables

Chapter 1

Introduction

Global energy consumption continues to be dominated by fossil fuels. This dependence has become a major contributor to climate change and environmental degradation. The Intergovernmental Panel on Climate Change (IPCC) reported in 2018 that human activities had already increased the average global surface temperature by about 1°C compared to pre-industrial levels, with projections indicating a further rise to 1.5°C by around 2030 if current trends persist[1]. This warming is strongly linked to the combustion of carbon-based fuels, which are responsible for significant greenhouse gas emissions and their associated environmental impacts.

Energy statistics for 2023 reveal a record-high level of primary energy consumption, coinciding with the warmest year ever recorded. Non-renewable sources such as oil and coal still accounted for roughly 80% of the total energy mix, highlighting the slow pace of the transition toward cleaner alternatives[2, 3]. In the same year, the share of renewable energy, including solar, wind, hydrothermal, and thermoelectric sources, increased to about 15%, marking its highest contribution to date. Despite this progress, the overall shift toward renewable energy remains insufficient to address the climate challenge, primarily due to the limited conversion efficiencies of existing green technologies and the difficulty in ensuring continuous power generation under variable environmental conditions [4].

A significant but often underutilized opportunity lies in recovering waste heat, which constitutes nearly 50–70% of the primary energy loss across industrial processes, power plants, data centers, and even domestic systems [5, 6, 7]. Besides being a wasted resource, waste heat contributes to thermal pollution and intensifies the greenhouse effect. Various approaches have been developed to capture and reuse this heat. For example, using waste heat from data centers to supply district heating for warming houses. But large-scale conversion to electricity remains challenging [8]. Waste heat can be extracted from solid, liquid, or gaseous media and transformed into usable energy in different ways. Among these, solid-state thermoelectric (TE) conversion is particularly attractive because it requires no moving parts, operates silently without vibration and emissions, and offers high durability. However, maintaining stable electrical and thermal junctions over extended operation remains a challenge, as thermal stresses and interfacial diffusion can gradually degrade device performance. By directly converting waste heat into electrical energy, TE materials provide a viable route for sustainable power generation and reduction in dependence on fossil fuels [9, 10, 11].

1.1 Thermoelectric materials

The materials that can directly convert waste heat into electricity, and conversely, electrical energy into a temperature gradient, are thermoelectric materials. The underlying physical principles of thermoelectric phenomena are described by three fundamental effects: the Seebeck, the Peltier, and the Thomson effects[12, 13]. In 1821, Thomas Johann Seebeck discovered that when two dissimilar metals are joined at two junctions, maintained at different temperatures, an electric current is induced in the closed circuit; a phenomenon known as the Seebeck effect[14]. It is the power generation mode of thermoelectric devices. If ΔT is the temperature gradient, and ΔV is the potential difference induced by it, the Seebeck coefficient is defined as

$$S = -\frac{\Delta V}{\Delta T} \tag{1.1}$$

The reverse phenomenon, discovered by Jean Charles Athanase Peltier in 1834, is the Peltier effect. In Peltier effect, passing of an electric current through a junction of two different conductors results in either heat absorption or heat release, that depends on the direction of current. The Peltier effect is also known as

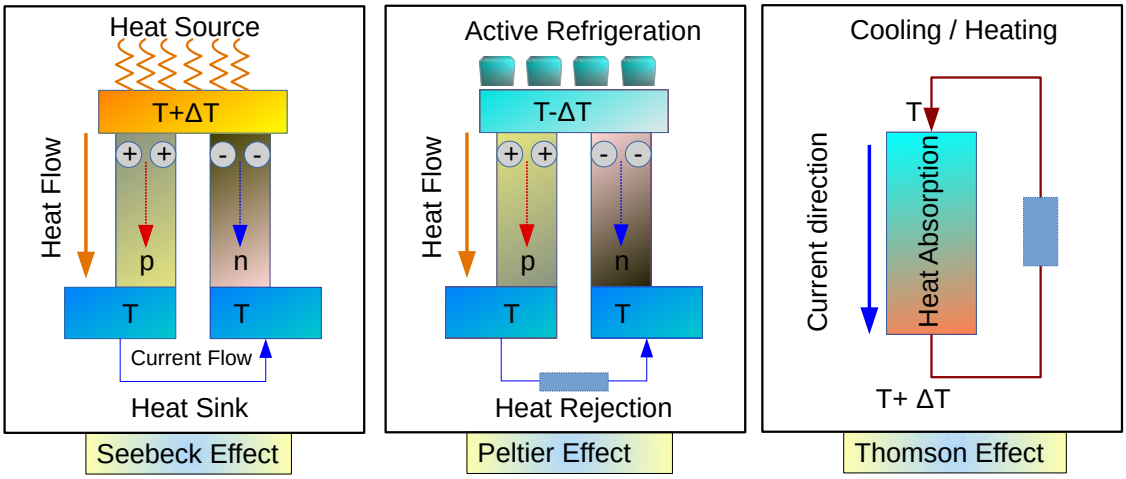

Figure 1.1: Schematic representation of Seebeck effect, Peltier effect, and Thomson effect

the refrigeration mode of the thermoelectric generator, and is the basis of TE refrigeration. Later, in 1854, William Thomson described another TE phenomenon, the Thomson effect. When an electric current passes through a single metal and a temperature gradient is set up across the length of the material, heat is either ejected or absorbed. Thomson also established a thermodynamic relation between the Seebeck and Peltier coefficients. For large-scale applications, TE devices are fabricated as modules containing multiple p-type and n-type TE legs connected electrically in series and thermally in parallel, with one side kept at a heat source and the other at a sink. Figure 1.1 shows the schematics of the TE module with n-type and p-type legs for the Seebeck and Peltier effect, along with the Thomson effect.

Earlier, thermoelectric (TE) materials have been used in specialized applications where reliability, longevity, and non-moving parts are critical. In aerospace and space exploration, thermoelectric generators (TEGs) have been employed to convert heat from radioactive decay of isotopes such as ^{238}Pu into electricity, providing a long-term power source for spacecraft and planetary probes [15, 16]. Seebeck and Peltier effects make thermoelectric phenomena highly valuable and offer a sustainable solution to reduce the overall energy consumption in the industry. In the automotive industry, TE modules have been explored as an alternative to conventional alternators, utilizing exhaust heat to generate electrical power and improve overall fuel efficiency [17]. In industrial settings, TEGs have been applied for waste heat recovery, contributing to enhanced energy efficiency in high-temperature processes[18].

With the advancement in material science, electronic device engineering, and miniaturization, the scope of TE applications has significantly broadened. For instance, hybrid photovoltaic-thermoelectric systems integrate TE elements with solar cells to utilize the waste heat generated during photovoltaic (PV) processes [19]. The major challenge of conventional PV cells is that with increasing temperature, the efficiency reduces. The hybridization of TE with PV devices enhances the solar energy conversion efficiency and addresses a key limitation of conventional PV systems[20, 21]. In the field of sensing, the inclusion of TE material in sensors can increase the sensitivity to temperature change of certain devices, improving precision in environmental monitoring, automotive sensors, etc [22, 23]. TE modules are also used for localized cooling and heating in medical devices like portable medical coolers and thermotherapy devices. Furthermore, the development of flexible thermoelectric materials is utilized as wearable TEGs, enabling the harvesting of body heat to power self-sustained electronics such as fitness trackers, health monitoring devices[24, 25]. These classical and modern applications highlight the adaptability of TE materials across distinct sectors, ranging from large space missions to small wearable devices[26]. However, despite these advantages, the widespread deployment of TE devices remains limited by their relatively low energy conversion efficiency.

The conversion efficiency of a thermoelectric material is quantified by the dimensionless figure of merit (ZT), defined as

$$ZT = \frac{S^2\sigma}{\kappa}T \tag{1.2}$$

S is the Seebeck coefficient, σ is the electrical conductivity, κ is the thermal conductivity composed of electronic part κ_e and lattice part κ_l, T is the operating temperature. A high value of ZT corresponds to a high conversion efficiency. To achieve a high ZT value, an ideal material should possess an high electrical conductivity comparable to that of metals ($\simeq 10^7 S/m$), a large Seebeck coefficient like a semiconductor

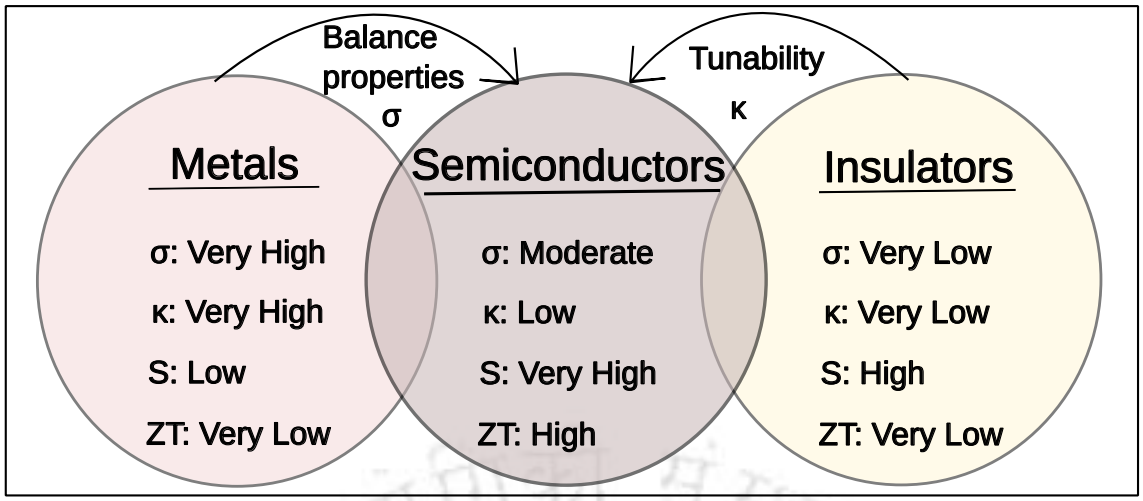

Figure 1.2: Schematic diagram demonstrating the transport coefficient range for different classes of solid state materials.

($100 \mu V/K$), and a low thermal conductivity similar to that of an insulator or glass ($\simeq 10^{-2} W/m\,K$). Such a combination is rarely achieved in a single material, but semiconductors strike the right balance, bridging between these competing requirements. This makes them the sought after candidates for thermoelectric conversion (Figure 1.2). For example, some of the most widely used commercial thermoelectric materials include heavily doped semiconductors Bi_2Te_3 and its alloys, with ZT values around 1.0-1.2 near room temperature, and lead telluride (PbTe) alloys with ZT values exceeding 1.5 at higher temperatures (500 K - 800 K)[27, 28]. More recently, tin selenide (SnSe) has achieved record ZT value above 2.5 in single crystals at high temperatures[29]. Other promising classes of thermoelectric materials are skutterudites, tetrahedrites, Zintl, SiGe, MgAgSb alloys, half-Heusler (HH) alloys [30, 31, 32, 33, 34, 35].

1.2 Optimization of Thermoelectric Properties

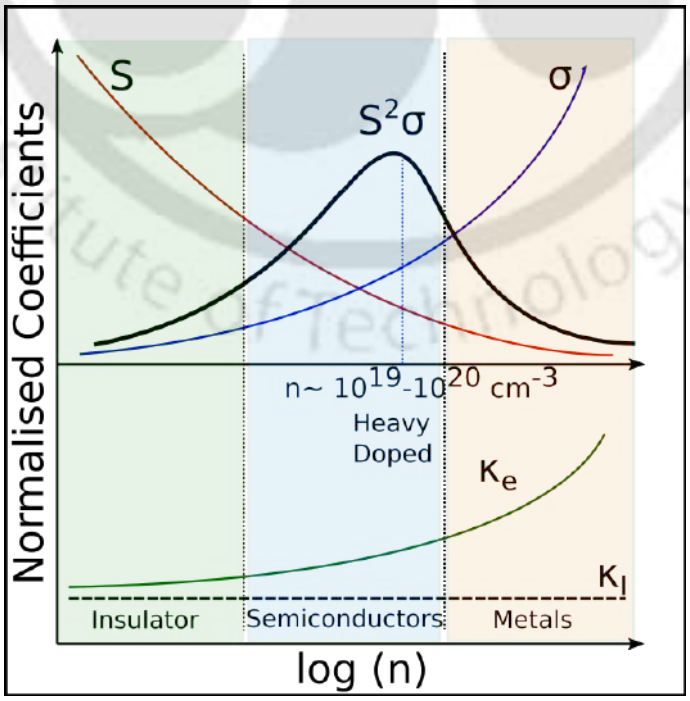

Figure 1.3: Variation of thermoelectric transport parameters as a function of carrier concentration. It shows that the heavily doped semiconductor leads to higher efficiency of thermoelectric materials.

Optimizing the transport coefficients, S, σ, and κ to achieve a high ZT value remains one of the main challenges in thermoelectric research. The difficulty arises due to the strong interdependence of these parameters. These parameters depend on the material's intrinsic characteristics like electronic band structure, carrier mobility (μ), and carrier concentration (n). The transport coefficients (S, σ, κ_e) can be expressed, in the parabolic band approximation[36, 37, 14], as,

$$S = \frac{8\pi^2}{3}\frac{k_B^2}{eh^2}m^*T(\frac{\pi}{3n})^{2/3} \tag{1.3}$$

$$\sigma = \frac{ne^2\tau}{m^*} \tag{1.4}$$

$$\kappa_e = L\sigma T \tag{1.5}$$

with e the electronic charge, n the carrier concentration, m^* the effective mass of carrier, k_B the Boltzmann constant, τ the carrier relaxation time, and L the Lorentz number. The equations indicate that S and σ exhibit an inverse dependence on n and m^*: a large effective mass increases S but reduces σ, while a low effective mass increases σ but lowers S. This trade-off constrains the enhancement of the power factor, PF= $S^2\sigma$. One of the possible ways to modulate the transport coefficients is by controlling n, which can be achieved by extrinsic doping or intrinsic defects, as illustrated in Figure 1.3. To enhance the figure of merit (ZT) value, an increased power factor ($S^2\sigma$) and low thermal conductivity are required.

1.2.1 Ways to Enhance the Power Factor ($S^2\sigma$)

The power factor ($S^2\sigma$) is the ability of a material to generate electrical power from a temperature gradient. It is the electronic contribution to the thermoelectric efficiency. A delicate balance between S and σ is required to achieve high PF, because of their strongly correlated behavior. In transport phenomena, the charge carriers in the energy states near the Fermi level participate actively. The S and σ depend on intrinsic quantities n, m^*, and electronic structure. Hence, by tuning these, PF can be enhanced. Widely used approaches for tuning these are band-gap tuning, band convergence, resonant state, and multi-band transport [38, 39] (Figure 1.4). In the following, we briefly discuss the idea associated with each of them.

Band gap Tuning

A material consists of majority and minority charge carriers. The minority charges have a negative correlation with S in TE materials. This is due to thermal excitations caused at higher temperatures, which increases n, leading to the bipolar effect and reduction of S. This suppresses the contribution of majority carriers towards S, hence S reduces[40, 41]. Along with this, κ_e also reduces, due to increased n. The minority carriers give rise to bipolar thermal conductivity (κ_{bi}) expressed as $\kappa_{bi} \propto exp(\frac{-E_g}{2K_BT})$ [42]. The increase in temperature increases κ_{bi}, which also suppresses the TE efficiency. The above-mentioned negative correlations can be suppressed by increasing the band gap. Enlarging the band-gap shifts the thermal excitation to higher temperatures, reducing the bipolar effect[43]. Doping and Alloying have been found to be effective approaches to tune the band gap. For instance, in Zr_3NiSb (Zintl compound), doping of the Te-atom increases the band-gap from 0.22 eV to 0.28 eV[44]. In the MNiSn half-Heusler compound, n-type doping enlarges the band gap compared to p-type doping, leading to an enhancement of the power factor for n-type doping [45].

Band Convergence

Seebeck coefficient (S) is directly proportional to the materials effective mass (m^*). The effective mass can be enhanced by modulating the band edge curvature; flat bands enhance the m^*. Another way to enhance m^*, is through increasing band degeneracy (N_v) as,

$$m^* = N_v^{3/2}\, m_b^* \tag{1.6}$$

where m_b^* represents single band effective mass. Enhancement of m_b^* comes with the penalty of reduced carrier mobility (μ), and reduction of σ, as a consequence. But enhancement of N_v by convergence of multiple conduction or valence band extrema near the Fermi level increases m^* without significantly affecting μ. The only requirement is that the band valleys should have light band curvature. Enhancement in N_v leads to a higher density of states near the Fermi level. Hence S increases and σ remains nearly unchanged. For

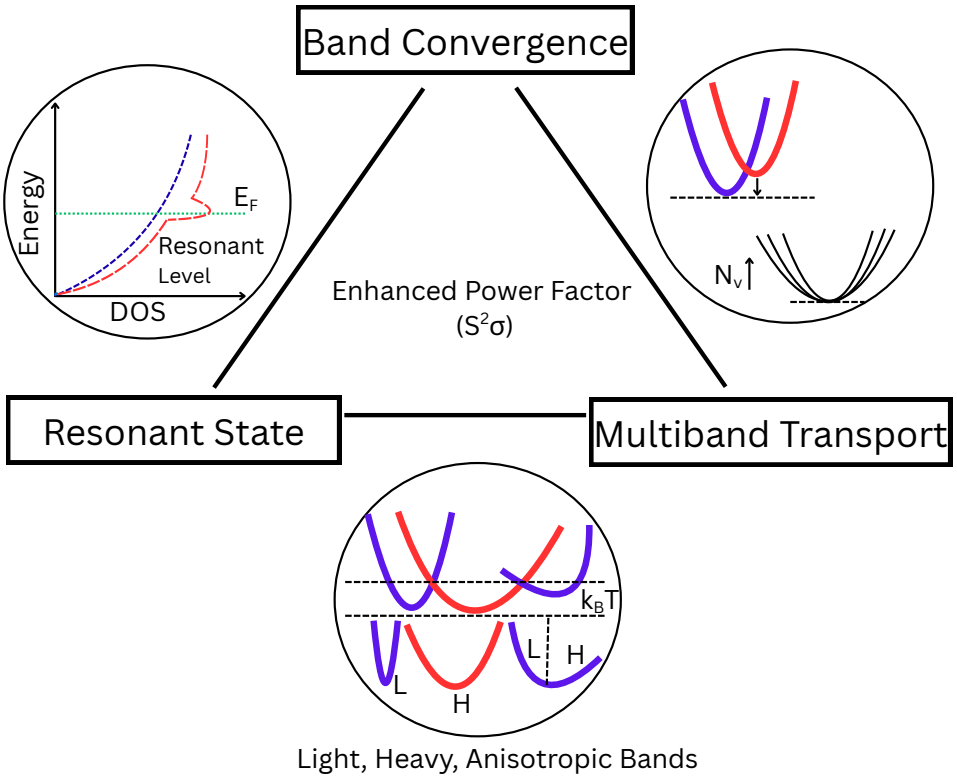

Figure 1.4: Schematic illustration of various approaches for optimizing the power factor ($S^2\sigma$).

example, alloying Se in PbTe lifts N_v from 4 to 8[28]. This resulted in an enhancement in PF leading to a ZT of about 2.0 at 900 K. Band convergence has been effective for other materials like Bi_2Se_3, Mg_2Si and Pb-doped GeTe [46, 47, 48, 49].

Resonant States

Doping sometimes leads to additional energy states in the host band structure due to creation of highly localized electronic states near the Fermi level, known as resonant states. The sharp peak in densities of states due to dopants increases m^*, and thereby the S. This enhancement occurs without affecting carrier concentration. Hence the PF increases with the trade-off of S and σ. In several experimental studies, these effects are found prominently. In half-Heusler $Hf_{0.75}Zr_{0.25}NiSn$, the inclusion of V results in a resonant state and enhanced PF compared to the pristine compound[50]. Similar effects were observed in Tl-doped PbTe, where doping increases S by 40%[51]. Doping of Sm in Zn_4Sb_3 also enhances S[52].

Multi-band Transport

In semiconductors having a complex band structure, both dispersive (light carriers) and flat bands (heavy carriers) contribute significantly to transport phenomena. Dispersive bands offer high carrier mobility, resulting in large σ, and flat bands offer a large density of states, resulting in large S. When both types of bands lie within an energy window of order k_BT of the Fermi level, their synergistic effect simultaneously enhances σ and S, hence PF increases. The effects are visible in experimental studies like alloying Mg_3Sb_2[53] with Bi-atom results in complex band structure and enhanced n-type PF by 20%. Similar alloys of PbTe with Sr and Se atoms are found to enhance PF [54].

1.2.2 Routes to reduce the Lattice Thermal Conductivity (κ_l)

Among the thermoelectric transport coefficients, the lattice thermal conductivity (κ_l) can be reduced independently without necessarily compromising electronic transport, making it a highly effective route for

enhancing ZT. The lattice thermal conductivity is defined as,

$$\kappa_l = \frac{1}{3} C_v v_g^2 \tau_{ph} \tag{1.7}$$

where C_v is the heat capacity, v_g is the phonon group velocity and τ_{ph} is the life time of phonons. The first two terms $C_v v_g^2$ describe the harmonic characteristics of the materials, whereas τ_{ph} describes anharmonic properties, phonon-phonon scattering. Reduction in v_g and enhancement in phonon-phonon scattering by different means, like introducing heavy dopants in crystals [55], nanostructuring [56], and complex crystal structures [57], can result in reduced κ_l. In the following, we briefly discuss each one of these.

Mass Disorder Scattering

Introducing atoms with different sizes and masses in the crystal lattice causes fluctuations in mass and force fields. Heavy atoms in a crystal reduce the group velocity of phonons. The mass difference creates a local perturbation in the crystal potential energy due to the breaking of translational symmetry. This acts as a scattering site for phonons. For example, in Si-Ge alloys, due to significant mass difference (Si-28 amu and Ge-73 amu), phonon scattering is strong which lowers κ_l drastically in comparsion to pure Si and Ge[58]. Similar effects have been observed in other TE materials PbTe-SnTe [59], Mg_2Si-Mg_2Sn[60], ZrCoSb half-Heusler[61], and others. However, certain dopants can increase carrier concentration (n), which may reduce S.

Nanostructuring

Nanostructuring in either nanomaterials or bulk materials containing nanocomposites produces nanometer to sub-micrometer scale grains. The resulting interfaces act as effective scattering centers for phonons. The nanostructuring in bulk materials affects the dynamics through the generation of grain boundaries of different sizes, which leads to the scattering of phonons of medium and long wavelengths. Defects and lattice distortions due to nanostructuring in bulk scatter phonons with shorter wavelengths. Such all-scale scattering caused by nanostructuring reduces κ_l drastically. In nanostructured Bi_2Te_3, the κ_l reduces by almost 60% compared to bulk, leading to an enhanced ZT value of 1.4 at room temperature [62, 63]. Similar, strategies have turned out effective in Cu_2Se and Bi_2Se_3.

Complex Crystal Structures and Rattling Atoms

Few thermoelectric materials, such as skutterudites, zintl, and clathrates, possess open cage-like crystal structures that can host loosely bound "rattler" atoms at void sites[64, 65, 66, 67]. These atoms oscillate with large amplitudes in a cage-like structure and resonantly scatter heat-carrying phonons, particularly acoustic phonons. The rattling phenomena effectively lowers v_g and τ_{ph}, leading to glass like κ_l. In La-filled $CoSb_3$ skutterudites, ultra-low κ_l ~2 W/m.K and ZT of 1.7 at 850 K were reported due to rattler-induced phonon scattering[68]. Similar reduction in κ_l was reported in zintl metal chalcogenides [65].

The above-mentioned mechanisms can be combined to achieve all-scale phonon scattering, thereby pushing κ_l towards its theoretical minimum without significantly affecting the electronic transport properties.

1.2.3 Bulk-to-2D Transition for Enhanced Thermoelectric Performance

In 1993, Hicks and Dresselhaus theoretically demonstrated that reducing the dimensionality of a material from bulk (3D) to low dimensions, such as two-dimensional (2D) layers, thin films, and super-lattices, can substantially enhance thermoelectric (TE) performance by relaxing the intrinsic coupling between transport coefficients[69]. This enhancement arises from unique features emerging due to reduced dimensionality. These include quantum confinement, increased surface-to-volume ratio, and enhanced boundary and interface phonon scattering (Figure 1.5). These effects collectively offer new degrees of freedom for decoupling the otherwise interdependent S, σ, and κ, enabling higher ZT values.

In two-dimensional (2D) materials, the motion of electrons is confined in one dimension, which quantizes the allowed momentum states and alters the electronic structure. This is known as quantum confinement phenomenon. Unlike the smooth, parabolic density of states of bulk systems, 2D systems exhibit step-like, sharp density of states near the band edges. This is related to van Hove-type singularities. This large density of states near the Fermi level enhances the S. Simultaneously, due to reduced scattering in the unconstrained directions, the σ values remain high as the in-plane mobility of charge carriers is intact. This combination can yield a substantial improvement in the PF. Hicks and Dresselhaus, in their study [69], predicted the

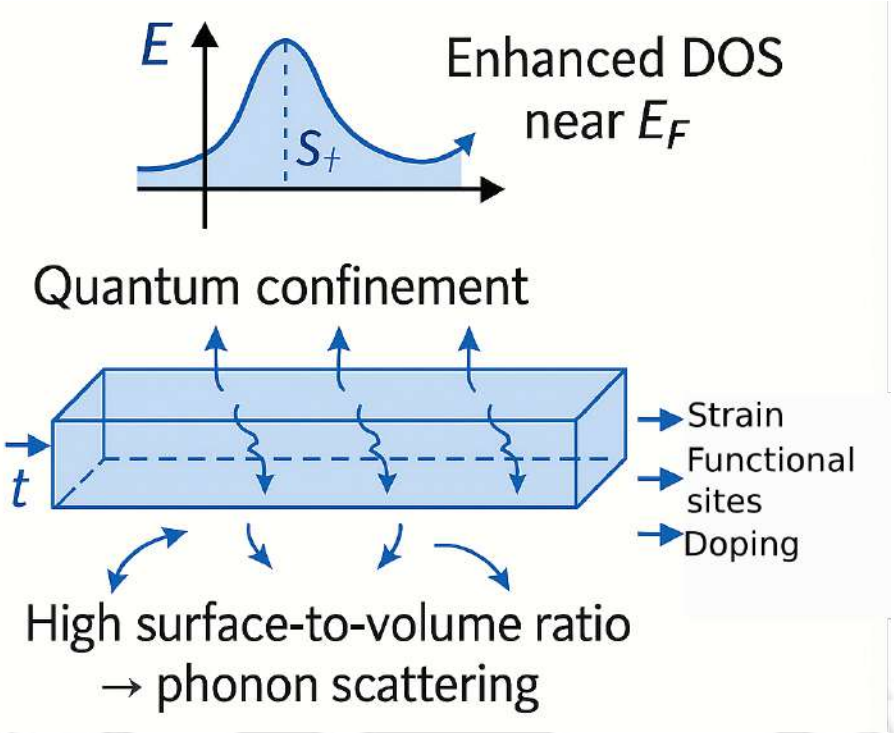

Figure 1.5: Schematic showing different phenomena in low-dimensional material.

enhancement of ZT by almost 2 times for 2D quantum wells and 6.5 times for 1D quantum wires compared to bulk materials like Bi_2Te_3[70]. Afterwards experimental study on Bi_2Te_3/Sb_2Te_3 superlattices showed a significant increase in ZT value to 2.4 at room temperature.

Reduced dimensionality also profoundly impacts the lattice thermal conductivity (κ_l). The physics associated with heat-carrying phonons in materials is fundamentally different in 2D systems compared to 3D. In 2D systems, the presence of numerous interfaces results in boundary scattering, which is effective at restricting the transport of acoustic phonons, the primary heat carriers. Subsequent reduction in κ_l can be achieved without affecting σ and S, provided the thickness of the 2D layer is greater than the electron mean free path. For example, in supperlatice Bi_2Te_3/Sb_2Te_3 cross-plane phonon scattering reduces κ_l[71].

Another unique feature in 2D materials is the presence of out-of-plane acoustic (ZA) phonons with quadratic dispersion near the Brillouin zone center (Γ)[72, 73]. Due to their quadratic nature, these flexural phonons have a comparatively large population at finite temperatures, which can strongly influence thermal transport through enhanced anharmonic scattering. In 2D lattices possessing mirror reflection symmetry, such as graphene, a reflection symmetry selection rule (RSSR) is imposed on ZA phonons[74]. This selection rule forbids certain three-phonon scattering processes involving an odd number of ZA phonons, thereby reducing the phase space for three-phonon interactions. As a result, higher-order processes, such as four-phonon scattering, can become relatively more significant in determining phonon lifetimes. This sensitivity of phonon–phonon scattering to lattice symmetry and dimensionality is a distinctive characteristic of 2D systems, with important implications for their lattice thermal conductivity[75].

In recent years, various two-dimensional materials have been explored for thermoelectric applications. Graphene, despite its ultrahigh electrical conductivity ($\sigma \approx 10^6$ S/cm), shows limited potential as a TE material due to its semi-metallic nature and extremely high lattice thermal conductivity ($\kappa_l \approx 3000$ W/m·K) [76]. This has driven attention toward semiconducting TMDCs such as MoS_2, which exhibit significantly lower κ_l and higher Seebeck coefficients. For example, MoS_2 monolayers have shown S up to 200 μV/K[77, 78] and power factors ($S^2\sigma$) around 8.5 mW/m.K^2[79], outperforming bulk Bi_2Te_3. Black phosphorus monolayers, owing to their puckered structure, exhibit strong in-plane anisotropy and S up to 335 μV/K, with reported ZT values near 1.1 [80, 81]. Among group IV–VI compounds, β-SnSe stands out with $ZT \approx 2.06$ at 300 K [82]. MXenes such as Ti_2CO_2 and V_2CH_2 have also emerged as promising candidates, offering low κ_l and subsequent ZT values approaching unity [83]. Recent studies have shown that symmetry reduction, such as in Janus TMDCs, leads to enhanced phonon scattering and reduced κ_l [84]. Functionalization, nanopattering, and graphene-based heterostructures have demonstrated increased S and reduced κ_l. Graphene's heterostructure with Bi_2Te_3 and MoS_2 has turned out to have enhanced thermoelectric proper-

ties compared to pristine graphene[85, 86, 87]. Strain engineering has similarly been found to effectively modulate both electronic and thermal transport in 2D materials. For example, strained MoS_2 exhibits S up to 280 μV/K [88]. Though many of these studies are done using state-of-the-art computational modeling and simulation, the trends, in particular, are trustworthy as the important microscopic effects have been taken into account.

1.3 First-principles Electronic Structure Methods and Simulation of Materials Properties

The discussion in the previous subsection clearly demonstrates that low-dimensional materials, due to the quantum confinement effect, provide new avenues to achieve higher conversion efficiency in thermoelectric generators. Understanding of intrinsic properties such as electronic structure, electron and phonon transport phenomena, mobility, scattering, and phonon dynamics is crucial for exploring the thermoelectric properties of novel two-dimensional materials. It becomes crucial to have prior insight into a material's intrinsic properties before attempting costly experiments. Modeling and simulation can provide a qualitative picture of a material's performance under various experimental conditions, such as doping, strain, and defects. This insight is highly beneficial for experimentalists in identifying suitable materials for specific applications.

Theoretically, these properties can be evaluated by utilizing different models and simulation techniques. To achieve accurate and reliable results, one needs to solve the many-body Schrödinger equation for electrons interacting with each other and with the atomic nuclei in a real solid-state system. However, the exact solution for such a many-body system is computationally infeasible due to its 3N-dimensional complexity. Hence, various approximations are considered to resolve this problem. Density Functional Theory (DFT) provides a robust framework to address the n-electron many-body problem by considering the electron density as the key variable rather than the wavefunction[89, 90]. The central concept in DFT involves mapping the interacting many-body system (the real system) onto a system of n non-interacting auxiliary systems, where all the important many-body effects are incorporated in an approximate manner. Consequently, DFT stands as a parameter-free first-principles approach, offering a highly effective way to determine many of a material's ground-state properties. In this thesis, we have considered DFT in conjunction with the semi-classical Boltzmann transport theory to evaluate the thermoelectric properties of novel two-dimensional materials[14].

1.4 Outline of the thesis

In this thesis, Density functional theory (DFT) combined with semi-classical Boltzmann transport theory for electrons and phonons has been used to investigate the effects of structure, composition, phonon scattering processes, and the effects of bi-axial strain on the thermoelectric transport of different families of 2D materials. Several distinct strategies have been explored to achieve high thermoelectric (TE) efficiency in them. The study begins with an analysis of structural arrangement effects on the TE behavior of hexagonal Si-X (X = N, P, As, Sb, Bi) monolayers. In the course of our investigations, the study progresses to symmetry and strain engineering in Janus MXenes, a class of 2D transition-metal carbides, demonstrating how asymmetric surface functionalization and biaxial strain influence phonon scattering and electronic transport. Subsequently, the investigation extends to Janus group IV–VI monochalcogenides, where intrinsic compositional asymmetry leads to anisotropic thermoelectric performances. Finally, the role of higher-order anharmonicity is explored through a study on h-NbN monolayer, incorporating four-phonon scattering processes to accurately assess the limitations of traditional three-phonon theories. The chapters in this thesis are organized as follows:

In **Chapter I** we introduce the fundamentals of thermoelectric energy conversion, the figure of merit (ZT), and its dependence on electronic and phonon transport properties. It highlights the limitations of conventional 3D materials and discusses why 2D systems have gained prominence. The chapter also outlines the motivation behind exploring structural and phonon engineering strategies adopted in this thesis.

In **Chapter II**, we describe the theoretical and computational approaches employed throughout this thesis. Density Functional Theory (DFT) is used to obtain the structural, electronic, and vibrational properties of the considered 2D materials. Thermoelectric transport properties are evaluated using the semi-classical Boltzmann transport theory. For electronic transport, the Boltzmann transport equation is solved within the rigid band approximation (RBA). In RBA, it is assumed that the electronic band structure remains unchanged under small shifts in the Fermi level. To estimate the electronic relaxation time, two approaches

are adopted: (i) the constant relaxation time approximation (CRTA), where the relaxation time is obtained using deformation potential (DP) theory, and (ii) the electron-phonon approximation (EPA), in which the energy-dependent relaxation time is evaluated by considering the full electron-phonon interaction in an averaged manner. The lattice thermal conductivity is computed by solving the Boltzmann transport equation for phonons using second- and third-order interatomic force constants (IFCs). Fourth-order IFCs are considered only in cases where four-phonon scattering processes are included, details of which are presented in this chapter.

In **Chapter III**, we systematically investigate the thermoelectric properties of Si-X (X = N, P, As, Sb, Bi) monolayers. The monolayers are theoretically predicted to exhibit the minimal formation energy in the hexagonal structure, indicating their feasibility for experimental synthesis. The focus of this study is to understand the effect of atomic-layer arrangement on the thermoelectric properties of these monolayers. The study reveals that such structural change significantly influences both electronic and phonon transport characteristics. It is found that consideration of an unconventional stacking arrangement reduces the lattice thermal conductivity, due to enhanced phonon-phonon scattering and reduced group velocities. Simultaneous increase in electrical conductivity is also observed. The combined effect leads to an enhancement in the thermoelectric figure of merit and efficiency. The results demonstrate a strong structure-property relationship that has been previously overlooked in these compounds. This study highlights that modulation of atomic-layer arrangement can be a viable design route for improving thermoelectric efficiency in 2D semiconductors.

Symmetry lowering and strain engineering have emerged as effective strategies for modulating phonon transport in two-dimensional materials, as demonstrated in several recent studies. These approaches influence the lattice dynamics and carrier transport by altering structural symmetry and bonding environments, thereby improving thermoelectric performance. In **Chapter IV**, we focus on the interrelation between reduced symmetry, electronic and thermal transport in the context of 2D thermoelectric materials. We investigate the thermoelectric properties of novel two-dimensional transition metal carbides known as MXenes. This study emphasizes how surface (symmetry-lowering) and strain engineering can be employed to modulate the electronic and transport properties. In the first part, we focus on symmetry lowering in parent M_2CO_2 MXenes by replacing one transition metal M atom with M$'$, creating a Janus compound MM$'$$CO_2$. A systematic comparison is carried out between the thermoelectric properties of Janus MXenes and their symmetric parent counterparts. The reduction in symmetry enhances the phonon-phonon scattering, resulting in a decrease in lattice thermal conductivity. An in-depth analysis is provided on the complex interplay of symmetry, electronic structure, bond strength, and anharmonicity to understand the thermoelectric properties. In the second part of the study, we consider Janus MXenes engineered by modifying the transition metal constituents and the surface-passivating functional groups. These surface-engineered materials are then subjected to biaxial strain. We find that in three Janus compounds, Zr_2COS, $ZrHfCO_2$, and ZrHfCOS, tensile strain modifies the electronic and thermal properties such that thermoelectric performance enhances. This work highlights the combined role of symmetry lowering and strain as effective design strategies for achieving high thermoelectric efficiency in two-dimensional MXene-based systems.

In **Chapter-V** we investigate the thermoelectric properties of a new class of Janus group IV-VI monochalcogenides. Two classes of Janus compounds are considered, M_2XY and MM$'$$X_2$ compounds (M = Ge, Sn, and X, Y = S, Se, Te), derived from parent MX compounds. The parent MX compounds are known to exhibit excellent thermoelectric properties in bulk and low-dimensional phases. Due to their puckered structure, the monochalcogenides possess significant in-plane anisotropy. The reduced symmetry in the Janus structure leads to asymmetric bonding. We focus on how asymmetry and intrinsic anisotropy affect both electronic and thermal transport properties. It is found that the figure of merit is higher along the y-direction for all considered Janus monochalcogenides. This is due to a combination of a higher power factor and a low lattice thermal conductivity along the y-direction. The high power factor originates from multi-valley and pudding-mold features in the electronic structure, while strong anharmonicity and low phonon group velocity contribute to low lattice thermal conductivity. This work presents an effective way to achieve high-performance anisotropic two-dimensional thermoelectric materials through structural anisotropy and band structure engineering.

In **Chapter VI**, we investigate the role of four-phonon scattering in determining the lattice thermal conductivity (κ_l) and thermoelectric performance of a newly predicted two-dimensional h-NbN monolayer. Recent studies have shown that flexural (ZA) phonons dominate thermal transport in 2D materials, and their scattering behavior is strongly influenced by symmetry selection rules. For example, in graphene, the presence of mirror symmetry suppresses odd-ZA scattering due to the reflection symmetry selection rule (RSSR), making four-phonon processes the dominant scattering mechanism. In h-NbN, mirror reflection is absent; as a result, RSSR is not applicable, yet h-NbN exhibits strong four-phonon scattering. Using first-

principles calculations and Boltzmann transport theory including fourth-order anharmonic interactions, we find that four-phonon scattering processes are comparable to three-phonon ones, hence significantly reducing κ_l. This is attributed to the presence of a large acoustic–optical phonon gap, quadratic ZA dispersion, and flat acoustic branches. The effect of tensile strain (+3%) is also examined, which further alters the phonon dispersion and influences the thermoelectric performance. It is found that the thermoelectric figure of merit increases by 2-3 fold with the inclusion of four-phonon scattering. This study highlights the critical role of higher-order phonon scattering in accurately predicting κ_l in 2D materials, even in the absence of mirror symmetry.

The concluding **Chapter VII** outlines open challenges in the field and proposes possible extensions of the work presented in this thesis.

Chapter 2

Methodology

In this chapter, we describe the theoretical methods that are used in this thesis for evaluating the materials' properties. The study carried out in this thesis is based on the Density Functional Theory (DFT). We provide a description of the Pseudopotential method and the projected augmented wave (PAW) as these implementations of DFT have been used in this thesis for evaluation of the ground state properties and electronic structure of the materials considered. A brief discussion on the semi-classical Boltzmann transport formalism for electrons and phonons is provided, since they are used for evaluation of the thermoelectric transport properties.

2.1 The many-body Hamiltonian

The non-relativistic, time-independent many-body Schrödinger equation for solving the electronic structure of a solid containing atoms and nuclei is written as

$$H\Psi = E\Psi \tag{2.1}$$

where Ψ is the many-body wavefunction of the form,

$$\Psi = \Psi(\mathbf{r}_1, \mathbf{r}_2, ..., \mathbf{r}_i, \mathbf{R}_1, \mathbf{R}_2, ..., \mathbf{R}_I, ...) \tag{2.2}$$

H is the Hamiltonian and E is the total electronic energy. The indices i and I are for electrons and atomic nuclei, respectively. The Hamiltonian H can be written as

$$H = -\frac{\hbar^2}{2}\sum_I \frac{\nabla_I^2}{M_I} + \frac{1}{2}\sum_{I\neq J}\frac{Z_I Z_J e^2}{|\mathbf{R}_I - \mathbf{R}_J|} - \frac{\hbar^2}{2}\sum_i \frac{\nabla_i^2}{m_i} + \frac{1}{2}\sum_{i\neq j}\frac{e^2}{|\mathbf{r}_i - \mathbf{R}_I|} - \sum_{i,I}\frac{Z_I e^2}{|\mathbf{r}_i - \mathbf{R}_I|} \tag{2.3}$$

Where Z_I and M_I are the charge and mass of the nucleus, the mass of the electron is m_i. $\mathbf{R}_I$ and $\mathbf{r}_i$ are the nuclear and electronic coordinates, respectively. The first and third terms in the Hamiltonian and kinetic energies of nuclei and electrons, respectively. The second, fourth, and fifth terms are Coulomb interactions between nuclei-nuclei, electrons-electrons, and electrons-nuclei, respectively. Due to the complex nature of the many-body Hamiltonian (Eq. 2.3), it becomes difficult to exactly solve it for solid state systems. Hence, approximations are required at different levels. In the next subsections, we discuss these.

2.2 The Born-Oppenheimer approximation

The many-body problem can be simplified by the Born-Oppenheimer approximation, proposed by Max Born and Robert Oppenheimer in 1927 [91]. The Born-Oppenheimer approximation uses the fact that the nuclei are much heavier than the electrons. Due to their heavier mass, nuclei move slowly compared to the rapidly moving electrons; hence, nuclei appear to be stationary in the electron's frame. As a result, their kinetic energy can be neglected, and the potential energy due to nucleus-nucleus interactions is assumed to be constant. Consequently, the problem reduces to the many-body contribution coming mainly from electrons and the electronic Hamiltonian, and is given by

$$H_{el} = -\frac{\hbar^2}{2}\sum_i \frac{\nabla_i^2}{m_i} + \frac{1}{2}\sum_{i\neq j}\frac{e^2}{|\mathbf{r}_i - \mathbf{r}_j|} - \sum_{i,I}\frac{Z_I e^2}{|\mathbf{r}_i - \mathbf{R}_I|} \\ = T_e + V_{ee} + V_{ext} \tag{2.4}$$

where T_e is the kinetic energy of the electrons, V_{ee} is the Coulomb energy due to electron-electron interaction, and V_{ext} is the interaction with external potential (electron-nucleus interaction).

2.3 Density Functional Theory (DFT)

In spite of the simplification of many-body Hamiltonian under Born-Oppenheimer approximation, it is still an extremely complicated many-body eigenvalue problem to solve due to 3N degrees of freedom of N electrons. The Density Functional Theory (DFT) overcomes this problem by considering electron density as the central player instead of the many-body wave function. In the early version of DFT proposed by Thomas [92] and Fermi [93], kinetic energy was represented in terms of one electron density. The all-important electron-electron interactions were incorporated by a mean field approximation, which was similar to the wave-function-based approaches, the Hartree and Hartree-Fock method[94, 95]. However, the early Thomas-Fermi approximation was a semi-classical approach that failed to address the important quantum mechanical effects, like the exchange and correlation effects in a many-body electronic system. In 1964, Hohenberg and Kohn[89] provided the required breakthrough. They proposed two theorems, which are the backbone of the current-day DFT formalism. The Hohenberg-Kohn (HK) theorems[96, 97] are,

1. **First Theorem:** It states that for every system there is a unique external potential, $V_{ext}(\mathbf{r})$ determined solely by the ground-state electron density $n(\mathbf{r})$. So the total energy is a unique function of density E[n].
2. **Second Theorem:** It states that the true ground state density $n(\mathbf{r})$ of a system minimizes the total energy functional E[n] and the minimum energy is the ground state energy E_0.

According to the above theorems, the ground state energy of interacting electrons in an external potential $V_{ext}(\mathbf{r})$ is described by an energy functional,

$$E[n] = F[n] + \int V_{ext}(\mathbf{r})n(\mathbf{r})\, d\mathbf{r} \tag{2.5}$$

$F[n]$ is a universal functional of electron density $n(\mathbf{r})$ accounting for the kinetic energy of the electrons and the electron-electron interactions. The second term represents the interaction of the electron with the external potential. The total energy in the ground state is realized through the minimization of $E[n]$ (variational principle in the framework of DFT). Therefore, the goal of DFT is to find the electron density $n(\mathbf{r})$ that minimizes the energy functional $E[n]$, which corresponds to the true ground-state density, and unambiguously determines the ground state properties of an interacting electronic system.

While the DFT approach offers a perspective different than the conventional methods, where the many-body wave function is a key player in determining the materials' properties. Even after the simplification of the many-body problem through the HK theorem, the challenge lies in evaluating the ground-state energy because the functional $F[n]$ is not known exactly. The success of the DFT lies in using the HK theorem in conjunction with the Kohn-Sham (KS) formalism [90]. In Kohn-Sham formalism, the many-body problem is mapped onto an auxiliary single-body problem. The idea is to simplify the complex many-body system by replacing it with an auxiliary non-interacting single-body system in an effective potential. This mapping of many-electron to single-electron system by Kohn and Sham resulted in a Schrödinger like equation.

$$(H_{KS} - \epsilon_i)\phi_i(\mathbf{r}) = 0 \tag{2.6}$$

Here, H_{KS} is the Kohn-Sham Hamiltonian operator consisting of the kinetic energy of electrons and the effective potential, ϵ_i and $\phi_i(\mathbf{r})$, are the energy eigenvalue and single-particle wavefunction (Kohn-Sham orbital) corresponding to the i^{th}-electron, respectively.

$$H_{KS} = -\frac{1}{2}\nabla^2 + V_{eff}\ (in\ \ Hartree\ \ units) \tag{2.7}$$

where,

$$V_{eff} = V_{ext}(\mathbf{r}) + V_{Hatree}(\mathbf{r}) + V_{xc}(\mathbf{r}) \tag{2.8}$$

The second term is called the Hartree potential,

$$V_{Hartree} = \frac{1}{2}\int \frac{n(\mathbf{r})n(\mathbf{r}')}{|\mathbf{r}-\mathbf{r}'|}d\mathbf{r}d\mathbf{r}' \tag{2.9}$$

and the last term is the exchange-correlation potential, is given as,

$$V_{xc} = \frac{\delta E_{xc}[n]}{\delta n(\mathbf{r})} \tag{2.10}$$

which includes electron-electron interaction beyond the Hartree term. The density is calculated from Kohn-Sham orbitals according to

$$n(\mathbf{r}) = \sum_{i=1}^{N} |\phi_i(\mathbf{r})|^2 \tag{2.11}$$

Integrating the obtained density, the total number of electrons is obtained as,

$$N = \int n(\mathbf{r})d(\mathbf{r}) \tag{2.12}$$

The ground state energy of an electronic system is given as,

$$E_{KS} = T_s[n] + \int V_{ext}(\mathbf{r})n(\mathbf{r})dr + E_{Hartree}[n] + E_{xc}[n] \tag{2.13}$$

The Kohn-Sham equation is solved iteratively, starting with an initial guess for the electron density, $n(\mathbf{r})$. Then evaluating the V_{eff}, the equations (2.5-2.12) are solved self consistently. Although the Kohn-Sham theory is exact in principle, further approximations are required as the exchange and correlation terms are not known exactly, except for the free electron gas (homogeneous). In the series of approximations, the simplest approach to obtain an approximate E_{xc} is the local density approximation (LDA) [90]. It assumes that the variation of density in a solid is insignificant locally, and thus the electron density in a solid can be considered as that of the homogeneous electron gas. The E_{xc} under LDA is given by,

$$E_{xc}^{LDA}[n] = \int n(\mathbf{r})\varepsilon_{xc}^{hom}(n(\mathbf{r}))d^3\mathbf{r} \tag{2.14}$$

where ε_{xc}^{hom} is the sum of the exchange and correlation energies of the homogeneous electron gas of density $n(\mathbf{r})$.

This LDA works reasonably where the charge density varies slowly, like covalent systems and simple metals. The surprising success of the LDA is partly due to the cancellation of errors in overestimating exchange energy (E_x) and in underestimating correlation energy(E_c), which implies LDA gives the correct sum rule for the exchange-correlation hole. However, real systems are not homogeneous and have varying density around the electrons. LDA ignores the exchange-correlation energy at point $\mathbf{r}$ due to nearby inhomogeneities in the electron density. An attempt to improve the LDA was made by introducing the gradient corrections on the electron density, the generalized gradient approximation (GGA) [98]. The GGA functional is given by,

$$E_{xc}^{GGA}[n] = \int d^3r\, n(\mathbf{r})\, \varepsilon_{xc}^{GGA}(n(\mathbf{r}), |\nabla n(\mathbf{r})|) \tag{2.15}$$

For systems where the charge density varies slowly, the GGA functional improves the results. Some well-known GGA functionals used in literature are: Perdew-Wang 1991 (PW91) [99], Perdew-Burke-Ernzerhof (PBE) [100], PBE for solids (PBEsol) [101].

The most challenging aspect of computational materials science is developing accurate and computationally efficient numerical methods to solve the Kohn–Sham equations, depending on the nature of the problem under consideration. The most commonly adopted methodologies include the pseudopotential (PP) method, the full-potential (FP) method, and the Green's function method.

2.4 Pseudopotential method

According to Bloch's theorem, the wavefunction of an electron in a crystal can be expanded using a discrete set of plane waves. However, a plane wave basis set is poorly suited to represent electronic wavefunctions in

all regions because a very large number of plane waves is required to describe the tightly bound core orbitals and the rapid oscillations of the valence wavefunctions near the core. The construction of pseudopotentials removes these rapid oscillations in the valence electron wavefunctions within the core region, resulting in smoother valence wavefunctions. Consequently, the pseudo-wavefunctions can be accurately represented using a reasonable number of plane waves, making the method computationally efficient. We next discuss the commonly used plane wave-based pseudopotentials for electronic structure calculations.

2.4.1 Norm-Conserving Pseudopotentials (NCPP)

The norm-conserving pseudopotentials (NCPP) were the first in the block of pseudopotentials that were computationally tractable. The NCPPs are constructed to ensure that the pseudo-wavefunctions outside a chosen core radius match the all-electron wavefunctions exactly and conserve the norm of the all-electron wavefunction within the core region. The condition is mathematically given as,

$$\int_0^{\mathbf{r}_c} \varphi^{PS*}(r)\varphi^{PS}(r)r^2dr = \int_0^{\mathbf{r}_c} \varphi^{AE*}(r)\varphi^{AE}(r)r^2dr \tag{2.16}$$

φ^{PS*} and φ^{AE} are the pseudo and all electron wavefunctions respectively. However, norm-conserving pseudopotentials often require a relatively large plane-wave basis set to accurately describe the wavefunctions, which can increase computational cost, particularly for systems with first-row or transition-metal elements (d and f elements).

2.4.2 Ultrasoft Pseudopotentials (USPP)

The limitation of norm-conserving pseudopotentials (NCPPs) is that inside the cutoff distance $\mathbf{r}_c$, it is unrealistic to make the pseudo-wavefunction completely smooth. As a result, a large plane-wave basis set is required, which is in contrast to the goal of achieving fast convergence in plane-wave-based calculations. To overcome this issue, in 1990, Vanderbilt proposed a new and radical idea for constructing pseudopotentials [102, 103]. This approach greatly reduces the number of plane waves needed to construct a basis set, but introduces some additional complications, which are:

- Since the pseudo-wavefunctions are not necessarily norm-conserving, a non-trivial overlap term appears in the secular equation.
- The pseudo charge density cannot simply be computed using $\sum \varphi^*\varphi$ as in norm-conserving pseudopotentials; instead, an augmentation term must be included in the core region.
- Relaxing the norm-conservation condition generally leads to less transferable pseudopotentials.

Nevertheless, the use of these ultrasoft pseudopotentials over the years in large-scale calculations has demonstrated their reliability in condensed matter simulations.

2.5 Projector Augmented Wave (PAW) Method

Despite their wide usage and efficiency, pseudopotential (PP) methods have inherent limitations. In pseudopotential approaches, the core electrons are eliminated from the calculation, and the strong oscillations of the valence wavefunctions near the nucleus are smoothed. While this greatly reduces the computational cost by enabling the use of a smaller plane-wave basis set, it also introduces certain drawbacks. Hence, the pseudopotential method can sometimes miss important information and lead to inaccurate results.

In 1994, Blöchl proposed a more general approach, the Projector Augmented Wave (PAW) method [104]. The PAW method was developed by combining ideas from the all-electron Linearized Augmented Plane Wave (LAPW) [105, 106, 107] and pseudopotential methods. The key concept of the PAW method is to divide the wavefunction into two parts: a partial-wave expansion in spheres around the atoms (augmentation regions) and envelope functions outside these spheres (interstitial regions). These two are connected by a linear transformation at the sphere radius. In this section, we present a brief description of this method.

In the PAW method, the all-electron wavefunction $|\psi_n\rangle$ is represented by a smooth auxiliary wavefunction $|\bar{\psi}_n\rangle$ through a linear transformation with the operator T:

$$|\psi_n\rangle = T|\bar{\psi}_n\rangle \tag{2.17}$$

Around each atom, an augmentation sphere ($|\mathbf{r} - \mathbf{R}^a| < r_c^a$) is constructed, where r_c^a is the cutoff radius, a is the atom index, and $\mathbf{R}^a$ is the atom position. The linear transformation operator T can be written as:

$$T = 1 + \sum_a T^a \tag{2.18}$$

where T^a acts only within the augmentation sphere. Within the augmentation region, the smooth wavefunction can be expanded in smooth partial waves $\bar{\phi}_i^a$:

$$|\bar{\psi}_n\rangle = \sum_{ia} c_{ni}^a |\bar{\phi}_i^a\rangle \tag{2.19}$$

Similarly, the all-electron wavefunction is expressed as:

$$|\psi_n\rangle = \sum_{ia} c_{ni}^a |\phi_i^a\rangle \tag{2.20}$$

The action of the linear transformation operator on the smooth partial waves gives:

$$|\phi_i^a\rangle = T|\bar{\phi}_i^a\rangle = (1 + T^a)|\bar{\phi}_i^a\rangle \tag{2.21}$$

Since T^a acts only inside the augmentation sphere, outside the sphere ($r > r_c^a$) we have:

$$|\phi_i^a\rangle = |\bar{\phi}_i^a\rangle \tag{2.22}$$

Combining these results, the true all-electron wavefunction can be expressed as (using Eqs. 2.19 and 2.12):

$$|\psi_n\rangle = |\bar{\psi}_n\rangle - \sum_{ia} c_{ni}^a |\bar{\phi}_i^a\rangle + \sum_{ia} c_{ni}^a |\phi_i^a\rangle \tag{2.23}$$

Since the transformation operator T is linear, the coefficients c_{ni}^a can be written as scalar products:

$$c_{ni}^a = \langle \bar{p}_i^a | \bar{\psi}_n \rangle \equiv \mathcal{P}_{ni}^a \tag{2.24}$$

where $\bar{p}_i^a$ are smooth projector functions. Therefore, the transformation operator T becomes:

$$\mathcal{T} = \sum_a \sum_i \left(|\phi_i^a\rangle - |\bar{\phi}_i^a\rangle \right) \langle \bar{p}_i^a | \tag{2.25}$$

Applying this transformation (Eq. 2.25), the Kohn–Sham wavefunction is given by:

$$\begin{aligned} |\psi_n\rangle &= |\bar{\psi}_n\rangle + \sum_a \sum_i \left(|\phi_i^a\rangle - |\bar{\phi}_i^a\rangle \right) \langle \bar{p}_i^a | \bar{\psi}_n \rangle \\ &= |\bar{\psi}_n\rangle + \sum_a \sum_i |\phi_i^a\rangle \langle \bar{p}_i^a | \bar{\psi}_n \rangle - \sum_a \sum_i |\bar{\phi}_i^a\rangle \langle \bar{p}_i^a | \bar{\psi}_n \rangle \end{aligned} \tag{2.26}$$

From Eq. 2.26, the wavefunction is decomposed into the smooth auxiliary wavefunction (smooth everywhere) plus a sum of differences between the one-centered all-electron contributions and the corresponding pseudo parts. Using Eq. 2.26 in Eq. 2.17, one can obtain compact expressions for various quantities in the PAW formalism. Throughout this thesis, we have used the PAW method as implemented in the VASP code [108].

2.6 Thermoelectric Transport Properties

In this section, we describe the theoretical framework used to evaluate the thermoelectric transport properties of the 2D materials studied in this thesis. The electronic and phonon transport coefficients are evaluated by solving the semi-classical Boltzmann transport equation (BTE)[14]. The BTE provides a statistical, non-equilibrium description of carrier dynamics under external perturbations, such as temperature gradients or electric fields, which cause the drift, diffusion, and scattering phenomena. This framework allows us to predict how materials conduct electricity through electrons and transport heat through both electrons and phonons under different conditions.

2.6.1 Electronic Transport Properties

The electronic transport coefficients, namely the Seebeck coefficient (S), electrical conductivity (σ), and electronic thermal conductivity (κ_e), are evaluated using first-principles electronic band structures in combination with the Boltzmann transport equation (BTE) framework.

In the BTE formalism, the carrier distribution function is defined as $f(\mathbf{r}, \mathbf{k}, t)\, d\mathbf{r}\, d\mathbf{k}$, which represents the number of carriers at point $\mathbf{r}$ with wave number $\mathbf{k}$ at time t within the small phase space volume $d\mathbf{r}\, d\mathbf{k}$. The total number of carriers can be obtained by integrating this distribution function. The challenging part is the time evolution of the distribution function $f(\mathbf{r}, \mathbf{k}, t)$. To describe the variation of the distribution function over time, the effects of external fields, temperature gradients, and the scattering process are taken into account for the carrier. These are considered to be the causes for the carrier transport and lead to diffusion, drift, and collisions. Including all these perturbations, the evolution of the distribution function can be written as

$$\frac{\partial f(\mathbf{r}, \mathbf{k}, t)}{\partial t} = \left.\frac{\partial f}{\partial t}\right|_{\text{diffusion}} + \left.\frac{\partial f}{\partial t}\right|_{\text{drift}} + \left.\frac{\partial f}{\partial t}\right|_{\text{collision}} \tag{2.27}$$

Each term can be described as follows

- **Diffusion term:** This term accounts for spatial variation in the carrier distribution. At fixed $\mathbf{k}$, with group velocity $\mathbf{v_k}$, it is:

$$\left.\frac{\partial f}{\partial t}\right|_{\text{diffusion}} = -\mathbf{v_k} \cdot \nabla_{\mathbf{r}} f \tag{2.28}$$

- **Drift term:** This term describes changes in momentum space due to external forces, such as electric fields. At fixed position $\mathbf{r}$:

$$\left.\frac{\partial f}{\partial t}\right|_{\text{drift}} = -\frac{d\mathbf{k}}{dt} \cdot \nabla_{\mathbf{k}} f \tag{2.29}$$

- **Collision term:** This term represents changes due to scattering processes. While generally complex, under the relaxation time approximation (RTA), it is simplified as:

$$\left.\frac{\partial f}{\partial t}\right|_{\text{collision}} = -\frac{f - f^0}{\tau(\mathbf{k})} \tag{2.30}$$

  where f^0 is the equilibrium Fermi-Dirac distribution and $\tau(\mathbf{k})$ is the relaxation time.

Combining these terms, the BTE takes the form:

$$\frac{\partial f}{\partial t} = -\mathbf{v_k} \cdot \nabla_{\mathbf{r}} f - \frac{d\mathbf{k}}{dt} \cdot \nabla_{\mathbf{k}} f - \frac{f - f^0}{\tau(\mathbf{k})} \tag{2.31}$$

At steady state, the time derivative of the distribution function is zero:

$$-\mathbf{v_k} \cdot \nabla_{\mathbf{r}} f - \frac{d\mathbf{k}}{dt} \cdot \nabla_{\mathbf{k}} f - \frac{f - f^0}{\tau(\mathbf{k})} = 0 \tag{2.32}$$

Solving the BTE under the RTA yields the distribution function, from which the transport coefficients are evaluated. For solving the BTE in conjunction with the first-principles derived band structure, we use the BoltzTrap2 package[109, 110]. The expressions for electrical conductivity tensor($\sigma_{\alpha\beta}(T, \mu)$), electronic thermal conductivity tensor($\kappa^o_{\alpha\beta}(T, \mu)$), and Seebeck coefficient tensor($S_{\alpha\beta}(T, \mu)$) are:

$$\sigma_{\alpha\beta}(T, \mu) = \frac{1}{\Omega} \int \bar{\sigma}_{\alpha\beta}(\epsilon) \Big[-\frac{\partial f(T, \epsilon, \mu)}{\partial \epsilon} \Big] d\epsilon \tag{2.33}$$

,

$$\kappa^o_{\alpha\beta}(T, \mu) = \frac{1}{e^2 T \Omega} \int \bar{\sigma}_{\alpha\beta}(\epsilon)(\epsilon - \mu)^2 \Big[-\frac{\partial f(T, \epsilon, \mu)}{\partial \epsilon} \Big] d\epsilon \tag{2.34}$$

$$S_{\alpha\beta}(T, \mu) = \frac{1}{eT\Omega\sigma_{\alpha\beta}(T, \mu)} \int \bar{\sigma}_{\alpha\beta}(\epsilon)(\epsilon - \mu) \Big[-\frac{\partial f(T, \epsilon, \mu)}{\partial \epsilon} \Big] d\epsilon \tag{2.35}$$

where

$$\bar{\sigma}_{\alpha\beta}(\epsilon) = \frac{e^2}{N} \sum_{i,k} \tau v_\alpha(i, k) v_\beta(i, k) \delta(\epsilon - \epsilon_{i,k}) \tag{2.36}$$

and

$$v_\alpha(i,k) = \frac{1}{\hbar}\frac{\partial \epsilon_{i,k}}{\partial k_\alpha} \tag{2.37}$$

Here, α and β denote tensor components, Ω is the unit cell volume, μ is the chemical potential, and f is the Fermi-Dirac distribution function. N is the number of sampled $\mathbf{k}$-points, and e is the electron charge. $v_\alpha(i,\mathbf{k})$ represents the α-component of the group velocity for the i-th energy band. Equations (2.33)–(2.37) show that the transport coefficients are computed from the group velocities derived from the DFT-calculated electronic band structure.

Another approximation considered to depict the doping analysis is the rigid band approximation (RBA), under which it is assumed that the band structure does not change with the shifting of the chemical potential. The RBA holds true for small shifts or small doping. For all the calculation presented in this thesis we have kept the doping range such that RBA is valid. To obtain the carrier relaxation time (τ) within the relaxation time approximation (RTA), we use two different approaches: deformation potential (DP) theory[111] and the electron-phonon averaged (EPA) method[112].

Deformation potential theory estimates τ by considering the scattering of charge carriers with long-wavelength acoustic phonons. For 2D materials, the relaxation time in the acoustic phonon scattering regime is given by:

$$\tau = \frac{2\hbar^3 C_{2D}}{3k_B T m^* E_D^2} \tag{2.38}$$

where C_{2D} is the 2D elastic modulus, m^* is the effective mass of the carrier, E_D is the deformation potential constant describing the shift of band edges with strain, k_B is Boltzmann's constant, T is the absolute temperature, and $\hbar$ is the reduced Planck constant. The elastic modulus is calculated as $C_{2D} = \frac{1}{S_o}(\frac{\partial^2 E}{\partial \delta^2})$, where $\delta = \frac{\Delta a}{a_o}$ is the small biaxial strain applied (-1.5% to 1.5%), where S_o and a_o are the equilibrium surface area and lattice constant. The DP constant $E_D = \frac{\partial E_{edge}}{\partial \delta}$, where E_{edge} is the valence or conduction band edges, depicts how the conduction or valence band edge shifts under applied strain. The shift with respect to the strain is linearly fitted, and E_D is obtained from the slope of the fit. The carrier effective mass is given as $m^* = \hbar^2\left[\frac{\partial^2 E(k)}{\partial k^2}\right]^{-1}$; k and $E(k)$ are the wave vector and the corresponding band energy, respectively. The effective masses reported in this thesis are the ones at the band edges, obtained by fitting the band edge energies. This analytical approach provides a simple and efficient way to estimate τ, widely used for screening and qualitative analysis of transport properties.

The electron-phonon averaged (EPA) method is a more detailed and accurate estimation of the relaxation time by explicitly averaging first-principles electron-phonon scattering rates across the Brillouin zone. Unlike DP theory, which assumes elastic acoustic phonon scattering only, EPA includes all relevant phonon modes and their coupling strengths. The energy-dependent relaxation time $\tau(\epsilon)$ is computed using:

$$\frac{1}{\tau(\epsilon)} = \frac{2\pi}{\hbar}\sum_{m,\nu,\mathbf{q}} |g_{n,m,\nu}(\mathbf{k},\mathbf{q})|^2 \delta(\epsilon_{m,\mathbf{k+q}} - \epsilon_{n,\mathbf{k}} \pm \hbar\omega_{\nu,\mathbf{q}}) \tag{2.39}$$

where $g_{n,m,\nu}(\mathbf{k},\mathbf{q})$ are the electron-phonon coupling matrix elements, $\epsilon_{n,\mathbf{k}}$ and $\epsilon_{m,\mathbf{k+q}}$ are electronic band energies, and $\omega_{\nu,\mathbf{q}}$ are phonon frequencies for branch ν and wavevector $\mathbf{q}$. This method accounts for inelastic and anisotropic scattering processes in detail, including both intervalley and intravalley scattering of charge carriers, providing an energy-dependent relaxation time that can be directly used to calculate transport coefficients with improved accuracy. In the EPA-based relaxation time $\tau(\epsilon)$ is obtained using the Eliashberg spectral function, which is computed from density functional perturbation theory (DFPT)-derived phonon linewidths and electron–phonon matrix elements. The scattering rate is integrated over phonon modes and weighted by the Bose–Einstein and Fermi–Dirac distributions to yield $\tau(\epsilon)$. The method essentially captures the averaged strength of electron–phonon coupling without requiring full interpolation of matrix elements on dense k/q grids. For this approach, first-principles calculations are performed using Quantum ESPRESSO[113].

2.6.2 Phonon Transport Properties

In this subsection, we present the methodology for calculating lattice thermal conductivity (κ_l) from first principles. We begin with the expansion of the crystal's total potential energy to define interatomic force

constants (IFCs) of various orders. The harmonic approximation is then employed to compute phonon dispersions and group velocities using second-order IFCs. Finally, the linearized phonon Boltzmann transport equation (PBTE) is solved, incorporating anharmonic scattering rates derived from higher-order IFCs, to evaluate κ_l with high accuracy[114].

Potential Energy Expansion

The potential energy of the crystal is expanded as a Taylor series of atomic displacement u_i^α (displacement of atom i along α):

$$U = U_0 + \frac{1}{2}\sum_{i,j}\sum_{\alpha,\beta}\Phi_{ij}^{\alpha\beta}\,u_i^\alpha\,u_j^\beta + \frac{1}{6}\sum_{i,j,k}\sum_{\alpha,\beta,\gamma}\Psi_{ijk}^{\alpha\beta\gamma}\,u_i^\alpha\,u_j^\beta\,u_k^\gamma + \frac{1}{24}\sum_{i,j,k,l}\sum_{\alpha,\beta,\gamma,\delta}\Xi_{ijkl}^{\alpha\beta\gamma\delta}\,u_i^\alpha\,u_j^\beta\,u_k^\gamma\,u_l^\delta + \cdots \tag{2.40}$$

where $\Phi_{ij}^{\alpha\beta}$ are the harmonic IFCs, $\Psi_{ijk}^{\alpha\beta\gamma}$ are the third-order (anharmonic) IFCs, and $\Xi_{ijkl}^{\alpha\beta\gamma\delta}$ are the fourth-order IFCs. The third-order terms describe three-phonon scattering processes, while the fourth-order terms capture four-phonon scattering effects.

These IFCs are calculated using the finite displacement method by systematically displacing atoms in supercells and evaluating the resulting forces. Accurately determining these IFCs is crucial for predicting harmonic and anharmonic properties and, therefore, the lattice thermal conductivity.

Harmonic Approximation and Phonon Dispersion

Phonon transport properties are fundamentally connected to the lattice dynamics of the crystal. It becomes important to understand the lattice dynamics for thermal transport and thermoelectric studies. The starting point for phonon calculations is the harmonic approximation, where the potential energy of the system is expanded to second order in atomic displacements. The harmonic interatomic force constants (IFCs) are defined as the second derivatives of the total energy with respect to atomic displacements:

$$\Phi_{ij}^{\alpha\beta}(l,l') = \frac{\partial^2 U}{\partial u_i^\alpha(l)\,\partial u_j^\beta(l')} \tag{2.41}$$

Here, i and j label atoms in the basis, l and l' denote unit cell indices, and α,β indicate Cartesian directions. The displacement $u_i^\alpha(l)$ represents the deviation of atom i in cell l along the Cartesian direction α.

These harmonic IFCs are computed using the finite displacement method (FDM) by generating supercells with small atomic displacements and evaluating the resulting forces from first-principles calculations. The dynamical matrix is then constructed from the harmonic IFCs and diagonalized to obtain the phonon frequencies $\omega_\nu(\mathbf{q})$ and eigenvectors at each wavevector $\mathbf{q}$:

$$D_{ij}^{\alpha\beta}(\mathbf{q}) = \frac{1}{\sqrt{M_i M_j}}\sum_{l'}\Phi_{ij}^{\alpha\beta}(0,l')\,e^{i\mathbf{q}\cdot\mathbf{R}_{l'}} \tag{2.42}$$

Here, M_i and M_j are the masses of atoms i and j, respectively, and $\mathbf{R}_{l'}$ is the lattice vector of unit cell l'. Diagonalization of $D(\mathbf{q})$ yields the phonon dispersion relations $\omega_\nu(\mathbf{q})$, which are essential for determining phonon group velocities and occupation populations.

Phonon Boltzmann Transport Equation (PBTE)

The phonon Boltzmann Transport Equation (PBTE) provides a statistical framework to describe phonon transport under a temperature gradient. It governs the evolution of the phonon distribution function $n_\nu(\mathbf{q})$, which represents the occupancy of phonon mode ν at wavevector $\mathbf{q}$:

$$\frac{\partial n_\nu(\mathbf{q})}{\partial t} + \mathbf{v}_\nu(\mathbf{q})\cdot\nabla_{\mathbf{r}} n_\nu(\mathbf{q}) = \left.\frac{\partial n_\nu(\mathbf{q})}{\partial t}\right|_{\text{scattering}} \tag{2.43}$$

Here, $\mathbf{v}_\nu(\mathbf{q})$ is the phonon group velocity, obtained from the phonon dispersion as:

$$\mathbf{v}_\nu(\mathbf{q}) = \nabla_{\mathbf{q}}\omega_\nu(\mathbf{q}) \tag{2.44}$$

The scattering term incorporates all phonon-phonon interactions, including three-phonon and four-phonon processes, as well as isotope and boundary scattering if applicable. Solving the PBTE requires evaluating these scattering rates accurately.

Unlike the simplified relaxation time approximation (RTA), which assumes that each phonon mode independently relaxes to equilibrium with a single lifetime, this work employs the iterative solution of the linearized PBTE. The iterative approach fully accounts for the coupling between different phonon modes and accurately captures collective phonon behavior, including normal and Umklapp processes. This results in a more realistic description of thermal transport, particularly in materials where momentum-conserving (normal) scattering significantly redistributes phonon populations.

The lattice thermal conductivity tensor κ_l is calculated from the steady-state non-equilibrium phonon distribution as:

$$\kappa_{l,\alpha\beta} = \frac{1}{\Omega} \sum_{\nu} \int \hbar\omega_{\nu}(\mathbf{q}) v_{\nu,\alpha}(\mathbf{q}) F_{\nu,\beta}(\mathbf{q}) \frac{d\mathbf{q}}{(2\pi)^3} \tag{2.45}$$

where $F_{\nu,\beta}(\mathbf{q})$ is the deviation function obtained from the iterative solution of the PBTE.

In this work, harmonic and anharmonic interatomic force constants (IFCs) are obtained from first-principles calculations using the finite displacement method. Phonon dispersions are computed with PHONOPY, while three-phonon and four-phonon scattering rates are calculated using ShengBTE and FourPhonon, respectively. The PBTE is solved iteratively with ShengBTE to determine the lattice thermal conductivity with high accuracy.

Phonon Boltzmann Transport Equation (PBTE)

The phonon Boltzmann Transport Equation (PBTE) describes the evolution of the phonon distribution function n_λ in response to external perturbations such as a temperature gradient. Here, λ is a composite index comprising both the phonon branch υ and wavevector $\mathbf{q}$. Two main factors influence the distribution function: diffusion driven by the temperature gradient ∇T, and scattering due to allowed phonon-phonon interactions.

Under steady-state conditions, the linearized PBTE is expressed as:

$$\frac{dn_\lambda}{dt} = \left.\frac{\partial n_\lambda}{\partial t}\right|_{\text{diffusion}} + \left.\frac{\partial n_\lambda}{\partial t}\right|_{\text{scattering}} = 0, \tag{2.46}$$

where the diffusion term is given by:

$$\left.\frac{\partial n_\lambda}{\partial t}\right|_{\text{diffusion}} = -\nabla T \cdot \mathbf{v}_\lambda \frac{\partial n_\lambda}{\partial T}, \tag{2.47}$$

and $\mathbf{v}_\lambda$ is the phonon group velocity obtained from the gradient of the phonon dispersion relation. The scattering term $\left.\frac{\partial n_\lambda}{\partial t}\right|_{\text{scattering}}$ accounts for phonon-phonon interactions, which can be analyzed using perturbation theory and include only three-phonon or both three-phonon and four-phonon processes, depending on the study.

For real solids under small temperature gradients, the distribution function can be expanded to first order in ∇T as $n_\lambda = n_0 + g_\lambda$, where n_0 is the equilibrium Bose-Einstein distribution and g_λ is the perturbative correction, linearly proportional to ∇T. This correction can be expressed as:

$$g_\lambda = -F_\lambda \cdot \nabla T \frac{dn_0}{dT}. \tag{2.48}$$

For multiple-phonon scattering processes, including two-, three-, and four-phonon interactions, the resulting linearized PBTE leads to the following relation:

$$\mathbf{F}_\lambda = \tau_\lambda^0 \left(\mathbf{v}_\lambda + \Delta_\lambda\right), \tag{2.49}$$

where τ_λ^0 is the mode-dependent relaxation time calculated under the relaxation time approximation (RTA), and Δ_λ is a measure of how much the population of a specific phonon mode. This term is obtained through iterative solutions that go beyond the RTA and account for collective phonon scattering behavior. The ΔT and τ_λ^0 are computed as,

The deviation term Δ_λ, which captures the mode-coupling effects beyond the relaxation time approximation, is given by:

$$
\begin{aligned}
\Delta_\lambda =& \frac{1}{N}\sum_{\lambda'\lambda''}\Gamma^{(+)}_{\lambda\lambda'\lambda''}\left(\xi_{\lambda\lambda''}F_{\lambda''}-\xi_{\lambda\lambda'}F_{\lambda'}\right)\\
&+\frac{1}{2N}\sum_{\lambda'\lambda''}\Gamma^{(-)}_{\lambda\lambda'\lambda''}\left(\xi_{\lambda\lambda''}F_{\lambda''}+\xi_{\lambda\lambda'}F_{\lambda'}\right)\\
&+\frac{1}{2N}\sum_{\lambda'\lambda''\lambda'''}\Gamma^{(++)}_{\lambda\lambda'\lambda''\lambda'''}\left(\xi_{\lambda\lambda'''}F_{\lambda'''}-\xi_{\lambda\lambda'}F_{\lambda'}-\xi_{\lambda\lambda''}F_{\lambda''}\right)\\
&+\frac{1}{2N}\sum_{\lambda'\lambda''\lambda'''}\Gamma^{(+-)}_{\lambda\lambda'\lambda''\lambda'''}\left(\xi_{\lambda\lambda'''}F_{\lambda'''}-\xi_{\lambda\lambda'}F_{\lambda'}+\xi_{\lambda\lambda''}F_{\lambda''}\right)\\
&+\frac{1}{6N}\sum_{\lambda'\lambda''\lambda'''}\Gamma^{(--)}_{\lambda\lambda'\lambda''\lambda'''}\left(\xi_{\lambda\lambda'''}F_{\lambda'''}+\xi_{\lambda\lambda'}F_{\lambda'}+\xi_{\lambda\lambda''}F_{\lambda''}\right)\\
&+\frac{1}{N}\sum_{\lambda'}\Gamma^{(\mathrm{iso})}_{\lambda\lambda'}\,\xi_{\lambda\lambda'}F_{\lambda'}.
\end{aligned}
\tag{2.50}
$$

Here, N is the total number of $\mathbf{q}$-grid points used in the Brillouin zone sampling. The factor $\xi_{\lambda\lambda'}$ is defined as $\xi_{\lambda\lambda'}=\omega_{\lambda'}/\omega_\lambda$, where ω_λ is the phonon frequency of mode λ. The superscripts $(\pm)$ and $(\pm\pm)$ denote three-phonon (3ph) and four-phonon (4ph) scattering processes, corresponding to momentum conservation conditions $q''=q\pm q'+Q$ and $q'''=q\pm q'\pm q''+Q$, respectively. Here, Q is a reciprocal lattice vector, with $Q=0$ indicating a normal process that conserves crystal momentum within the first Brillouin zone. The Γ terms denote the scattering rates for different processes, computed from the corresponding anharmonic scattering probability matrices obtained via perturbation theory.

The three-phonon scattering rates can be expressed as:

$$
\Gamma^{(+)}_{\lambda\lambda'\lambda''}=\frac{\pi}{4}\frac{n^0_{\lambda'}-n^0_{\lambda''}}{\omega_\lambda\omega_{\lambda'}\omega_{\lambda''}}\,|V^{(+)}_{\lambda\lambda'\lambda''}|^2\,\delta(\omega_\lambda+\omega_{\lambda'}-\omega_{\lambda''}),
\tag{2.51}
$$

$$
\Gamma^{(-)}_{\lambda\lambda'\lambda''}=\frac{\pi}{4}\frac{n^0_{\lambda'}+n^0_{\lambda''}+1}{\omega_\lambda\omega_{\lambda'}\omega_{\lambda''}}\,|V^{(-)}_{\lambda\lambda'\lambda''}|^2\,\delta(\omega_\lambda-\omega_{\lambda'}-\omega_{\lambda''}),
\tag{2.52}
$$

The four-phonon scattering rates are given by:

$$
\begin{aligned}
\Gamma^{(++)}_{\lambda\lambda'\lambda''\lambda'''}=&\frac{2\pi}{8N}\frac{(1+n^0_{\lambda'})(1+n^0_{\lambda''})n^0_{\lambda'''}}{n^0_\lambda}\frac{|V^{(++)}_{\lambda\lambda'\lambda''\lambda'''}|^2}{\omega_\lambda\omega_{\lambda'}\omega_{\lambda''}\omega_{\lambda'''}}\\
&\times\delta(\omega_\lambda+\omega_{\lambda'}+\omega_{\lambda''}-\omega_{\lambda'''}),
\end{aligned}
\tag{2.53}
$$

$$
\begin{aligned}
\Gamma^{(+-)}_{\lambda\lambda'\lambda''\lambda'''}=&\frac{2\pi}{8N}\frac{(1+n^0_{\lambda'})n^0_{\lambda''}n^0_{\lambda'''}}{n^0_\lambda}\frac{|V^{(+-)}_{\lambda\lambda'\lambda''\lambda'''}|^2}{\omega_\lambda\omega_{\lambda'}\omega_{\lambda''}\omega_{\lambda'''}}\\
&\times\delta(\omega_\lambda+\omega_{\lambda'}-\omega_{\lambda''}-\omega_{\lambda'''}),
\end{aligned}
\tag{2.54}
$$

$$
\begin{aligned}
\Gamma^{(--)}_{\lambda\lambda'\lambda''\lambda'''}=&\frac{2\pi}{8N}\frac{n^0_{\lambda'}n^0_{\lambda''}n^0_{\lambda'''}}{n^0_\lambda}\frac{|V^{(--)}_{\lambda\lambda'\lambda''\lambda'''}|^2}{\omega_\lambda\omega_{\lambda'}\omega_{\lambda''}\omega_{\lambda'''}}\\
&\times\delta(\omega_\lambda-\omega_{\lambda'}-\omega_{\lambda''}-\omega_{\lambda'''}).
\end{aligned}
\tag{2.55}
$$

The three-phonon matrix elements $V^{(\pm)}$ are defined as:

$$
V^{(\pm)}_{\lambda\lambda'\lambda''}=\sum_{ijk}\sum_{\alpha\beta\gamma}\frac{\Phi^{\alpha\beta\gamma}_{ijk}}{\sqrt{M_iM_jM_k}}\,e^\alpha_\lambda(i)\,e^{\pm\beta}_{\lambda'}(j)\,e^{\mp\gamma}_{\lambda''}(k)\,e^{\pm i\mathbf{q}'\cdot\mathbf{r}_j}\,e^{\mp i\mathbf{q}''\cdot\mathbf{r}_k},
\tag{2.56}
$$

where $\Phi^{\alpha\beta\gamma}_{ijk}$ are the third-order force constants, M_i is the atomic mass, $e^\alpha_\lambda(i)$ is the phonon eigenvector component for mode λ, and $\mathbf{r}_j$ is the position vector of atom j.

The four-phonon matrix elements $V^{(\pm\pm)}$ are given by:

$$
\begin{aligned}
V^{(\pm\pm)}_{\lambda\lambda'\lambda''\lambda'''}=&\sum_{ijkl}\sum_{\alpha\beta\gamma\theta}\frac{\Phi^{\alpha\beta\gamma\theta}_{ijkl}}{\sqrt{M_iM_jM_kM_l}}\,e^\alpha_\lambda(i)\,e^{\pm\beta}_{\lambda'}(j)\,e^{\pm\gamma}_{\lambda''}(k)\,e^{\mp\theta}_{\lambda'''}(l)\\
&\times e^{\pm i\mathbf{q}'\cdot\mathbf{r}_j}\,e^{\pm i\mathbf{q}''\cdot\mathbf{r}_k}\,e^{\mp i\mathbf{q}'''\cdot\mathbf{r}_l},
\end{aligned}
\tag{2.57}
$$

where $\Phi_{ijkl}^{\alpha\beta\gamma\theta}$ are the fourth-order force constants.

In these expressions, n_{λ}^{0} denotes the Bose-Einstein distribution at thermal equilibrium, and ω_{λ} is the phonon frequency of mode λ. Energy conservation is enforced by the Dirac delta function δ. The matrix elements $V^{(\pm)}$ and $V^{(\pm\pm)}$ represent the three-phonon and four-phonon interaction strengths, respectively, and are computed from the Fourier transforms of the third- and fourth-order interatomic force constants. Here, i, j, k, l are atomic indices within the unit cell, $\alpha, \beta, \gamma, \theta$ are Cartesian directions, M_i is the mass of atom i, $e_{\lambda}^{\alpha}(i)$ is the phonon eigenvector component, and $\mathbf{r}_j$ is the position vector of atom j.

In this thesis, we have used the Phonopy[115], ShengBTE[116], and FourPhonon[117] packages in conjunction with first-principles calculations to evaluate the lattice thermal conductivity.

2.7 Computational Details

All first-principles calculations in this thesis were carried out using the projector-augmented wave (PAW) method within the framework of density functional theory (DFT)[89, 90], as implemented in the Vienna Ab initio Simulation Package (VASP)[108]. The exchange-correlation interactions were treated using Perdew-Burke-Ernzerhof (PBE) functional within the generalized gradient approximation (GGA)[98]. Structural optimizations and total energy calculations employed appropriate exchange-correlation functionals with well-converged plane-wave energy cutoffs and **k**-point meshes to ensure reliable accuracy. For all studies, a tight convergence criteria of 10^{-7}eV and 10^{-3}eV/Å were used for the total energy and the Hellmann-Feynman forces, respectively. These convergence tests confirmed that total energy is well converged with variations below 1 meV/atom. We have considered a vacuum of 20 Å along the z-direction, to avoid interactions between the periodic images of layers.

Electronic transport properties were evaluated by solving the Boltzmann transport equation using the BoltzTraP2 code[109]. The carrier relaxation time was obtained using either the deformation potential (DP) approach or the electron-phonon approximation (EPA) method[111, 112].

For lattice dynamics, harmonic interatomic force constants (IFCs) were obtained using the finite displacement method (FDM) with the Phonopy package[115]. Anharmonic IFCs up to third and fourth order were also calculated using FDM implemented in thirdorder.py and fourthorder.py scripts. The displacement magnitude of 0.01 Å was set for evaluting the IFCs. The obtained IFCs were used to evaluate the higher-order phonon scattering processes. The lattice thermal conductivity (κ_l) was determined by solving the linearized phonon Boltzmann transport equation using ShengBTE for three-phonon scattering and FourPhonon for four-phonon scattering contributions[116, 117]. To obtain accurate κ_l for two-dimensional compounds, the `scalebroad` parameter was set to 1.0 while solving the PBTE. The calculated κ_l values were then normalized by the factor c/z, where c is the length of the simulation cell along the out-of-plane direction (vacuum spacing) and z is the thickness of the 2D monolayer.

Structural stability was verified through multiple criteria. Mechanical stability was assessed by calculating the full elastic constant tensor and confirming it satisfies the Born-Huang stability criteria[118]. The elastic constants were determined using the energy-strain method, in which the total energy is fitted to the quadratic form

$$E(V, \epsilon) = E_0 + \frac{V_0}{2} \sum_{i,j} C_{i,j} \epsilon_i \epsilon_j \tag{2.58}$$

where E_0 and V_0 are the equilibrium energy and volume, C_{ij} are the elastic constants and ϵ_i are the applied strains. We have considered small deformations within the range of -1.5% to +1.5% with a step of 0.5%. The resulting strain-energy data were fitted to the above relation to extract the elastic constants. Dynamical stability was checked by ensuring the absence of imaginary phonon modes in computed phonon dispersion relations. Thermal stability was further evaluated using ab initio molecular dynamics (AIMD)[119] simulations in the canonical (NVT) ensemble at 800 K, reflecting the high-temperature conditions relevant to thermoelectric applications. For post-processing and visualization purposes, VESTA[120], VASPKIT[121], and the Sumo Python[122] module were used.

Chapter 3

Effects of atomic arrangement on thermoelectric properties of SiX (X= N, P, As, Sb, Bi) monolayers*

3.1 Introduction

In recent years, a few-layer mono and di-chalcogenides of group III materials with A_2B_2 type single layer structures, which show novel electronic properties, have been synthesised [123, 124, 125, 126]. The valence band structures in these compounds show a large number of states at the band edge, suggesting an enhancement in the contribution to ZT that comes from the electronic transport. Moreover, the dispersions in the valence band correspond, in a general way, to additional dimensional reduction [127]. It is, therefore, expected that layered group IV-V compounds, isoelectronic to III-VI ones, may exhibit improved thermoelectric properties. After the successful synthesis of group IV-V 2D binary compounds, SiP, SiAs, GeP, and GeAs [128], the quest got an impetus. In the bulk form, these are found to crystallise in a monoclinic structure with the C2/m space group [129]. A recent computational exploration of possible structures for Si_xP_y monolayers [130] revealed that A_2B_2 type SiP monolayer in $P\bar{6}m2$ space group can be easily cleaved into monolayers from the bulk form. Subsequently, Burak et al. studied the electronic and vibrational properties of A_2B_2-type group IV-V compounds by considering two hexagonal structural symmetries with $P\bar{6}m2$ and $P\bar{3}m1$ space groups. They found that all the compounds except CP, CAs, CSb, and CBi have lower total energy with $P\bar{6}m2$ symmetry [131]. Taking cue from this, thermoelectric properties of several group IV-V compounds in their monolayers and with crystal structures conforming to $P\bar{6}m2$ symmetry were investigated by first-principles computational methods. While Radha *et al.* investigated the thermoelectric properties of Si-X (=N, P, As, Sb, and Bi) monolayers [132], Huang *et al.* explored the potentials of SiSb, GeSb, and SnSb as thermoelectric materials [133]. While a maximum ZT of 1.01 in SiSb was obtained by considering only the electronic part in thermal conductivity [132], a value close to 2 was obtained for the same system upon inclusion of the lattice contributions to thermal conductivity [133]; the other systems in both studies exhibiting lower values of ZT. This suggests that the phonons play an important role in these systems. One important aspect that remains unaddressed in both studies is the impact of the atomic arrangement. Very recently, first-principles Density Functional Theory (DFT) based calculations have demonstrated a drastic reduction in thermal conductivity and subsequent enhancement in ZT of group-III chalcogenide monolayer due to an alternative arrangement of atomic layers [134].

Motivated by these developments, in this chapter, we have investigated the structural, electronic, and thermoelectric properties of SiN, SiP, SiAs, SiSb, and SiBi monolayers using DFT-based techniques. We find that the inclusion of lattice contribution to thermal conductivity and consideration of different atomic arrangements in the layers significantly affect the thermoelectric parameters and thus the ZT. We find that a substantial enhancement in ZT occurs for systems in which the atomic arrangement, different from the conventional one, is stable. This provides important feedback to the experimentalists in designing group IV-V compounds for thermoelectric applications and may open up a route to explore the structure-thermoelectric property relationship in compounds from other groups. This chapter, therefore, contributes to the thesis by exploring how atomic arrangement influences thermoelectric performance in group IV-V monolayer systems.

*The contents of this chapter are published in 2023 J. Phys. D: Appl. Phys. 56 295501.

3.2 Computational Details

For the total energy calculations, a kinetic energy cutoff of 450 eV was employed. The Brillouin zone was sampled with a $14 \times 14 \times 1$ **k**-point grid. Electronic transport properties were evaluated with the constant relaxation time approximation (CRTA) and rigid band approximation (RBA). The carrier relaxation time was estimated using deformation potential (DP) theory. For the phonon calculation, a $4 \times 4 \times 1$ supercell with a $4 \times 4 \times 1$ **k**-mesh was used to calculate harmonic interatomic force constants (IFCs). Third-order anharmonic IFCs were calculated up to the fifth nearest neighbor using a $3 \times 3 \times 1$ supercell and a $4 \times 4 \times 1$ **k**-mesh. Lattice thermal conductivity was evaluated by solving the phonon Boltzmann transport equation, with a $20 \times 20 \times 1$ **q**-grid for Brillouin zone sampling.

3.3 Results and discussion

3.3.1 Structural Stability

The unit cell of Si-X monolayer is a hexagonal one with space group $P\bar{6}m2$ and consists of four atoms, two Si and two X, occupying four different planes. The conventional stacking pattern [131, 132, 133] has two Si atoms occupying the inner planes while the group-V X atoms reside in the outer planes(Fig. 3.1a). Such X-Si-Si-X stacking along the z-axis is named Configuration(1) in the present work. As is the case of III-VI compounds with A_2B_2-type monolayers, an alternative configuration (Configuration(2)) with stacking pattern Si-X-X-Si (Fig. 3.1b) is also possible. This configuration was never considered in References [131, 132, 133]. In the present work, we have considered both stacking patterns and made estimates of the impact they have on the physical properties.

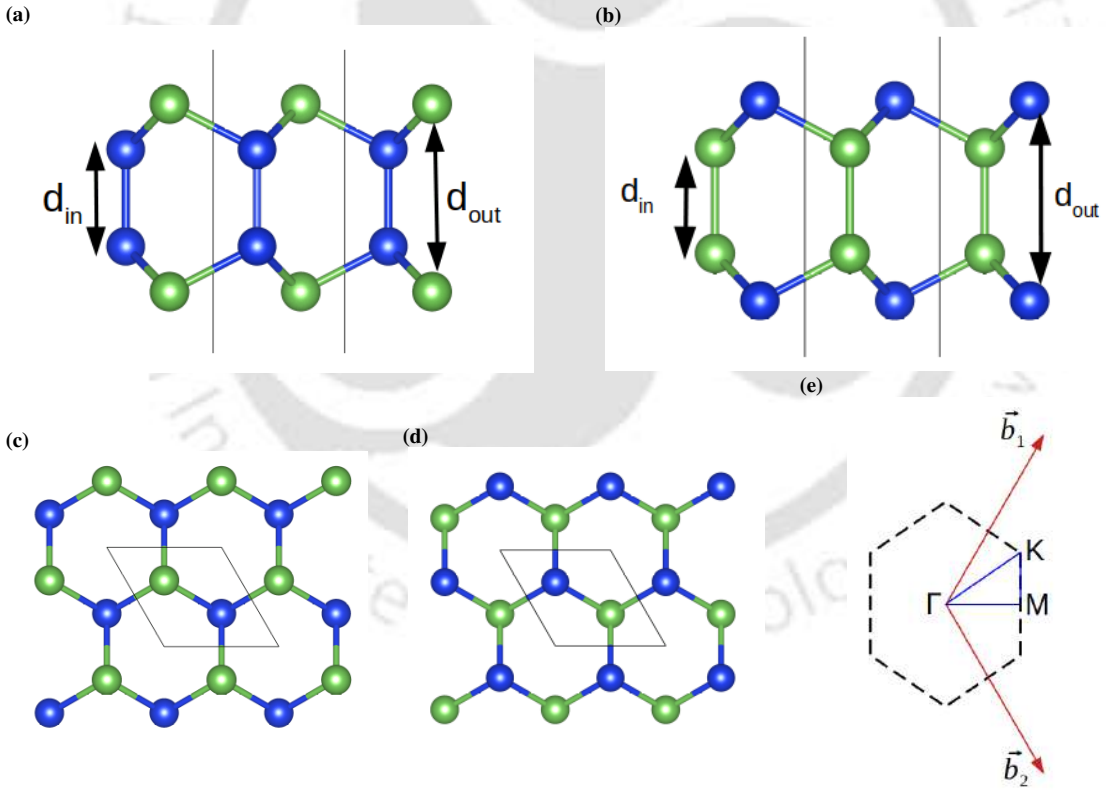

Figure 3.1: (a,c) Side and top view of Si-X monolayer in configuration(1). (b,d) side and top view of Si-X monolayer in configuration(2). (e) represents the Brillouin zone of Si-X monolayers. d_{in} and d_{out} are the interplanar distances between inner and outer planes, respectively. The black solid line represents the unit cell consisting of four atoms. Blue and green spheres are the Si and group-V atoms, respectively.

In Table 3.1 we present the lattice parameter a and interplanar distances d_{in}, d_{out} depicted in Figures (3.1a),(3.1b). The calculated lattice parameters for configuration(1) agree with previously reported values [132, 131]. The gradual increase of a from SiN to SiBi is due to the gradually larger ionic radius of X, the group-V element. This trend can be seen in configuration(2) as well, with very little difference in the values across the configurations. Significant differences are, however, observed in interplanar distances.

In configuration(1), the interplanar distance d_{in} between the inner planes has a weak variation, ostensibly due to the fact that these planes are occupied by Si atoms. In configuration(2), the variations in d_{in} across compounds are substantial and non-monotonic. The systems with X having the smallest and largest ionic radii, SiN and SiBi, have much larger distances between planes containing X atoms. The distance between outer planes, d_{out}, however, increases as one goes from SiN to SiBi, irrespective of the configuration, though the magnitudes are much larger in the case of configuration(2). This is consistent with the trend that d_{in}, as a general trend, is larger in configuration(2).

System	Configuration(1)			Configuration(2)		
	a(Å)	d_{in}(Å)	d_{out}(Å)	a(Å)	d_{in}(Å)	d_{out}(Å)
SiN	2.90	2.42	3.54	2.88	3.27	4.49
SiP	3.53	2.37	4.40	3.52	2.29	4.50
SiAs	3.69	2.36	4.57	3.73	2.56	4.86
SiSb	4.01	2.36	4.82	4.05	2.92	5.42
SiBi	4.15	2.35	4.90	4.22	3.14	5.67

Table 3.1: Lattice constant a(Å) and interplanar distances (d_{in}(Å) and d_{out}(Å)) of Si-X monolayers in both configurations.

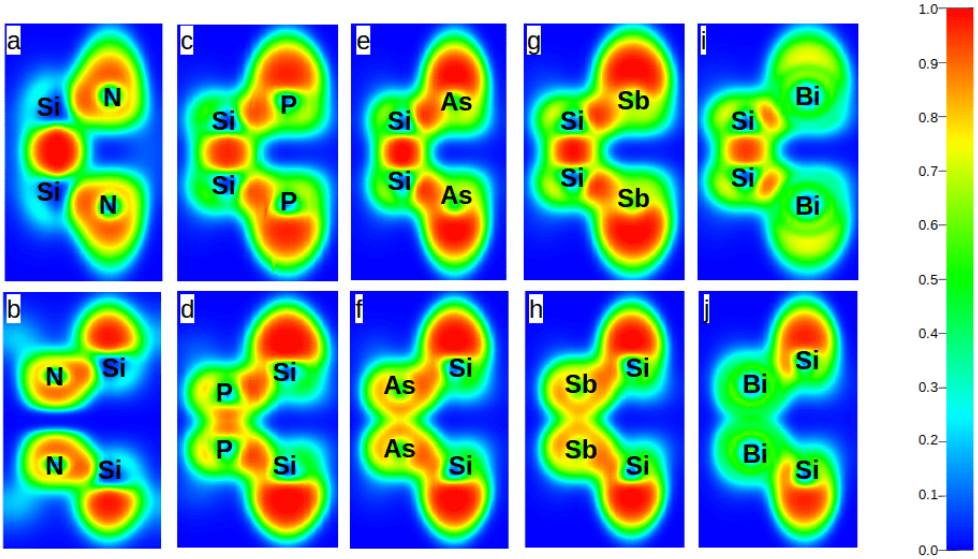

Figure 3.2: Electron localization function of all the 2D Si-X monolayers in both configuration(1)[a,c,e,g,i] and configuration(2)[b,d,f,h,j].

To get an insight into the consequences of the anomaly in d_{in} for SiN and SiBi, we look at the bonding characteristics of the Si-X monolayers in both configurations by computing the electron localisation function (ELF)[135]. The results are presented in Fig.3.2. The value of ELF varies from 0 to 1, with 1(0) implying complete (no) localisation. This also implies the relative strengths of the covalent bonds formed. Our results suggest that monolayers in configuration(1) have stronger covalent bonds between the two inner plane atoms(Si-Si). The Si-X bonds for all cases except SiBi are comparatively weaker, though only slightly. Si-Bi bonds in SiBi are substantially weaker than others. The scenario is very different in configuration(2). The electrons in the inner plane are less localised as compared to configuration(1), implying weaker covalent bonds between X-X atoms. This has a substantial effect on the thermal conductivity, as can be seen later. The strengths of Si-X bonds, however, are comparable to those in configuration(1). A stark contrast is observed in cases of SiN and SiBi. In these two compounds, in configuration(2), there is no significant covalent bonding among N-N and Bi-Bi lying in the inner planes. This can be correlated with anomalously large d_{in} observed for these two and may have serious effects on their stabilities in this configuration.

To examine the stability of the monolayers in different configurations, we next investigate their energetic, dynamical, and mechanical stabilities. The energetic stability is checked by the computation of their formation energies.

$$E_f = [E_{Si-X} - n_{Si}E_{Si} - n_X E_X]/(n_{Si} + n_X) \tag{3.1}$$

where, E_{Si}, E_X are the total energies of isolated single atom, E_{Si-X} is the total energy of the monolayer, and n_X, n_{Si} denote the number of Si and group-V atoms in the unit cell. The results are shown in Table 3.2.

System	Formation energy (eV/atom)	
	Configuration(1)	Configuration(2)
SiN	-7.50	-6.71
SiP	-5.49	-5.17
SiAs	-5.05	-4.67
SiSb	-4.58	-4.24
SiBi	-4.36	-3.93

Table 3.2: Formation energies of Si-X monolayers in both configurations.

We find that irrespective of the stacking pattern, all compounds form in their monolayers with respective elemental phases as references. The formation energies in configuration(2) are lower in all cases, suggesting less energy requirement to form the compounds in this configuration.

The dynamical stabilities of the systems are examined by computing the phonon dispersion relations and densities of states. The results are presented in Figures.3.3 and 3.4. Except for SiN and SiBi in configuration(2), (Fig.3.4b and 3.4d), all other structures are dynamically stable. The dynamical instability in these two compounds in configuration(2) can be correlated to the weak covalent bonds between the X-X pairs as seen in Fig. 3.2. Since these two compounds in configuration(2) are dynamically unstable, they will not be considered for further discussion. Inspection of phonon spectra of the stable systems shows that in all cases, out of the three acoustic modes, two are linear, while one is quadratic at the Γ point. The quadratic behaviour of out-of-plane acoustic (ZA) mode at the Γ point is an essential requirement for 2D materials[136]. We also find a lot of anti-crossing of the modes, more prominently in configuration(2). Since this leads to enhanced anharmonic scattering, lowering of thermal conductivity is expected. The partial phonon densities of states clearly show that the acoustic(optical) branches are dominated by heavier(lighter) atoms except for SiP (Figures 3.3c, 3.3d) where the comparable masses of the constituents lead to comparable contributions from both of them throughout the spectrum.

Finally, we investigate the mechanical stability of only the systems that are dynamically stable by computing their elastic constants and checking whether the conditions related to the Born criteria are satisfied[118]. According to the Born criteria, $C_{11} > C_{12}$, $C_{11} > 0$, where C_{11} and C_{12} are the independent elastic constants. Computed values of C_{11} and C_{12} for the stable monolayers are shown in Table 3.3. The results clearly demonstrate that the criteria for mechanical stability are satisfied in all cases.

System	Configuration(1)		Configuration(2)	
	C_{11}(N/m)	C_{12}(N/m)	C_{11}(N/m)	C_{12}(N/m)
SiN	295.02	81.97	-	-
SiP	132.95	24.13	110.92	20.78
SiAs	110.19	22.13	86.78	18.89
SiSb	82.32	18.63	67.97	16.63
SiBi	68.63	18.14	-	-

Table 3.3: Elastic constants, C_{11} and C_{12} of the Si-X structures for both configurations.

3.3.2 Band Structure and Electronic properties

The electronic band structures for all the stable monolayers are shown in Fig. 3.5. All systems are semiconducting in nature, irrespective of the stacking pattern. The computed band gap values are presented in Table 3.4. Calculated band gaps in configuration(1) have an excellent agreement with earlier work [132]. For both configurations, the band gap decreases as we move from SiN to SiBi, the exception being SiAs in configuration(1). There is a substantial decrease in band gaps when the stacking pattern changes from configuration(1) to configuration(2). This implies that the ideal operational temperatures for optimal thermoelectric effect are expected to be lower for configuration(2) [9]. In configuration(1), all band gaps are

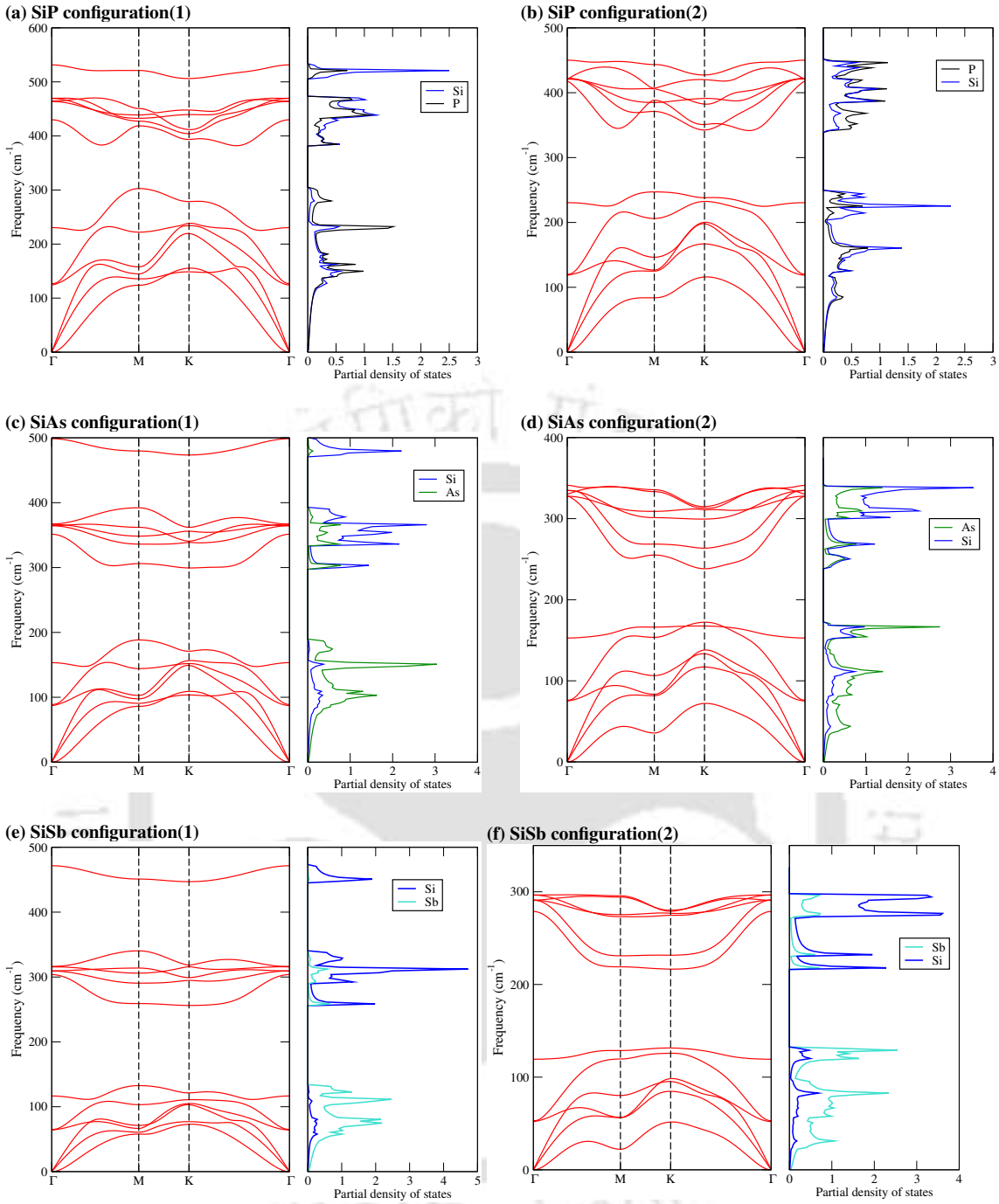

Figure 3.3: Phonon dispersions and densities of states of SiP, SiAs, and SiSb in both configurations.

indirect ones with the conduction band minima (CBM) at M point, and the valence band maxima (VBM) at the Γ point for SiAs, SiBi, and SiSb. The VBM for SiN and SiP are along $\Gamma - K$ direction. In configuration(2), the VBM moves to the K point for SiP and SiAs, while CBM is at K for SiAs and SiSb and at M in the case of SiP, transforming SiAs from an indirect to a direct band gap semiconductor. A feature common to all three monolayers in configuration(2) is the presence of flat bands near CBM, in stark contrast to the bands in configuration(1). This would have a significant impact on the transport properties as there will be non-negligible changes in the electron effective masses.

In order to understand the key features in the band structures and to get a possible explanation for the significant decrease of band gaps in configuration(2), we compute the total and atom-projected densities of states (Fig. 3.6). One of the key features in configuration(1) is the presence of a sharp peak right below the Fermi levels in SiP, SiAs and SiN. These Van Hove singularities in the densities of states are the manifes-

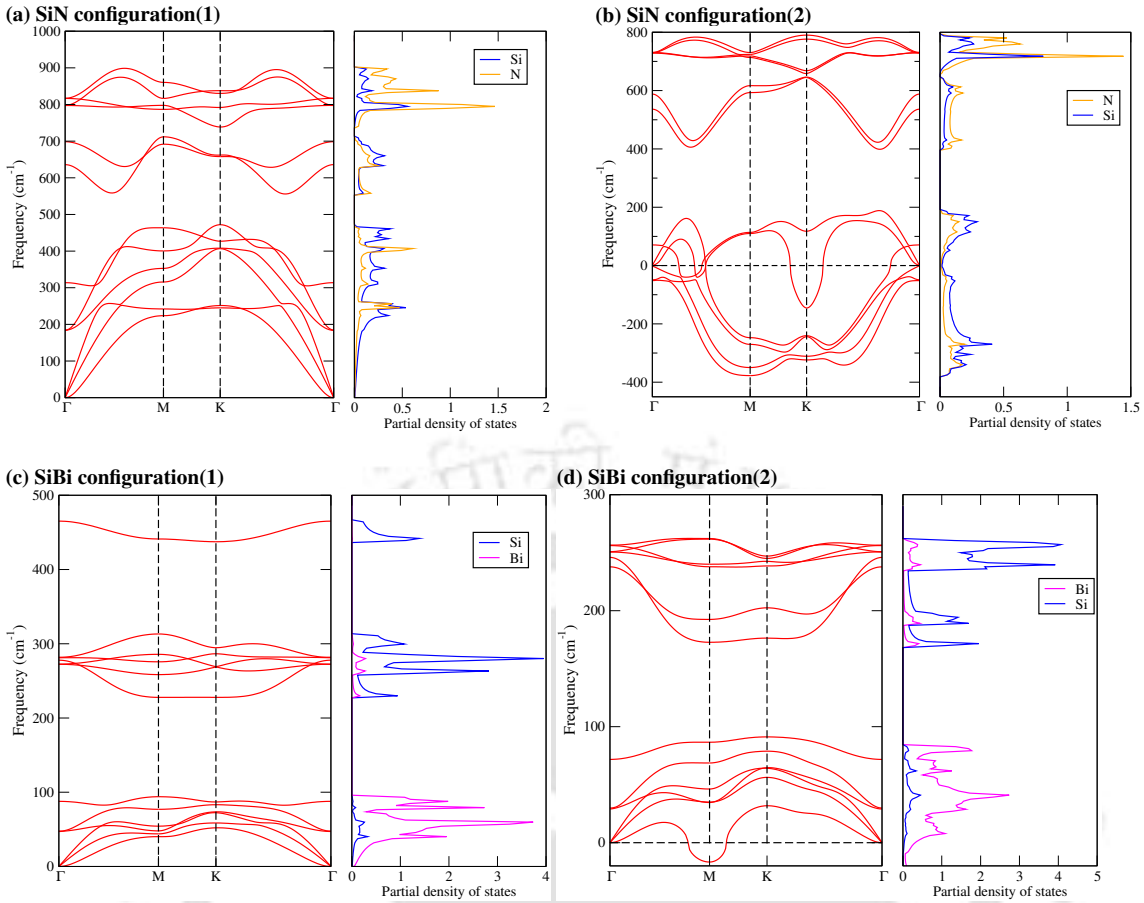

Figure 3.4: Phonon dispersions and densities of states of SiN and SiBi in both configurations

System	Band gap (E_g eV)	
	Configuration(1)	Configuration(2)
SiN	1.74	-
SiP	1.52	0.91
SiAs	1.63	0.64
SiSb	1.18	0.66
SiBi	0.67	-

Table 3.4: Electronic band gap E_g (in eV) calculated for Si-X monolayers in both configurations.

tations of the flat nature of VBM in these compounds. For all monolayers in configuration(1), the VBM is contributed by the p states of Si and X. The CBM regions are dominated by the p orbitals of the X atom. In configuration(2), the sharp peak corresponding to the Van Hove singularity in VBM of SiP moves away from the band edge while it appears at the VBM of SiSb. These features are consistent with the changes in the VBM as shown in Fig. 3.5. The VBM of all three compounds is now contributed by s-orbitals (along with p orbitals) of both atoms. The CBM now results from significant hybridisation of Si p and both s and p orbitals of the X atoms. This results in a shift of the CBM towards lower energies and a reduction in electronic band gaps.

In what follows, we explore the carrier transport phenomena using the deformation potential (DP) theory developed by Bardeen and Shockley [111]. According to DP theory, the carrier mobilities in a semiconductor are primarily determined by the interaction of electrons and acoustic phonons. The carrier mobility is calculated using the following expression:

$$\mu_{2D} = \frac{2e\hbar^3 C_{2D}}{3k_B T|m^*|^2(E_D)^2} \tag{3.2}$$

μ_{2D} is the carrier mobility, C_{2D} is the in-plane stiffness constant, m* the effective mass of the carrier (elec-

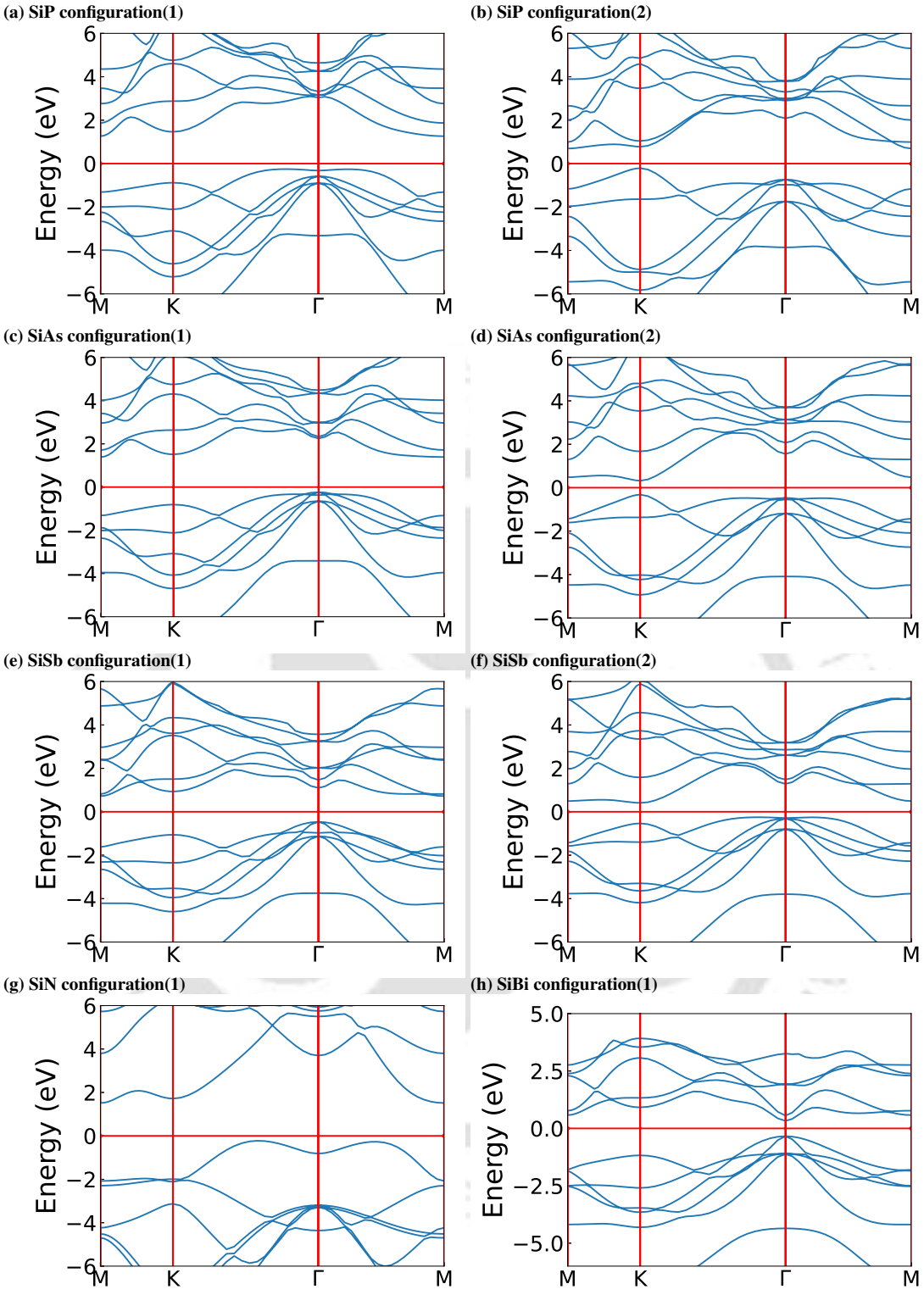

Figure 3.5: Band structures of Si-X(=N, P, As, Sb, Bi) monolayers in both configurations.

tron/hole), E_d the deformation potential, e and $\hbar$ the electron charge, and Planck's constant, respectively. The in-plane stiffness is evaluated using $C_{2D} = \frac{1}{A_0}\left(\frac{\partial^2 E}{\partial \delta^2}\right)$, where δ is the biaxial strain, and A_0 is surface area at equilibrium volume. The biaxial strain is defined as $\delta = \frac{\Delta a}{a_0}$, where a_0 is equilibrium lattice constant. The Effective mass $m^* = \hbar^2\left[\frac{\partial^2 E(k)}{\partial k^2}\right]^{-1}$, is obtained by quadratic fitting of band edges, where k and $E(k)$ are the wave vectors and band energies, respectively. The deformation potential constant is a

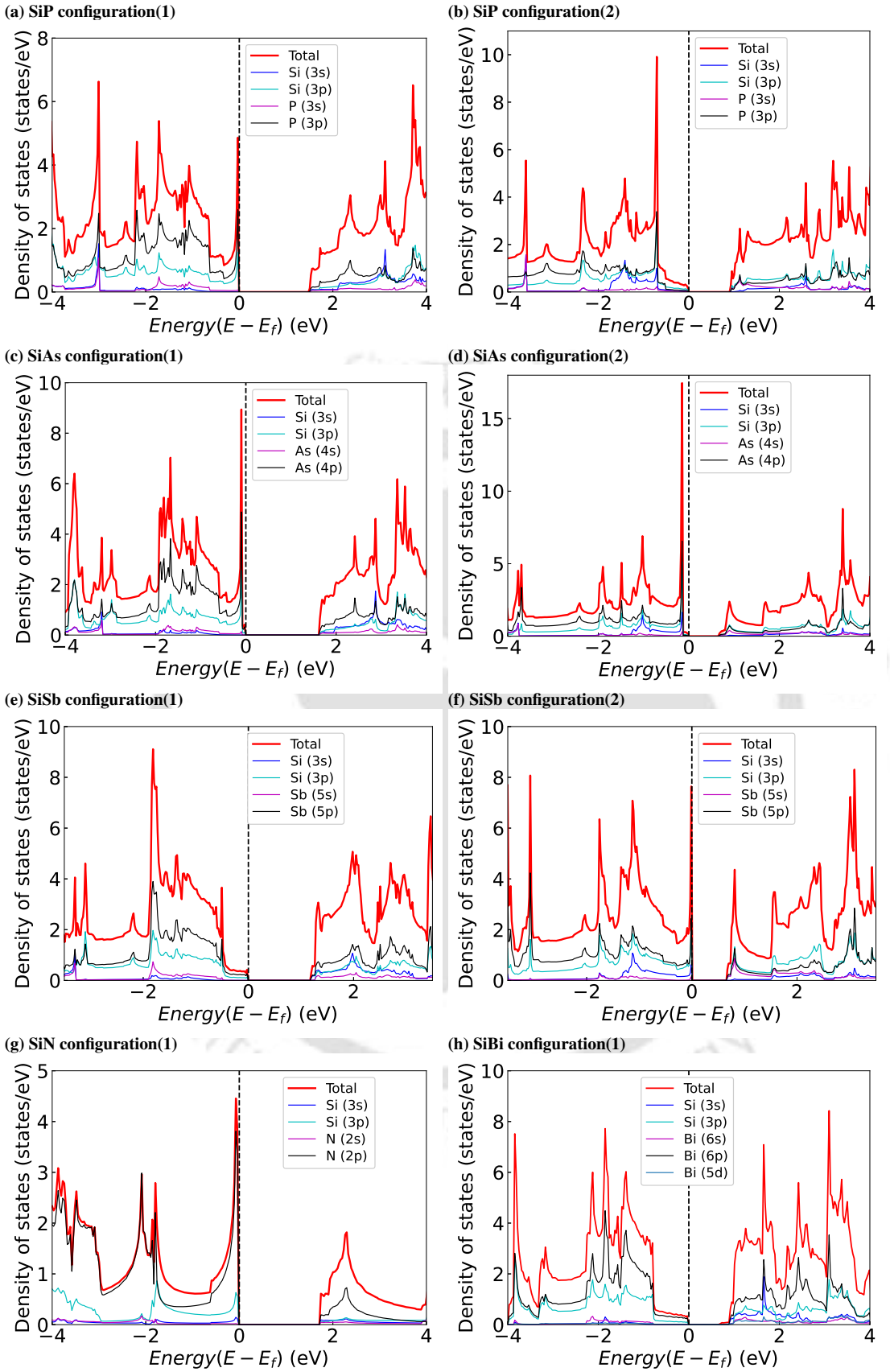

Figure 3.6: Total and atom-projected density of States (a-b) SiP, (c-d) SiAs, (e-f) SiSb in both configurations, and (g) SiN, (h) SiBi in configuration(1).

measure of the strength of electron-phonon coupling in the valence and conduction regions. DP constant $E_d = \frac{\partial E_{edge}}{\partial \delta} = \frac{\Delta E_{CBM/VBM}}{\Delta strain(\%)}$, depicts how the conduction or valence band edges shift under the applied strain. Once all the parameters required in Equation (3.2) are known, we calculate the carrier mobility μ. The relaxation time τ for the carriers is calculated using $\tau = \frac{\mu m^*}{e}$.

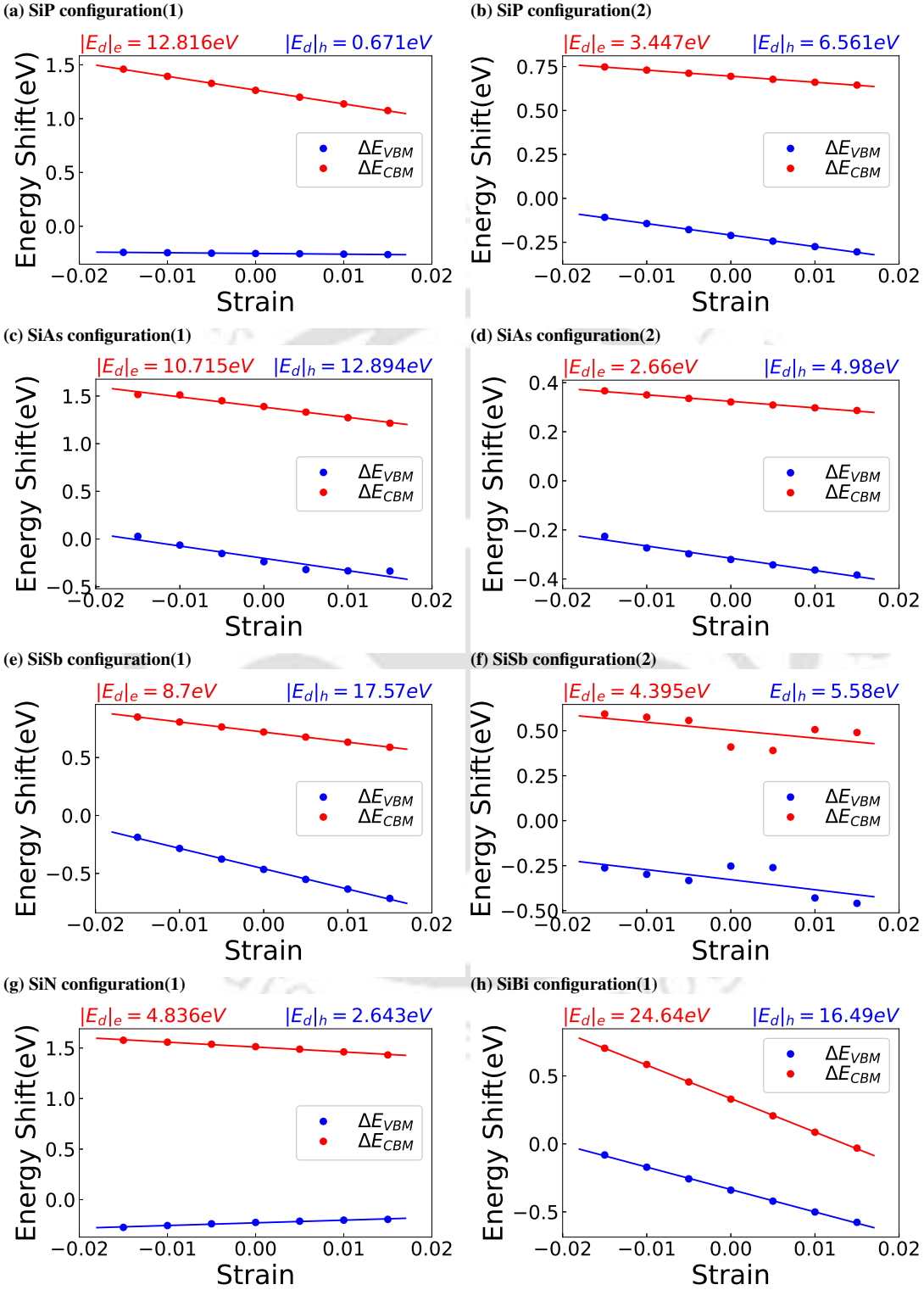

Figure 3.7: Shift in band edges of Si-X monolayers due to biaxial strain. Blue(red) circles stand for $\Delta E_{VBM}(\Delta E_{CBM})$, the shift in valence band maxima(Conduction band minima). Solid lines show linear fitted values.

In order to compute C_{2D} and E_d, we applied biaxial strain from -1.5% to 1.5% for all the monolayers. Fig. 3.7 shows the shift of the band edges with applied strain. The calculated value of m^*, E_d, C_{2D}, μ, and τ

System	Carrier	Configuration(1)								
		m^*/m_0	$E_d(eV)$	$C_{2D}(N/m)$	$\mu(10^4 cm^2V^{-1}s^{-1})$			$\tau(fs)$		
					$T=300K$	$T=500K$	$T=800K$	$T=300K$	$T=500K$	$T=800K$
SiN	e	0.384	4.8	750.00	0.3075	0.1845	0.1153	671.48	402.9	251.806
	h	0.786	2.6		0.2458	0.1474	0.0921	1098.68	659.20	412.00
SiP	e	0.132	12.8	314.19	0.1552	0.0931	0.0582	116.46	69.88	43.67
	h	1.974	0.6		0.2531	0.1518	0.0950	2841.17	1704.70	1065.4
SiAs	e	0.130	10.7	264.65	0.1929	0.1156	0.0723	142.60	85.50	53.44
	h	0.552	12.8		0.0073	0.0044	0.0027	23.10	13.91	8.69
SiSb	e	0.185	8.7	201.91	0.1102	0.0661	0.0413	115.88	69.53	43.46
	h	0.477	17.5		0.0040	0.0024	0.0015	11.03	6.62	4.14
SiBi	e	0.096	24.6	173.55	0.0438	0.0263	0.0164	23.93	14.35	8.97
	h	0.466	16.4		0.0041	0.0025	0.0015	11.01	6.60	4.13

Table 3.5: Effective mass, DP constant, In-plane stiffness, Carrier mobility, and Relaxation times of electrons and holes for configuration(1) of Si-X monolayers.

System	Carrier	Configuration(2)								
		m^*/m_0	$E_d(eV)$	$C_{2D}(N/m)$	$\mu(10^4 cm^2V^{-1}s^{-1})$			$\tau(fs)$		
					$T=300K$	$T=500K$	$T=800K$	$T=300K$	$T=500K$	$T=800K$
SiP	e	0.254	3.4	263.43	0.4856	0.2914	0.1821	701.52	420.91	263.07
	h	0.248	6.5		0.1406	0.0843	0.0527	198.34	119.00	74.37
SiAs	e	0.224	2.6	211.36	0.8414	0.5048	0.3155	1071.78	643.07	401.92
	h	0.195	4.9		0.3167	0.1900	0.1187	351.26	210.75	131.72
SiSb	e	0.385	4.3	169.21	0.0835	0.0501	0.0313	182.87	109.72	68.57
	h	2.226	5.5		0.0015	0.0009	0.0005	19.62	11.77	7.36

Table 3.6: Effective mass, DP constant, In-plane stiffness, Carrier mobility, and Relaxation times of electrons and holes for configuration(2) of Si-X monolayers.

for configuration(1) and configuration(2) are presented in tables 3.5 and 3.6. The largest E_d for both carriers is obtained for SiBi in configuration(1) due to the largest variations in ΔE. In general, E_d for configuration(2) is smaller than that in configuration(1), due to weaker variations of the band edges with strain in configuration(2). In configuration(2), variations in ΔE_{CBM} are less than variations in ΔE_{VBM} leading to larger E_d for holes. There is no such trend in configuration(1). On the other hand, C_{2D} decreases monotonically as the atomic number of X increases in SiX(from SiN to SiBi). This decrease in the in-plane stiffness constant as X changes from N to Bi is indicative of the gradual weakening of the bonds. This is consistent with the features observed in the ELF plots. Smaller values of C_{2D} in configuration(2) for each of the three materials suggest that for a given system, bonds are weaker when the stacking changes with middle planes occupied by the group-V elements, a result corroborating the interpretations of the ELF. Clear trends are observed for the effective masses m^* and mobilities μ. In configuration(1), $m_h^* > m_e^*$; $m_h^*(m_e^*)$ is the effective mass of holes(electrons). In configuration(2), it is the opposite with little difference between m_h^* and m_e^* except SiSb where m_h^* is significantly larger than m_e^*. If we compare between the two configurations, the general trend is m_e^*(configuration(1)) < m_e^*(configuration(2)), m_h^*(configuration(1))> m_h^*(configuration(2)), only exception being SiSb where m_h^*(configuration(1))< m_h^*(configuration(2)). The trends can be understood from the features in the band structure near VBM and CBM. The flat bands near VBM in configuration(1) give rise to larger hole effective mass while the larger electron effective mass in configuration(2) is due to bands getting flatter near CBM. The comparative features of effective masses across configurations too can be understood from the band structures. Carrier mobility μ too exhibit clear trends: in configuration(1), $\mu_e > \mu_h$ except for SiP, $\mu_e > \mu_h$ for all three systems in configuration(2),μ_e(configuration(1))(μ_h(configuration(2))< μ_e(configuration(2))(μ_h(configuration(1)) for all systems except SiSb(SiAs). The variations in μ can be understood from the variations in E_D and m^* as they appear as square terms in Equation 3.2. In configuration(2), since $m_h^* \sim m_e^*$, larger E_d values for holes lead to smaller hole mobility. In configuration(1), E_d for holes are larger than E_d for electrons except in cases of SiP and SiN. About 20 times larger E_d values for electron carriers in SiP become a decisive factor, making $\mu_h > \mu_e$. The effects are not so large for SiN, hence the trends among electron and hole mobilities follow the rest. The trends of carrier mobilities across configurations can also be explained the same way. It turns out that E_d is the deciding factor in most cases. Among all the studied monolayers, the maximum mobility is observed for electrons in SiAs in configuration(2). As a general trend, significant differences in carrier mobilities of the two carrier types help avoid charge recombination and have impactful consequences in the transport properties. Calculated relaxation times show significantly larger values for electrons when the systems are in configuration(2). Our results qualitatively agree with those of Reference [132].

3.3.3 Thermoelectric properties

The flat bands at the band edge, giving rise to Van Hove singularities in the densities of states, and configuration-dependent moderate to low band gaps propel us to further study the transport properties, leading to the assessment of the potential of these compounds in thermoelectric applications.

Electronic transport properties

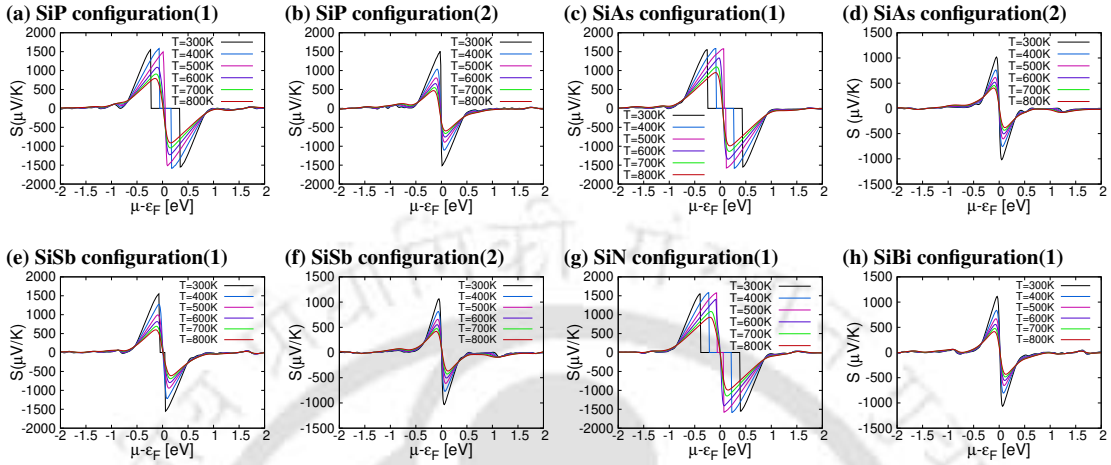

Figure 3.8: Seebeck coefficient (S) of Si-X monolayers in different configurations as a function of chemical potential (μ).

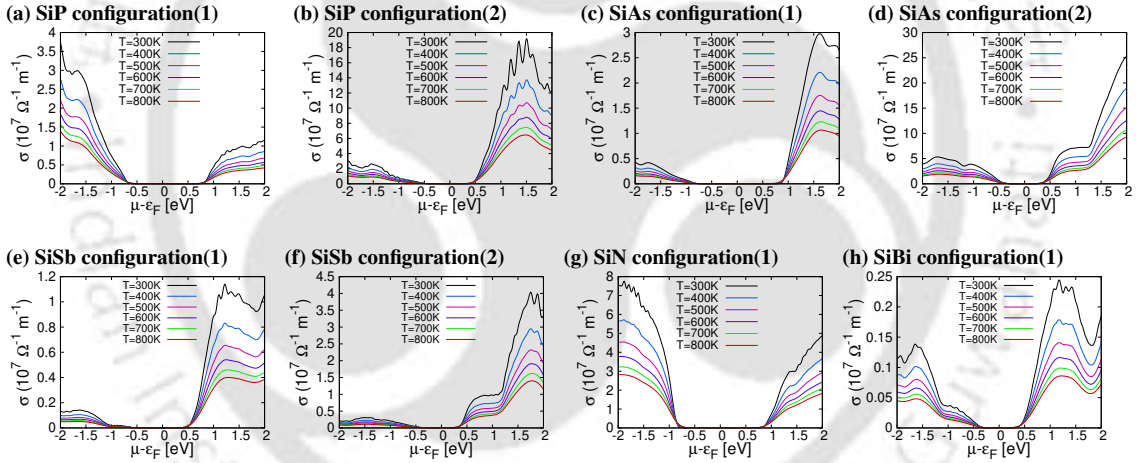

Figure 3.9: Electrical conductivity (σ) of Si-X monolayers in different configurations as a function of chemical potential (μ).

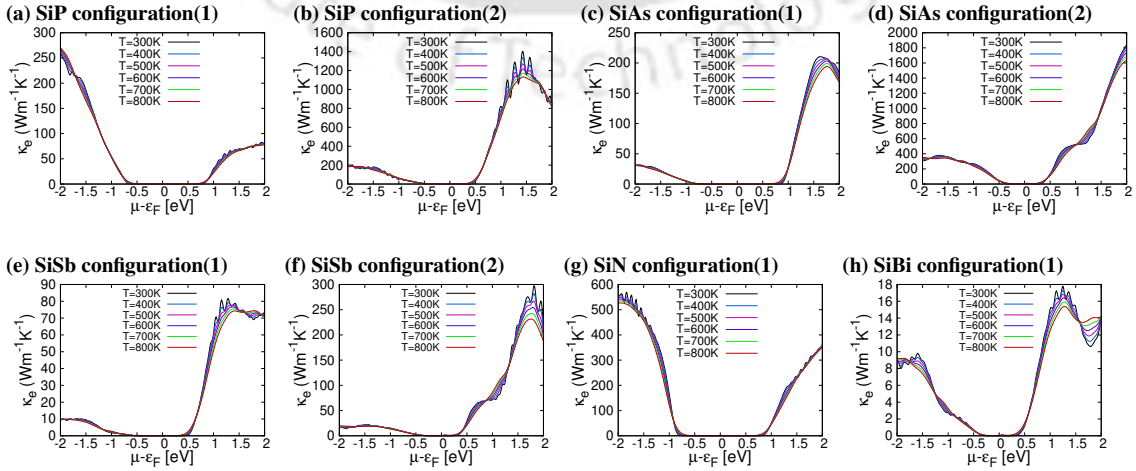

Figure 3.10: Electronic thermal conductivity (κ_e) of Si-X monolayers in different configurations as a function of chemical potential (μ).

In order to determine the thermoelectric figure of merit, we need to calculate the Seebeck coefficient (S), electrical (σ), and thermal conductivities (κ). Employing constant relaxation time approximation(CRTA) and rigid band approximation (RBA) we calculate $S, \sigma/\tau$, and κ_e/τ. Using the τ calculated from DP theory, σ and κ_e can be obtained. The results for S, σ and κ_e are shown in Figures 3.8,3.9,and 3.10, respectively. The results indicate the following trends: (1) S (configuration(1))> S(configuration(2)) (2)σ (configuration(1))< σ (configuration(2)) and (3) κ_e (configuration(1)) < κ_e (configuration(2)). In configuration(1), the maximum value of S is 1500 $\mu V/K$, whereas, in configuration(2), S is 1000 $\mu V/K$ for all studied monolayers. Seebeck coefficient depends on several factors; for parabolic band and energy independent scattering, S is directly proportional to effective mass (m^*) and inversely proportional to the carrier concentration n; the relation being $S = \frac{8\pi^2 k_B^2 m^* T}{3eh^2}\left(\frac{\pi}{3n}\right)^{2/3}$. This proportionality between S and m^* is reflected in our calculated results. Larger m_h^* in configuration(1) gives rise to larger Seebeck coefficient. The qualitative trend in the configuration dependence of σ observed in our calculations can be understood from the fact that S and σ have an inverse relationship. The electronic part of thermal conductivity, κ_e, follows σ as obtained in our calculations. This is consistent with Wiedmann-Franz law relating the two transport parameters as $k_e = L\sigma T$.

Lattice thermal conductivity

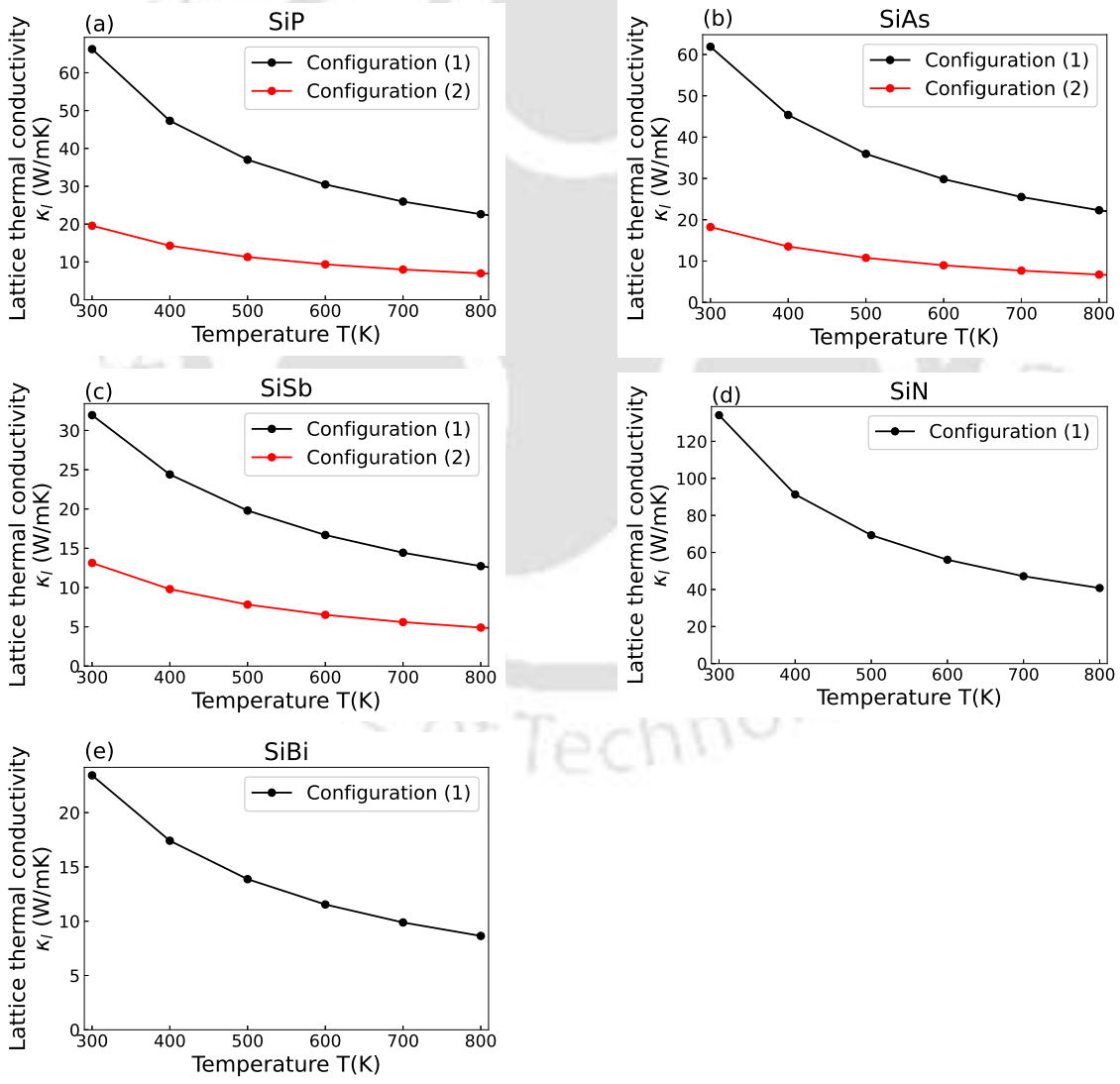

Figure 3.11: Lattice thermal conductivity κ_l as a function of temperature for of (a) SiP, (b) SiAs, (c) SiSb, (d) SiN, and (e) SiBi monolayers. Results for both configurations of SiP, SiSb, SiAs and for configuration(1) of SiN and SiBi are shown.

Lattice thermal conductivity (κ_l) may play a significant role when the stacking pattern changes, as is seen in the case of group III-VI monolayers with hexagonal symmetry[134]. Regarding the electronic transport coefficients, we found that σ and κ_e are substantially higher for configuration(2). This might reduce the figure-of-merit when planes are stacked according to configuration(2). In semiconductors or dielectrics, phonons are the majority of heat carriers. So if by any means (phonon-phonon scattering, impurity scattering, doping, etc.) heat carriers are stopped from reaching one end to the other of the material, lattice thermal conductivity decreases. Inclusion of lattice thermal conductivity is, therefore, crucial as it will provide the figure-of-merit values closer to reality, a requirement to understand the real potential of these monolayers as thermoelectric materials. Using the second (harmonic) and third (anharmonic) order force constants, κ_l is calculated for the monolayers in two different configurations. The results are presented in Fig. 3.11. We find a lowering of κ_l by about 60% as the configuration changes from 1 to 2. Further, in both configurations κ_l undergoes substantial reduction as temperature increases. Such an inverse relationship of thermal conductivity and temperature suggests that the Umklapp process can be considered to better address the phonon scattering. At 300K, κ_l values in configuration(2) are substantially lower than the ones reported for technologically important 2D materials; graphene [73], h-BN [137] and MoS_2 [138] having κ_l values of 3716.6 W m^{-1} K^{-1}, 791 W m^{-1} K^{-1} and 34.5 W m^{-1} K^{-1}, respectively.

To better understand the issue, in Fig. 3.12, we show the normalised cumulative thermal conductivities (κ_c/κ_l) as a function of phonon frequency. The results are presented for 300 K only. Phonons with mean free paths below a threshold are responsible for κ_c/κ_l to become 1.

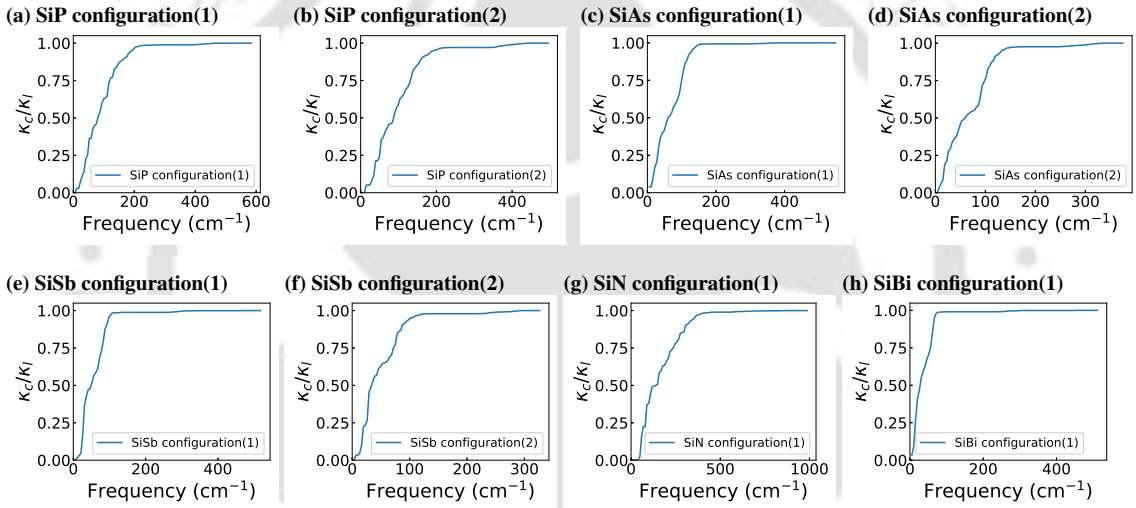

Figure 3.12: Normalized cumulative lattice thermal conductivity of Si-X monolayers as a function of phonon frequency at 300 K .

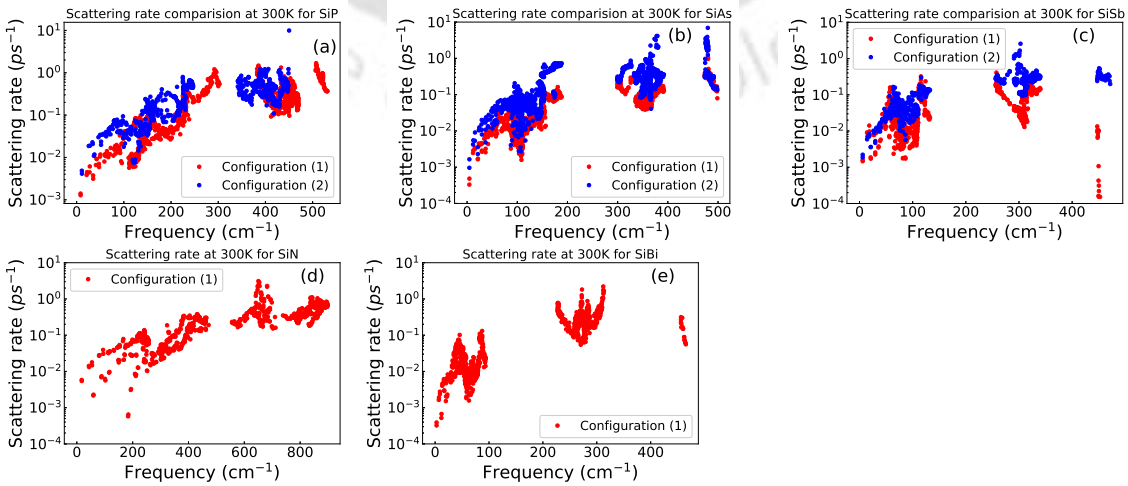

Figure 3.13: Anharmonic scattering rates of (a) SiP, (b) SiAs, (c) SiSb, (d) SiN, and (e) SiBi monolayers at 300 K.

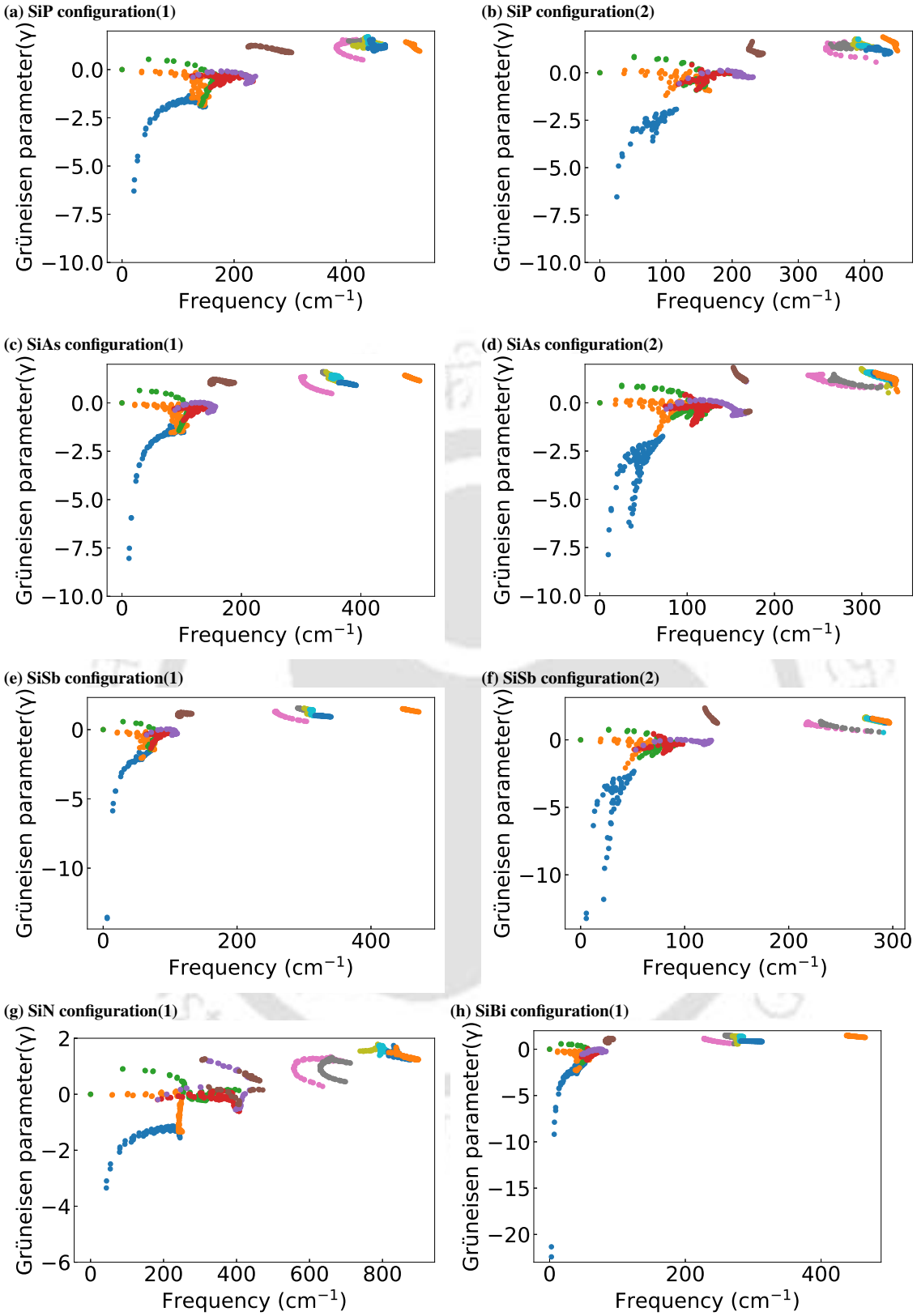

Figure 3.14: Gruneisen parameters (γ) for Si-X monolayers in both configurations.

Our calculations show that for all the monolayers, irrespective of configurations, the phonon modes contributing maximum to the cumulative thermal conductivities are the three acoustic and two optical modes. That these are the modes responsible largely for the lattice thermal conductivity can also be understood from their locations in the phonon spectra and the anti-crossing behaviour demonstrated in Figures (3.3a)-(3.3f).

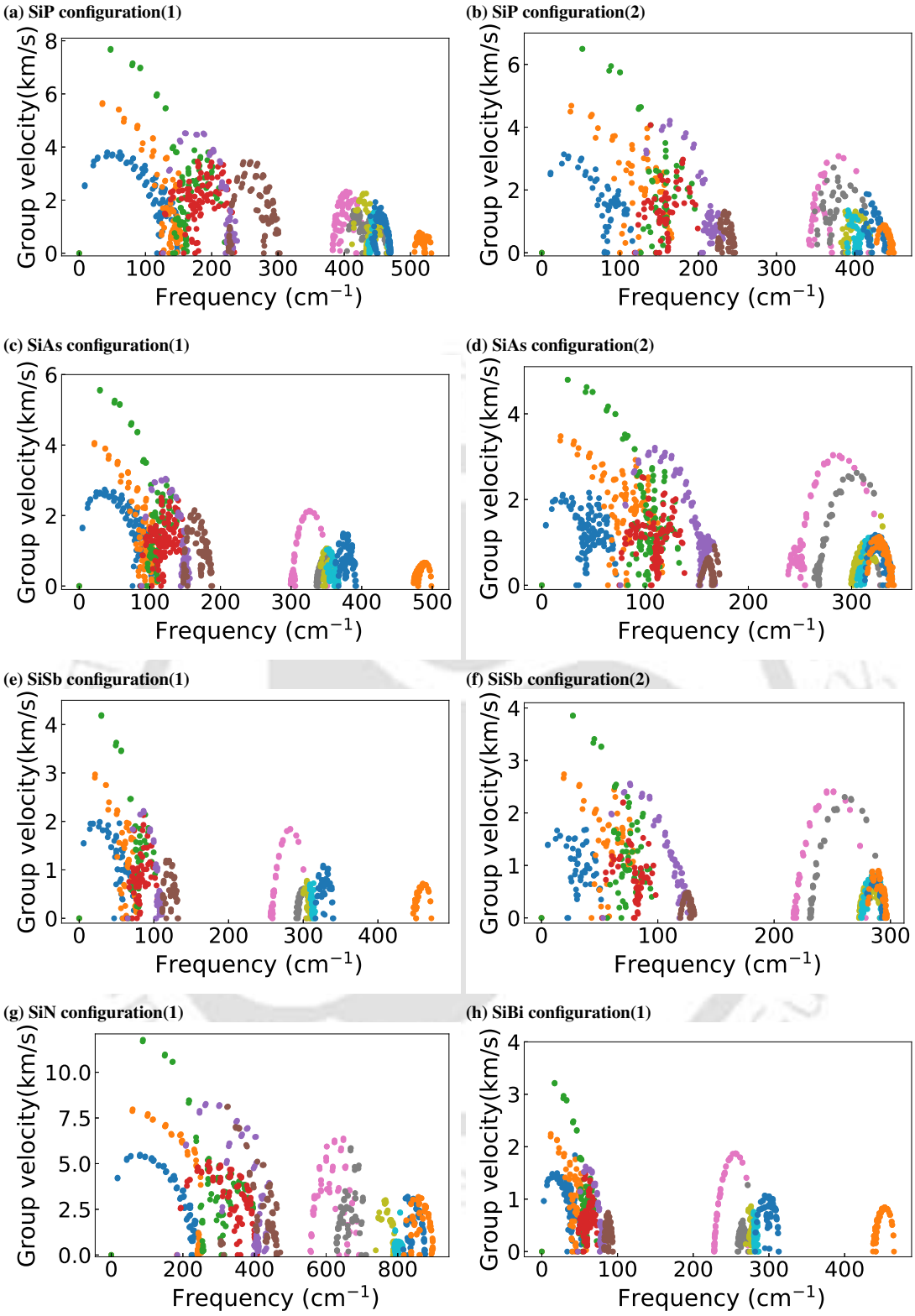

Figure 3.15: Calculated phonon group velocity (v_g) of Si-X monolayers in both configurations.

Anharmonic phonon-phonon scattering is known to be the dominating factor for thermal conductivity κ_l. We further explore the role of anharmonic scattering to understand the low values of κ_l and their dependences on configurations by analysing the third-order force constants obtained from first-principles calculations. We do so by looking at the anharmonic scattering rates (Fig. 3.13), Gruneisen parameter γ (Fig. 3.14,) which is a measure of anharmonic scattering strengths and phonon group velocities (Fig. 3.15) in both configurations.

Analysis of the scattering rates confirms that the scattering occurs mostly in the frequency region contributed by the three acoustic and two optical modes. The lower scattering rate leads to a higher thermal conductivity. The results of Fig. 3.13 are consistent with this: the largest κ_l in configuration(1) of SiN is due to crowding of modes with lower scattering rates. Similarly, a larger weight in the higher scattering rate for SiBi is responsible for the lowest κ_l in configuration(1). The thermal conductivities of SiP and SiAs undergo more significant reductions in configuration(2). This can be correlated to the availability of more phonon channels with higher scattering rates as shown in Fig. 3.13.

The results of the Grüneisen parameter γ reveal the following: (1) the low-frequency acoustic phonons are more anharmonic than the optical phonons, and (2) for a given system in configuration(2), the acoustic modes are more anharmonic than those in configuration(1). More anharmonic means strong phonon-phonon coupling, a higher value of the Grüneisen parameter, and thus the reduced value of κ_l [139]. These perfectly correlate with the variations of κ_l with stacking pattern, and that the anharmonicity is largely due to the low-frequency acoustic modes. The variations in the phonon group velocity are also in agreement with this interpretation.

In Fig. 3.15, SiN in configuration(1) has the largest group velocities of the low-frequency modes, leading to the highest κ_l, while the opposite happens for SiBi. For SiP and SiAs, v_g in configuration(2) is visibly less than those in configuration(1), while for SiSb, the difference is less. This explains the relatively large reduction in κ_l for the former two.

Figure of merit

In Fig. 3.16, we present the calculated figure of merit, $ZT = (S^2\sigma/\kappa)T$, as a function of carrier concentration(n) at temperatures 300-800 K. Results for all configurations and for both electron and hole doping are shown. The carrier concentration n is taken to be $\sim 10^{20}$ cm^{-3}. We find that for all three cases where structures are stable in both configurations, stacking pattern configuration(2) leads to $\sim$ 2-6 times larger maximum ZT in comparison with configuration(1). The highest ZT, 3.23 at 800 K, is obtained for SiP in configuration(2) for electron doping. The maximum ZT decreases consistently as the size of the X atoms becomes larger. However, in all three systems with stable configuration(2), a minimum of $ZT \sim 1.4$ is obtained. In configuration(1), this is the maximum value of ZT obtained for SiN. While for configuration(2), the maximum ZT is obtained for electron doping, no such trend is observed in the case of configuration(1). The lowest ZT is obtained for SiBi, the maximum value being 0.13 only. The largest ZT for SiP in configuration(2), however, cannot be attributed to lattice thermal conductivity κ_l alone. On the contrary, at 800K, κ_l had the highest value in the case of SiP among the three systems. Also, κ_e for SiP in configuration(2) was significantly higher than SiSb (which had a lower κ_l than SiP) in the same configuration. However, electrical conductivity σ and Seebeck coefficient S for SiP in configuration(2) are higher than SiAs and SiSb in configuration(2). Thus, though the larger ZT as one changes the configuration from (1) to (2) can be attributed to lower κ_l and higher σ in configuration(2), the trend in ZT among the compounds in configuration(2) is determined largely by the electrical conductivity parameters. This is qualitatively different from the case of group-III-VI chalcogenides [134] where lattice thermal conductivity was the key factor. Since all relevant factors are incorporated, our results are supposed not to deviate too much from the results of experimental measurement, although some differences are expected as approximations like consideration of only three-phonon scattering for lattice thermal conductivity calculation and use of CRTA for electronic transport parameters are invoked. In either case, our results might be overestimated. Nevertheless, overestimations in electronic and lattice thermal conductivities may cancel each other, and thus our calculated ZT may not be too far from reality. Also, in the recent literature [139], it has been found that considering a higher (fourth) order anharmonic scattering term further reduces the kappa. But the effect is small. Including the four-phonon scattering demands high computational power. So, for the present work, we refrain ourselves from considering higher-order scattering terms.

Finally, the thermoelectric efficiency of the compounds can be assessed by calculating thermoelectric conversion efficiency η, which is related to Carnot efficiency and ZT the following way

$$\eta = \frac{T_h - T_c}{T_h} \frac{\sqrt{1+ZT}-1}{\sqrt{1+ZT}+T_c/T_h}$$

T_h, T_c are temperatures at the hot and cold edges of the device, respectively. The Carnot efficiency is given by $\frac{T_h - T_c}{T_h}$. By taking $T_c = 300$K and T_h ranging from 300-800K, we calculated η for SiX monolayers. We find that only SiP in configuration(2) has a maximum efficiency of 27%. Therefore, we can infer that SiP in configuration(2) will have the best efficiency as a thermoelectric material. The maximum efficiency of

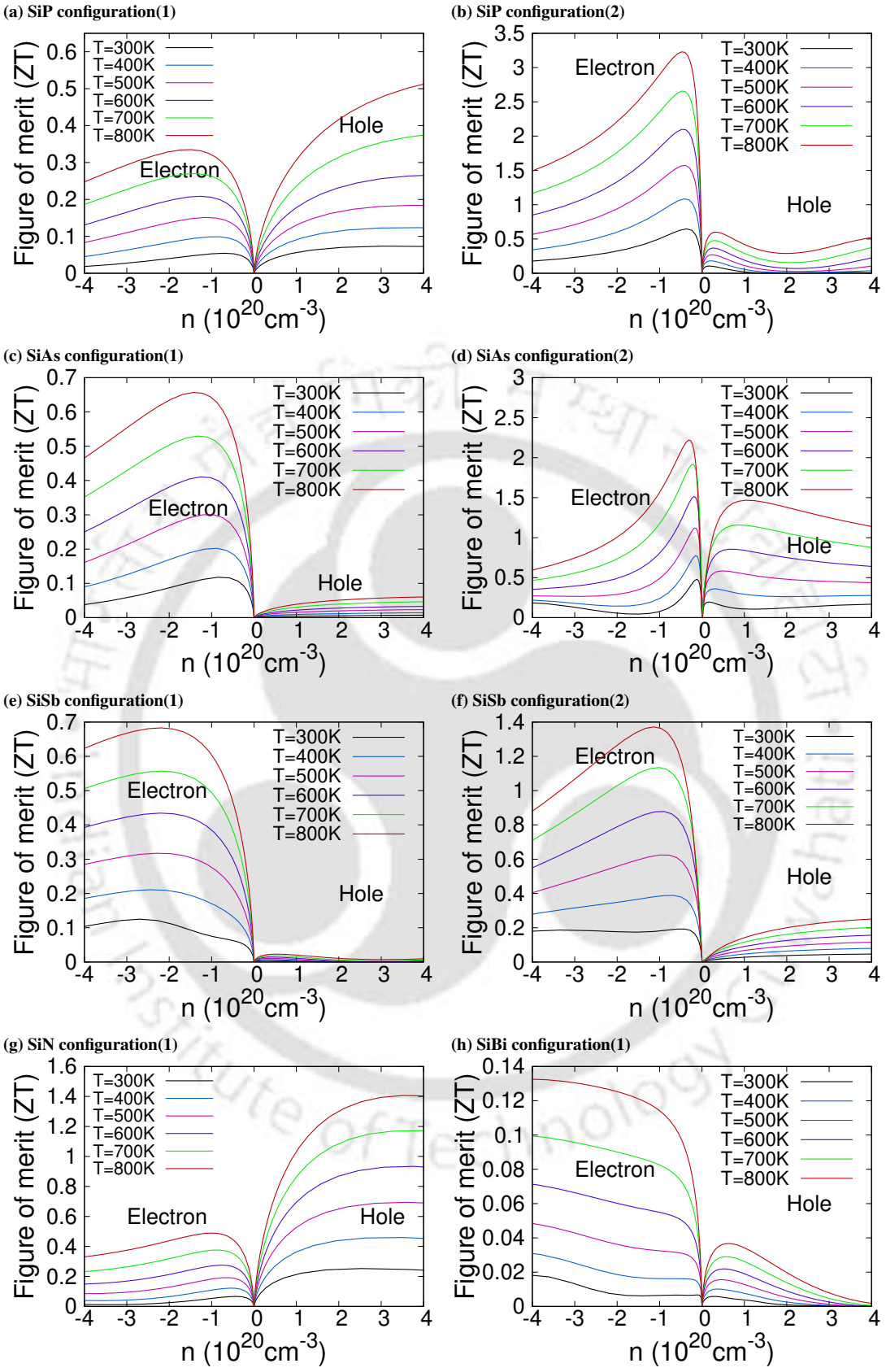

Figure 3.16: Thermoelectric figure of merit (ZT) of Si-X monolayers between 300 and 800 K.

SiAs(SiSb) in configuration(2) is $\sim$ 22%(18%). This means that the atomic arrangement in these monolayers is extremely crucial for exploiting their potential as thermoelectric devices.

3.4 Conclusions

In this chapter, we have systematically investigated the electronic, dynamical, and thermoelectric properties of hexagonal 2D Si-X (X=N, P, As, Sb, Bi) monolayers using first-principles calculations. With regard to the thermoelectric properties, earlier works on this series of compounds either did not incorporate the phonon contributions to the thermal conductivity or did not consider the structural effect through alternative stacking of Si and X planes. We have carried out a systematic comparative study of these compounds by incorporating lattice thermal conductivity and by investigating the changes in transport parameters due to the stacking of X-X planes in the inner layers as opposed to Si-Si planes in the conventional setup. We have shown that out of the five compounds, SiP, SiAs, and SiSb are stable in both configurations. We found significantly low lattice thermal conductivity and high electrical conductivity in configuration(2) for all cases, leading to larger values of the figure-of-merit. All three compounds in configuration(2) have the highest figure-of-merit greater than 1, with SiP having the largest value of 3.23 at 800 K. The origin of this lies in the flatness of the band edges, weaker bonds indicated by the ELF plots, and stiffness constant C_{2D}. The increased anharmonicity in the low-lying acoustic modes responsible for the lowering of the lattice thermal conductivity contributes as well. However, the trend in the figure-of-merit values among the compounds in configuration(2) is attributed mostly to the variations in the electronic transport parameters. This work demonstrates that Si-group V monolayers can be used as thermoelectric devices by tweaking the structural arrangement. This paves the way for the exploration of other compounds for thermoelectric applications and provides useful feedback to the experimentalists for the synthesis of new materials.

Chapter 4

Impacts of surface modification and strain engineering on thermoelectric properties of MXenes*

4.1 Introduction

MXenes, a unique class of 2D transition metal carbides and nitrides, were discovered in 2011. MXenes are the 2D derivates of ternary transition metal carbides/nitrides, the MAX compounds, obtained by selective etching of the "A" layer [140]. MXenes have the chemical formula $M_{n+1}X_nT_n$ (n=1-3), where M is the transition metal, X is carbon/nitrogen, and T is the functional group passivating the surfaces. The compositional flexibility of MXenes has made them useful for a multitude of applications [141, 142, 143]. Various first-principles simulations on different MXenes investigated structure-property relationships and provided useful information about their thermoelectric properties. Large S and κ_l smaller than reference 2D materials like Graphene and MoS_2 were obtained for Sc_2CT_x MXenes [144]. Calculations on Ti_2CT_x showed that despite larger specific heat and group velocity, phonon relaxation time lowered κ_l significantly in Ti_2CO_2 [145]. A comparative study of Ti_2CO_2, Zr_2CO_2 and Hf_2CO_2 [146] attributed comparatively lower κ_l (and higher ZT) in Ti_2CO_2 to increased Umklapp scattering involving acoustic and optical phonon branches. Investigations into the effects of structure on thermoelectric properties for these systems inferred that symmetry lowering can improve ZT drastically, mainly by lowering κ_l [147].

Lowering of symmetry in MXenes can be accomplished by changing the chemical composition of the transition metal surfaces. A large power factor in $Mo_2TiC_2T_x$ MXene was experimentally obtained at room temperature [148], enabling its use as a thermoelectric nanogenerator. A power factor higher by two orders of magnitude than $Ti_3C_2T_x$ films was obtained for $Mo_2Ti_2C_3T_x$ at 800 K [149]. First-principles simulations predicted high ZT values ~3 for p-type Ti_2MoCF_2 [150] and $Cr_2TiC_2(OH)_2$ MXenes [151], with low κ_l attributed to increased phonon-phonon anharmonic scattering. In M_2X MXenes, manipulation of transition metal surfaces through substitution leads to Janus MXenes with chemical formula MM′X. Janus 2D compounds are obtained by breaking inversion symmetry by replacing the constituents of one of the two chemically identical surfaces [152, 153]. In the MXene family, high ZT (~ 3) has been obtained for Janus compounds such as $TiZrCO_2$ and $TiHfCO_2$ [154], suggesting that such out-of-plane ordering in MXenes can be explored to achieve thermoelectric materials with superior properties.

Although the results for various MXenes suggest that lowering the symmetry leads to improved ZT via substantial reduction of κ_l due to increased anharmonicity, other findings imply that this connection is complex. For example, a large reduction in κ_l has been obtained even without changes in symmetry [151], while in some cases symmetry breaking promoted κ_l by weakening anharmonic scattering [155]. These observations indicate a connection between symmetry, bond strengths, and anharmonic scattering that has not been addressed in depth.

Strain engineering, too, is found to be a low-cost and feasible method to enhance the thermoelectric properties of 2D materials [156, 157, 158, 159]. The effect of strain is prominently seen in the electronic band structures and phonon transport. In 1T-TiS_2 monolayer, a semi-metal to semiconductor transition is observed under tensile strain. In this compound, a 6% tensile strain opens up a band gap of 0.57 eV[160]. Band convergence can be achieved by the application of strain that, in turn, affects the electronic transport

*The contents of this chapter are published in 2024 Nanoscale, 16, 11336-11349, 2024 J. Phys.: Condens. Matter 36 445703

coefficients. It is also found that the tensile biaxial strain reduces κ_l by nearly 50% [161, 162]. Due to increased phonon-phonon scattering, it was found that the tensile strain reduces the κ_l from 16.97 W/m-K to 6.88 W/m-K at 300 K for $PtSe_2$[162]. A 7% tensile strain in p-type HfS_2 was found to lead to a maximum ZT of approximately 3.3 [163].

Motivated by these considerations, in this chapter, we have addressed the two studies, the effect of symmetry lowering and strain engineering on the thermoelectric properties of MXenes. Firstly, we investigate the thermoelectric parameters of Ti_2CO_2, Mo_2CO_2, Zr_2CO_2, and Hf_2CO_2 MXenes and five Janus compounds $TiMoCO_2$, $ZrMoCO_2$, $HfMoCO_2$, $TiZrCO_2$, and $TiHfCO_2$. Our goal is to explore the possibility of achieving high ZT through inversion symmetry breaking and to provide insights into the interrelations between symmetry lowering, electronic structure, lattice dynamics, and transport parameters, with special emphasis on harmonic and anharmonic phonon contributions. Secondly, we examine the effect of biaxial strain on the three Janus compositions derived from Zr_2CO_2: (a) Zr_2COS, obtained by substituting one -O with -S, (b) $ZrHfCO_2$, formed by replacing Zr with Hf on one surface, and (c) ZrHfCOS, combining both metal and functional group asymmetry. This chapter thus examines the impact of both surface compositional engineering and biaxial strain on the thermoelectric performance of a novel class of 2D materials, MXenes.

4.2 Computational Details

In this work, structural optimizations were done with a kinetic energy cutoff of 550 eV and dense Γ-centered k-point grids, ensuring convergence of forces below 10^{-3} eV/Å and total energies to 10^{-7} eV. Ab initio molecular dynamics (AIMD) simulations were conducted in the canonical (NVT) ensemble with a Nosé-Hoover thermostat to assess thermal stability. Supercells of size $3\times3\times1$ and $4\times4\times1$ k-point meshes were used, with simulations running for 12–20 ps.

For electronic transport properties, a Γ-centered k-point mesh of $32\times32\times1$ was used to evaluate the Kohn-Sham eigenvalues. These were interpolated to a finer k-grid of 15000 k-points in the irreducible part of the Brillouin zone for evaluation of electronic transport coefficients. Harmonic and anharmonic interatomic force constants (IFCs) were computed with supercells up to $6\times6\times1$, and $4\times4\times1$, respectively, ensuring convergence. Interaction up to eight nearest neighbors was considered during the evaluation of anharmonic IFCs. The lattice thermal conductivity (κ_l) was determined by solving the phonon Boltzmann transport equation using the iterative approach. The calculated κ_l values were scaled appropriately for the vacuum thickness. Convergence with respect to supercell size and q-point mesh was systematically checked, with differences below 1%.

4.3 Surface modification and thermoelectric properties of MXenes

4.3.1 Structural Parameters, Bond Strengths and Band Structures

Fig. 4.1 shows the possible sites of surface passivation by functional groups in M_2C and $MM'C$ Janus MXenes. The possible sites for functionalization are C (above and below the C atom), H (hollow sites above and below the transition metal atom), and T (exactly above the transition metal atom). Thus there are 9 possible structural models for functionalized Janus MXenes. The ground state structures are obtained from DFT calculations by calculating total energies corresponding to structural models that differ from each other depending upon the sites of passivation by -O. The models along with their total energies are shown in Fig. 4.1, 4.2.

In Table 4.1, the total energies of all models for each one of the five Janus MXenes considered in the work, are shown. Results for non-degenerate structural models are shown only. While Mo-containing Janus compounds have -O preferring a HC combination, for the non-Mo ones it is HH (Fig. 4.2).

The ground state structural parameters of M_2CO_2 and $MM'CO_2$, (M, M′)=Ti, Mo, Zr, Hf), are presented in Table 4.2. We find that the sites of passivation on the M and M′ surfaces in the Janus compounds remain unchanged from those in their M_2C counterparts (Fig. 4.3). The calculated lattice constants are in excellent agreement with the available results. Expectedly, the lattice constants of Janus $MM'CO_2$ MXenes are in between those of end point MXenes M_2CO_2 and M'_2CO_2. Since the inversion symmetry of the M_2CO_2 MXenes is broken in Janus MXenes (the space group of M_2CO_2 compounds is $P\bar{3}m1$ while that of Janus $MM'CO_2$ is $P3m1$), there is significant fluctuations in the M/M′-O/C bond lengths, as is evident from Table 4.2. For Janus compounds with Mo as M′ element, Mo-C(M-C) and Mo-O(M-C) bonds increase (decrease) slightly in comparison to those in parent Mo_2CO_2(M_2CO_2) compounds. However, the common feature across parent and Janus compounds is that the M/M′ -O bonds are shorter than the M/M′-C bonds. The

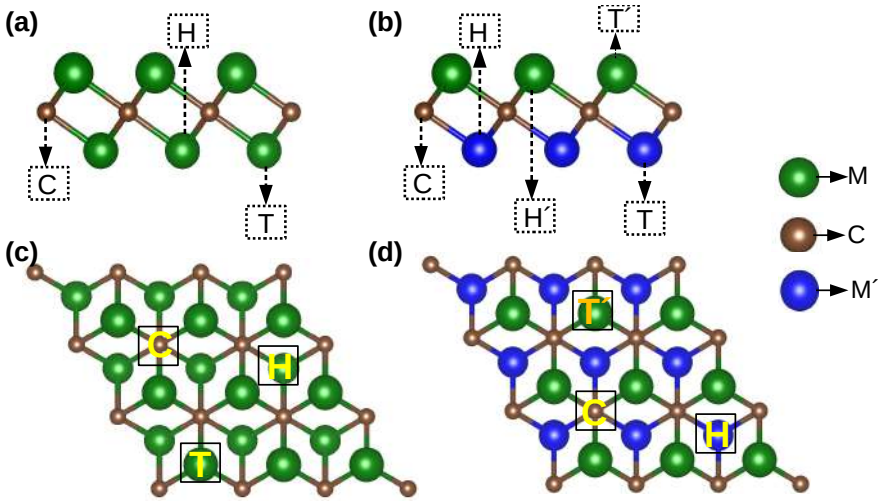

Figure 4.1: Schematic diagram showing the possible sites of surface passivation in M_2C ((a): side view, (c): top view) and MM′C MXenes ((b): side view, (d): top view).

Models(MD)	Energy (eV)				
	$TiMoCO_2$	$ZrMoCO_2$	$HfMoCO_2$	$TiZrCO_2$	$TiHfCO_2$
MD1 (TT′)	-43.8985	-44.3654	-46.9871	-44.8060	-46.5082
MD2 (HH′)	-45.4814	-45.9024	-47.7030	**-45.3306**	**-47.2035**
MD3 (CH′)	-44.7065	-45.4717	-47.0970	-44.5926	-46.5123
MD4 (CC)	-45.0784	-45.5988	-47.5484	-43.8902	-45.5739
MD5 (HC)	**-45.9870**	**-46.4794**	**-48.3104**	-44.8059	-46.4587

Table 4.1: Total energy (eV) of different structural models for all Janus-MXenes considered in this work. The lowest energy in each case is shown in bold.

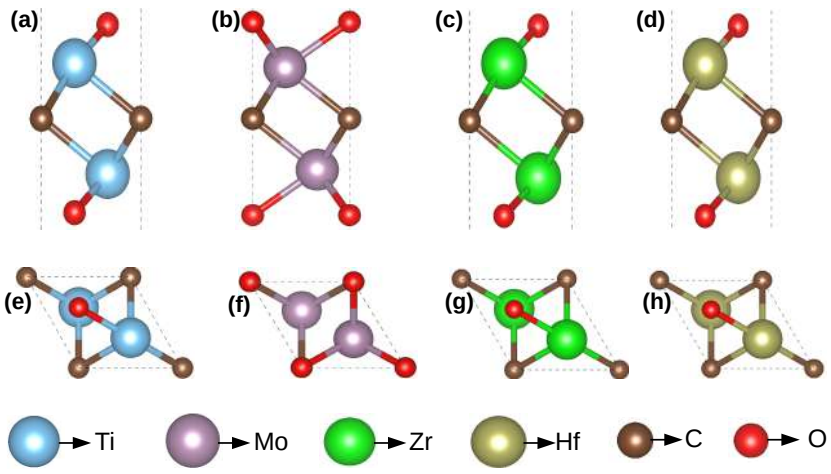

Figure 4.2: Ground state structures of M_2CO_2 MXenes considered in this work. The top(bottom) row shows side(top) views of the systems.

fluctuations in the bond lengths lead to fluctuations in the bond strengths, resulting in anharmonicity in the system, which has an effect on the lattice thermal conductivity κ_l.

An assessment of the bond strengths and it's correlation with the dispersions in the M/M′-C/O bond lengths is done by the Crystal Orbital Hamilton Population (COHP) method [165] as implemented in LOBSTER code[166]. In this method, a measure of the bond strengths are obtained from the energy integrated COHP, that is, from the energy averaged bond-weighted densities of states between a pair of atoms. In Table

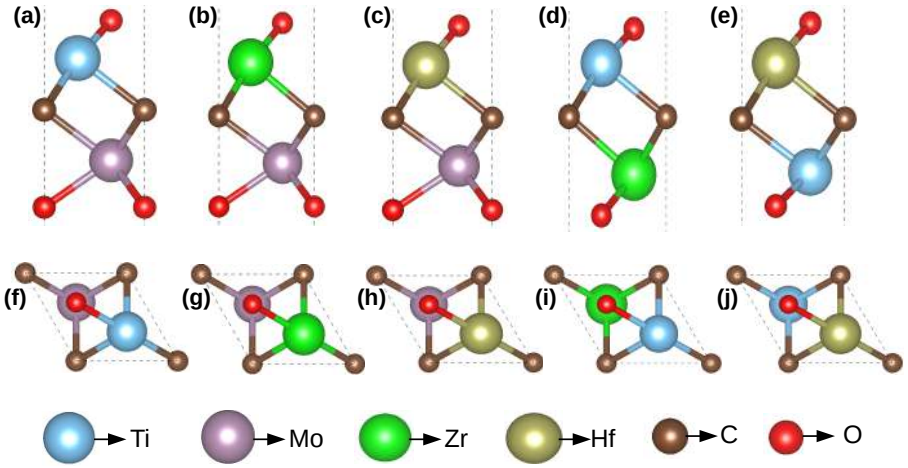

Figure 4.3: Ground state structure of Janus MXenes, (a)-(e) side view, (g)-(k) top view

MXenes	GS-Model	a (Å)	E_g (eV)	d_{M-C} (Å)	d_{M-O} (Å)	$d_{M'-C}$ (Å)	$d_{M'-O}$ (Å))
Ti_2CO_2	HH	3.03 (3.03)[146]	0.32	2.18	1.97	-	-
Mo_2CO_2	CC	2.89(2.88)[164]	-	2.15	2.06	-	-
Zr_2CO_2	HH	3.31(3.26)[146]	0.97	2.36	2.12	-	-
Hf_2CO_2	HH	3.26(3.26)[146]	1.03	2.33	2.10	-	-
$TiMoCO_2$	HC	2.95	0.16	2.15	1.95	2.13	2.08
$ZrMoCO_2$	HC	3.10	0.18	2.29	2.07	2.18	2.13
$HfMoCO_2$	HC	3.08	0.29	2.26	2.05	2.18	2.12
$TiZrCO_2$	HH′	3.18	0.74	2.25	2.01	2.31	2.08
$TiHfCO_2$	HH′	3.16	0.72	2.24	2.00	2.28	2.07

Table 4.2: Structural parameters (lattice constant (a), bond length ($d_{M/M'-C/O}$)) and electronic band gaps (E_g) for the systems considered. GS-Model refers to the ground state structural model described in Fig.4.2.

4.3, the strengths between various bonds in parent and Janus compounds are shown. We find that the bond strengths are clearly correlated with the variations in the bond lengths. Among the parent M_2CO_2 MXenes, M-C and M-O bond strengths are comparable in case of Mo_2CO_2. For the other three compounds, M-O bonds are significantly stronger than the M-C bonds. For $TiZrCO_2$ and $TiHfCO_2$ Janus compounds, Ti-O and Ti-C bonds weaken considerably while M′-O and M′-C bonds strengthen, in comparison to those for their respective parent M_2CO_2 MXenes. For $MMoCO_2$ Janus, Mo-C and Mo-O bonds weaken only slightly while M-O and M-C bonds strengthen with respect to the respective bond strengths in the corresponding parent compounds.

MXenes	Bond strength (eV)			
	M-C	M-O	M′-C	M′-O
Ti_2CO_2	-2.85	-3.88	-	-
Mo_2CO_2	-3.42	-3.56	-	-
Zr_2CO_2	-3.15	-4.14	-	-
Hf_2CO_2	-2.99	-4.18	-	-
$TiMoCO_2$	-2.91	-4.01	-3.37	-3.41
$ZrMoCO_2$	-3.37	-4.53	-3.36	-3.10
$HfMoCO_2$	-3.37	-4.51	-3.31	-3.16
$TiZrCO_2$	-2.46	-3.50	-3.34	-4.39
$TiHfCO_2$	-2.48	-3.56	-3.31	-4.37

Table 4.3: Bond strengths for parent (M_2CO_2) and Janus ($MM'CO_2$) MXenes obtained from COHP analysis.

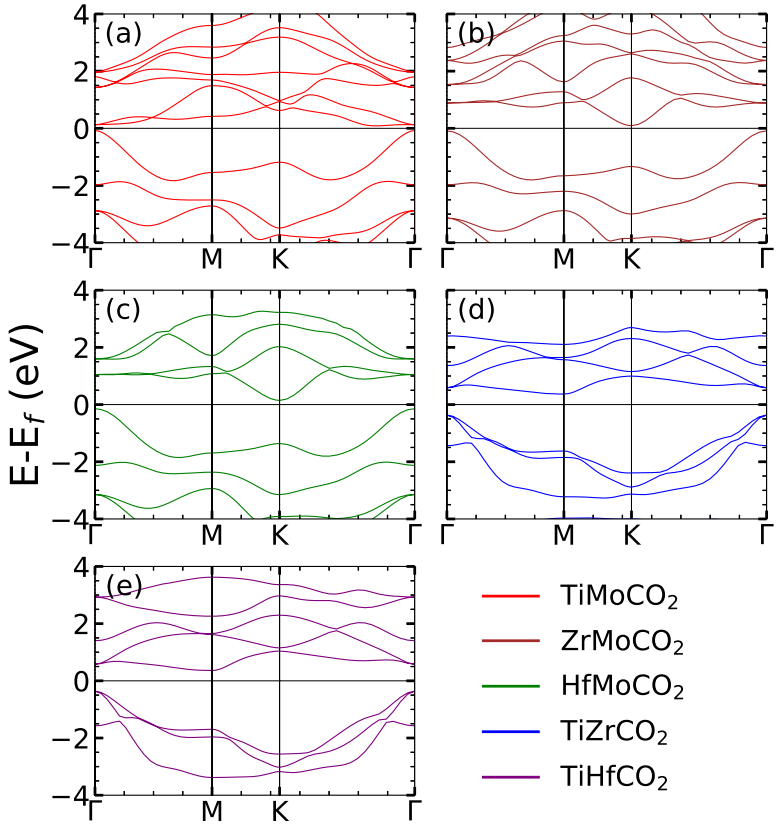

Figure 4.4: Electronic band structures of the Janus MXenes considered.

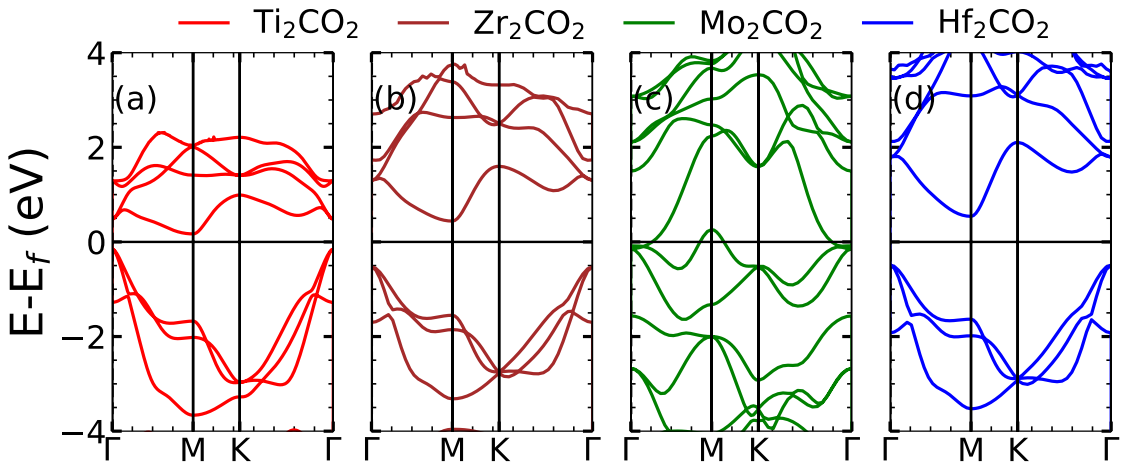

Figure 4.5: Band structures of M_2CO_2 MXenes considered in this work.

The band structures of Janus and the parent MXenes are shown in Fig. 4.4 and Fig. 4.5, respectively. Densities of states of the Janus MXenes are shown in Fig. 4.6. In agreement with existing results, we find that except Mo_2CO_2 which is a semi-metal, all M_2CO_2 MXenes considered are semiconductors. However all $MM'CO_2$ Janus compounds, even with Mo as M′ component, are semiconductors. The semiconducting nature of Mo-based Janus MXenes are due to the presence of the other transition metal constituent. The electronic structures in Fig. 4.6, clearly show that in the anti-bonding part of the spectra, hybridisations between *d* orbitals of Mo and the other transition metals that are located higher in energy, open the gaps in Mo-based Janus compounds. The magnitude of the gap depends on the position of the conduction band of the M element in $MM'CO_2$ MXene. The band gaps of $TiZrCO_2$ and $TiHfCO_2$ decrease considerably in comparison with Zr_2CO_2 and Hf_2CO_2, respectively (Table 4.2). Once again, the reductions are due to

the positions of Ti states that are closer to the Fermi levels. Analysing the band structures, we find that for $ZrMoCO_2$ and $HfMoCO_2$, the valence band maxima (VBM) and conduction band minima (CBM) are located at the Γ and K points, respectively. In contrast, they are located at Γ and M points, respectively, for $TiZrCO_2$ and $TiHfCO_2$. The electronic structure of $TiMoCO_2$ has very distinctive features. The VBM and CBM are located at Γ and along K-Γ direction, respectively. The band structure shows a flat band close to the Fermi level in the conduction region, the presence of which is reflected in the large Van Hove singularity in the densities of states. The presence of such a flat band near the Fermi level would have a profound impact on electronic transport properties, as the effective mass of different carriers will be significantly different.

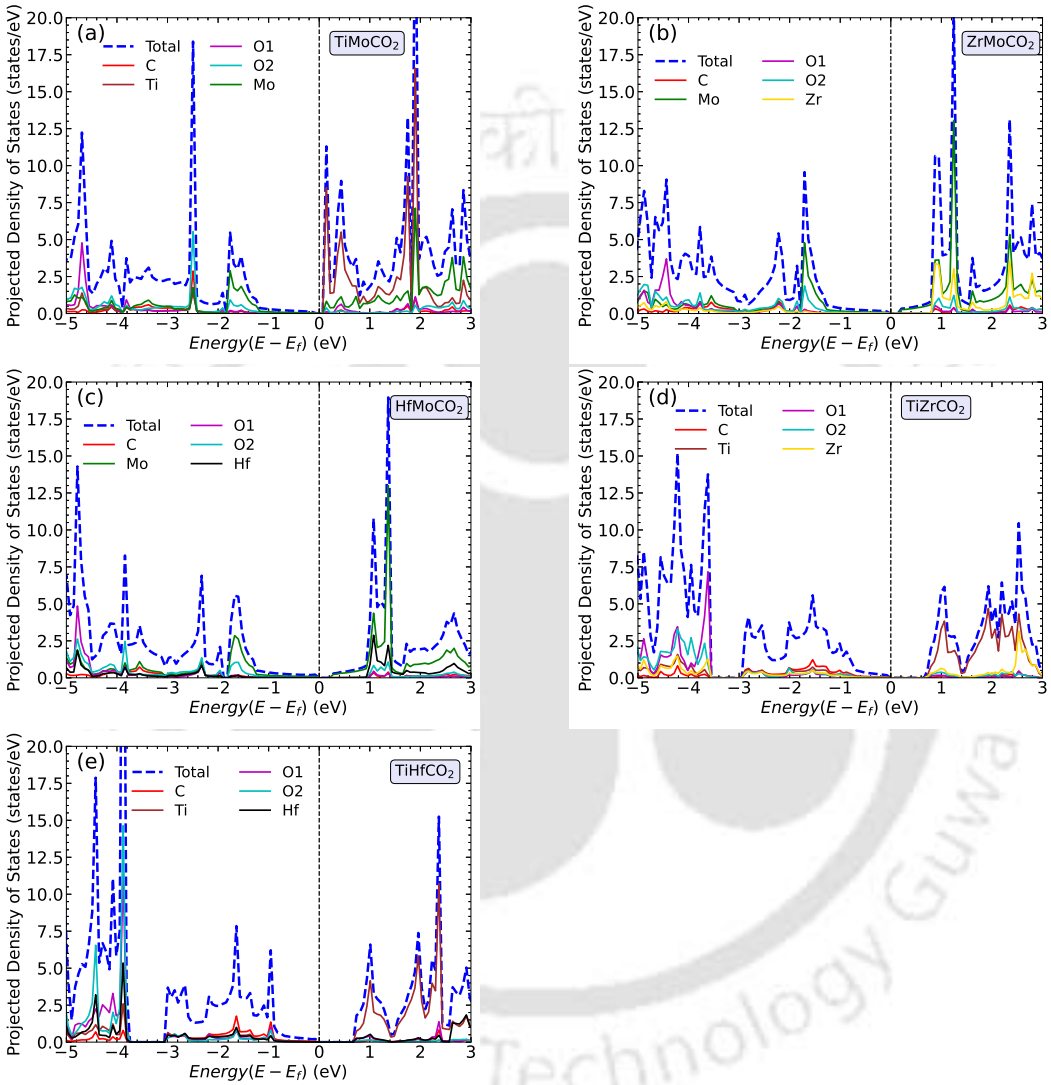

Figure 4.6: Densities of States of the Janus MXenes considered.

.

4.3.2 Phonon spectra and dynamical stability

Dynamical stabilities of the Janus compounds are assessed by computing their phonon spectra. The phonon dispersion curves and the phonon partial density of states for $MM'CO_2$ (M_2CO_2) Janus (parent) MXenes are shown in Fig. 4.7 (Fig. 4.8).

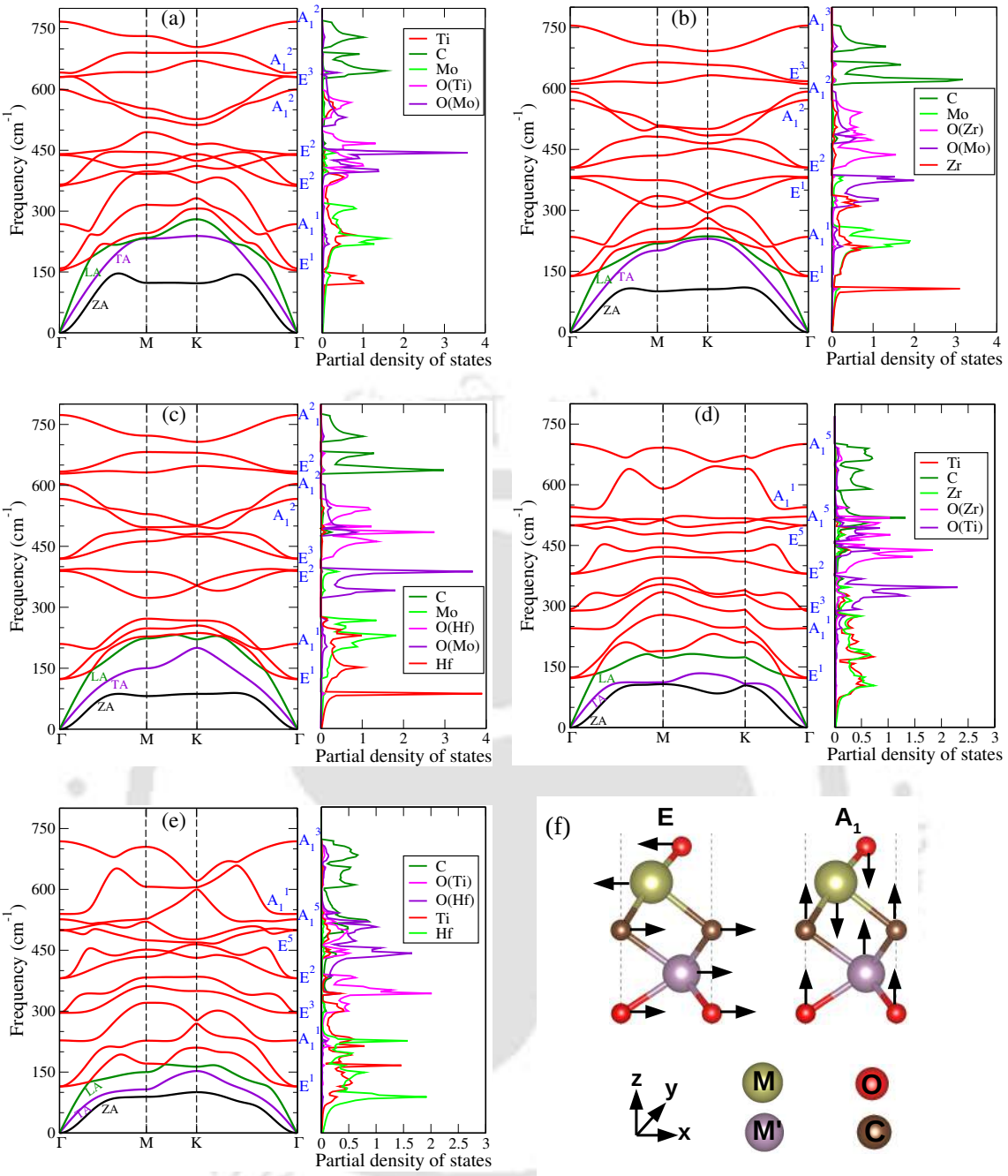

Figure 4.7: (a)-(e) Phonon dispersion and phonon density of states of the Janus MXenes considered. (f) The schematic diagram for vibration modes

We find all systems to be dynamically stable in their respective ground states. For M_2CO_2 MXenes, the heavier elements (Ti, Mo, Zr, and Hf) dominate the low-frequency (acoustic and lower optical modes) phonon modes, while O and the lightest C atoms dominate the mid and high-frequency optical modes (Fig. 4.8). Similarly, in Janus MXenes, M and M′ atoms majorly contribute in the lower frequency range (Fig. 4.7). Mid-frequency optical modes show significant hybridization between two O atoms attached to M and M′ surfaces. C atoms are responsible for the high frequency vibrations. We have performed the group theory analysis to identify the Raman and infrared (IR) active modes for Janus(for parent MXenes Fig. 4.9) MXenes. According to group theory, these vibrations can be expressed as irreducible representations ($\Gamma(vib)$) of C_{3v} point group and can be represented as

$$\Gamma(vib) = 4A_1 + 4E \tag{4.1}$$

where A_1 refers out-of-plane vibrations, and E denotes the in-plane vibrations, that are doubly degenerate at the Γ point. For this point group, all modes are Raman and IR active. Vibrational patterns for the modes

are schematically shown in Fig. 4.7(f) (Vibration patterns corresponding to all E and A_1 modes are shown in Fig.4.9).

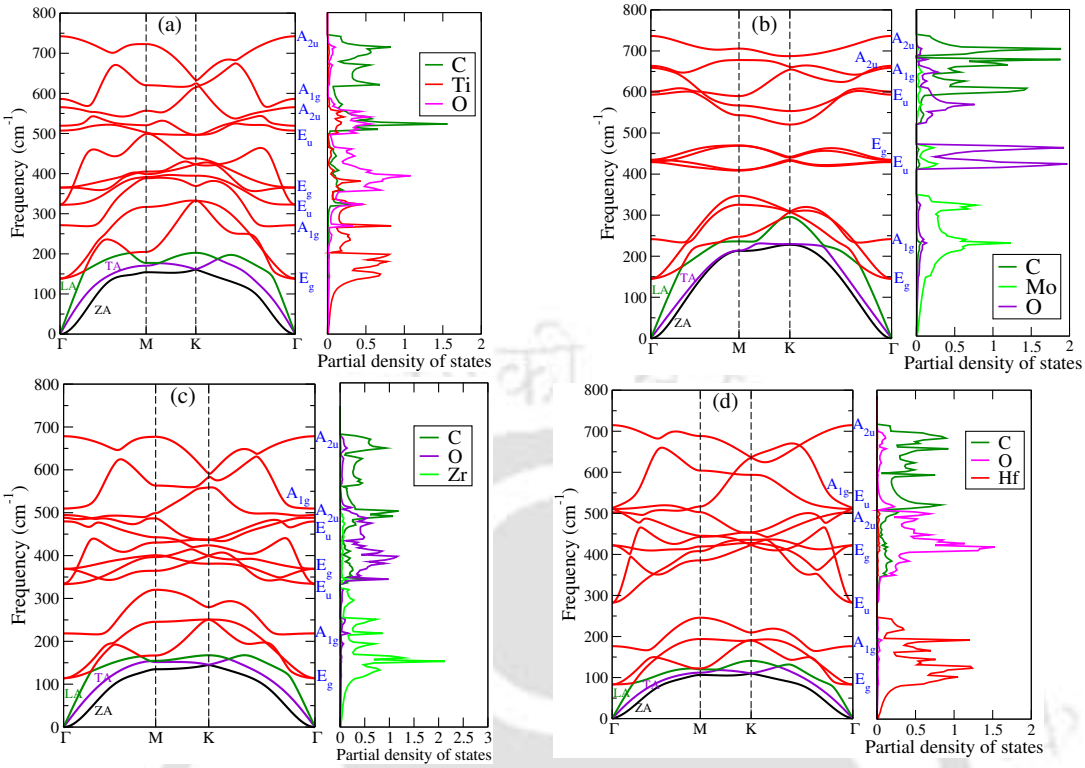

Figure 4.8: Phonon spectra and densities of states of M_2CO_2 MXenes considered.

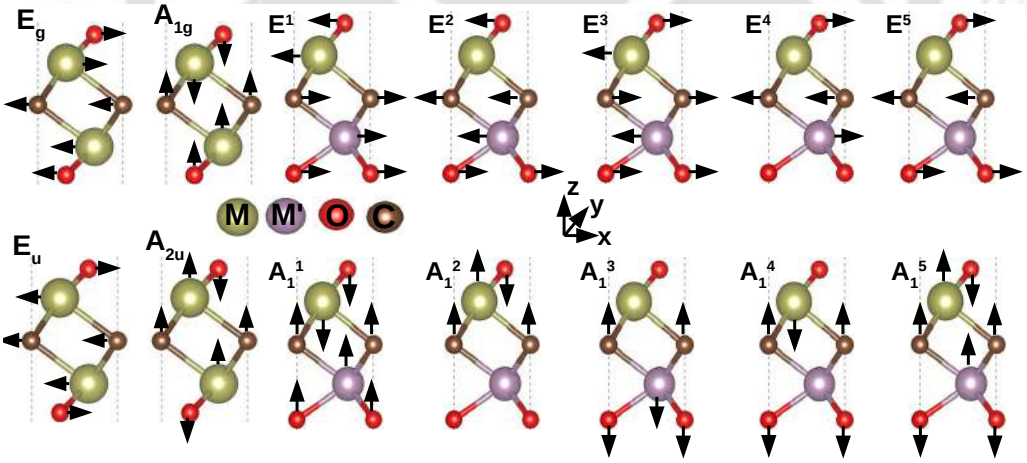

Figure 4.9: Schematic diagram of phonon mode vibration at Γ point for different frequencies

4.3.3 Transport properties

In this section we discuss the electronic and thermal transport properties of M_2CO_2 and $MM'CO_2$ MXenes. By making a comparative assessment of Janus MXenes and the corresponding end point compounds, we analyse the effects of inversion symmetry breaking on the transport properties.

Electronic transport parameters

In Fig. 4.10, 4.11 and 4.12, we show results for variations of Seebeck coefficient (S), electrical conductivity (σ) and electronic part of thermal conductivity (κ_e) with energy, at three different temperatures, respectively.

The transport coefficient are obtained under CRTA and RBA provide $S, \sigma/\tau$ and κ_e/τ, τ (carrier relaxation time) is calculated from DP theory calculation details for τ are discussed in the detailed in chapter 2.

The results suggest that $TiZrCO_2$ and $TiHfCO_2$ Janus have significantly higher values of S($\sim$1000μV/K) in comparison to the ones containing Mo($\sim$250μV/K). Among the parent MXenes, Hf_2CO_2 and Zr_2CO_2 have large values of S($\sim$1600μV/K) in comparison with the other two. Our results for parent MXenes agree well with existing results [146, 147, 167, 164]. Moreover, the calculated values of S for the Janus MXenes are either higher or are comparable to those for the established thermoelectric materials [168, 169].

The comparative behaviour of the electrical conductivity (σ), on the other hand, is different for different charge carriers. For p-type carrier, Ti_2CO_2 has significantly large σ in comparison to Zr_2CO_2 and Hf_2CO_2, which have comparable values. For n-type carrier, σ is highest for Hf_2CO_2, followed by Zr_2CO_2 and Ti_2CO_2. However, all three have comparable values of σ. Mo_2CO_2 has almost negligible electrical conductivity in comparison to the rest of the parent MXenes, irrespective of the type of charge carrier. In the case of Janus compounds, too, different trends are observed for different charge carriers. For p-type carriers, Mo-based Janus compounds have substantially lower values of σ in comparison to $TiZrCO_2$ and $TiHfCO_2$, which have almost identical magnitudes. For n-type carriers, the trend is exactly opposite. Like S, the maximum σ for Janus compounds is noticeably smaller in comparison with that of the parent MXenes. The behaviour of electronic thermal conductivity κ_e follows the trends of σ. This is consistent with the Widemann-Franz relationship $\kappa_e \propto \sigma$.

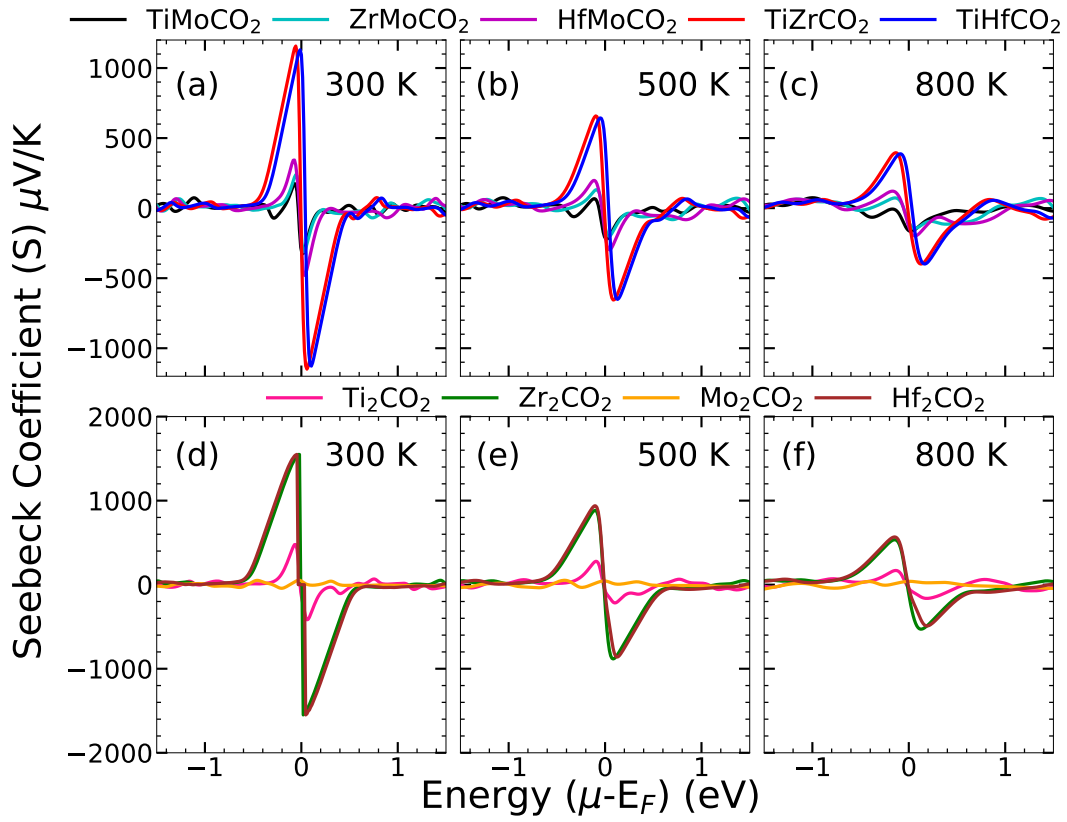

Figure 4.10: Seebeck coefficient ($S(\mu V/K)$) as a function of energy at different temperatures. The top(bottom) panel shows results for Janus(Parent) MXenes.

The trends in the electronic transport parameters S and σ can be qualitatively understood from the trends of the effective mass of the carriers, m_h^* (holes) and m_e^* (electrons), the band gaps E_g, the mobilities μ_h and μ_e of electrons and holes, respectively. The effective masses and the mobilities of the carriers for parent and Janus MXenes considered in this work are computed using DP theory and are presented in Table 4.4. For parabolic bands and energy independent scattering $S \propto \frac{m^*}{n^{2/3}}$ where m^* is the effective mass of the carrier and n the carrier density. Considering the parent compounds first, we find that $m^*_{h,Ti_2CO_2}(m^*_{e,Ti_2CO_2}) < (>) m^*_{h,Zr_2CO_2}(m^*_{e,Zr_2CO_2}) \approx (>) m^*_{h,Hf_2CO_2}(m^*_{e,Hf_2CO_2})$. Since the band gap of Ti_2CO_2 is substantially smaller than that of the other two, it has a larger electron density n. As a result S for Zr_2CO_2 and Hf_2CO_2 are much larger than Ti_2CO_2 irrespective of the carrier type. The reason for quantitatively smaller (larger) S

System	Carrier	m^*/m_0	$E_d(eV)$	$C_{2D}(N/m)$	$\mu(10^4 cm^2V^{-1}s^{-1})$			$\tau(fs)$		
					$T=300K$	$T=500K$	$T=800K$	$T=300K$	$T=500K$	$T=800K$
Ti_2CO_2	e	0.408	11.39	713.02	0.0466	0.0280	0.0175	108.26	64.96	40.59
	h	0.190	3.37		2.4579	1.4747	0.9217	2655.73	1593.44	995.89
Zr_2CO_2	e	0.310	13.94	692.76	0.0524	0.0314	0.0196	92.42	55.45	34.66
	h	0.404	6.48		0.1428	0.0857	0.0535	328.21	196.92	123.08
Hf_2CO_2	e	0.257	13.59	732.73	0.0849	0.0509	0.0318	124.07	74.44	46.53
	h	0.439	5.65		0.1683	0.1009	0.0631	420.22	252.13	157.58
$TiMoCO_2$	e	2.14	1.97	866.32	0.0689	0.0413	0.0258	838.35	503.014	314.383
	h	0.31	8.48		0.1818	0.1091	0.0682	316.42	189.85	118.65
$ZrMoCO_2$	e	0.44	4.32	783.51	0.3135	0.1881	0.1176	775.68	465.41	290.88
	h	0.46	8.48		0.0721	0.0432	0.0270	189.54	113.72	71.08
$HfMoCO_2$	e	0.43	6.02	821.10	0.1708	0.1024	0.0640	420.54	252.32	157.70
	h	0.53	7.50		0.0721	0.0432	0.0270	219.29	131.57	82.23
$TiZrCO_2$	e	0.46	11.77	680.28	0.0316	0.0190	0.0118	84.33	50.59	31.62
	h	0.29	4.35		0.5683	0.3410	0.2131	966.35	579.81	362.38
$TiHfCO_2$	e	0.44	12.45	704.64	0.0336	0.0201	0.0126	83.61	50.16	31.35
	h	0.29	5.34		0.3959	0.2375	0.1484	668.69	401.21	250.76

Table 4.4: Effective mass(m^*), DP constant(E_d), In-plane stiffness(C_{2D}), Carrier mobility(μ) and Relaxation times(τ) of electrons and holes for the compounds considered in this work.

for Janus $TiZrCO_2$ and $TiHfCO_2$ in comparison with Zr_2CO_2, Hf_2CO_2 (Ti_2CO_2) can also be understood in a similar way. The effective masses of Mo-based Janus compounds, irrespective of charge carrier type, are larger than those of the three parent MXenes considered. The band gaps follow exactly the opposite trend, implying that the carrier densities of Janus are larger. However, S of Janus $ZrMoCO_2$ and $HfMoCO_2$ are significantly smaller in comparison to S of Zr_2CO_2 and Hf_2CO_2. Reduction of such magnitude is probably due to a substantial reduction of band gaps in Janus compounds, which has a larger effect on n, superseding the effect of m*. A comparison between S of $TiMoCO_2$ and Ti_2CO_2 shows that $S_{TiMoCO_2} \gtrsim S_{Ti_2CO_2}$. This is because of two reasons: (a) the reduction in the band gap in $TiMoCO_2$ in comparison with Ti_2CO_2 is not as large as is the case of the other two sets of Janus-parent MXenes and (b) the increase in the effective mass in $TiMoCO_2$ in comparison with Ti_2CO_2 is much larger with respect to the other two sets. Such an increase in effective mass in $TiMoCO_2$ is due to flatter bands in comparison to the other systems.

The comparative magnitudes of S for the five Janus MXenes can also be understood by comparing the effective masses of holes and electronic band gaps. From the results presented in Table 4.2 and Table 4.4, we find that $m^*_{h,TiMoCO_2} < m^*_{h,ZrMoCO_2} < m^*_{h,HfMoCO_2} > m *_{h,TiZrCO_2} = m^*_{h,TiHfCO_2}$ and $E_{g,TiMoCO_2} < E_{g,ZrMoCO_2} < E_{g,HfMoCO_2} << E_{g,TiZrCO_2} \approx E_{g,TiHfCO_2}$. As a result $n_{TiMoCO_2} > n_{ZrMoCO_2} > n_{HfMoCO_2} >> n_{TiZrCO_2} \approx n_{TiHfCO_2}$. The large electron densities in the Mo-based Janus compounds, as compared with $TiZrCO_2$ and $TiHfCO_2$, nullify the effect of larger m^*_h in Mo-based Janus MXenes. Consequently, the Mo-based Janus MXenes have a much smaller Seebeck coefficient as compared to the rest.

The electrical conductivity $\sigma \propto \mu n$. For the parent and Janus MXenes considered in this work, we find that the trends in σ are largely dictated by μ of the carriers. In case of parent Mxenes, the hole mobilities are related as $\mu^h_{Ti_2CO_2} >> \mu^h_{Zr_2CO_2} \approx \mu^h_{Hf_2CO_2}$ while the electron mobilities follow $\mu^e_{Hf_2CO_2} > \mu^e_{Zr_2CO_2} \approx \mu^e_{Ti_2CO_2}$. The corresponding σ for these compounds exactly follow these trends. Mo_2CO_2 is not considered in this context as it has an extremely low σ and it being a semi-metal, mobilities associated with different charge carriers is irrelevant. For Janus compounds, the hole mobilities follow the trend $\mu^h_{TiZrCO_2} > \mu^h_{TiHfCO_2} >> \mu^h_{TiMOCO_2} > \mu^h_{ZrMoCO_2} \approx \mu^h_{HfMoCO_2}$ while the electron mobilities are related as $\mu^e_{ZrMoCO_2} > \mu^e_{HfMoCO_2} >> \mu^e_{TiMoCO_2} > \mu^e_{TiZrCO_2} \approx \mu^e_{TiHfCO_2}$. For the hole carriers, trend of σ exactly follows the trend in carrier mobility. For the electron carriers, σ of Mo-based Janus compounds are significantly higher than the remaining two. This cannot be explained by the trend in μ^e alone. The Mo-based Janus have much lower band gaps compared to the other two leading to very high carrier density n resulting in substantially high σ. Even among the three Mo-based Janus, the qualitative trend of σ for electron carriers can be explained only if both μ^e and n are considered. The mobility turns out to be the deciding factor too for explaining the comparative trends between parent and Janus MXenes. For hole carriers, $\mu^h_{Zr_2CO_2} << \mu^h_{TiZrCO_2} << \mu^h_{Ti_2CO_2}$ and $\sigma_{Zr_2CO_2} < \sigma_{TiZrCO_2} < \sigma_{Ti_2CO_2}$. Same behaviour is observed for $TiHfCO_2$. For Mo-based Janus MXenes, hole mobilities are much smaller than those of Ti_2CO_2, $TiZrCO_2$ and $TiHfCO_2$. This explains the reason behind significantly smaller σ of Mo-based Janus compounds in comparison with the other MXenes considered. For electron carriers, electrical conductivity of $TiZrCO_2$ and $TiHfCO_2$ are not very different from that of the corresponding parent MXenes. This is consistent with close values of their electron mobilities.

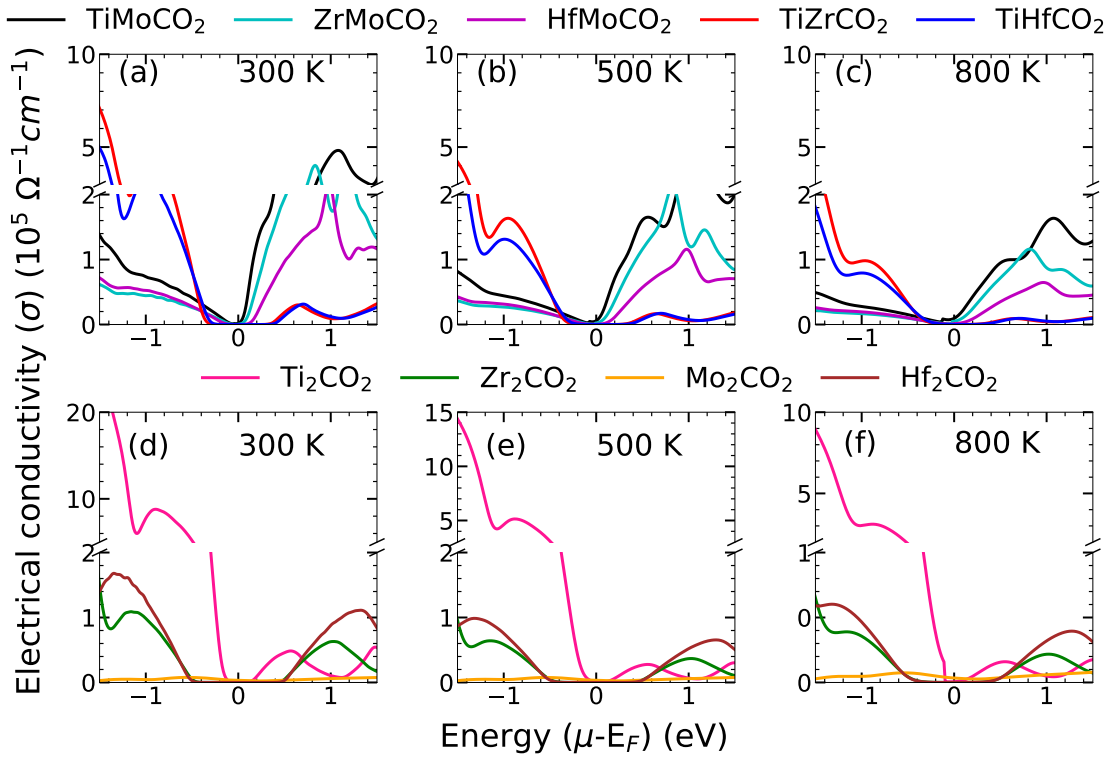

Figure 4.11: Electrical conductivity (σ ($\Omega^{-1}cm^{-1}$)) as a function of energy at different temperatures. The top(bottom) panel shows results for Janus(Parent) MXenes.

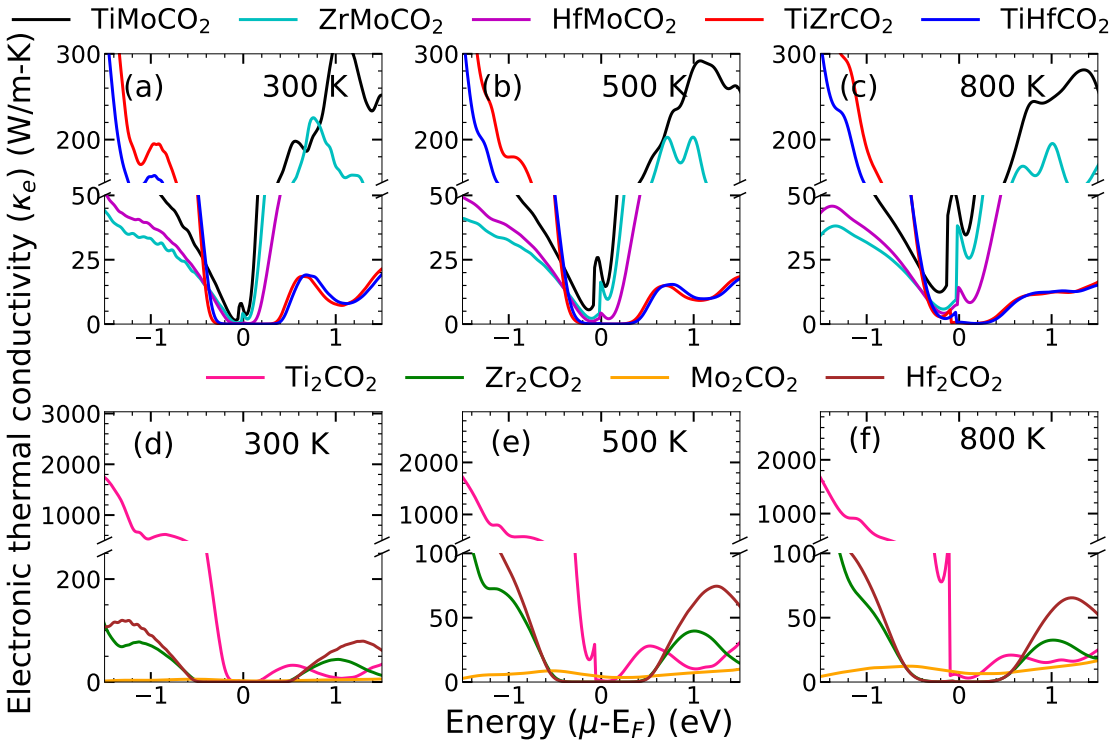

Figure 4.12: Electronic thermal conductivity (κ_e(W/m-K)) as a function of energy at different temperatures. The top(bottom) panel shows results for Janus(Parent) MXenes..

According to DP theory [111], carrier mobility μ depends upon the carrier effective mass m^*, the in-plane stiffness constant C_{2D} and the DP constant E_d, a measure of electron-phonon coupling strength, the following way: $\mu \propto \frac{C_{2D}}{|m^*|^2(E_d)^2}$. It is expected that m^* and E_d will have more profound effects on μ. From the calculated values of these quantities presented in Table 4.4, we infer that the trends in μ for different charge carriers are dictated by m^* which in turn is decided by the curvatures of the top(bottom) of valence(conduction)bands. For example, a noticeably large value of m_e^* for $TiMoCO_2$ in conjunction with small E_d is responsible for small μ^e. The large value of m_e^* is due to the flattest bottom of the conduction band among the series of compounds investigated. For $TiHfCO_2$ and $TiZrCO_2$ Janus compounds, $m_e^*(m_h^*)$ increase (decrease) in comparison with parent compounds Hf_2CO_2 and Zr_2CO_2. This behaviour is due to the fact that in Janus compounds bottom of the conduction bands (top of the valence bands) are less(more) dispersive. In case of the three Mo-based Janus, larger values of m^*, in comparison with Ti_2CO_2, Zr_2CO_2 and Hf_2CO_2,irrespective of charge carrier type, are also an artefact of the band structures near Fermi level.

The electronic transport parameters show two overall trends. First, maximum values of the transport parameters are less upon breaking of inversion symmetry in parent MXenes and second, based upon the quantitative trends, the five Janus compounds can be grouped into two distinct sets: three Mo-based compounds and the remaining two. The trends in the electronic transport parts clearly imply that if only the electronic transport is considered, the inversion symmetry breaking to form Janus MXenes may not lead to higher figure of merit (as compared to parent compounds) as the Seebeck coefficient would be dominant due to its higher power in the expression for ZT. Therefore, the contribution of lattice thermal conductivity will be crucial. In the next subsection we explore this in detail.

Lattice thermal conductivity

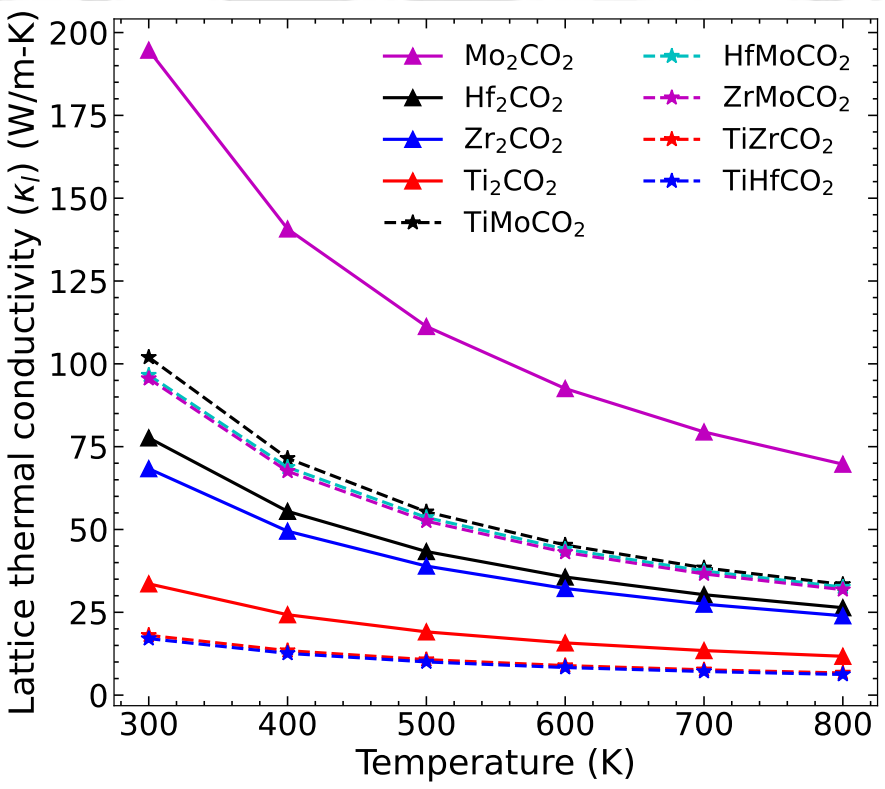

Figure 4.13: Lattice thermal conductivity (κ_l (W/m-K)) as function of temperature for the MXenes considered.

Fig. 4.13 shows the lattice thermal conductivity (κ_l) as a function of temperature T in the range 300-800 K for the parent and Janus MXenes considered in this work. Three distinct features are observed in the behaviour of κ_l: (1) Among the parent MXenes, Mo_2CO_2 (Ti_2CO_2) has the highest (lowest) κ_l with the following quantitative trend: $\kappa_l^{Mo_2CO_2} >> \kappa_l^{Hf_2CO_2} \gtrsim \kappa_l^{Zr_2CO_2} > \kappa_l^{Ti_2CO_2}$, (2) Among the Janus MXenes, the three Mo-based compounds have higher κ_l as compared to the remaining two with the quantitative trend

as $\kappa_l^{TiMoCO_2} > \kappa_l^{ZrMoCO_2} \approx \kappa_l^{HfMoCO_2} > \kappa_l^{TiZrCO_2} \gtrsim \kappa_l^{TiHfCO_2}$ and (3) Thermal conductivities of Mo-free Janus compounds are significantly lower than the relevant parent MXenes ($\kappa_l^{TiZrCO_2} \approx \kappa_l^{TiHfCO_2} < \kappa_l^{Ti_2CO_2} << \kappa_l^{Zr_2CO_2} < \kappa_l^{Hf_2CO_2}$) while lattice thermal conductivity of the three Mo-containing Janus are substantially lower than Mo_2CO_2 and greater than the other three parent MXenes Zr_2CO_2, Hf_2CO_2 and Ti_2CO_2. The trends are encouraging and intriguing as well. It, therefore, warrants a detailed analysis which has hitherto been unavailable. For example, though lattice thermal conductivities of Ti_2CO_2, Zr_2CO_2 and Hf_2CO_2 have been calculated [146, 147] and our results agree well with them, any discussion on the trends based upon quantitative analysis was absent.

Lattice thermal conductivity of non-metallic solids has been understood by a simple qualitative model [170]. According to this model, crystal structure, average atomic mass ($\bar{m}$), bond strength and anharmonicity are the factors deciding κ_l. $\bar{m}$ and the bond strengths that comprise of the harmonic effects influencing κ_l are manifested through a single quantity, the average acoustic Debye temperature Θ_D:

$$\frac{1}{\Theta_D^3} = \frac{1}{3}\left(\frac{1}{\Theta_{ZA}^3} + \frac{1}{\Theta_{TA}^3} + \frac{1}{\Theta_{LA}^3}\right) \tag{4.2}$$

$\Theta_i = \frac{\hbar\omega_i^{max}}{k_B}$; ω_i^{max} is the frequency of i^{th} acoustic mode at the zone boundary [171], ZA, TA, LA are the out-of-plane, transverse and longitudinal acoustic modes, respectively. According to Ref [170], $\kappa_l \propto \Theta_D$ and heavier $\bar{m}$ and weak bond strengths will lead to lower value of Θ_D, and consequently lower κ_l. Heavier mass and weaker bonding will also lead to lower phonon group velocity and lower κ_l. In Fig. 4.14, $\bar{m}, \Theta_D$ and κ_l for all MXenes considered in this work are shown. The results depict a few contradictions with the qualitative model [170]. According to the model, Ti_2CO_2 should have lattice thermal conductivity larger than Zr_2CO_2 and Hf_2CO_2. This is because its $\bar{m}$ is the lowest while the bond strengths (Table 4.3) are not drastically lower in comparison with the other two. The calculated values of Θ_D corroborate this anomaly. In Fig. 4.14 we find that the Θ_D decreases as one moves from Ti_2CO_2 to Hf_2CO_2 but κ_l instead of decreasing in the same direction, increases. Similarly, this model cannot explain why $\kappa_l^{Mo_2CO_2}$ is substantially higher than $\kappa_l^{Zr_2CO_2}$ when $\bar{m}$ of the two compounds are almost same. Θ_D of Mo_2CO_2 turns out to be substantially higher in comparison with Θ_D of Zr_2CO_2 (Fig. 4.14) providing the explanation for behaviour of κ_l. However, this happens inspite of no clear trends in the bond strengths. The phonon spectra of these two MXenes (Fig. 4.8) offer some clues to the behaviour of Θ_D. The maximum frequencies of the three acoustic modes are noticeably higher in the case of Mo_2CO_2, leading to larger Θ_D and larger κ_l as a consequence. Moreover, large gaps between the four-fold degenerate optical mode around 400 cm^{-1} and the two-fold degenerate optical mode around 550 cm^{-1} implies a suppression of phonon-phonon scattering due to decrease in phonon population [14] leading to subsequent elevation of κ_l. Nevertheless, these are only indirect evidence and do not provide a definite mechanism with quantitative estimates.

No such anomaly is encountered if one inspects the two groups of Janus compounds, the Mo-based ones and the remaining two, separately. In both groups, $\bar{m} \propto \frac{1}{\Theta_D} \propto \frac{1}{\kappa_l}$ is satisfied. The impact of the bond strengths, however, is not clear. The bond strengths of $TiZrCO_2$ and $TiHfCO_2$ are hardly different, so that Θ_D is completely determined by the differences in their masses. The maximum frequencies of the three acoustic modes also explain the behaviour of Θ_D. The same is true for the three Mo-based Janus compounds. The results become unexplainable in terms of the simple model with harmonic parameters only when comparison is made between members belonging to different groups. $TiMoCO_2$ and $TiZrCO_2$, despite having identical $\bar{m}$ have very different Θ_D. Like the parent compounds Zr_2CO_2 and Mo_2CO_2, Θ_D of $TiMoCO_2$ is higher, albeit not as substantially as is the case for parent MXenes. This, however, has a profound impact on κ_l; $\kappa_l^{TiZrCO_2}$ is less than $\kappa_l^{TiMoCO_2}$ by about 80% . This trend is found for other compounds too, which implies that the quantitative variation cannot be explained in terms of variations in the harmonic parameters alone.

The limitation of the model appears more pronounced when comparison is made between the lattice thermal conductivities of the parent and Janus groups. For example, $\bar{m}^{Zr_2CO_2} > \bar{m}^{TiZrCO_2} > \bar{m}^{Ti_2CO_2}$ but $\Theta_D^{Ti_2CO_2} > \Theta_D^{TiZrCO_2} < \Theta_D^{Zr_2CO_2}$. Though the trend in Θ_D is consistent with the trend in κ_l for these three compounds, the trends in $\bar{m}$ and Θ_D contradict the harmonic model. Even the trends in the bond strengths (Table 4.3) contradict the model. A comparison between Mo_2CO_2 and Mo-based Janus compounds also corroborates this. For this group of MXenes, Θ_D and κ_l of Mo_2CO_2 are always greater than the Janus compounds inspite of the $\bar{m}$ of Janus compounds being equal to (in case of $ZrMoCO_2$) or greater (in case of $HfMoCO_2$) than $\bar{m}$ of Mo_2CO_2. The Janus bonds, too, are stronger.

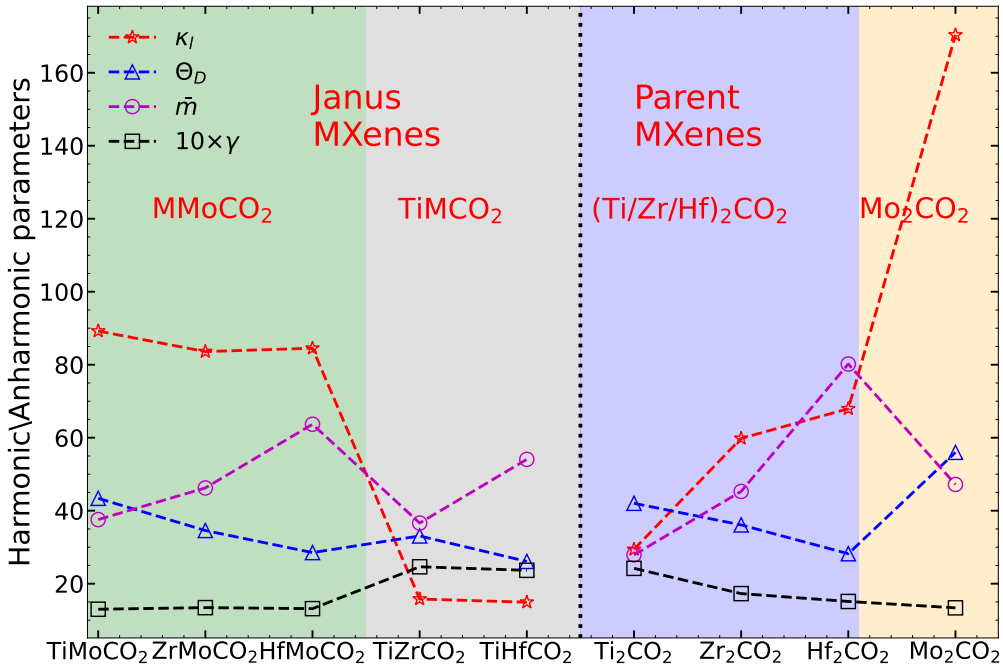

Figure 4.14: Variation of lattice thermal conductivity (κ_l) (W/m-K), Debye temperature (Θ_D) (K), average atomic mass ($\bar{m}$) (amu) and average Grüneisen parameter (γ) across different MXenes. The results are for 300 K.

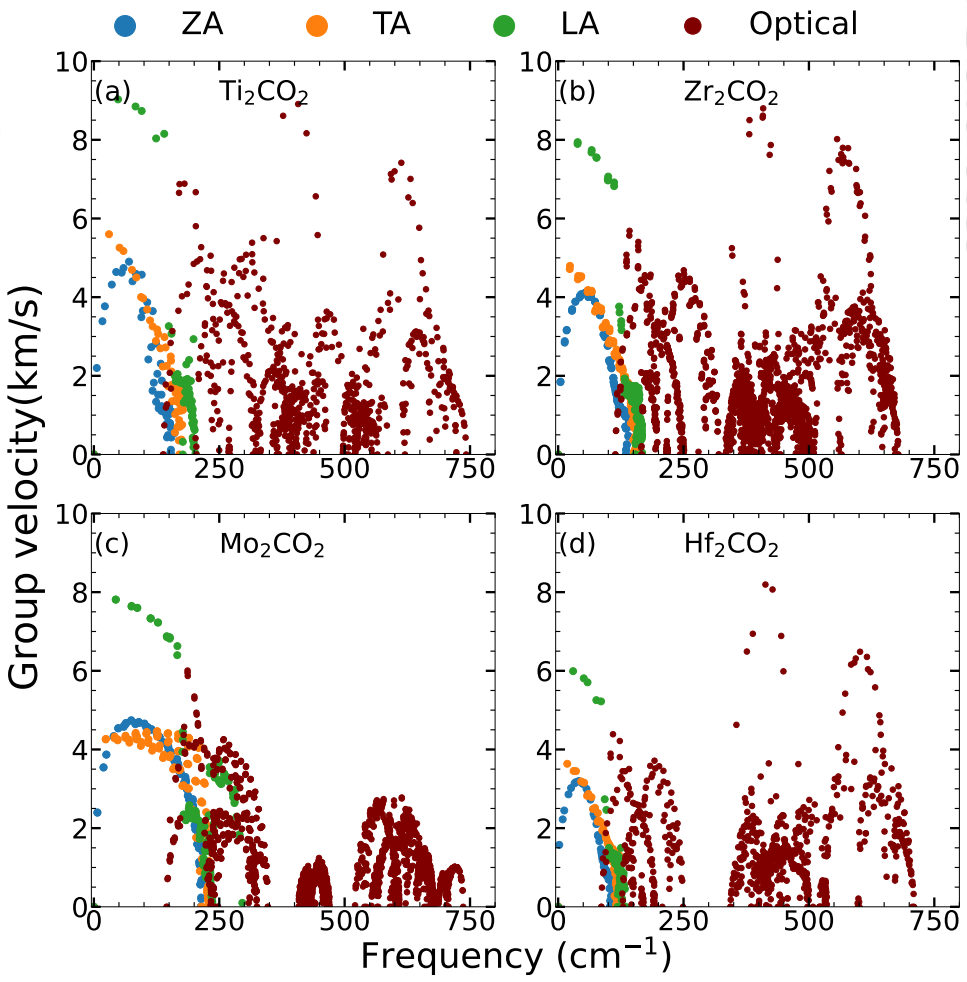

Figure 4.15: Group velocities of phonon modes in M_2CO_2 MXenes. Blue, orange, green, and brown colors indicate the ZA, TA, LA, and optical modes, respectively

One more hindrance in understanding the trends of harmonic parameters and κ_l across all parents and Janus compounds using the harmonic model [170] is that the symmetry of the members of two different groups of compounds (one containing Mo and the other consists of the remaining ones) is different due to different site preference of the -O functional group. Therefore, we next compute the phonon group velocities as they are directly proportional to lattice thermal conductivity (Equation (2.45)). The results are presented in Fig. 4.15 and 4.16. The results still cannot resolve the anomalies. For example, Hf_2CO_2 has group velocities lower than Ti_2CO_2 and $TiHfCO_2$, $HfMoCO_2$ have group velocities comparable to $TiZrCO_2$. But the trends in their κ_l do not support this behaviour.

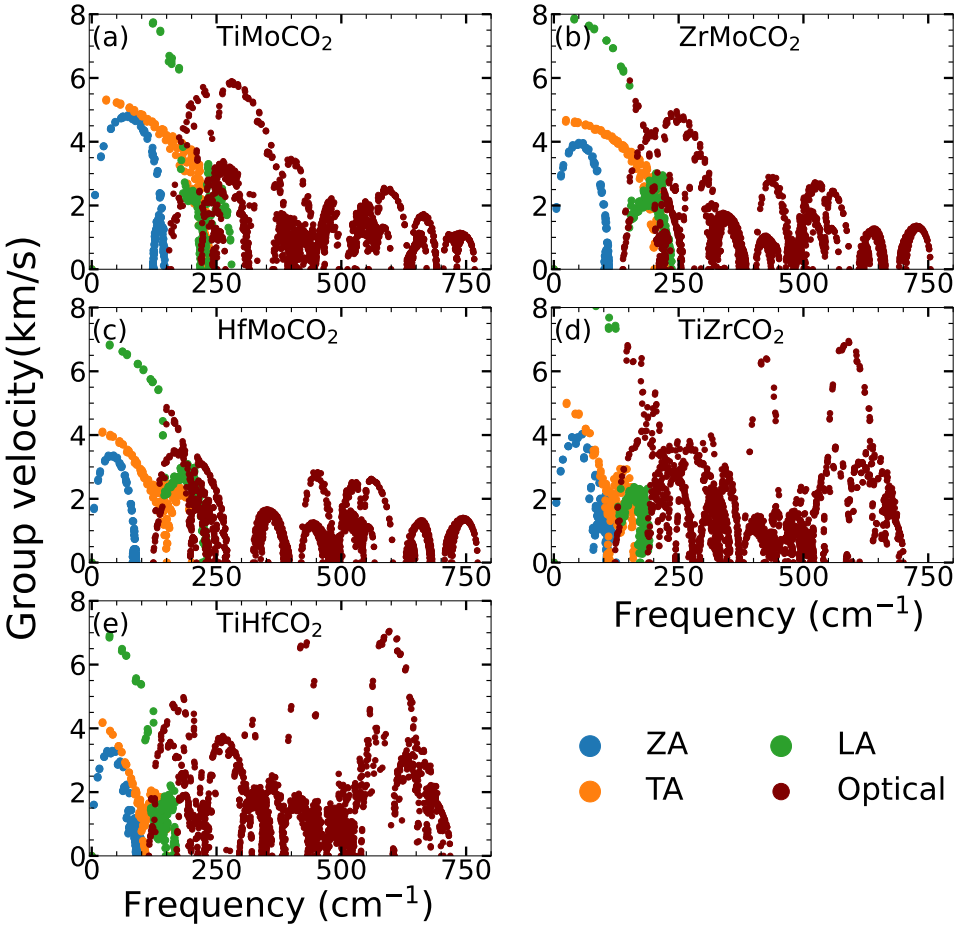

Figure 4.16: Group velocities of phonon modes in $MM'CO_2$ Janus MXenes. Blue, orange, green, and brown colors indicate the ZA, TA, LA, and optical modes, respectively

These anomalies, therefore, indicate that anharmonicity plays a key role in understanding the trends in κ_l. Earlier works on parent compounds Ti_2CO_2, Zr_2CO_2 and Hf_2CO_2 [146, 147] indicated this by analysing the phonon dispersions. However, they did not analyse the reasons behind the trend among the compounds , neither did they quantify the extent of anharmonicity. In what follows, we compute various quantities associated with the anharmonicity in the systems. In Fig. 4.14, we show the total Gruneisen parameter γ , the measure of the strength of anharmonicity in the system, calculated using phonon BTE [116]. Among the parent MXenes, γ decreases monotonically from Ti_2CO_2 to Mo_2CO_2 suggesting that largest (smallest) anharmonicity in Ti_2CO_2 (Mo_2CO_2) can be the reason for the smallest(largest) κ_l in Ti_2CO_2(Mo_2CO_2). The comparable γ values of Zr_2CO_2 and Hf_2CO_2 explains their near identical κ_l that are between Mo_2CO_2 and Ti_2CO_2. Among the Janus MXenes, larger anharmonicity is found in compounds without Mo, with their γ values being largest among all parent and Janus considered. γ for three Mo-based MXenes are almost identical that fits perfectly into the trends of their κ_l. A comparison between γ of parent and Janus MXenes too perfectly correlate with the trends in the lattice thermal conductivities.

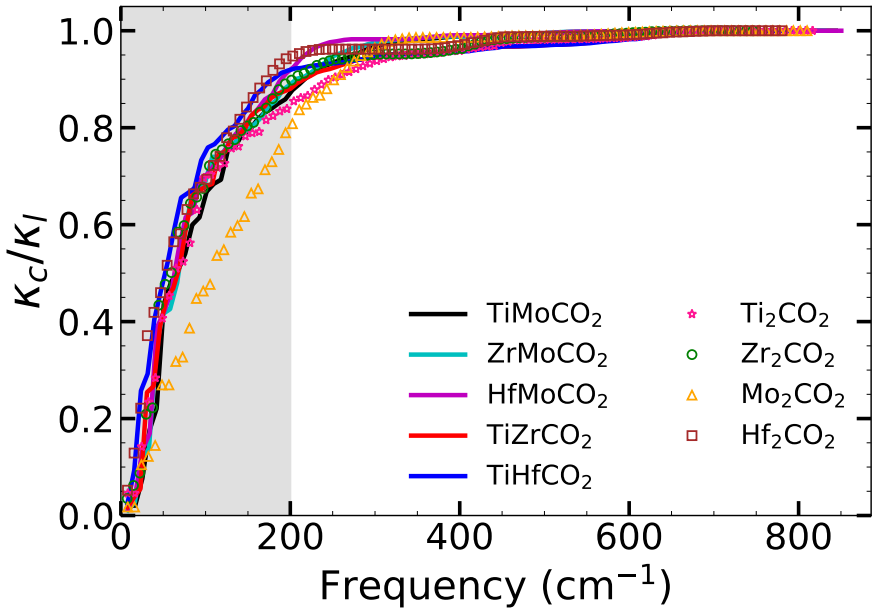

Figure 4.17: Normalised cumulative lattice thermal conductivity as a function of frequency for the MXenes considered.

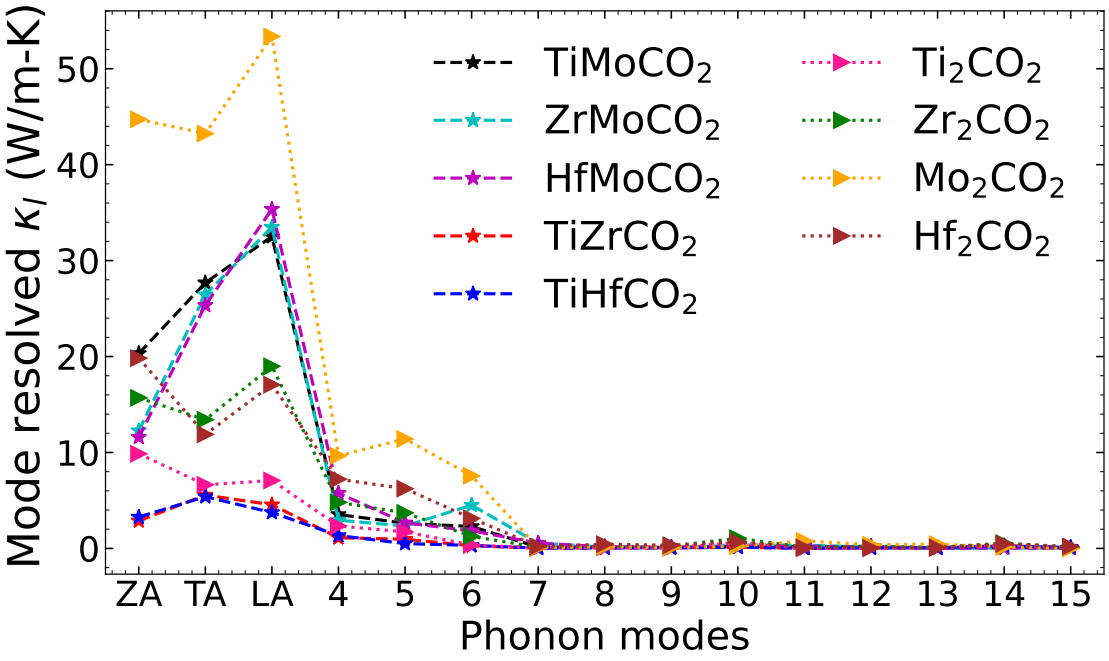

Figure 4.18: Mode resolved lattice thermal conductivity for all MXenes considered. The 3 acoustic and 12 optical modes in ascending order of frequency are plotted along x-axis.

In order to completely understand the extent of anharmonic effects and develop a microscopic picture, we next look into the phonon modes responsible and the strengths of phonon-phonon scattering. To this end, we first look at the frequency range and the corresponding modes that are major contributors to κ_l. In Fig. 4.17, we show the variations in normalised cumulative lattice thermal conductivity (κ_c/κ_l) as a function of frequency. The results are presented for 300 K only. The results show that for all systems considered, phonon modes with frequencies upto 200 cm^{-1} are the major contributors to κ_l. The mode resolved κ_l, presented in Fig. 4.18, corroborates this. We find that for all systems the three acoustic (ZA, TA, and LA) and first three optical modes (numbered 4,5,6 in the figure) contribute almost entirely to the lattice thermal

conductivity. A noticeable feature is that for Mo_2CO_2, the contributions from acoustic and optical modes towards κ_l are significantly different. This is also true for the Janus compounds containing Mo. On the other hand, Ti_2CO_2, $TiZrCO_2$ and $TiHfCO_2$ have near equal contributions from acoustic and optical modes implying strong phonon-phonon interactions.

To connect the behaviour of mode-resolved κ_l with anharmonicity, we first look at mode-resolved Grüneisen parameters (γ_λ) calculated using third-order IFCs [172]. The results are presented in Fig. 4.19. We find that among the parent compounds, Zr_2CO_2 has larger γ_λ than Mo_2CO_2 in the relevant frequency range, implying significant large anharmonicity in the former. This can be correlated to their very different κ_l with $\kappa_l^{Zr_2CO_2}$ much smaller than that of the other. γ_λ for Zr_2CO_2 and Hf_2CO_2 in the same frequency range are comparable. Ti_2CO_2 has the highest γ_λ among all parents. The γ_λ in non-Mo Janus compounds are 2-3 times higher than Ti_2CO_2. The Mo-based Janus compounds, on the other hand, have extremely low γ_λ. These trends nicely explain the behaviour of κ_l. In fact γ_λ turns out to be a better indicator than γ for comparing the degree of anharmonicity among compounds. For example, γ of Ti_2CO_2 and $TiHfCO_2$ are same. But γ_λ of the later is much higher in the relevant frequency range. The differences in their κ_l values, thus, can only be explained by γ_λ.

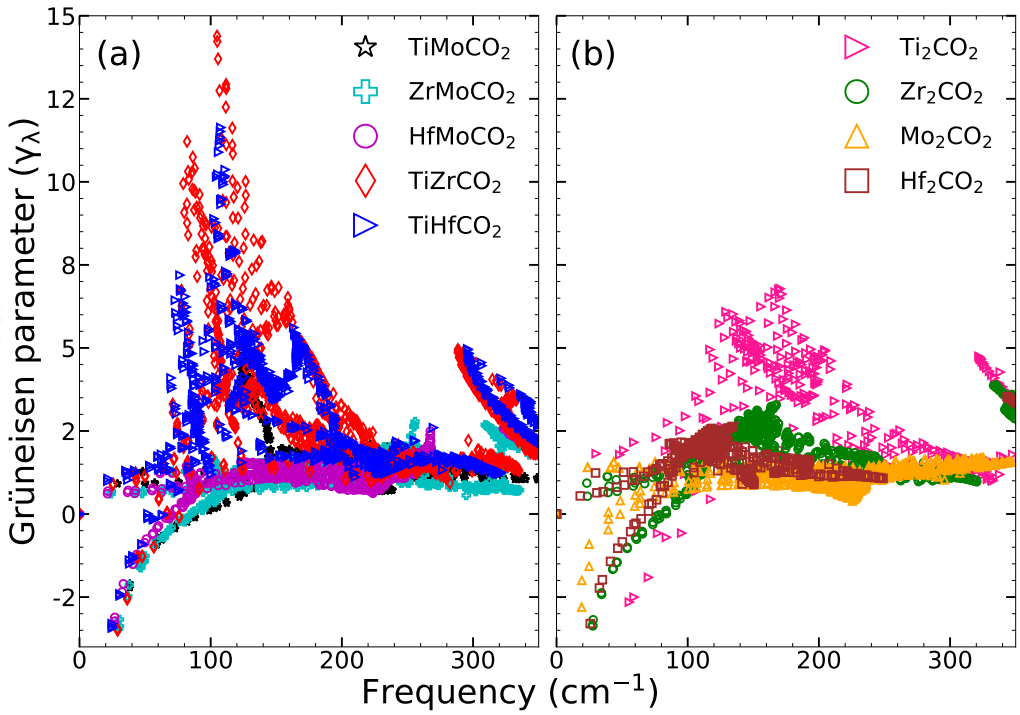

Figure 4.19: Grüneisen parameter for the (a) Janus and (b) parent MXenes considered.

We further understand the degree of anharmonic effects as quantified by γ_λ by calculating the anharmonic scattering rates over the frequency region. The results for Janus (parent) MXenes are shown in Fig. 4.20(Fig. 4.21). Among the parent compounds, Ti_2CO_2 has appreciably large scattering rates in comparison with other three. Mo_2CO_2 has the lowest scattering rate, scattering rates of the other two lie in between these two. The large scattering rate of Ti_2CO_2 finally resolves the anomaly regarding its lowest κ_l as compared to other parent compounds despite all harmonic parameters indicating the opposite. The lattice thermal conductivity is directly proportional to the group velocity v_g and the phonon relaxation time τ^0 (Equation 2.45). Since scattering rate is inversely proportional to τ^0, the effect of larger v_g of Ti_2CO_2 discussed earlier is nullified by the small τ^0, yielding lowest κ_l among the parent compounds. Among Janus compounds, higher scattering rates are observed for $TiZrCO_2$ and $TiHfCO_2$. This explains their higher values of γ_λ and consequently lower κ_l among the MXenes considered.

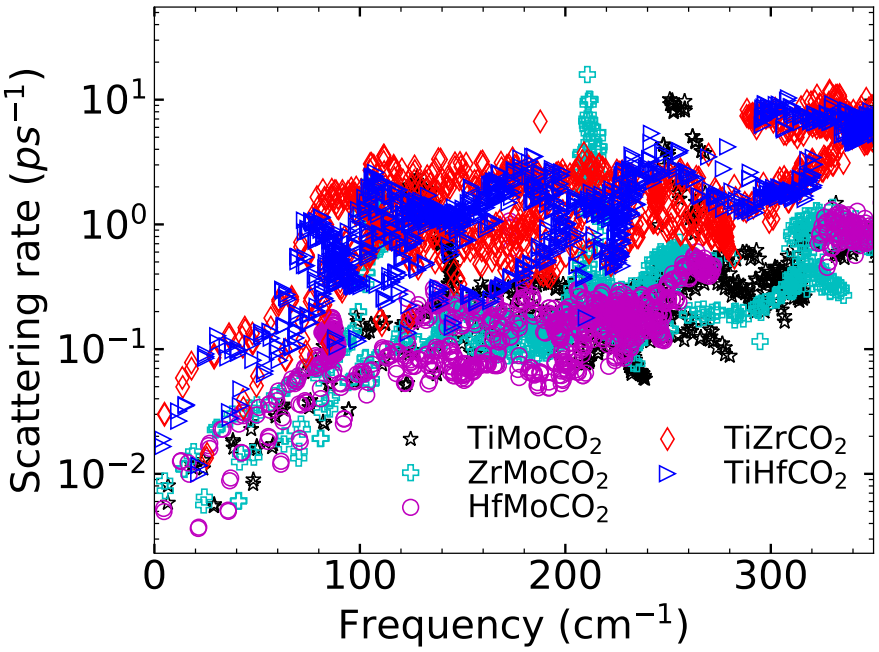

Figure 4.20: Anharmonic scattering rates as a function of frequency for Janus MXenes considered .

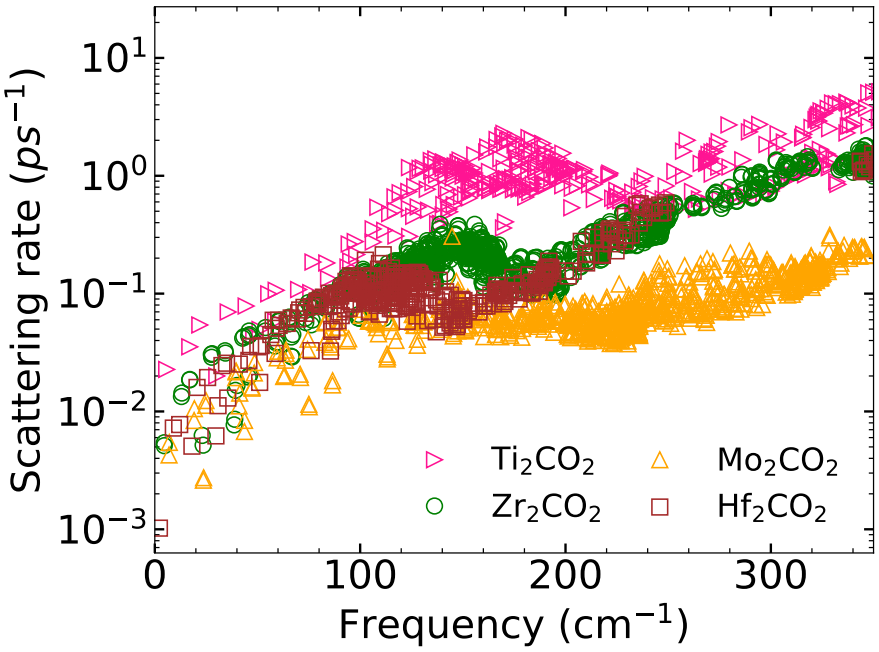

Figure 4.21: Anharmonic scattering rates as function of phonon frequency for parent MXenes considered.

In Fig. 4.22, a comparison between scattering rates in Janus and parent compounds is made. The noticeable trend observed in this comparison is that while the scattering rates of $MMoCO_2$ Janus compounds lie in between that of M_2CO_2 and Mo_2CO_2, the scattering rates of $TiZrCO_2$ and $TiHfCO_2$ are higher than the corresponding parent MXenes. To find the reason, we first look at the accessible phase space for phonon scattering since τ^0 (and thus κ_l) is inversely proportional to the accessible phase space [173, 174]which is determined by the condition of phonon energy and momentum conservation.

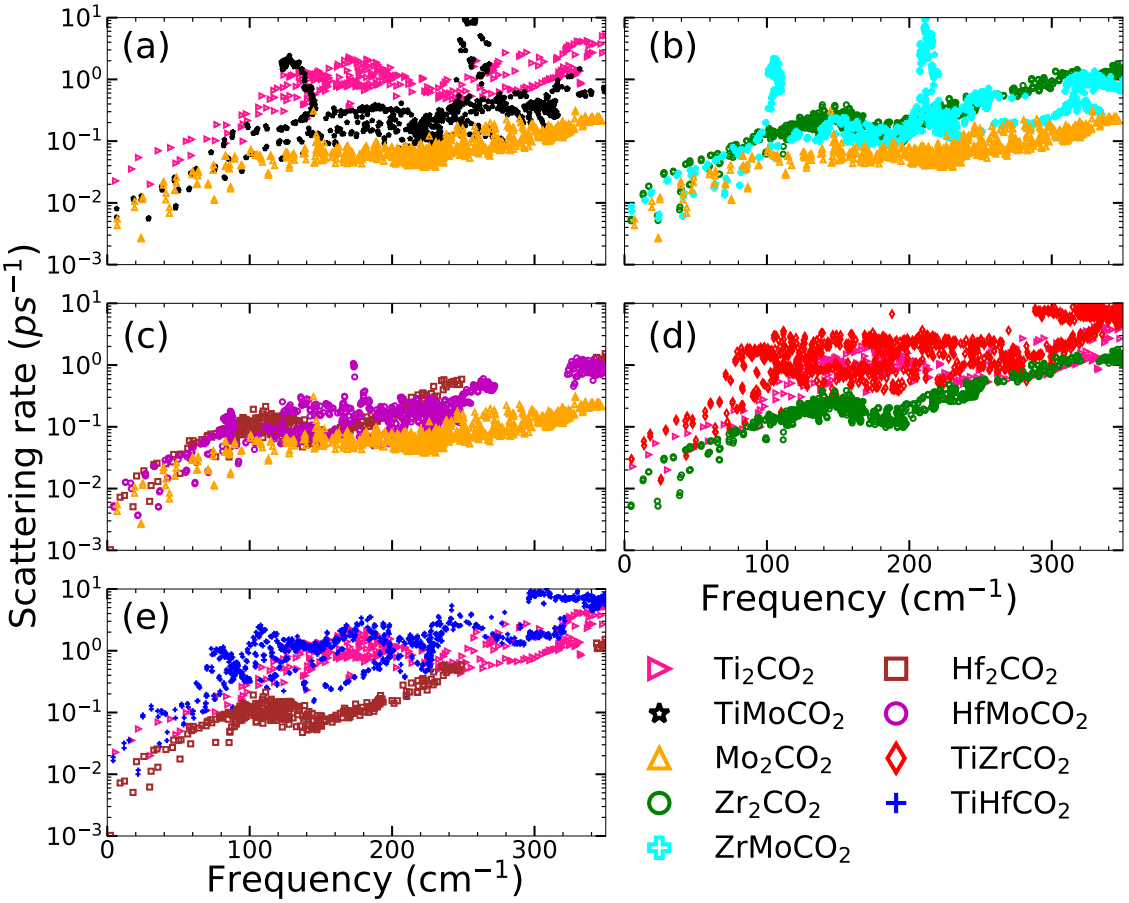

Figure 4.22: Comparison of anharmonic scattering rates between Janus and corresponding parent MXenes.

Fig. 4.23(a)((b)) shows the weighted scattering phase space (possible three-phonon scattering processes weighted by the frequencies) accessible to the parent(Janus) MXenes. Among the Janus MXenes, available phase spaces for Mo-based ones are lower than those of the others. $TiHfCO_2$ has a more accessible phase space than $TiZrCO_2$. More phase spaces are available for three-phonon scattering, which can be the explanation for the higher scattering rates seen in these two Janus MXenes. But this proposition is violated in the case of the parent MXenes. We find that Ti_2CO_2 has less accessible phase space compared to Hf_2CO_2 and Zr_2CO_2. Even $TiHfCO_2$ has less accessible phase space in comparison with Hf_2CO_2 in the frequency range 100-150 cm^{-1}, the range most responsible for anharmonic scattering. Therefore, the trends in the anharmonic scattering rates cannot be understood in terms of accessible phase space. To resolve this issue, we present the results on the strength of scattering matrix elements $|\phi^{\pm}_{\lambda\lambda'\lambda''}|^2$, which is a measure of the strength of three phonon scattering and depends on the anharmonic IFCs (Equation (2.56)). Fig. 4.23(c)(Fig. 4.23(d)) shows the average scattering matrix elements as a function of frequency for parent(Janus) MXenes. It is clear from Fig.4.23(c) that throughout the frequency range, the scattering strength in Ti_2CO_2 is more than Hf_2CO_2. Therefore, despite Hf_2CO_2 having more available phase space than Ti_2CO_2, it has lower scattering rate. Among the Janus compounds, $TiZrCO_2$ has the largest scattering strength with $TiHfCO_2$ competing closely. Therefore, the degree of anharmonicity among the parent and among the Janus can be finally understood in terms of the anharmonic scattering strengths. Comparison between parents and Janus, however, shows an anomaly: scattering strengths in Ti_2CO_2 in the frequency range of interest is still slightly higher than those in $TiZrCO_2$. Despite this, larger anharmonicity in $TiZrCO_2$ can be attributed to a higher number of scatterings, as can be understood by comparing Fig. 4.23 (c) and (d).

The inversion symmetry breaking in the Janus MXenes produces dispersions in the bond strengths (Table 4.3). We find that such dispersion can be connected to the degree of anharmonicity in Janus. The phonon densities of states of $TiHfCO_2$(Fig. 4.7(e)) shows that in the frequency range 100-200 cm^{-1}, the vibrations are dominated by the Ti atoms. In this Janus Ti-anion bond strengths weaken considerably as compared to the corresponding ones in parent Ti_2CO_2. The Hf-cation bond strengths strengthen, on the other hand, in comparison to those in parent MXene Hf_2CO_2. In Janus $TiZrCO_2$ (Fig. 4.7(d)), both Ti and Zr vibrations contribute in the relevant frequency range. Here too we find significant dispersion in bond strengths, similar

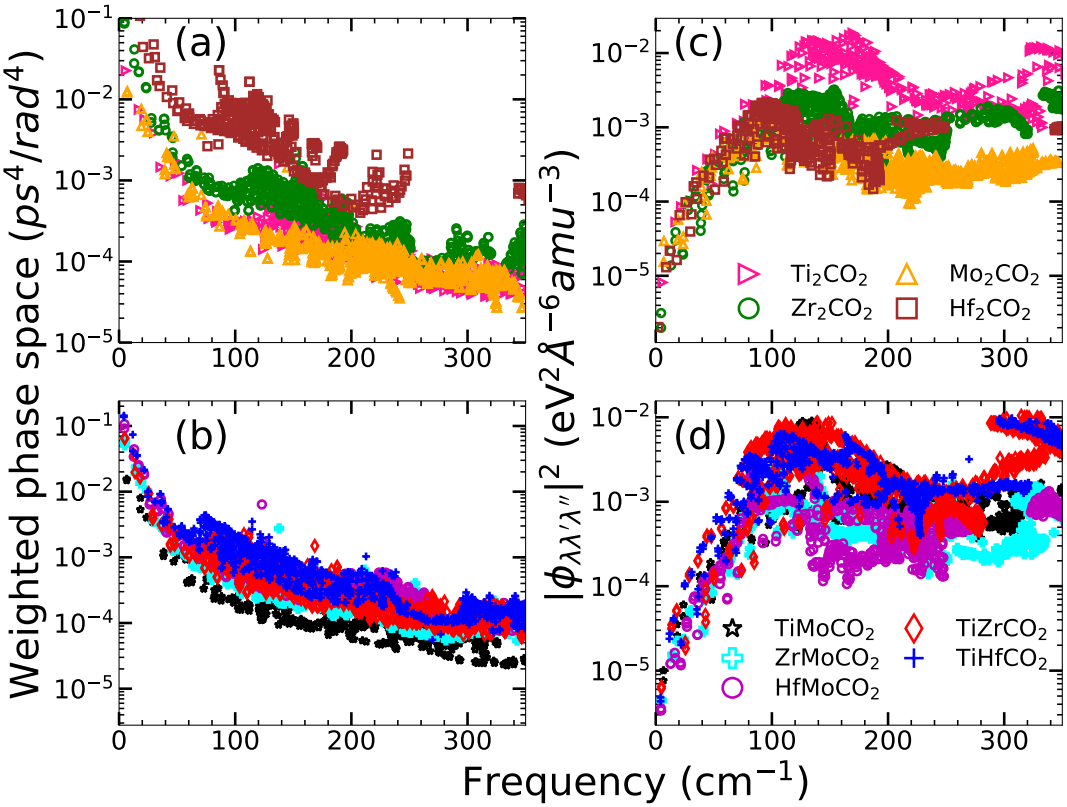

Figure 4.23: (a,b) Available weighted phase space as a function of phonon frequency for the MXenes considered. (c,d) Average scattering matrix element $|\phi^{\pm}_{\lambda\lambda'\lambda^e}|^2$ as function of frequency for all MXenes considered

to $TiHfCO_2$. In the Mo-based Janus $ZrMoCO_2$ and $HfMoCO_2$, these dispersions are much less. Although dispersions are there in $TiMoCO_2$, the Ti-cation bond strengths have hardly changed in comparison with Ti_2CO_2. Since the vibrations in the frequency range of interest is overwhelmingly dominated by the Ti atoms, the Ti-anion bond strengths decide the extent of anharmonicity.

Figure of Merit

Fig. 4.24 shows the maximum value of the figure of Merit ZT as a function of temperature for all parent and Janus MXenes. Energy window from -1.5 to 1.5 eV and carrier concentration $\sim 10^{20}$ cm^{-3} are used to extract maximum ZT. We find that surface engineering by forming Janus greatly enhances the ZT. The maximum ZT of 3.5 at 800K is obtained for $TiZrCO_2$ in the case of p-doped systems. This is more than double the maximum ZT obtained in any of the parent MXenes (a maximum ZT value of 1.6 at 300 K is obtained for Ti_2CO_2). p-doped $TiHfCO_2$ also yields a high ZT of $\sim$ 3 at 800K. These two Janus compounds, even when n-doped, produce a maximum ZT of 2 while none of the parent compounds and the Mo-based Janus could produce a maximum ZT more than 1. The dominant reason for such high ZT in these two systems, irrespective of the type of doping, is due to their extremely low κ_l. High values of S and σ for p-doped $TiZrCO_2$ and $TiHfCO_2$ are responsible for substantially higher ZT in these systems when they are doped by p-type carriers in comparison to doping by n-type one. Thus, desired values of maximum ZT can be obtained by breaking the inversion symmetry in MXenes.

The evaluated σ and κ_e values might be overestimated because of constant relaxation time approximation (CRTA) and deformation potential approximation (DPA) used to evaluate these coefficients. In the DPA method, it is assumed that electrons interact only with the acoustic phonons. This may result in an overestimated carrier relaxation time (τ). This can have serious consequences on the electronic transport properties, particularly for systems having components with significant differences in their electronegativities [175, 176]. More accurate calculation of τ is possible by the electron-phonon coupling (EPC) method[176] that includes interactions between electrons and optical phonons. However, in this work, we have focused on how asymmetrization of surfaces by making Janus out of its end point MXenes improves the thermoelectric performance. Since the same DP theory has been used for M_2C and Janus MM′C MXenes, we expect there

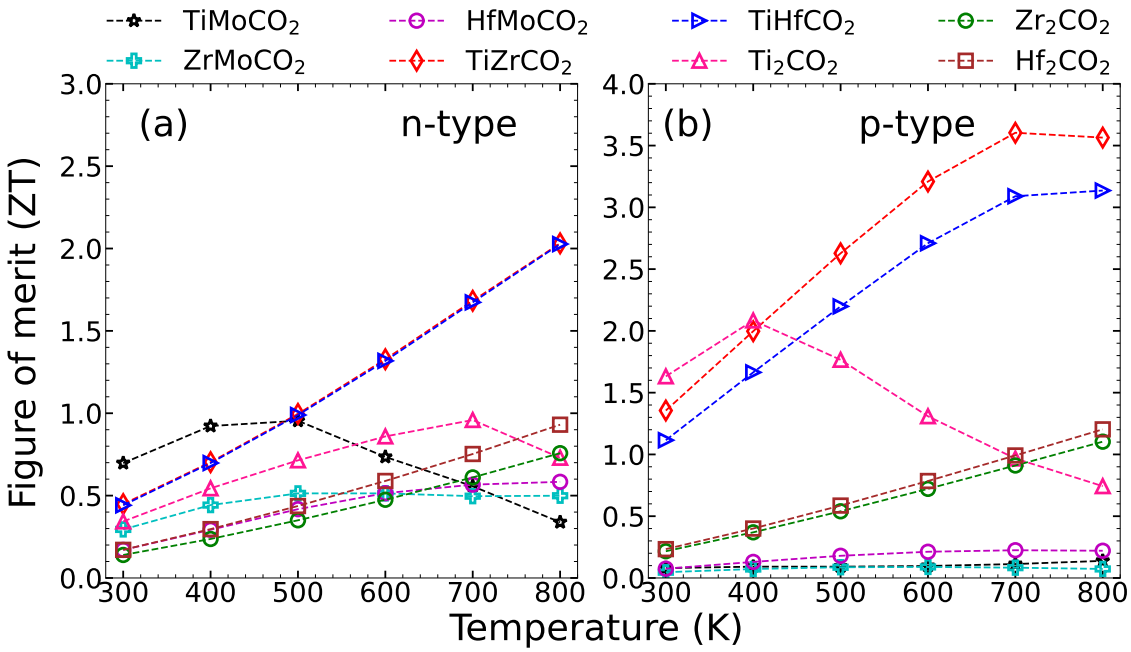

Figure 4.24: Maximum Figure of merit (ZT) of all MXenes considered, as a function of temperature. Results for both n and p-doped systems are shown.

wouldn't be drastic changes in the qualitative trends if we include electron-optical phonon coupling in the estimation of electronic transport parameters. This is because in the estimation of ZT, the overestimation that creeps in σ will be more or less balanced by the error in κ_e. Thus, even from a quantitative point of view, the changes in ZT may not be substantial. Therefore, given that the EPC method is computationally very demanding, the qualitative trends focused on in this work may not be significantly affected, and the quantitative estimation of ZT may not be starkly different; we have not attempted any comparative study of results obtained from DP and EPC methods. In a future communication, we would like to focus on this.

4.3.4 Thermodynamical stability

Since the Janus compounds presented in this work are yet to be synthesised experimentally, it is important to check their thermodynamic stabilities at the maximum temperature at which these are proposed to be used as thermoelectric devices. To this end, we have performed the *ab initio* molecular dynamics (AIMD) simulations for all five Janus MXenes considered. The simulations are performed at 800K, the maximum temperature at which thermoelectric parameters are calculated. Fig. 4.25 shows the fluctuations in Free energy (red curves) and temperature (green curves). The top and side views of the initial (at T=0 K) and final structures (at T=800 K) are shown in the insets. The Free energies and the temperatures fluctuate about their average values and remain constant for the simulation time cycle of 20 ps. No signature of bond distortion or loss of structural symmetry is observed, which ensures that these Janus MXenes possess good thermal stability and can be used for thermoelectric applications at significantly high temperatures.

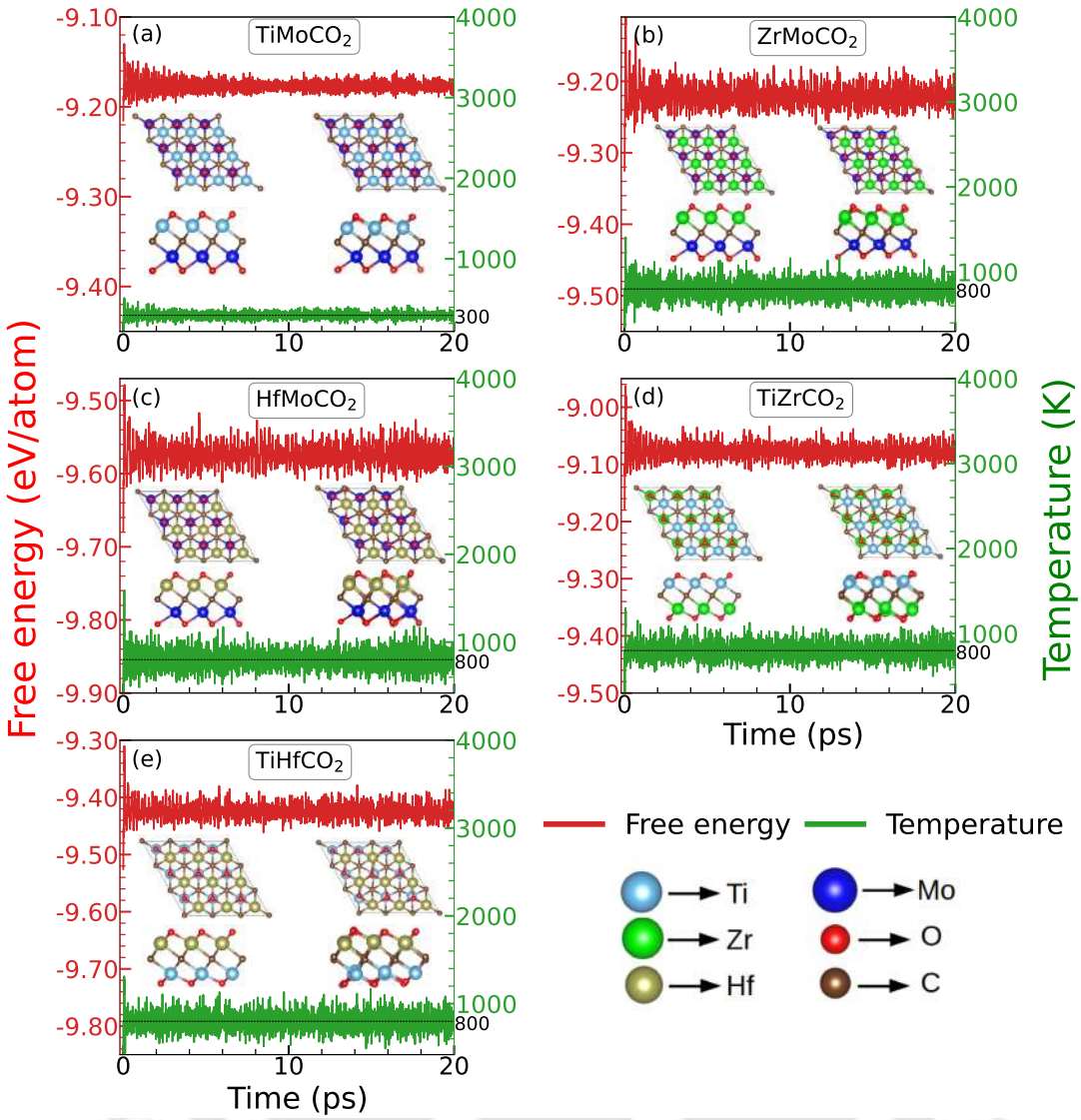

Figure 4.25: AIMD simulations for the Janus MXenes considered.

4.4 Strain engineering and thermoelectric properties of Janus MXenes

As mentioned in the introduction strain is found to be another route to tune the electronic and thermal tranport properties. In the following, we present the effect of strain on Janus MXenes Zr_2COS, $ZrHfCO_2$, and ZrHfCOS, in detail. Reasons behind picking these three for strain engineering has been discussed in section 4.1.

4.4.1 Structural parameters and stability

The Janus monolayers considered here are obtained from Zr_2C pristine MXene. The ground state structures are obtained from DFT calculations by calculating total energies corresponding to all possible structural models, as discussed earlier. The structural model with minimum total energy is considered the ground state. We find that both -O and -S atoms occupying the H site (the hollow site corresponding to the transition metal atoms) minimise the total energy in all cases. The ground state structure in each of the three Janus compounds is shown in Fig. 4.26.

In Table 4.5, the structural parameters of the systems as a function of bi-axial strain $\epsilon(\epsilon = (\frac{a-a_0}{a_0}) \times 100\%)$, where a_0(a) is the lattice constant for unstrained (strained) system) are shown. To ensure stability of the compounds, the range of strain considered here is kept limited between -4% and +4%. We find

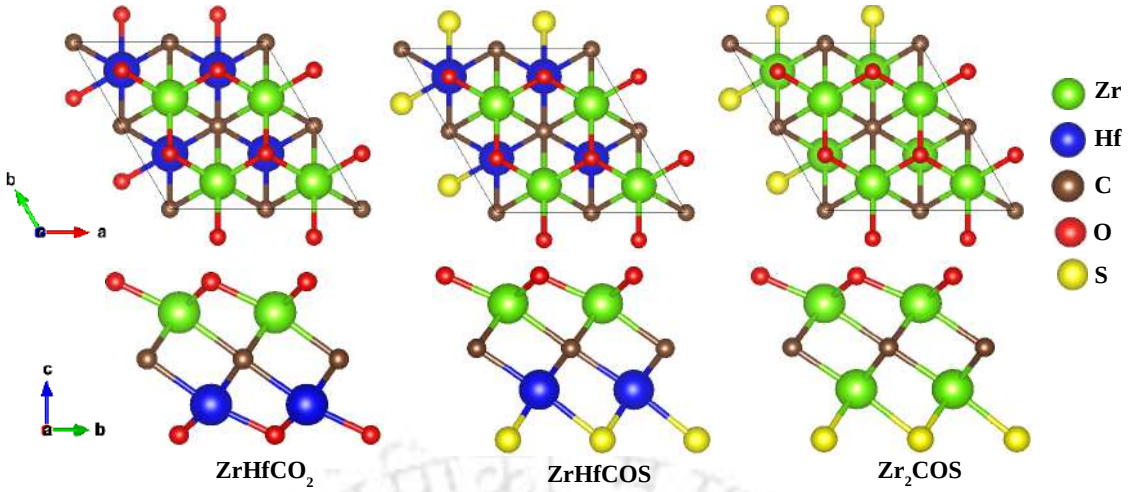

Figure 4.26: Ground state structures of Janus MXenes. The top (bottom) panel shows the top (side) view.

Compound	Strain (ϵ) %	a (Å)	E_g (eV)	Bond length (Å)			
				Zr-C	Hf-C	Zr-O_u	Hf-O_d
$ZrHfCO_2$	-4	3.16	0.61	2.30	2.28	2.04	2.03
	-2	3.22	0.82	2.33	2.31	2.07	2.07
	0	3.29	0.99	2.36	2.34	2.11	2.10
	+2	3.35	1.13	2.39	2.37	2.14	2.14
	+4	3.42	1.24	2.42	2.40	2.18	2.17
				Zr-C	Hf-C	Zr-O	Hf-S
ZrHfCOS	-4	3.23	-	2.35	2.28	2.10	2.49
	-2	3.30	-	2.37	2.31	2.11	2.49
	0	3.37	-	2.40	2.34	2.13	2.50
	+2	3.44	0.02	2.43	2.37	2.16	2.51
	+4	3.50	0.22	2.45	2.40	2.18	2.52
				Zr_u-C	Zr_d-C	Zr_u-O	Zr_d-S
Zr_2COS	-4	3.25	-	2.35	2.31	2.10	2.52
	-2	3.32	-	2.38	2.34	2.12	2.52
	0	3.39 (3.44[177])	-	2.40	2.36	2.14	2.52
	+2	3.46	-	2.43	2.39	2.16	2.53
	+4	3.52	0.18	2.46	2.46	2.18	2.54

*Zr_d (O_d) and Zr_u (O_u) are the Zr (O) atoms at the (00-1) and (001) surfaces of Zr_2COS ($ZrHfCO_2$) MXene, respectively

Table 4.5: Lattice constant (a), band gap (E_g), and bond lengths corresponding to different pairs of atoms in the three Janus MXenes.Results are tabulated for different ϵ.

significant dispersions in the M-C and M-T bond lengths. When the functional group T is -O (-S), the M-C bonds are about 13% (2-7%) longer (shorter) than the M-T bonds. Such fluctuations in bond lengths as a result of surface manipulation introduce anharmonicity in the system and directly affect the lattice thermal conductivity.

Since the Janus MXenes considered in this work are yet to be synthesised experimentally, their mechanical, thermal, and dynamical stabilities as a function of strain are crucial. In what follows, we have investigated these by varying the strain from the compressive to the tensile region. The mechanical stability of the optimized structures at each strain is examined by computing the elastic constants C_{ij}. Since the symmetry of the Janus structure is hexagonal, three elastic constants C_{11}, C_{12}, and C_{66} =(C_{11}-C_{12})/2 are computed. Table 4.6 shows the evaluated elastic constants of the three compounds at each value of ϵ.

System	Strain (ϵ) (%)	Elastic Constants		
		C_{11}=C_{22} (Nm^{-1})	C_{12} (Nm^{-1})	C_{66} (Nm^{-1})
$ZrHfCO_2$	-4	339.16	95.95	121.61
	-2	311.06	85.82	112.62
	0	278.19	78.51	99.84
	+2	246.94	72.04	87.45
	+4	214.34	67.60	73.37
ZrHfCOS	-4	256.38	68.36	94.01
	-2	232.63	63.69	84.47
	0	219.35	61.55	78.90
	+2	196.14	56.86	69.64
	+4	170.05	57.67	56.19
Zr_2COS	-4	252.81	72.46	90.18
	-2	210.54	56.54	77.00
	0	213.66	63.42	75.12
	+2	185.22	56.05	64.59
	+4	163.97	56.36	53.80

Table 4.6: The Calculated Elastic Constants (C_{11}, C_{22}, C_{12}, C_{66}) as a function of strain are shown for the three compounds.

We find that the criteria[178] for mechanical stability, $C_{11} > 0$ and $C_{11} > C_{12}$, are satisfied in each case, suggesting the mechanical stability of each compound for the entire range of strain considered.

The thermal stability of a compound at higher temperatures is vital for thermoelectric (TE) applications. The thermal stability of all three Janus compounds at each strain is calculated by *ab initio* molecular dynamics (AIMD) simulations. Variations in the free energy and the temperature with time at 800 K, along with the initial (T = 0 K) and final (T = 800 K) structures, are shown in Fig. 4.27 (for zero strain) and Fig.4.28 (for different strains). The results suggest that even at this high temperature, none of the structures distort over time, ensuring thermal stability of all compounds, irrespective of the amount of strain. The stability at 800 K, the highest temperature for calculations of TE parameters, also ensures that the structures are stable at lower temperatures and under various strains.

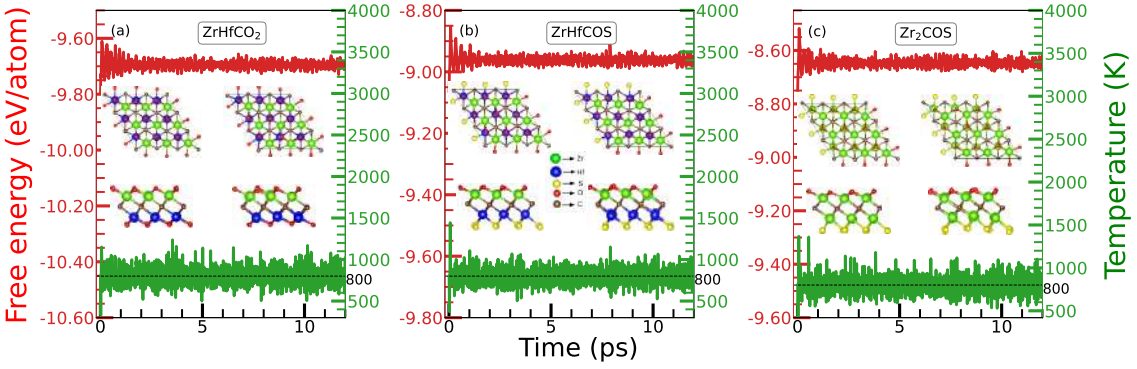

Figure 4.27: Variations in the Free Energy and the Temperature of the three compounds, over a time of 12 ps. The calculations are done on the systems at zero strain. The temperature considered for the calculations is 800 K.

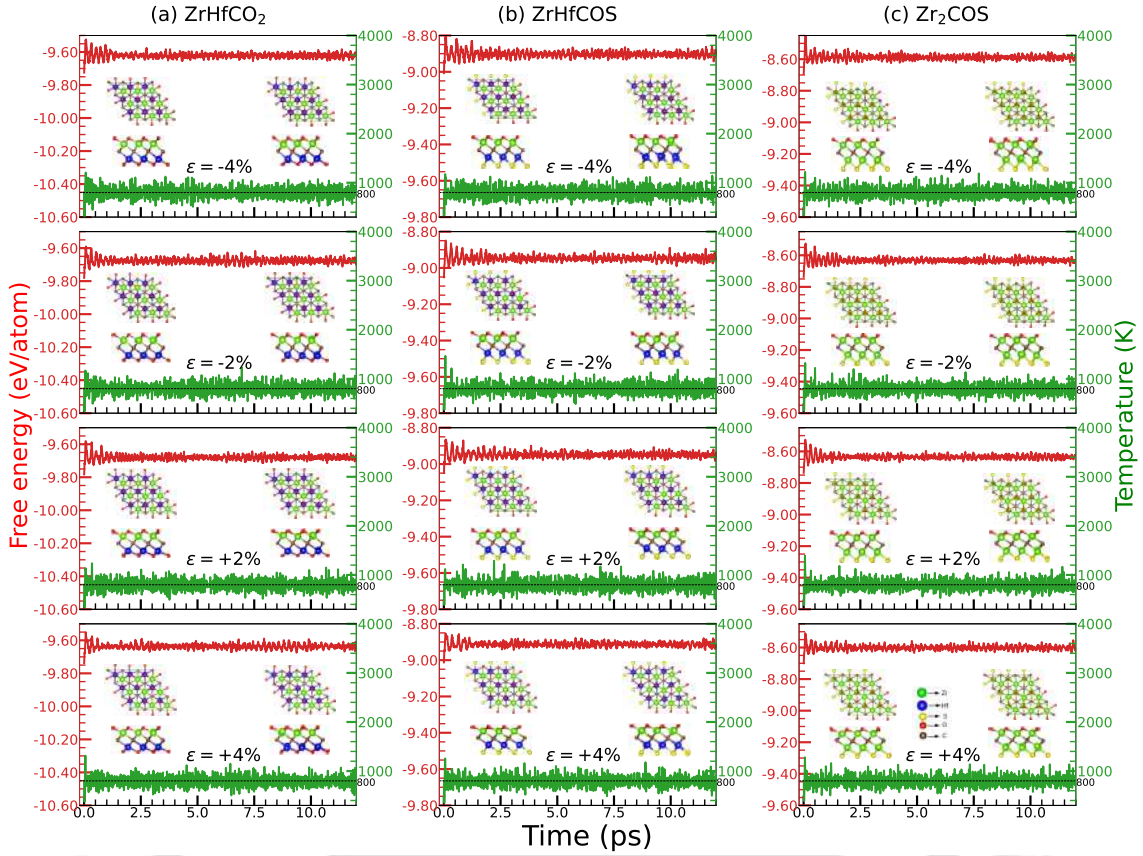

Figure 4.28: Variations in the Free Energy and the Temperature of the three compounds, subjected to various biaxial strains, over a time of 12 ps. The temperature considered in the calculations is 800 K.

The dynamical stability of the compounds on application of strains is assessed by computing the phonon dispersion relations. The results are shown in Fig. 4.29 (Fig. 4.30) for the unstrained (strained) Janus MXenes. The results imply that all three systems with and without strains are dynamically stable. Therefore, these three systems satisfy the necessary stability criteria in the temperature window of thermoelectric operation for the range of strains used in this work.

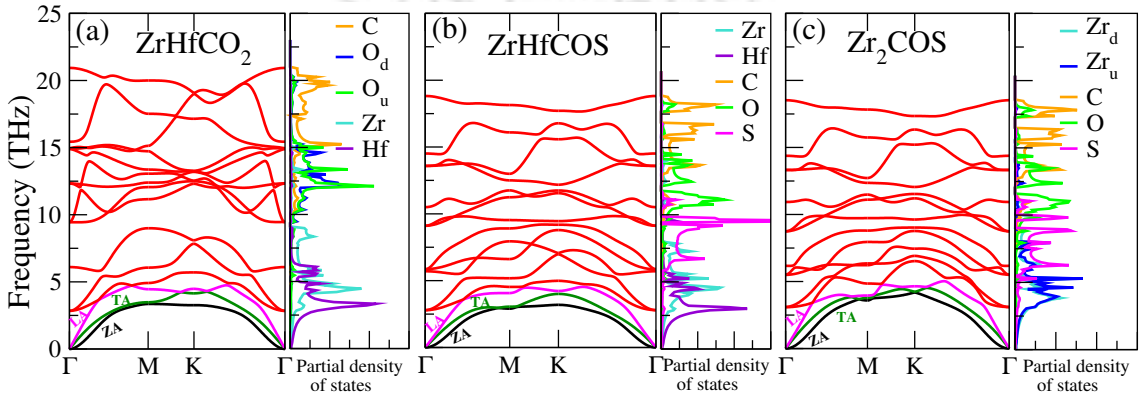

Figure 4.29: Phonon dispersions and atom-projected phonon densities of states for the three Janus compounds at zero strain.

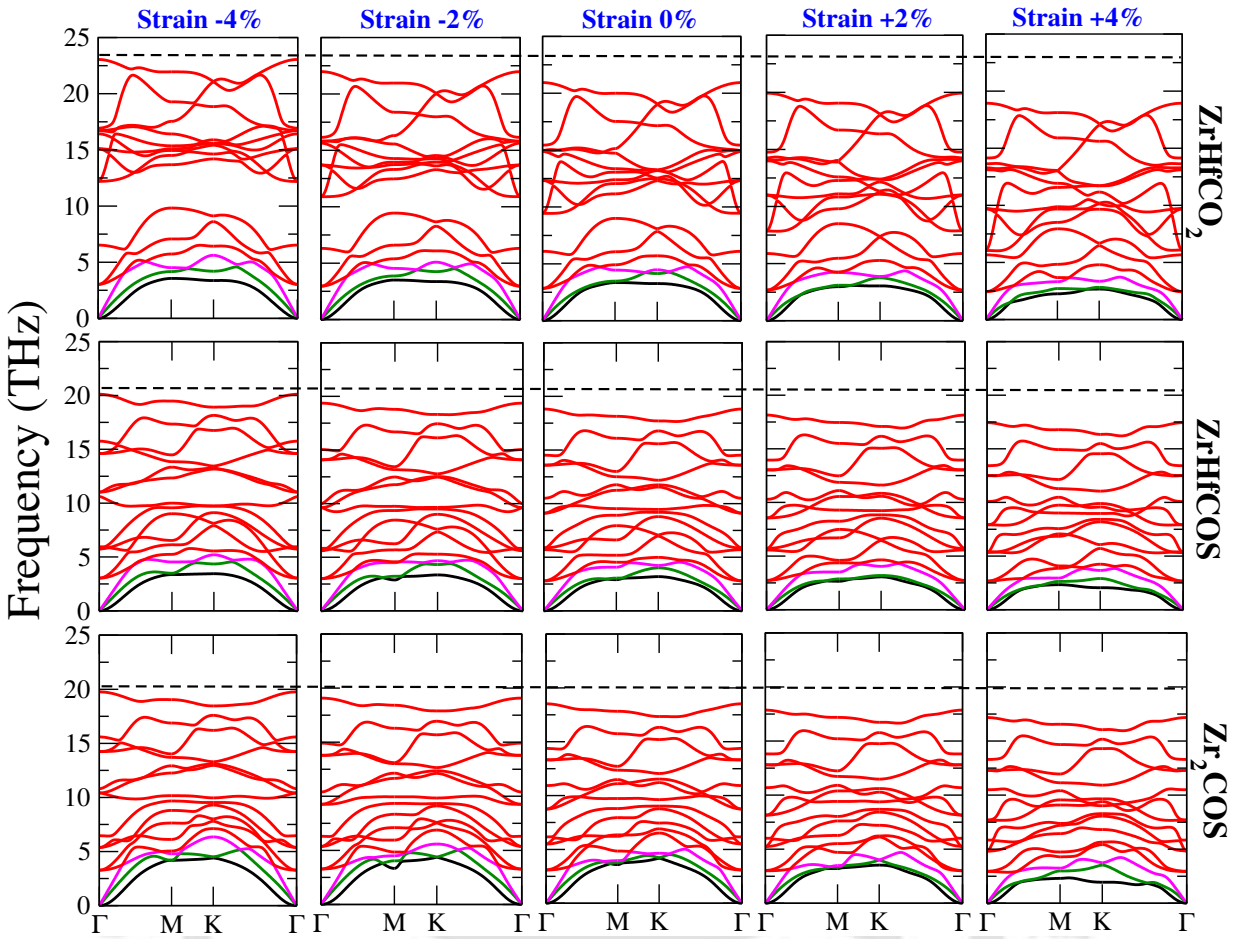

Figure 4.30: Phonon dispersions of the three compounds at zero and finite strains.

4.4.2 Electronic structure

Features in the electronic structures provide clues to the expected behaviours of electronic transport parameters associated with the thermoelectric figure of merit. In Figure 4.31 we present the electronic band structures and atom-projected densities of states of the three compounds at different strains. Without strain, $ZrHfCO_2$ is an indirect semiconductor ,whereas ZrHfCOS and Zr_2COS exhibit semi-metallic behaviour. Application of strain is quite significant for these three as the band gap changes upto about 39% for the semiconductor and the semiconducting gaps open in the other two. The band gaps increase (decrease) with tensile (compressive) strains for all three; the largest band gap is found for a strain of +4%. The evolution of the band gap with strain is shown in Table 4.5. The positions of conduction band minima (CBM) and valence band maxima (VBM) of the three compounds remain invariant with strain, the CBM (VBM) being located at the M (Γ) point. With the application of tensile (compressive) strain, the conduction band edges for all three compounds become flatter (dispersive). Moreover, the CBM for all the compounds is flatter than the VBM. This may result in a higher S for n-type doping.

The atom projected densities of states for all three compounds indicate significant contributions from p orbitals of C and T and d orbitals of M in both valence and conduction bands. However, the features and contributions near the band edges vary with composition and strain. For Zr_2COS and ZrHfCOS, a sharp peak dominated by S shapes up with the increase in the tensile strain. Although no such sharp peak is observed in the case of $ZrHfCO_2$, the sharpness of the band edges is found to increase with tensile strain as well. This is consistent with the flatter CBM as tensile strain is increased. This may result in a larger Seebeck coefficient with tensile stress. In the next sub-section, we will examine this.

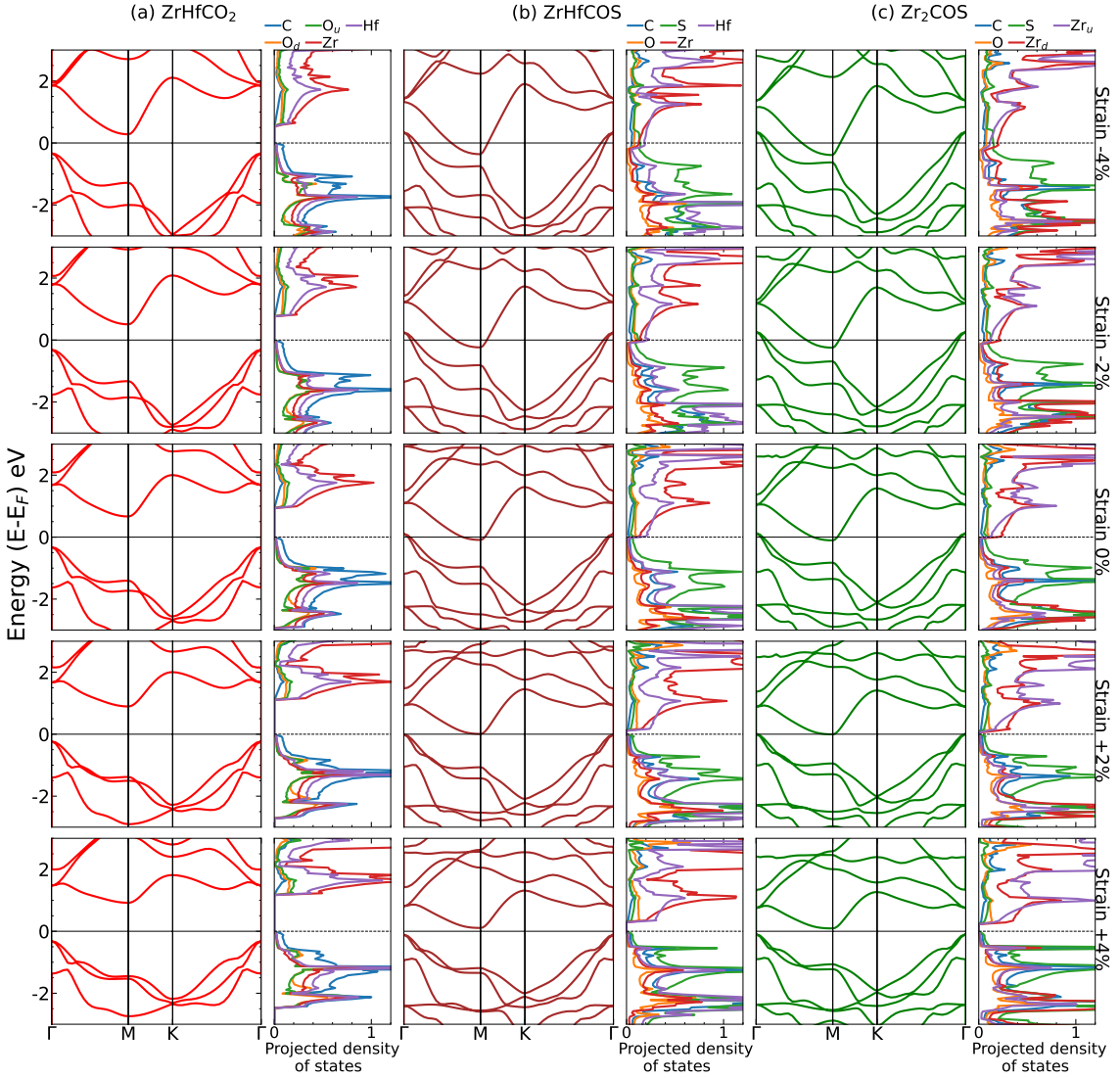

Figure 4.31: Electronic band structures and atom-projected densities of states for the three Janus MXenes. The three panels represent (a) $ZrHfCO_2$, (b) ZrHfCOS, and (c) Zr_2COS, for strains between -4% and +4%.

4.4.3 Electronic transport properties

Seebeck coefficient (S) is the measure of the ability of a material to convert a temperature gradient into electrical voltage[36]. A high value of S, therefore, is desired for better TE conversion efficiency. For a semiconductor, a negative (positive) value of S depicts that the majority-charge carriers are electrons (holes). Fig. 4.32 (Fig. 4.33) shows the Seebeck coefficient S as a function of n-type (p-type) carrier concentration at different temperatures and strains. Among the three Janus compounds, n-$ZrHfCO_2$ has the maximum value of $S(\sim 1200\ \mu$V/K at 300 K), irrespective of strain. The qualitative variation of S with electron concentration changes as the temperature is increased. For example, at 300 K, the absolute value of S of $ZrHfCO_2$ decreases monotonically (following the inverse relation of S and n, the carrier concentration[179]). For higher temperatures, the variation is non-monotonic[180], that is, S first increases then decreases with n. The position of the peak shifts with the increase in temperature. Similar behaviour is visible in ZrHfCOS and Zr_2COS even at 300 K. This behaviour of S at low n and high T for the narrow band gap semiconductors can be attributed to the bipolar conduction effect[181]. For n-type Janus structures, although electrons are the majority carriers, the contribution from holes (minority carriers) is non-negligible. Therefore, for the bipolar conduction regime, we observe, for our narrow band gap systems, a deviation from standard $S \propto n^{-2/3}$ behaviour. Such deviation of S due to minority carriers has been reported in earlier studies [182, 183, 184].

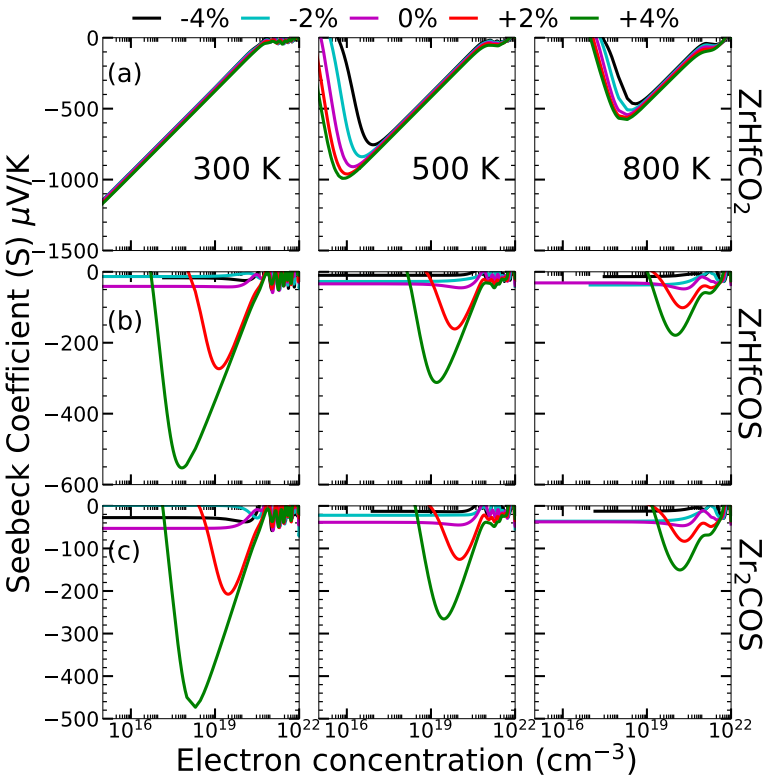

Figure 4.32: Seebeck coefficient (S (in μV/K)) as a function of electron concentration (in cm^{-3}) for n-type Janus MXenes ((a) $ZrHfCO_2$, (b) ZrHfCOS, and (c) Zr_2COS) at different temperatures. Results are shown for various ϵ.

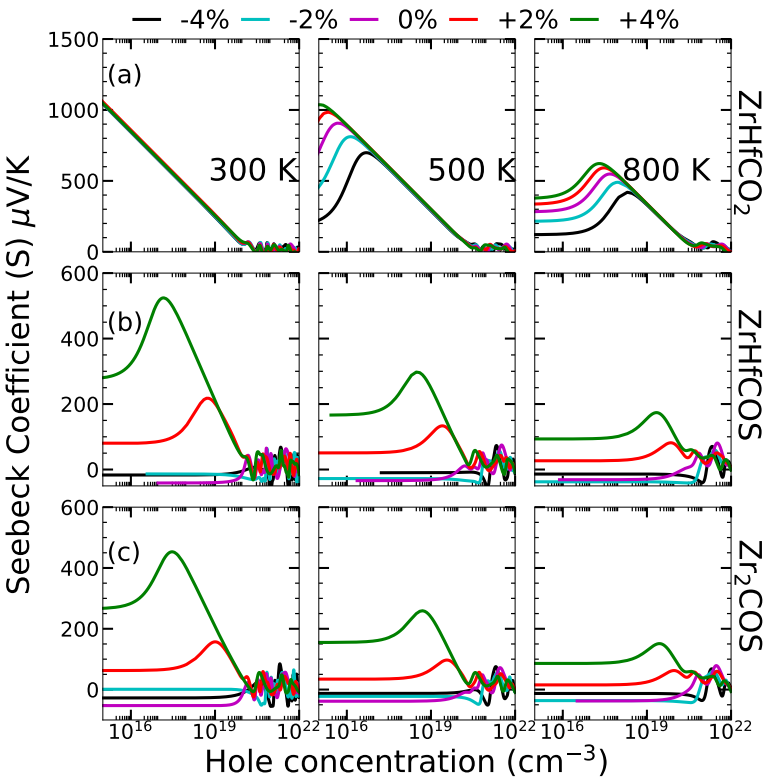

Figure 4.33: Seebeck coefficient (S (in μV/K)) as a function of hole concentration (in cm^{-3}) for p-type Janus MXenes at different temperatures. Results are shown for various ϵ

The effect of strain is visible on all three compounds. As the tensile (compressive) strain is applied, the S value increases (decreases). For n-type ZrHfCOS and n-type Zr_2COS, the effect of strain is more prominent. For these two compounds, S at 4% tensile strain is 6-8 times higher than S when no strain is applied. The explanation for such enhancement in S can be done from the changes in the densities of states and the band gaps (E_g). The emergence of sharp edges with application of tensile strain (Fig. 4.29) and flattening of the bands increases the effective mass (m^*) leading to an increase in S, since $S \propto m^*$[179], m^* the effective mass. Such a substantial effect is not seen in $ZrHfCO_2$ as the changes in the band edges with strain are not so drastic. Neverthelss, at any value of ϵ, $S_{ZrHfCO_2} > S_{ZrHfCOS} \sim S_{Zr_2COS}$. This is due to the significantly larger band gap of $ZrHfCO_2$ in comparison with the other two. The variations of S with concentration of p-type carrier, temperature, and strain are shown in Fig. 4.33. The S of all three compounds, obtained with p-type carriers, is slightly smaller than the corresponding n-type counterpart, irrespective of the strain and temperature. This is because of the dispersive nature of valence band edges in all three compounds as compared to the corresponding conduction band edges. It is worth mentioning that the evaluated values of S for these three compounds are, in general, higher or comparable to those of some established thermoelectric materials[169, 168, 185]. This raises the prospect of these materials as ones with higher TE efficiency.

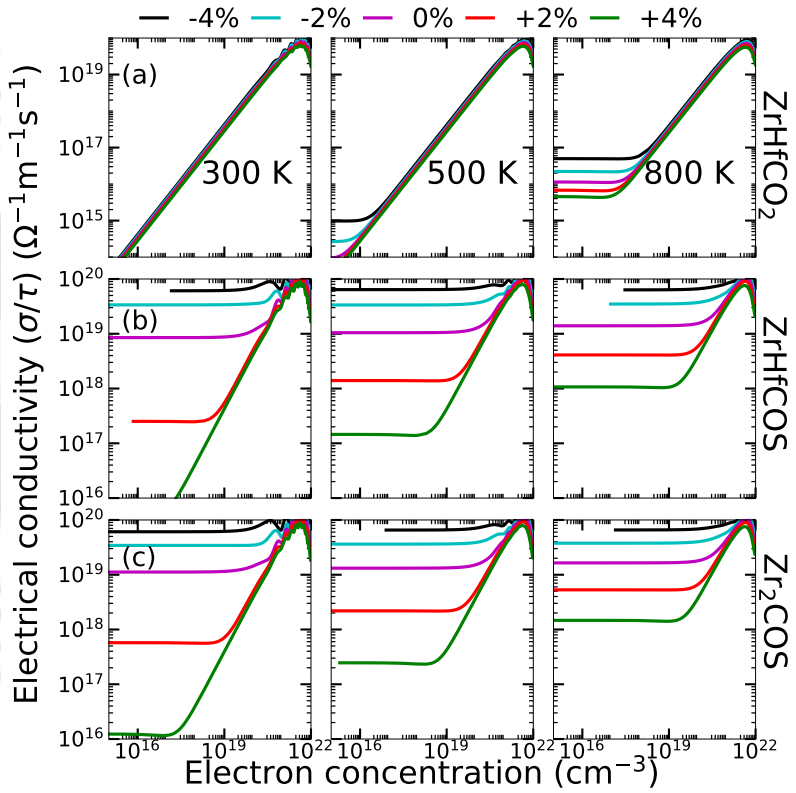

Figure 4.34: Electrical conductivity (σ/τ) as a function of electron concentration (in cm^{-3}) for n-type Janus MXenes ((a) $ZrHfCO_2$, (b) ZrHfCOS, and (c) Zr_2COS) at different temperatures. Results are shown for various ϵ

Fig. 4.34,4.35 show electrical conductivity(σ) and electronic thermal conductivity (κ_e) of the three compounds, scaled by the relaxation time (τ), as a function of n-type carrier concentration, strain and temperature. On comparing the σ/τ of the three Janus compounds, we find that $\sigma_{ZrHfCO_2} < \sigma_{ZrHfCOS} \sim \sigma_{Zr_2COS}$. The behaviour is exactly opposite to that of S. In general, for high value of carrier concentration n, σ/τ increases linearly with n which is consistent with standard $\sigma \propto n$ relation. However, a weak dependence of σ/τ on carrier concentration is observed for smaller n. The κ_e/τ follows the trends of σ/τ, validating the Wiedemann-Franz law ($\kappa_e \propto \sigma$). Similar variations in σ/τ and κ_e/τ are found when the carrier is p-type (Fig. 4.36 and Fig. 4.37). Thus, in all three Janus MXenes, the biaxial strain is found to affect the electronic transport properties substantially. The conversion efficiency, nevertheless, is constrained by the inverse dependence of S and σ. The lattice thermal conductivity may, thus, be decisive.

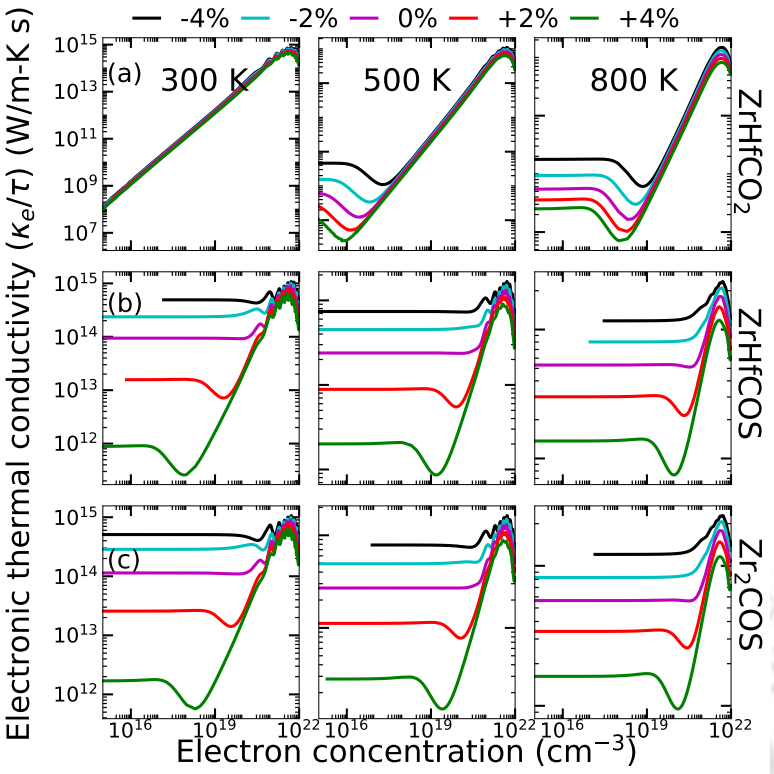

Figure 4.35: Electronic thermal conductivity (κ_e/τ) as a function of electron concentration (in cm^{-3}) for n-type Janus MXenes ((a) $ZrHfCO_2$, (b) ZrHfCOS, and (c) Zr_2COS) at different temperatures.Results are shown for various ϵ.

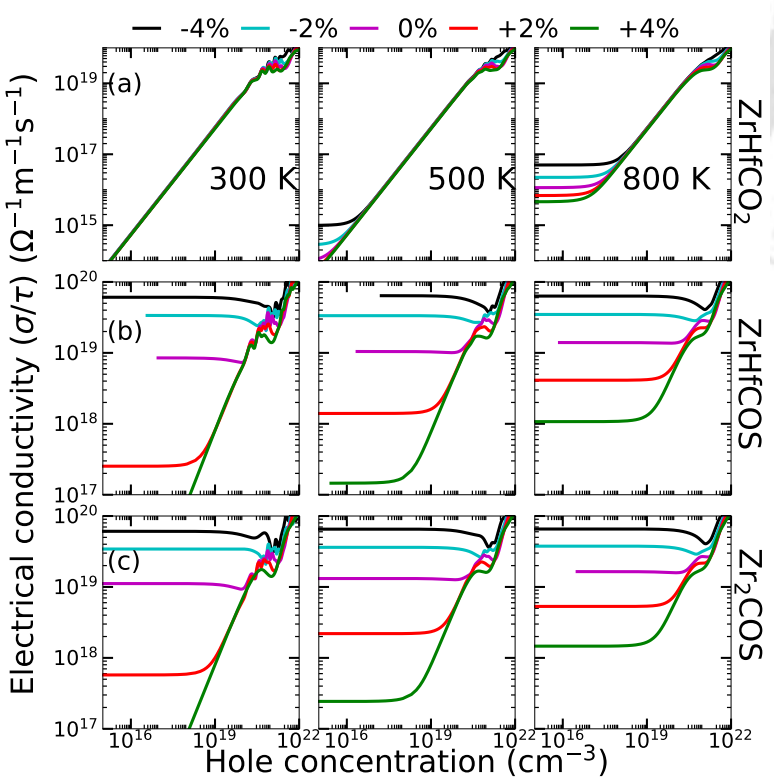

Figure 4.36: Electrical conductivity (σ/τ) as a function of hole concentration (in cm^{-3}) for p-type Janus MXenes at different temperatures. Results are shown for various ϵ.

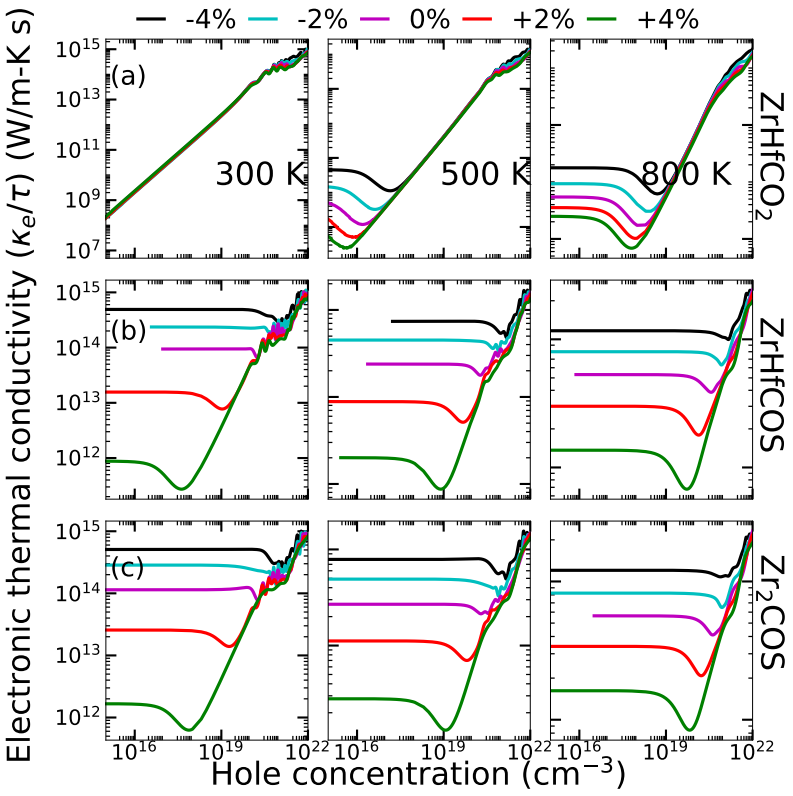

Figure 4.37: Electronic thermal conductivity (κ_e/τ) as a function of hole concentration (in cm^{-3}) for p-type Janus MXenes at different temperatures. Results are shown for various ϵ.

4.4.4 Phonon dispersion and Lattice thermal conductivity

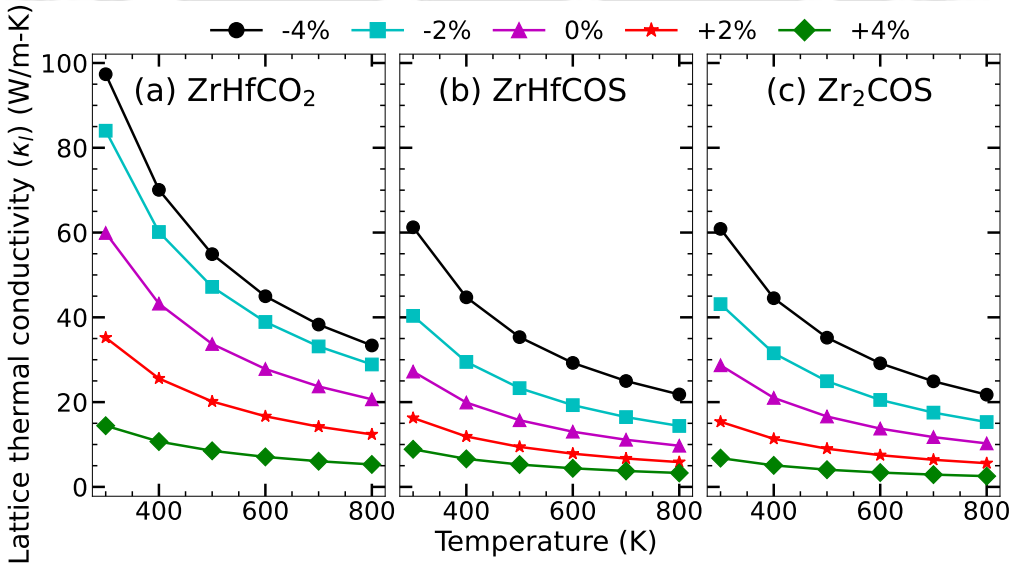

Figure 4.38: The lattice thermal conductivity as a function of temperature for the three compounds. Results are shown for different ϵ.

The phonon dispersion relations and densities of states shown in Fig. 4.29 and Fig.4.30, provide hints at possible effects of surface and strain engineering on lattice thermal conductivity κ_l. For all three Janus compounds, quadratic behaviour of the ZA mode near Γ, a hallmark of 2D systems, is observed. Phonon densities of states (Fig. 4.29) show that the acoustic and first three optical modes are dominated by the

vibrations from the transition metal atoms. C and the functional group elements (O and S) dominate the rest of the frequency spectra. As compared to $ZrHfCO_2$, the phonon modes shift towards lower frequencies in ZrHfCOS and Zr_2COS. This is due to the inclusion of S in the system replacing O, as S is heavier. As a result, the lower optical modes get closer to the acoustic modes (an effect of surface engineering). Such overlapping acoustic-optical phonon modes promote three-phonon scattering and restrict heat transfer. Similar behaviour is observed when biaxial strain is applied (Fig. 4.30). The phonon modes of all three systems shift to lower (higher) frequencies if the applied strain is tensile (compressive). Such shifts in phonon modes imply that the material's Debye temperatures (θ_D) and group velocity reduce[170]. Consequently, lattice thermal conductivities (κ_l) are expected to decrease with tensile strain.

That this indeed is the case for the systems considered here is validated by the variations of κ_l with strain. In Fig. 4.38 we present the variations in κ_l as a function of temperature and strain for all three Janus MXenes. To substantiate the accuracy of our calculations, the convergence of κ_l with respect to q-grid size is shown in Fig. 4.39. For each case, the calculated κ_l varies inversely with temperature. This suggests that intrinsic three-phonon (anharmonic) scattering dominates as temperature increases. We find that without any strain, ZrHfCOS ($ZrHfCO_2$) has the lowest (largest) κ_l of 27.19 W/m-K (59.88 W/m-K) at 300 K. This means that increasing surface asymmetry by heterogeneous passivation reduces κ_l more (a reduction of about 55% is observed in this case). Tensile biaxial strain in these compounds reduces κ_l further. At 300 K, compared to the zero-strain case, κ_l reduces by ~76% for $ZrHfCO_2$ and Zr_2COS, while it is 67% for ZrHfCOS. The lowest κ_l found for $ZrHfCO_2$, ZrHfCOS, and Zr_2COS at +4% strain and 300 (800) K are 14.42 (5.28) W/m-K, 8.85 (3.28) W/m-K, and 6.79 (2.53) W/m-K, respectively. These values are significantly less than those of some well-studied TMDCs [186, 187].

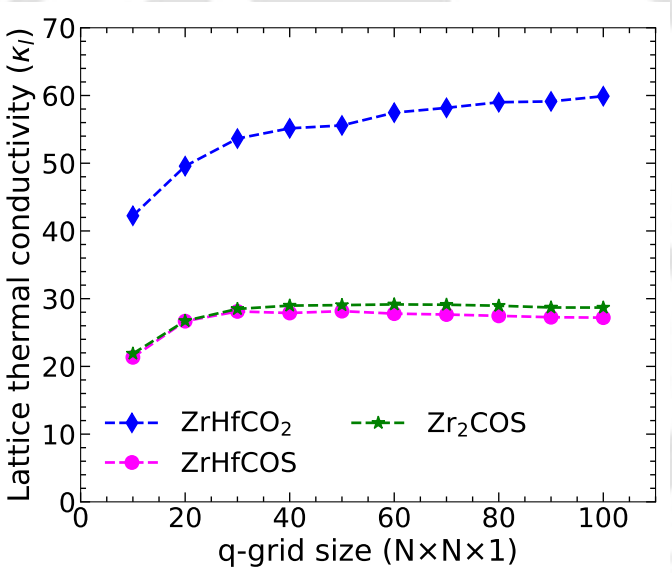

Figure 4.39: Variations of κ_l (W/m-K) with the size of q-grid is shown for Janus MXenes considered here. The results are for zero strain.

In order to understand the reasons behind such drastic reductions of κ_l with increasing asymmetry and tensile strain, we have performed an analysis from various angles. First, we look into it from the perspective of structural parameters. To this end, we have done a qualitative analysis of the strengths of bonds between different atomic pairs, as weaker (stronger) bond strengths imply larger (smaller) anharmonicity and lower (higher) κ_l as a consequence. Significant variations in the bond lengths in these compounds, particularly with changes in the composition (Table 4.5), indicate dispersions in the bond strengths. Using the Crystal orbital Hamilton Population (COHP) method[165] as implemented in the LOBSTER package[166], we have estimated the bond strengths (Integrated COHP or ICOHP). The results are shown in Fig. 4.40. The results provide some insights regarding connections between bond strengths, strain, and surface engineering to understand the trends in κ_l. In case of zero and compressive strains only, there are noticeable differences between the M-T bond strengths. The two compounds having S in one of the surfaces have weaker M-T bonds; the strengths of M-T bonds of these two compounds are comparable. The difference surely is due to the presence of longer bonds associated with S atoms. Also, irrespective of strain, the dispersions in bond strengths is more in the two compounds containing S. This, along with stronger bonds at zero and

compressive strains in $ZrHfCO_2$ as compared to the other two compounds and subsequent large value of κ_l indicate larger anharmonicity in S containing compounds. With an increase in tensile strain, such differences reduce considerably. The reason lies in the relative changes of the M-T bond lengths. In $ZrHfCO_2$, the Hf-O bond length increases by 7% as the strain changes from -4% to +4%. The corresponding bond in the other two compounds, that is, Hf-S in ZrHfCOS and Zr_d-S in Zr_2COS, changes by only 1% over the same changes in strain. As a result, the Hf-O bond strength reduces substantially with an increase in strain in $ZrHfCO_2$ while there is hardly any change in the strengths of Hf-S and Zr_d-S bonds in ZrHfCOS and Zr_2COS, respectively.

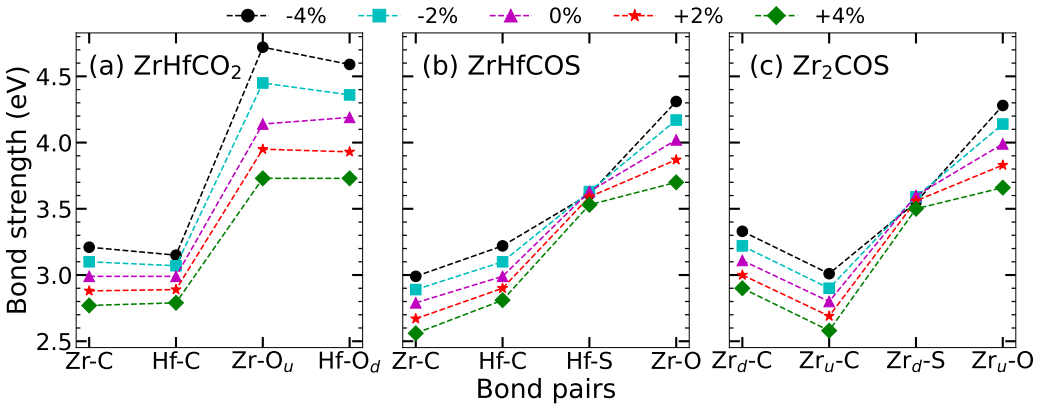

Figure 4.40: Bond strength (ICOHP (in eV)) for different atomic pairs of the three compounds. Results are shown for different ϵ.

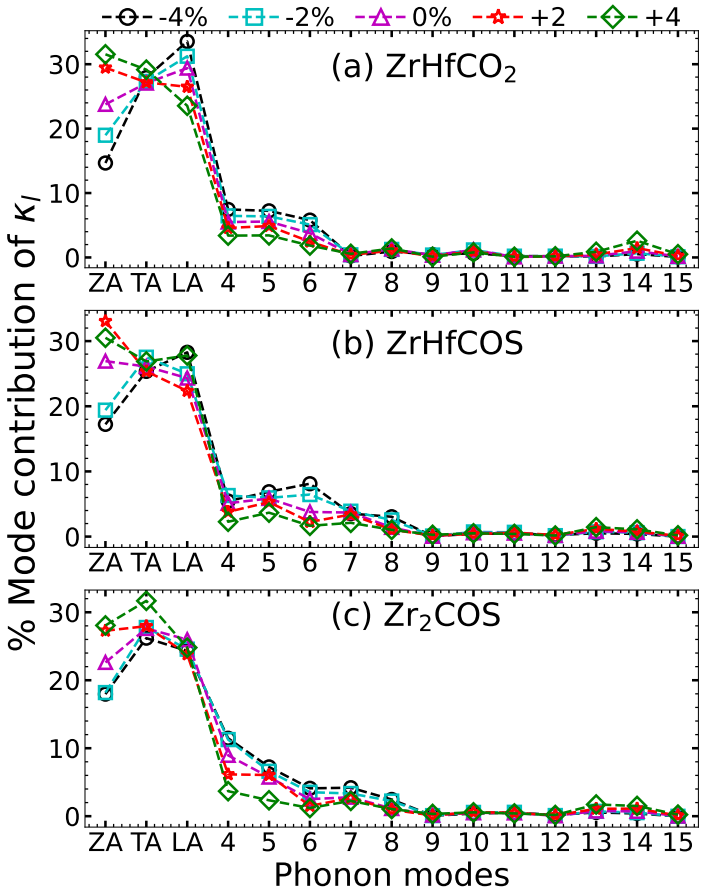

Figure 4.41: Phonon mode resolved contributions to lattice thermal conductivity (in %) for the three compounds at 300 K. Results are shown for different ϵ.

Next, we focus on the quantitative estimates of anharmonicity in the systems and the roles of surface and strain engineering. To this end, the first thing is the identification of the largest contributors towards heat transport from among the phonon modes. We do this by calculating the percent contribution of each of the phonon modes to κ_l (Fig. 4.41). Across the compounds, irrespective of the strain, the major contributions are from the acoustic modes ($\sim 80\%$) and the first three optical modes ($\sim 15\%$). The noticeable differences are (a) for compressive (tensile) strains, the LA (ZA) mode is the major contributor among acoustic modes, and (b) the contribution from the first three optical modes is more significant in the case of compressive strains. Since these results suggest that frequencies lower than 6 THz are the primary contributors to κ_l, further analyses will be restricted to this frequency region only. Moreover, for the sake of qualitative understanding, cases with $\epsilon = -4, 0, +4\%$ only will be discussed.

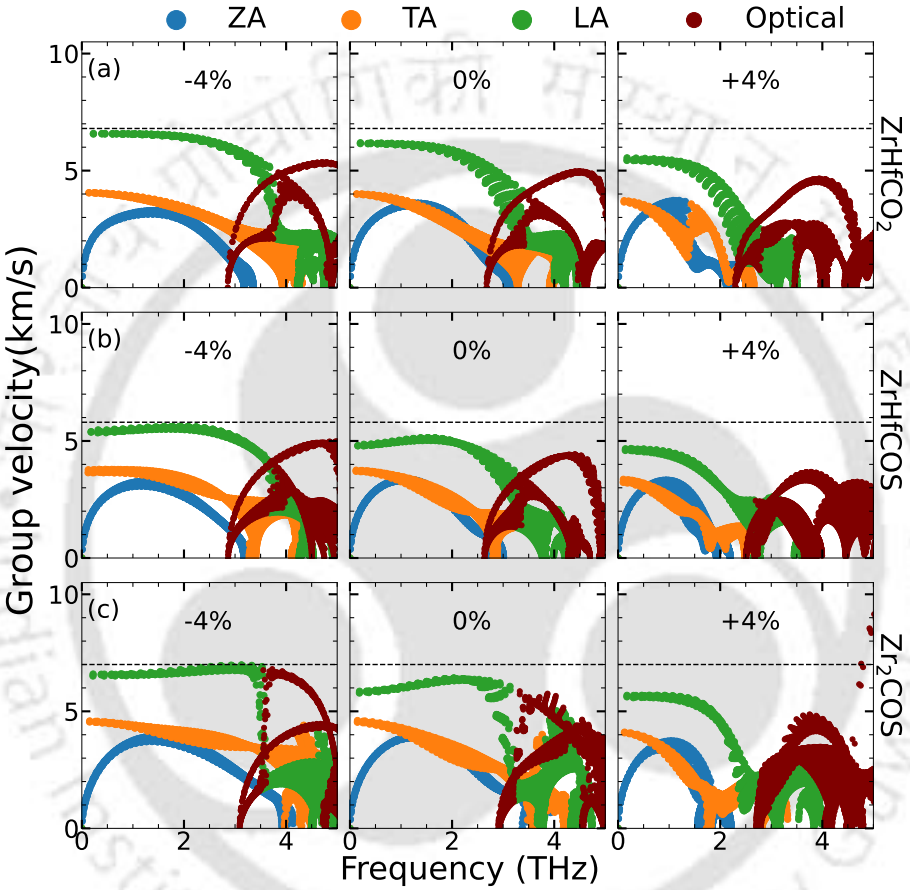

Figure 4.42: Phonon group velocity (v_g (in km/s)) for the three compounds shown as a function of phonon frequency. The value of ϵ in each case is given in the inset. The dashed line in each panel marks the highest v_g for the parameters associated with the panel.

As discussed earlier, the changes in the phonon dispersions with increasing strain point towards a drop in phonon group velocities and consequently κ_l. The variations in group velocity v_g at three values of ϵ are shown in Fig. 4.42. We find that for each of the three compounds, v_g decreases (increases) with tensile (compressive) strain. This indeed explains the variations in κ_l with ϵ for a given compound as $\kappa_l \propto v_g^2$ (Equation 2.45). Moreover, the quantitative comparison among v_g of the three compounds at any ϵ including $\epsilon = 0$ is consistent with the qualitative variation of κ_l across compounds for a given bi-axial strain.

Mode resolved Grüneisen parameter (Γ_λ) is one of the parameters that quantify the degree of anharmonicity in a compound. In Fig. 4.43, we present results of Γ_λ as a function of phonon frequencies, calculated using anharmonic IFCs[172]. At zero and 4% tensile strain, Zr_2COS has largest Γ_λ followed by ZrHfCOS and $ZrHfCO_2$. This trend is consistent with the trend in κ_l at 300 K. For a compressive strain of -4%, larger and near equal contributions towards Γ_λ between 2 and 4 THz for ZrHfCOS and Zr_2COS in comparison to $ZrHfCO_2$ too explains the trends in κ_l among the compounds and strain values.

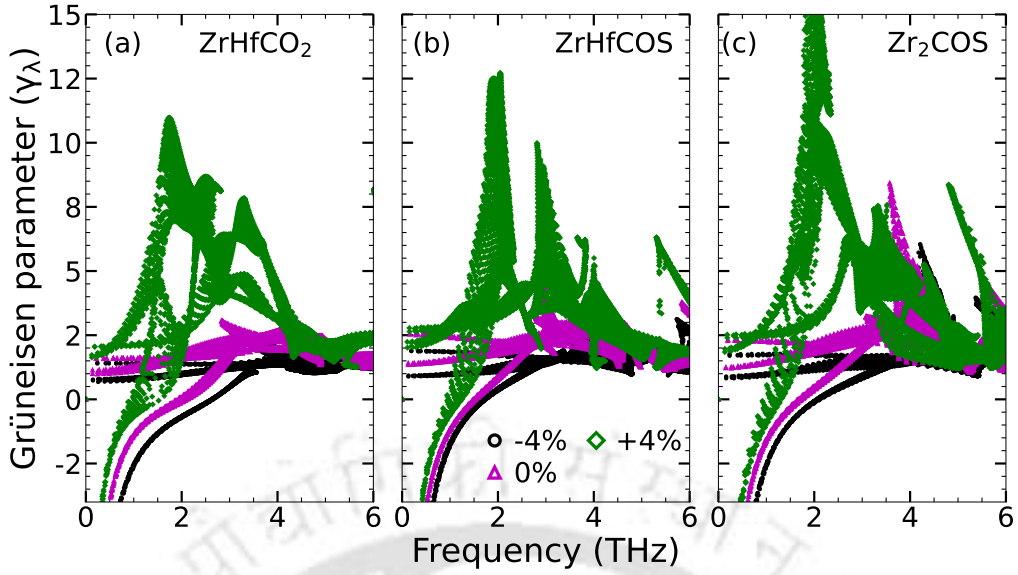

Figure 4.43: Grüneisen parameter (Γ_λ) for three compounds at 300 K. Black, magenta, and green indicate results for $\epsilon = -4, 0, 4\%$, respectively.

In order to understand the trends in the strengths of anharmonicity as seen in the variations of Γ_λ in terms of phonon-phonon scattering, we next look at the anharmonic scattering rates. Fig. 4.44 shows the calculated anharmonic scattering rates for the relevant frequency region. The higher scattering rates for S containing Janus in comparison with $ZrHfCO_2$ at any ϵ including $\epsilon = 0$ explains the trends in κ_l with composition and strain. To understand the reason behind higher scattering rates in S-containing Janus, we have evaluated the weighted scattering phase space (WP_3) accessible to the compounds (Fig. 4.45). Results are shown for three values of ϵ. For each compound, we find that $WP_3^{+4\%} > WP_3^{0\%} > WP_3^{-4\%}$. This explains the trends in the scattering rates and thus that of κ_l. However, the information obtained from WP_3 do not have the clarity to explain higher anharmonic scattering rates in Janus containing S. We, therefore, conclude that the higher anharmonic scattering rates in Janus containing S in comparison with $ZrHfCO_2$ for compressive and zero strains can be understood from the comparative rates of scattering between 1-4 THz. The greater proximity of the acoustic and optical branches due to the overall downward shift of phonon frequencies brought about by the replacement of O with heavier S leads to higher scattering rates in these two Janus compounds. This is an important contribution of surface engineering.

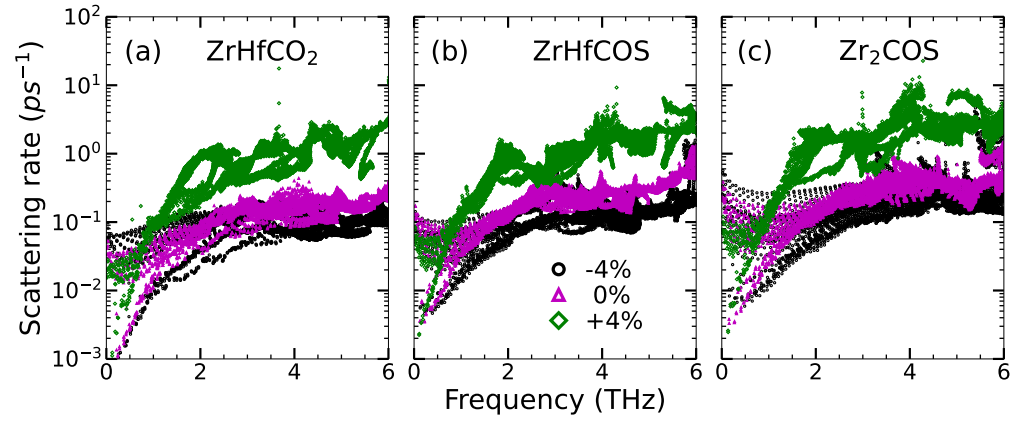

Figure 4.44: Anharmonic scattering rates for three compounds at 300 K. Black, magenta, and green indicate results for $\epsilon = -4, 0, 4\%$, respectively.

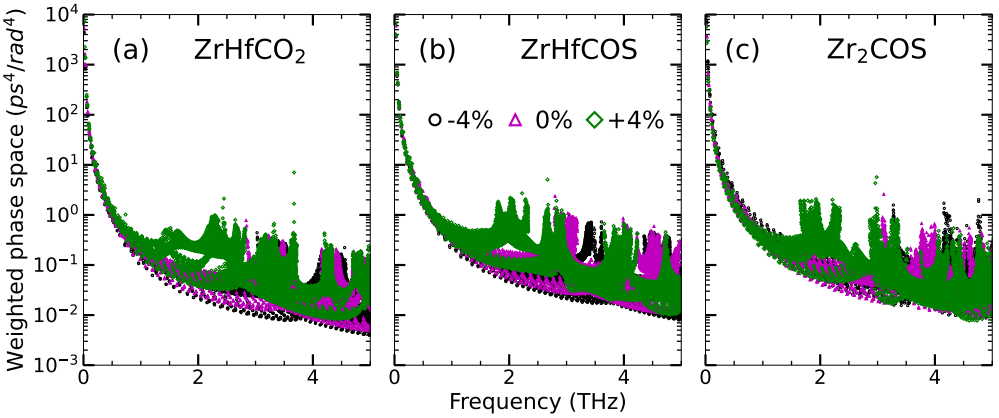

Figure 4.45: Weighted scattering phase spaces WP_3 available to the Janus MXenes as a function of phonon frequency are shown. The calculations are done at 300 K. Results are shown for three values of ϵ (given as ligands in panel (b)).

4.4.5 Figure of merit (ZT)

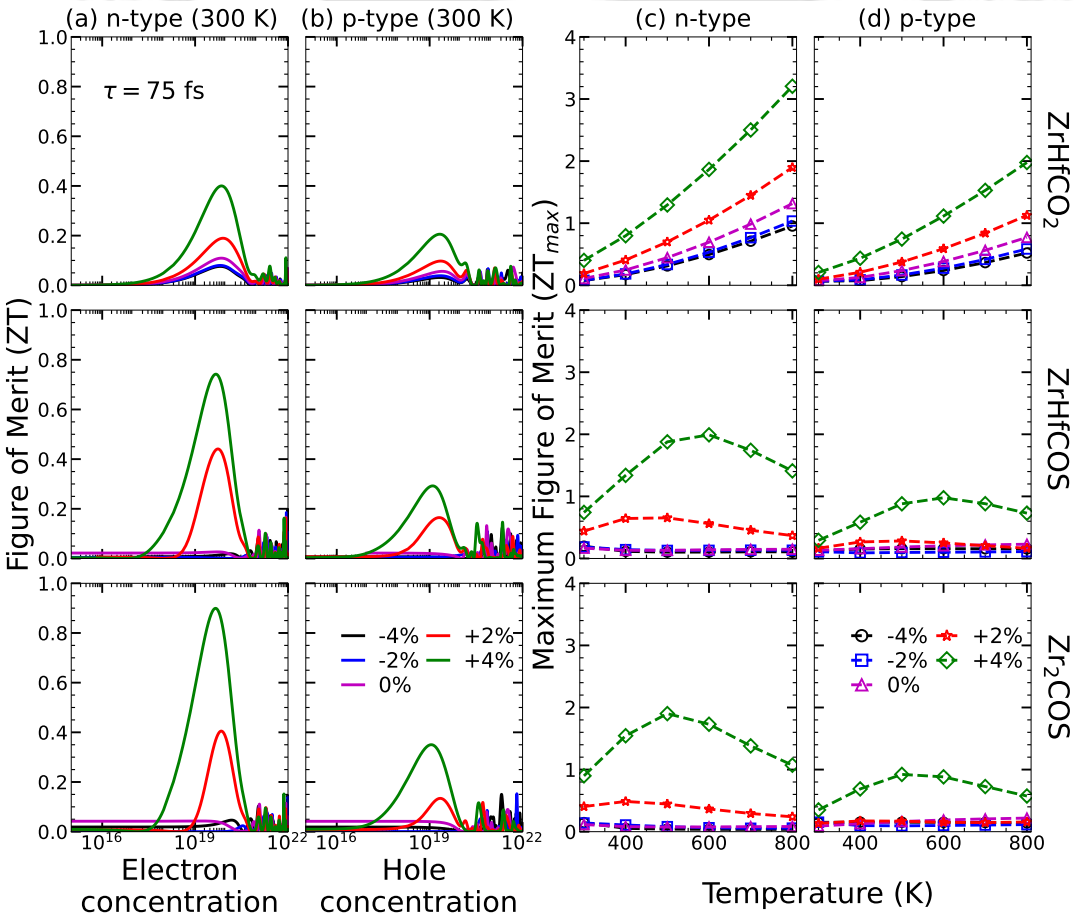

Figure 4.46: Figure of merit as a function of carrier concentration at 300 K (column a,b) and maximum figure of merit as a function of temperature (column c,d) for the three Janus MXenes. Results are shown for various ϵ. The calculations are done with carrier relaxation time $\tau = 75 fs$.

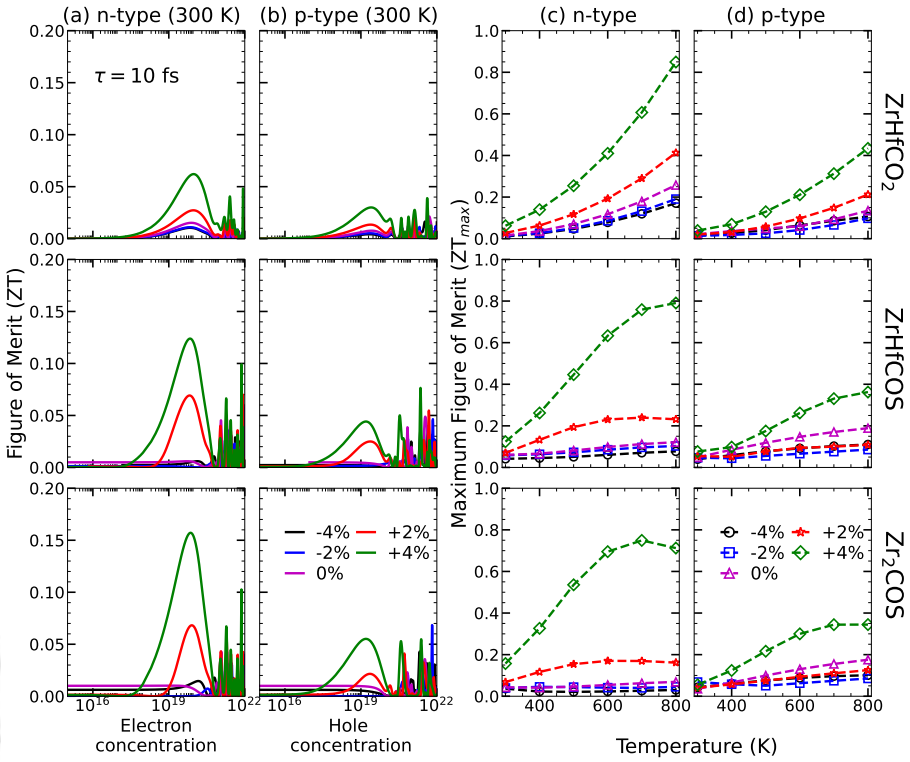

Figure 4.47: Figure of merit as a function of carrier concentration at 300 K (column a,b) and maximum figure of merit as a function of temperature (column c,d) for the three Janus MXenes. Results are shown for various ϵ. The calculations are done with carrier relaxation time $\tau = 10 fs$.

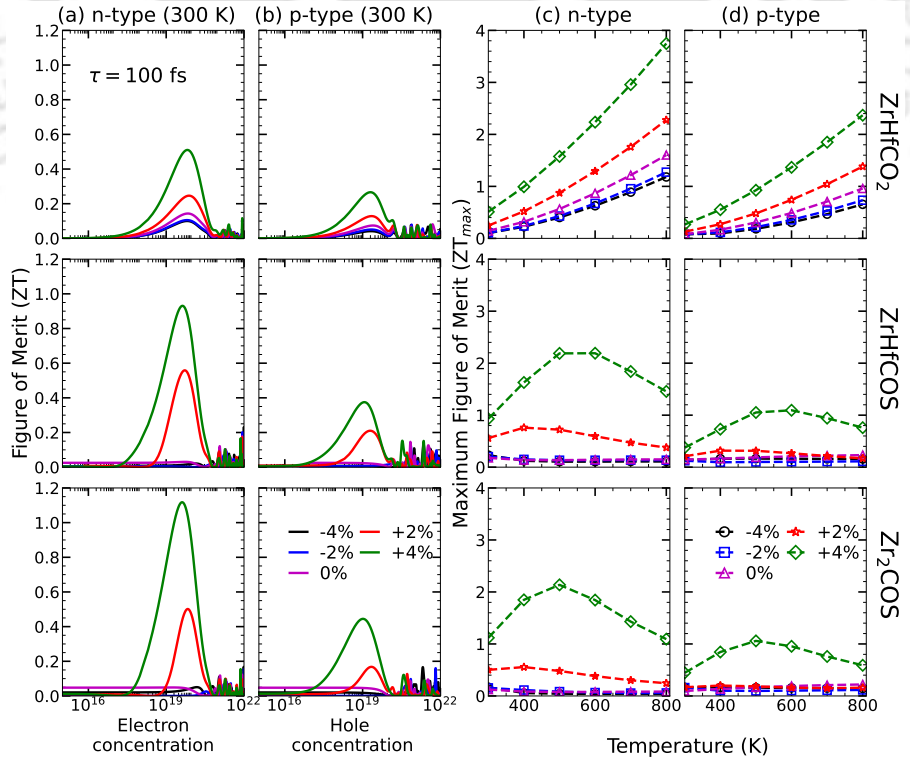

Figure 4.48: Figure of merit as a function of carrier concentration at 300 K (column a,b) and maximum figure of merit as a function of temperature (column c,d) forthe three Janus MXenes. Results are shown for various ϵ. The calculations are done with carrier relaxation time $\tau = 100 fs$.

Apart from temperature, ZT depends on the carrier concentration n and relaxation time τ since the transport parameters are calculated under RBA and CRTA. In Fig. 4.46 (a)-(b), we show the variation of ZT as a function of carrier concentrations for different strains, at 300 K. For n-type (p-type) doping of compounds, the variations of maximum ZT with strain and temperature are shown in Figure 4.46(c) (Figure 4.46(d)). The results presented are for τ=75 fs. We have chosen this particular value of τ as values close to it have been used successfully for various 2D thermoelectrics [188], including MXenes [150, 151]. ZT as a function of carrier concentration, strain (at 300 K), and maximum ZT as a function of temperature and strain for each compound, calculated for different τ, are shown in Figures 4.47,4.48. The results suggest that irrespective of value of τ, maximum ZT is obtained around the carrier concentration of 10^{19}-10^{20} cm^{-3}. This, too, agrees with the results of previous works. Irrespective of the systems and the type of carrier, the maximum ZT increases as one moves from the region of compressive to that of the tensile strain. However, the ZT values for n-doped systems are higher in all cases. The increase (decrease) of maximum ZT with tensile (compressive) strain is due to reduction (elevation) in κ_l, while larger (smaller) ZT for n-type (p-type) doping is due to the trends in the electronic transport parameters. The increase of maximum ZT with τ for all systems, irrespective of ϵ, is an artefact of the increase in the electronic transport coefficients with τ. Finally, we find a substantial impact of surface and strain engineering on the variation of maximum ZT with temperature. Although the qualitative effects of strain in this case are identical for all three systems, the values and the qualitative variations differ across the systems. For the maximum tensile strain considered, a maximum ZT of 3.2 is obtained in $ZrHfCO_2$ at 800 K, while for ZrHfCOS (Zr_2COS) it is $\sim$ 2 at 600 K (500 K). This difference is mostly due to the variations in the electronic transport parameters, notably the Seebeck coefficient S. Since with an increase in temperature, the differences of κ_l among the three compounds for the maximum tensile strain reduce considerably in comparison with that at 300 K, the differences in maximum ZT are purely due to electronic transport. Nevertheless, the maximum ZT for all three compounds, obtained at a tensile strain of 4%, are close to those obtained in other surface-engineered MXenes [150, 154]. Moreover, such high ZT values are desirable to obtain from the thermoelectric device, a Carnot efficiency at par with a Carnot refrigerator.

4.5 Conclusions

Inversion symmetry breaking in two-dimensional materials has turned out to be the driving force behind many material properties. In the context of thermoelectric properties of materials, this aspect has not been addressed in detail. Strain engineering has also proved to be an effective and feasible approach to enhance thermoelectric performance in 2D materials. In this chapter, the interplay of symmetry breaking and strain engineering on electronic structure, lattice dynamics, and transport properties has been investigated with the help of DFT-based first-principles techniques and semi-classical Boltzmann transport theory.

First, the systems chosen are from the MXene family, whose compositional flexibility is ideal to study such structure–property relationships. The inversion symmetry in M_2CO_2 MXenes is broken by manipulating its surfaces through substitution of transition metal atoms, resulting in Janus MXenes. Our calculations predict two Janus compounds, $TiZrCO_2$ and $TiHfCO_2$, with thermoelectric figure of merit $\sim$ 3, much larger in comparison with M_2CO_2 MXenes considered. In the MXene family of compounds, only two have been reported to possess such a large figure of merit. With great detail, we have systematically done a comparative study of the thermoelectric parameters of the Janus and corresponding parent MXenes to develop a microscopic understanding of the trends in these parameters. We infer that the dispersions in the bond strengths and weakening of metal-anion bonds on one particular surface, due to lowering of symmetry, are responsible for the degree of anharmonicity in the Janus compounds. This, in turn, affects their lattice thermal conductivities in particular and the thermoelectric figure of merit subsequently.

Subsequently, we find that while strain is the primary factor affecting the electronic transport parameters like Seebeck coefficient S, electrical conductivity σ, and electronic thermal conductivity κ_e, both composition (surface manipulation) and strain substantially affect the lattice thermal conductivity κ_l. As a consequence, we obtain excellent thermoelectric figure of merit ZT for all three compounds within a temperature window of 500 K. The tensile strain on one hand modifies the electronic band gap and the electronic structures of the compounds, thus improving the electronic parameters, while on the other hand, it increases anharmonicity through enhancement of phonon-phonon scattering. The interplay of the electronic and lattice transport parameters in the three compounds that differ in their compositions is understood to be the reason behind the higher maximum ZT obtained in $ZrHfCO_2$, in spite of undergoing the least engineering of its surfaces. This work establishes that application of moderate tensile strain on Janus systems, obtained from manipulation of surfaces through the functional groups attached to the transition metal components in 2D materials like MXenes, can be an efficient way to obtain materials with potentially high thermoelectric

conversion efficiencies. This chapter is a demonstration of the fact that both surface compositional engineering and strain engineering are effective strategies to enhance the thermoelectric performance of Janus MXenes.

Chapter 5

Anisotropic transport in Janus monochalcogenides and its effects on the thermoelectric properties

5.1 Introduction

Group IV-VI monochalcogenides (MX; M= Ge, Sn and X= = S, Se, Te) are another family of materials extensively investigated for a variety of applications [189, 190, 191, 192, 193]. Recent investigations project them as promising candidates for thermoelectric applications too [194, 195, 196]. Like black phosphorus, in their bulk phases, these materials exist in orthorhombic puckered layered structures, where multiple MX layers are held together by weak van der Waals forces[197, 198]. Experimentally, few-layer and monolayer MX structures have been successfully exfoliated from bulk MX. The monolayers inherit the crystal structures of the bulk and are analogous to that of 2D phosphorene[199, 200]. MX compounds are found to exist in different stable polymorphs α, β, and γ[201, 202, 203], both in bulk and in 2D, which gives rise to versatile functional properties and make them candidates for use as anode material in batteries, and in exciton physics[204, 205], for example. Their potentials as thermoelectric materials originate in their unconventional band structures. Their electronic band structures exhibit pudding-mold-shaped features characterized by flat bands at the top and dispersive bands at the side. These features enhance the electric conductivity and thermopower[190, 194]. The calculated ZT of Bulk α-SnSe is 2.6 at 923 K. Such a high thermoelectric figure of merit is attributed to its ultra-low thermal conductivity of 0.25 W/m.K[194]. Various first-principles calculations predict high values of ZT for 2D SnSe(at 700K, the reported values are 2.46,2.63, and 3.27)[206, 207], indicating superior thermoelectric performance compared to its bulk phase. Subsequently, various studies have been conducted on 2D MX monolayers, demonstrating their potential as a promising TE material[207, 208, 209]. Recently, thermoelectric parameters of several Janus monochalcogenides have been calculated by first-principles computational methods. These studies report high thermoelectric figure-of-merits for $\gamma-$SnSSe (3.0 at 700K) [210], $\alpha-Sn_2SSe$ (1.93 at 700K) [211] and for $\alpha-Ge_2SeTe$ (2.12 at 300K) [212]. These investigations, though, demonstrate enough promises for Janus compounds in the IV-VI monochalcogenide family with regard to thermoelectric applications, but have two limitations. These studies focused only on M_2XY Janus, where the asymmetry is with respect to the group VI constituents, making the investigations on this family of compounds incomplete. The more serious limitation is in the approximations used in the evaluation of the transport parameters. In these works, the transport parameters are calculated by considering the interactions between electrons and acoustic phonons only. As a result, the calculated ZT values may turn out to be overestimated.

To address these limitations, in this chapter, we have calculated the electronic, vibrational, and thermoelectric properties of monolayers of two types of Janus monochalcogenides M_2XY and $MM'X_2$ (M, M$'$ = Ge, Sn; X, Y = S, Se, Te) with better approximations where the interactions of electrons with both acoustic and optical phonons have been taken into account. Subsequently, we have provided a systematic and in-depth analysis of the transport properties of both classes of Janus monochalcogenides.

5.2 Computational Details

For this study, a plane-wave kinetic energy cutoff of 450 eV was used. Structural optimizations employed a $14 \times 12 \times 1$ **k**-mesh for relaxation and a denser $30 \times 28 \times 1$ grid for self-consistent electronic calculations. Thermal stability was assessed via AIMD simulations in the NVT ensemble at 800 K using a $3 \times 3 \times 1$ supercell, over a time of 12 ps. Harmonic IFCs were calculated using a $4 \times 4 \times 1$ supercell and a $6 \times 4 \times 1$ **k**-mesh. Anharmonic IFCs included interactions up to 5 Å using the same supercell and k-mesh. The lattice thermal conductivity was evaluated with a $70 \times 70 \times 1$ **q**-grid, enforcing the rotational sum rule on harmonic IFCs. The electronic transport coefficients were computed using EPA-derived relaxation times. The relaxation times were obtained from self-consistent runs on a $14 \times 12 \times 1$ **k**-mesh and phonon eigenvalues on an $8 \times 8 \times 1$ **q**-grid interpolated to a $36 \times 34 \times 1$ larger mesh with energy spacing of 0.6 eV.

5.3 Result and Discussion

5.3.1 Structural information and Electronic structure

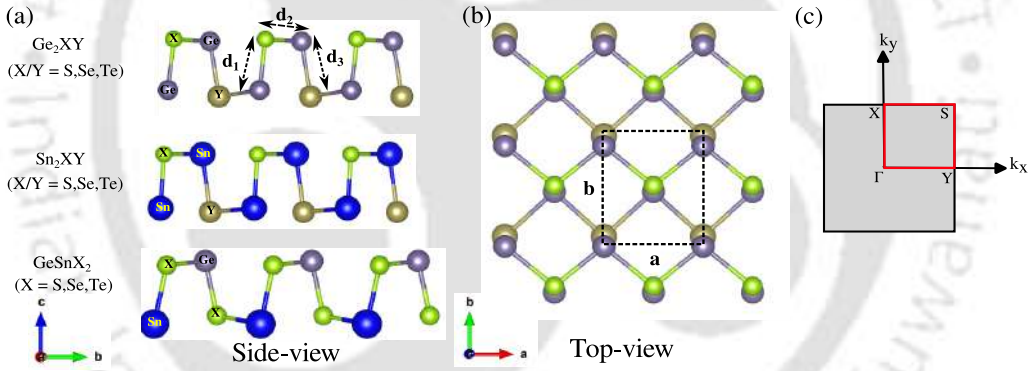

Figure 5.1: (a) side view and (b) top view of Ge_2XY, Sn_2XY, and $GeSnX_2$ Janus Monochalcogenides. d_1 d_2, and d_3 are the bond lengths. d_1 and d_3 are the out of plane ones while d_2 is the in-plane bond distance. The black dotted line in (b) is the unit cell. The corresponding Brillouin zone, highlighting the high-symmetry points and transport directions along-x (Γ-Y) and along-y (Γ-X), is shown in (c).

Fig. 5.1 illustrates the crystal structures and atomic arrangements of the Janus monochalcogenides considered here. Both M_2XY and $MM'X_2$ Janus crystallize in a puckered, 2D phosphorene-like structure, similar to their parent MX compounds. We obtain the Janus structures considered here by atomic substitutions at either M or at X sites of optimized MX monochalcogenides. Subsequently, the symmetry of the Janus compounds is lowered in comparison to their parents; from $Pmn2_1$ (in parent monochalcogenides) to Pm (in Janus monochalcogenides). In Table 5.1, we present the ground-state structure-related information of all Janus compounds considered. The calculated lattice constants are in good agreement with existing results[213]. We find that there is considerable dispersion in the bond lengths of all compounds considered; the dispersion is maximum in M_2STe Janus. This indicates substantial anharmonicity in the lattices. Another noteworthy feature in the calculated results is the anisotropy factor estimated by (b/a). We find that it is maximum in Ge_2SSe and $GeSnS_2$. Across both series considered here, it decreases with an increase in the atomic radii of the constituent elements. Both have consequences on transport properties that will be discussed later.

Janus	Lattice Constants (Å)			Bond Length (Å)			Band Gap (eV)
	a	b	b/a	d_1	d_2	d_3	E_g
Ge_2SSe	3.79	4.43	1.16	2.40	2.50	2.56	1.38
Ge_2STe	3.99	4.46	1.11	2.38	2.54	2.76	0.99
Ge_2SeTe	4.14	4.36	1.05	2.52	2.69	2.75	0.87
Sn_2SSe	4.15	4.43	1.07	2.59	2.74	2.72	1.26
Sn_2STe	4.39	4.60	1.05	2.58	2.77	2.94	0.92
Sn_2SeTe	4.46	4.55	1.02	2.72	2.91	2.93	0.80
$GeSnS_2$	3.84	4.45	1.16	2.59	2.51	2.41	1.51
$GeSnSe_2$	4.17	4.37	1.05	2.72	2.71	2.54	1.20
$GeSnTe_2$	4.43	4.55	1.03	2.91	2.92	2.76	0.92

Table 5.1: The lattice constants (Å), anisotropy parameters (b/a), bond lengths (Å), and electronic band-gaps (eV) in the ground states of M_2XY and $MM'X_2$ Janus compounds considered in this work.

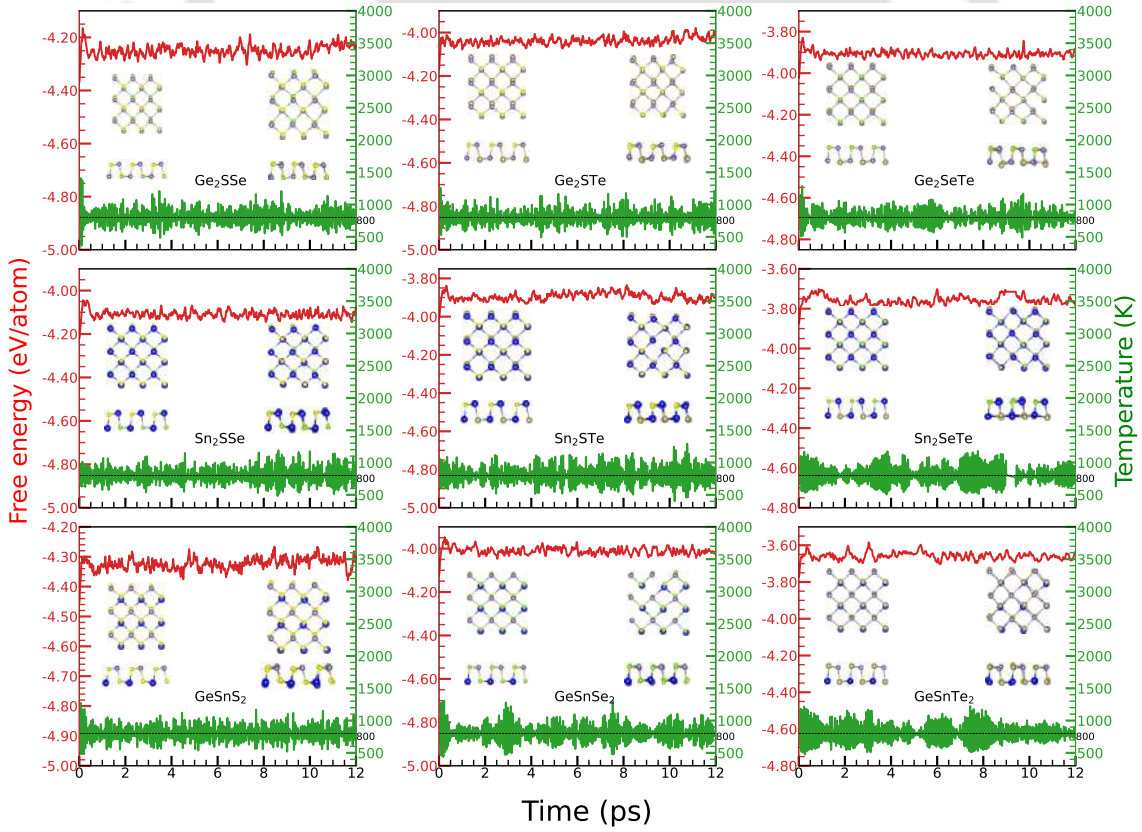

Figure 5.2: Free energy and temperature variations of the Janus monochalcogenides for a simulation time of 12 ps at 800 K.

Since these Janus compounds are yet to be realized experimentally, we check their thermal stability by performing ab initio molecular dynamics (AIMD) simulations. Fig. 5.2 presents the variations in tempera-

ture and free energy during the simulation, which is carried out for 12 ps at 800 K. The insets of Fig. 5.2 display the structures at 0 K and 800 K. It can be seen that no bonds are broken, and the crystal symmetry is intact, ensuring these Janus compounds are thermally stable at high temperature (= 800 K). Therefore, the compounds with the calculated optimized structures can be used further.

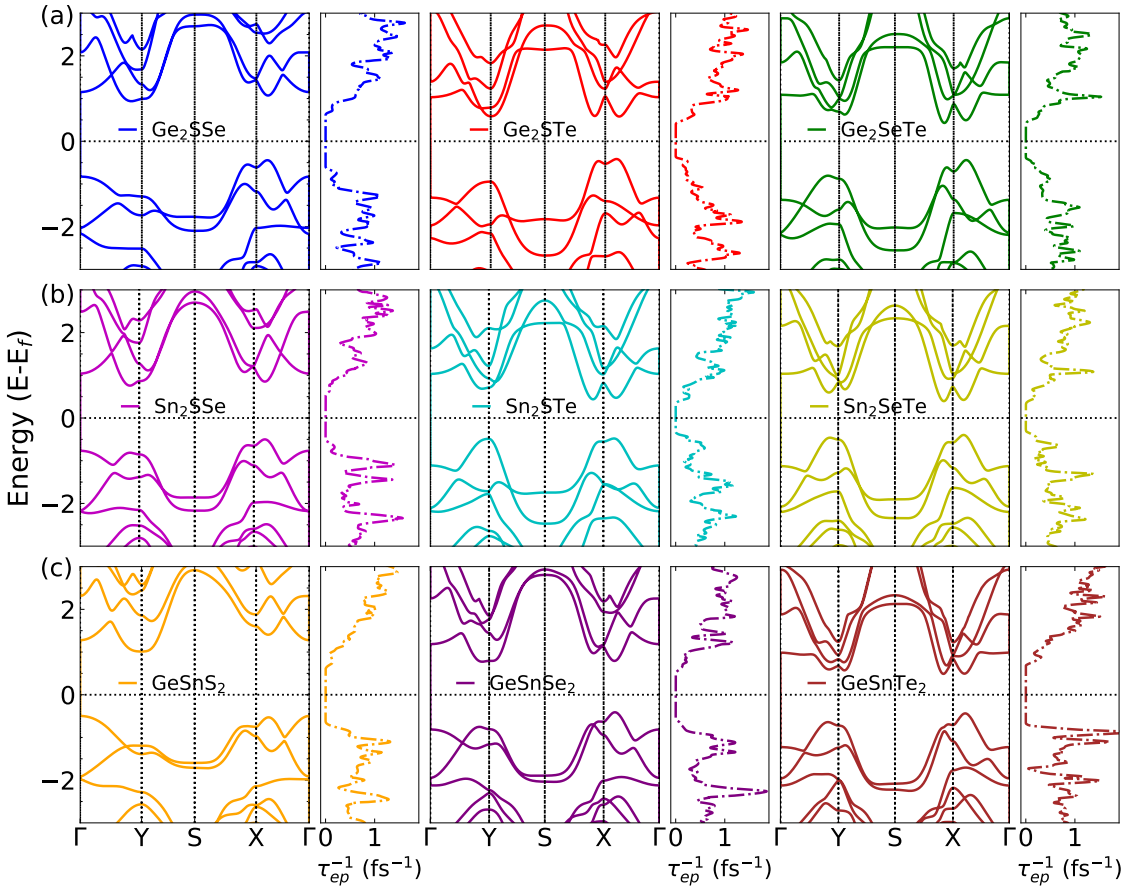

Figure 5.3: Electronic band structures and electron-phonon scattering rates (τ_{ep}^{-1} (fs^{-1})) at 300 K for (a) Ge_2XY, (b) Sn_2XY, and (c) $GeSnX_2$ Janus monochalcogenide.

In Fig. 5.3, we show the electronic band structures of these compounds along the high-symmetry directions. The energy-dependent electron-phonon scattering rates (τ_{ep}^{-1}) at 300 K are also presented. All Janus compounds considered are indirect band-gap semiconductors with band-gaps ranging from a minimum of 0.80 eV (Sn_2SeTe) to a maximum of 1.51 eV ($GeSnS_2$). A common feature observed is that as we move towards materials with heavier elements, the band structure becomes more symmetric about the S point in the Brillouin zone. This can be attributed to the reduction in the anisotropy factor. The larger anisotropies in the band structure may lead to anisotropic thermoelectric transport coefficients along the x- (Γ-Y) and y- (Γ-X) directions. The pudding mold-shaped band structure (flat at the edges and dispersive elsewhere) and multivalley band extrema near the Fermi level are inherited characteristics from the parent 2D compounds. It is important to note that the pudding mold shape of the band plays a crucial role in enhancing the power factor. The mixture of flat bands and valleys near the conduction and valence edges implies that these Janus compounds can be good thermoelectrics. The flat bands lead to large effective masses, enhancing the Seebeck coefficients (S). The valley pockets enhance carrier concentration (N). Previous studies have shown that a multivalley pocket in a band structure increases electrical conductivity (σ) without significantly reducing the Seebeck coefficient, boosting the power factor as a consequence[214, 215]. The τ_{ep}^{-1} is found to be larger (smaller) for systems having more valleys or dispersive (flat) band edges in the conduction and valence bands. In summary, the electronic band structure of these Janus compounds, possessing multiple band extrema, multiple pockets, and a pudding mold-shaped structure, can result in a large thermoelectric power factor either due to amplified S or σ. In the following, we explore how these features of electronic band structure, along with electron-phonon scattering rates, determine the transport properties of Janus compounds.

5.3.2 Thermal transport properties

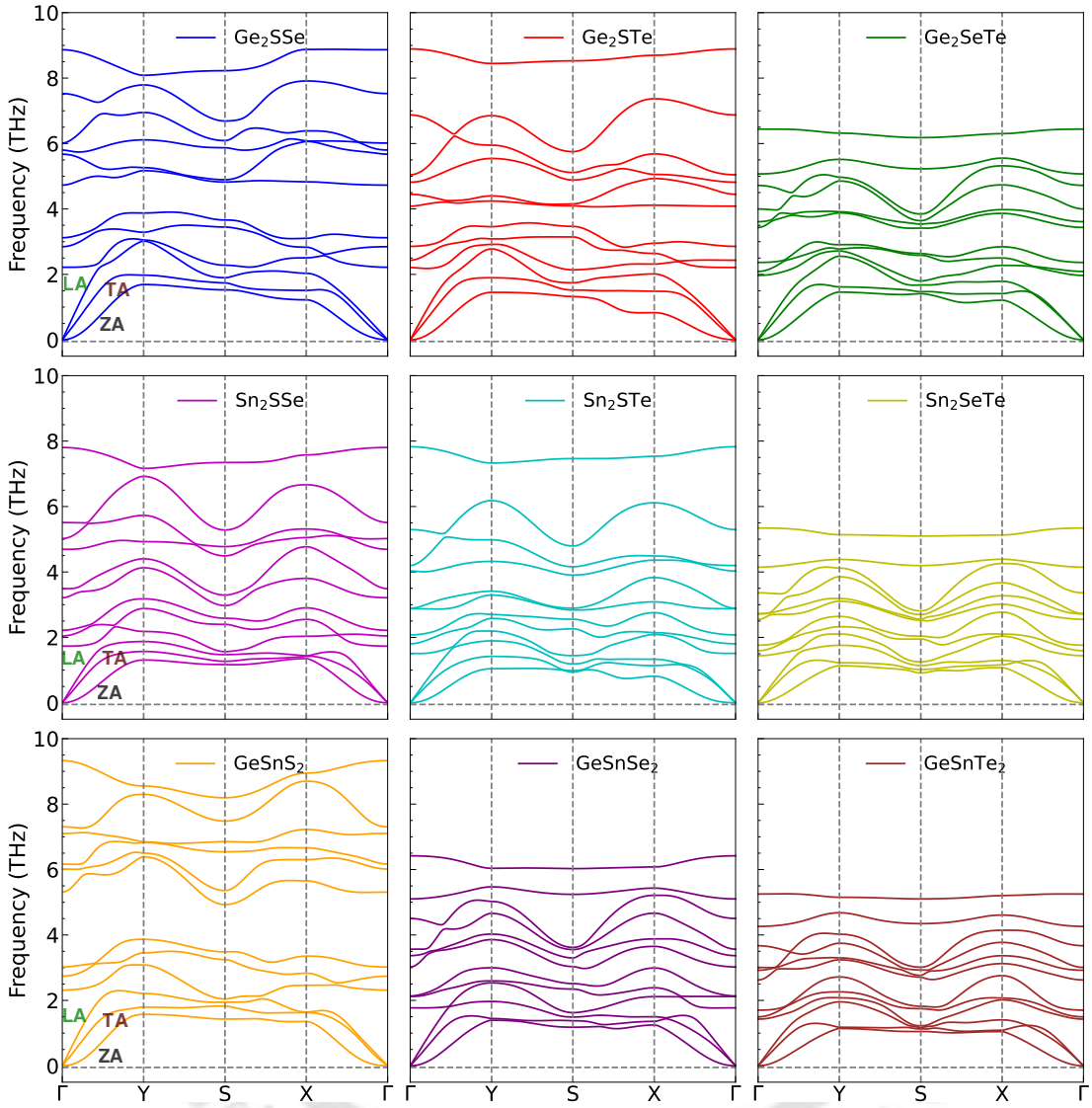

Figure 5.4: Phonon dispersion of the Janus monochalcogenides along the high-symmetry path in the Brillouin zone.

Fig. 5.4 shows the calculated phonon dispersion relations of these Janus monochalcogenides along the high-symmetry Γ-Y-S-X-Γ direction. The absence of imaginary modes in all ensures their dynamical stability. Among the twelve phonon modes (resulting from the four-atom unit cell), the first three low-frequency modes are the acoustic modes: flexural(ZA), transverse (TA), and longitudinal(LA). The remaining nine high-frequency modes are optical ones. Similar to other prototype 2D compounds[216], the LA and TA acoustic modes (in-plane vibration modes) of these compounds exhibit linear dispersion while the ZA modes (out-of-plane vibration modes) exhibit a quadratic dispersion near the Γ point. This behavior is a unique feature of 2D compounds and results from the rotational symmetry sum rules of inter-atomic force constants[217].

The lattice thermal conductivity (κ_l), shown in Fig. 5.5, decreases with increasing temperature. This behavior reflects intrinsic three-phonon scattering. Among all compounds across different series, Sn_2SeTe and Sn_2STe have lowest κ_l of 4.57 (2.86) W/m-K and 5.06 (2.42) W/m-K, respectively, at 300K along the x(y)-direction. Ge_2SSe, on the other hand, possesses the highest κ_l of 24.48 (9.08) W/m-K along the x(y)-direction at 300 K. The anisotropy in κ_l is found to be most pronounced in the Ge_2XY series. The anisotropy in κ_l is less and quantitatively close for compounds of the series Sn_2XY and $GeSnX_2$. The average relative difference in κ_l in two directions, a measure of anisotropy in κ_l, is approximately 65% , 44 % and 46 % for Ge_2XY, Sn_2XY and $GeSnX_2$ compounds, respectively. The reason for such high anisotropy is significantly

lower κ_l along the y-direction. This can be correlated to the softening of phonon branches in the Γ-X (y-direction) direction compared to Γ-Y (x-direction)(Fig. 5.4), a uniform qualitative feature observed across the three series. Table 5.2, present the mode-wise contribution to κ_l. The three acoustic modes contribute about 75-90%, whereas the optical modes contribute 10-25% to the total κ_l. Notably, the contribution from the optical phonons increases with the increase in average atomic mass across the series. This trend suggests that the shift of phonon modes towards lower frequency regions increases the involvement of optical phonons in heat transport phenomena. To further understand the trends in κ_l of these compounds, we next examine the harmonic (group velocity, specific heat) and anharmonic (phonon-phonon scattering) properties since κ_l increases with group velocity and decreases with scattering rates.

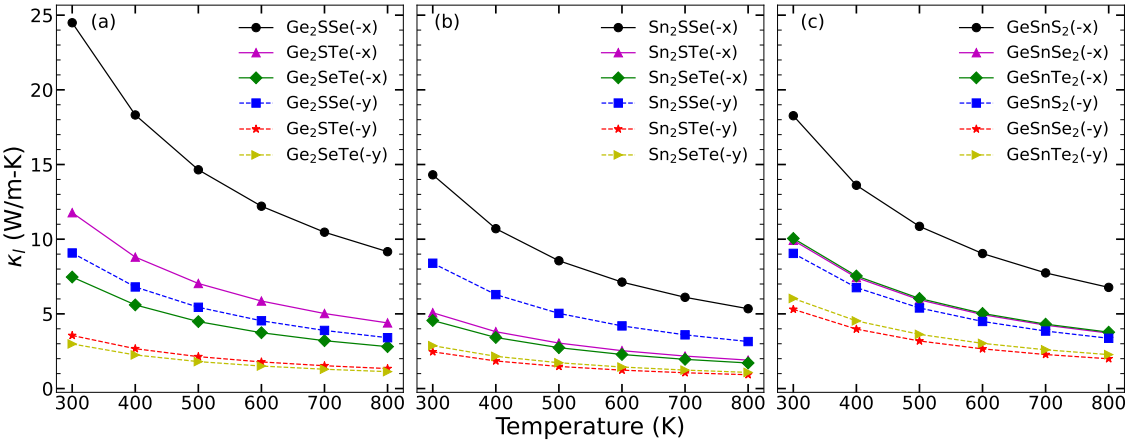

Figure 5.5: Lattice thermal conductivity (κ_l (W/m-K)) as a function of temperature for the Janus monochalcogenides.

Janus	ZA (%)		TA (%)		LA (%)		Optical (%)	
	x	y	x	y	x	y	x	y
Ge_2SSe	22.40	24.56	32.76	32.46	35.89	31.99	8.95	11.00
Ge_2STe	28.48	18.16	31.33	33.04	31.10	35.95	9.09	12.85
Ge_2SeTe	29.40	24.20	31.46	28.64	26.99	25.13	12.15	22.03
Sn_2SSe	25.28	32.89	36.05	27.58	28.53	24.43	10.13	15.09
Sn_2STe	27.28	20.09	38.60	37.67	20.74	21.97	13.38	20.26
Sn_2SeTe	24.97	22.15	35.94	31.71	19.80	19.26	19.29	26.89
$GeSnS_2$	27.81	39.45	26.52	26.21	38.72	23.59	6.94	10.75
$GeSnSe_2$	24.65	30.64	37.18	25.54	27.66	25.75	10.50	18.07
$GeSnTe_2$	18.58	21.40	36.27	29.22	28.99	24.45	16.16	24.93

Table 5.2: Percentage contribution to κ_l in x- and y-direction from acoustic (ZA, TA, and LA) and all-optical modes for each of the compounds considered.

Fig. 5.6 shows the small-grain-limit reduced thermal conductivity κ_{sg} for all Janus monochalcogenides considered. κ_{sg} for a direction α is defined as, $\kappa^{\alpha}_{sg} = \sum_{\lambda} C_{\lambda}(v^{\alpha}_{\lambda})^2$, where C_{λ} and v^{α}_{λ} are the specific heat and group velocity for phonon mode λ along $\alpha = x, y$ direction. It represents the harmonic contribution (group velocity and specific heat) to the total κ_l. Since group velocity is quadratic in the expression of κ^{α}_{sg}, we expect that it will have the most pronounced effect on κ^{α}_{sg}. That it is indeed so can be seen by comparing Fig. 5.6 with the variations of group velocity v^{α}_{λ} with frequency (Fig. 5.7). We find that in case of Sn_2XY series, the variations in κ_l follow that in κ_{sg}. This is not so for the other two series. We find that along both x- and y- directions $\kappa_l^{GeSnS_2} > \kappa_l^{GeSnTe_2} > \kappa_l^{GeSnSe_2}$ but $\kappa_{sg}^{GeSnS_2} > \kappa_{sg}^{GeSnSe_2} > \kappa_{sg}^{GeSnTe_2}$. For the Ge_2XY series, the discrepancy is in the case of the trends in the y-component of Ge_2STe and Ge_2SeTe. While $\kappa_{sg}^{y,Ge_2STe} < \kappa_{sg}^{y,Ge_2SeTe}, \kappa_l^{y,Ge_2STe} > \kappa_l^{y,Ge_2SeTe}$. These discrepancies indicate that the differences in κ_l cannot be fully explained by harmonic effects alone for these cases. To resolve this, we look into the anharmonic phonon-phonon scattering-related properties. The anharmonic properties are discussed for the dominant heat carrier phonons, focusing on the relevant frequency range (up to 3 THz).

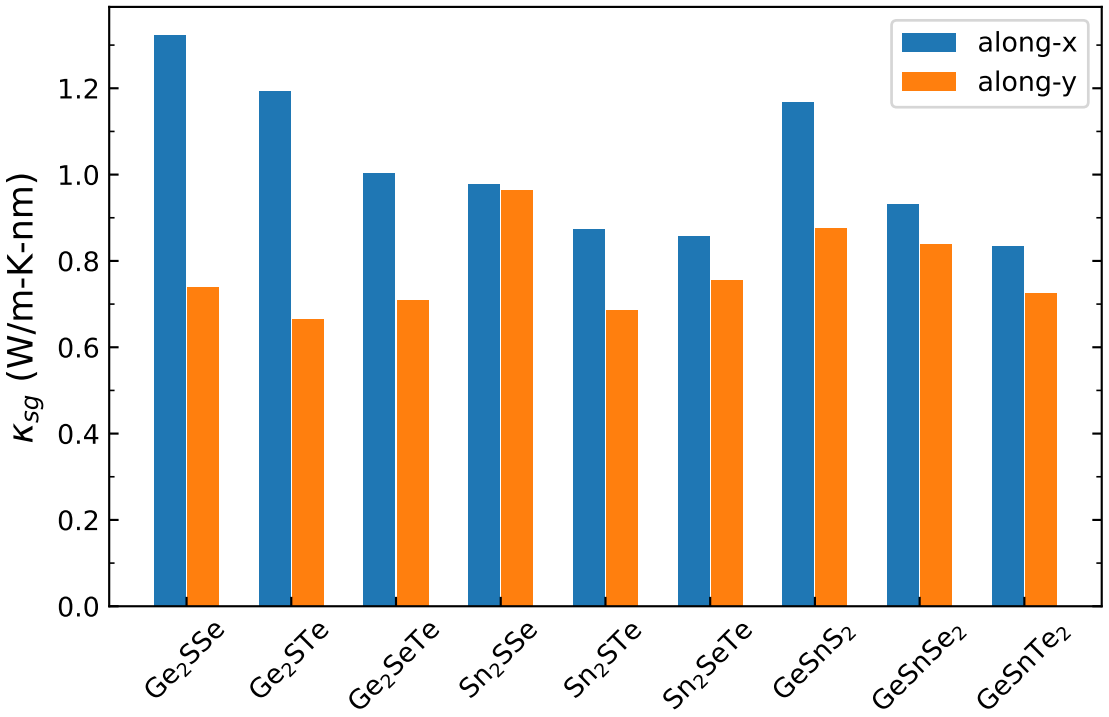

Figure 5.6: The small-grain-limit reduced thermal conductivity for the Janus monochalcogenides at 300 K

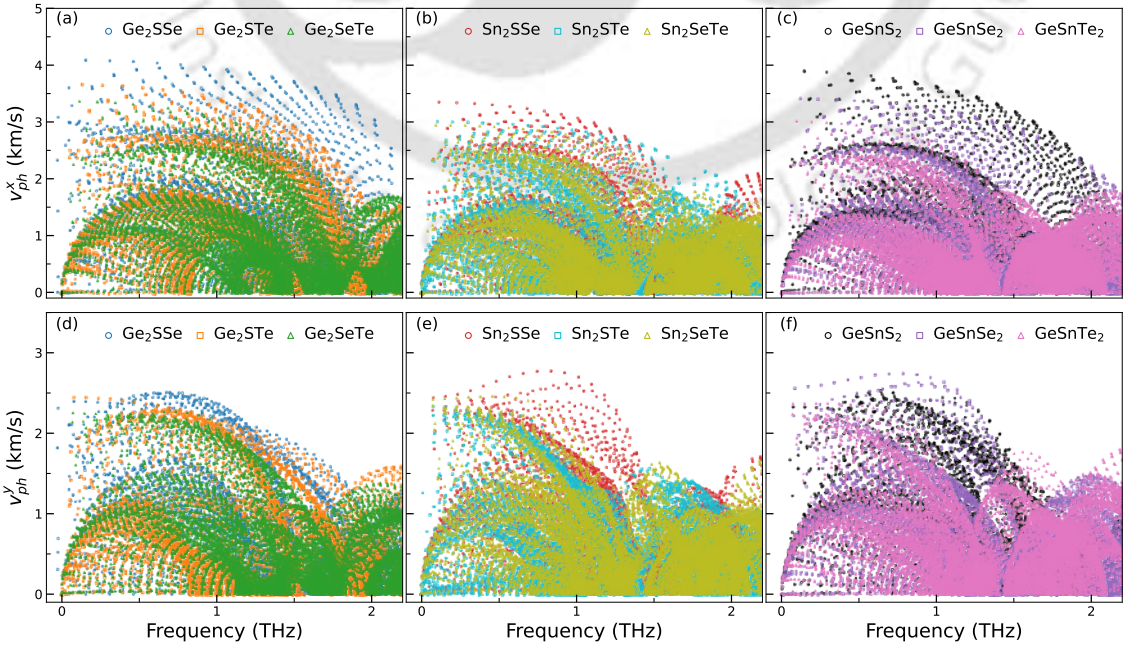

Figure 5.7: Phonon group velocity of Janus monochalcogenides considered, along x-direction (top panel) and y-direction (bottom panel).

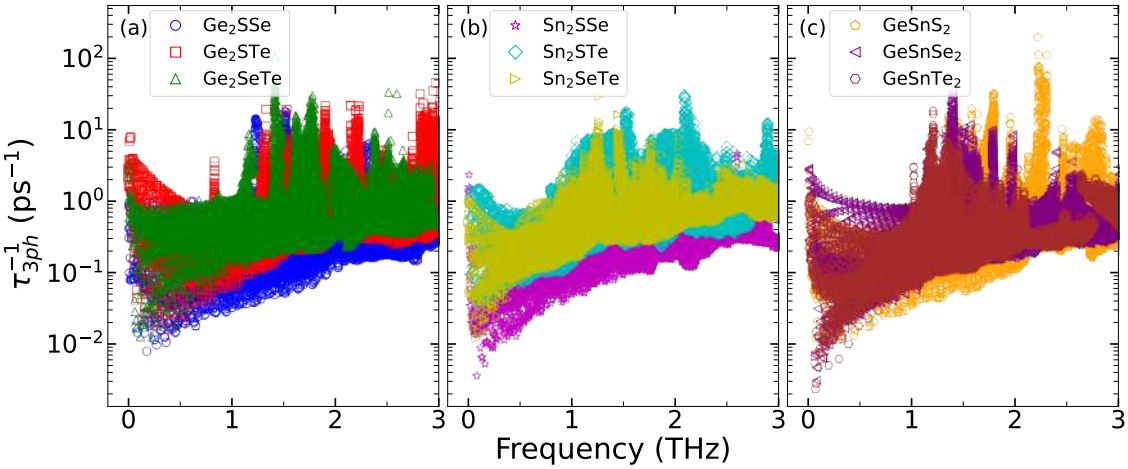

Figure 5.8: Three-phonon scattering (τ_{3ph}^{-1} (ps^{-1})) rates as a function of frequency for the Janus monochalcogenides.

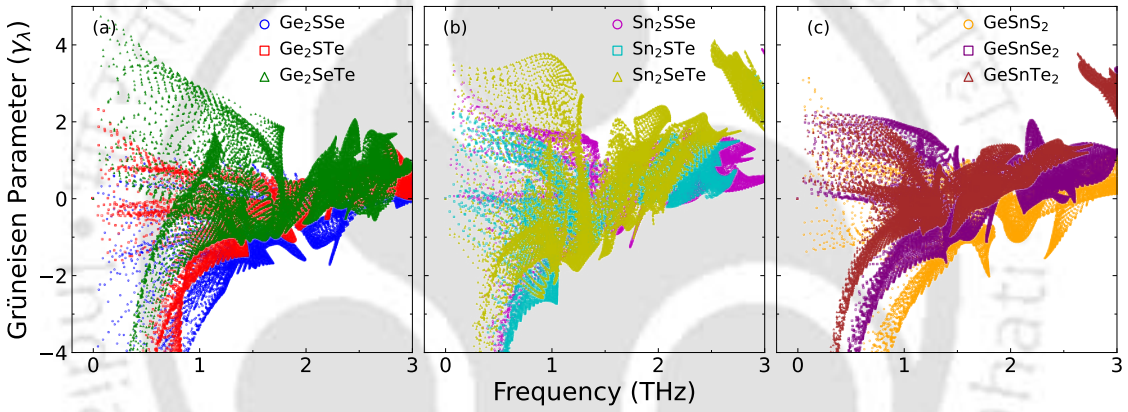

Figure 5.9: Mode-resolved Grüneisen parameter (γ_λ) as a function of frequency for the Janus monochalcogenides at 300 K.

Fig. 5.8 illustrates calculated room temperature three-phonon scattering rates of the compounds as a function of frequency. In the long-wavelength limit, the scattering rates exhibit a divergent behavior for all materials. This can be attributed to the low symmetry of the Janus compound, which lifts the restrictions on acoustic scattering processes imposed by the mirror-symmetry present in conventional 2D materials such as graphene and MoS_2[218, 219]. Due to unique quadratic behavior, the flexural phonon contributes to a higher phonon population, resulting in a larger divergent phonon scattering at long wavelengths. We also find that the scattering rates for all compounds are significant for high-frequency modes. This suggests that in the three-phonon scattering processes, along with acoustic-acoustic (a-a) phonon scattering, the acoustic-optical (a-o) phonon scattering plays a crucial role. Among Ge_2XY Janus, Ge_2SeTe exhibits the highest scattering rate for the frequencies in the middle of the range considered. When comparing the scattering rates of Ge_2STe and Ge_2SeTe in the longer and shorter wavelength limits, Ge_2STe has a higher scattering rate. Therefore, on average, the scattering rates of Ge_2SeTe and Ge_2STe are comparable. Consequently, the κ_{sg} should emerge as the deciding factor to explain the variation of κ_l among these two compounds in this series. Though this is in agreement with the trend in the x-component of the lattice thermal conductivity, the case of the y-component requires further investigation. Ge_2SSe clearly has the lowest scattering rate among the three compounds in this series. Thus, the highest κ_l of Ge_2SSe can be understood from both harmonic and anharmonic contributions. Among Sn_2XY Janus compounds, Sn_2SSe exhibits the weaker scattering rates within its group, which explains its highest κ_l. In contrast, for Sn_2STe and Sn_2SeTe, the scattering rates are comparable in strength, leading to minimal differences in their κ_l values. Thus, the qualitative trends in κ_l for these two compounds can be better understood in terms of the trends in κ_{sg}. For the $GeSnX_2$ compounds, κ_{sg} fails to explain the qualitative trend in κ_l as mentioned earlier.Thus, the anharmonic contributions must play a decisive role. Inspecting the scattering rates of the three compounds in this series, we indeed find that

the compounds can be arranged in the following ascending order of scattering rates: $GeSnS_2 \rightarrow GeSnTe_2 \rightarrow GeSnSe_2$.The reason for the larger scattering rates of $GeSnSe_2$ can be attributed to the stronger acoustic-acoustic coupling caused by the bunching effect. Thus, the trend in three-phonon scattering rates for the compounds in this series fully explains the trend in their κ_l.

In order to resolve the discrepancies with regard to Ge_2STe and Ge_2SeTe, we finally take recourse to the mode-resolved Grüneisen parameter (γ_λ), which quantifies how phonon frequencies vary with changes in volume and serves as a measure of anharmonicity in the system. Fig. 5.9 presents the computed mode Grüneisen parameters (γ_λ) for all compounds at 300K. We find that throughout the frequency range γ_λ for Ge_2SeTe is significantly higher than Ge_2STe. This implies substantially stronger anharmonicity in the former, the effect of which is a κ_l lower than in the latter. Thus, the trends in the Grüneisen parameter completely explain the trend in the κ_l of compounds in the Ge_2XY series in both directions. Overall, the trends in κ_l across the series can be explained by contributions of both harmonic and anharmonic effects in their lattice dynamics.

5.3.3 Power factor (PF) and Figure of merit (ZT)

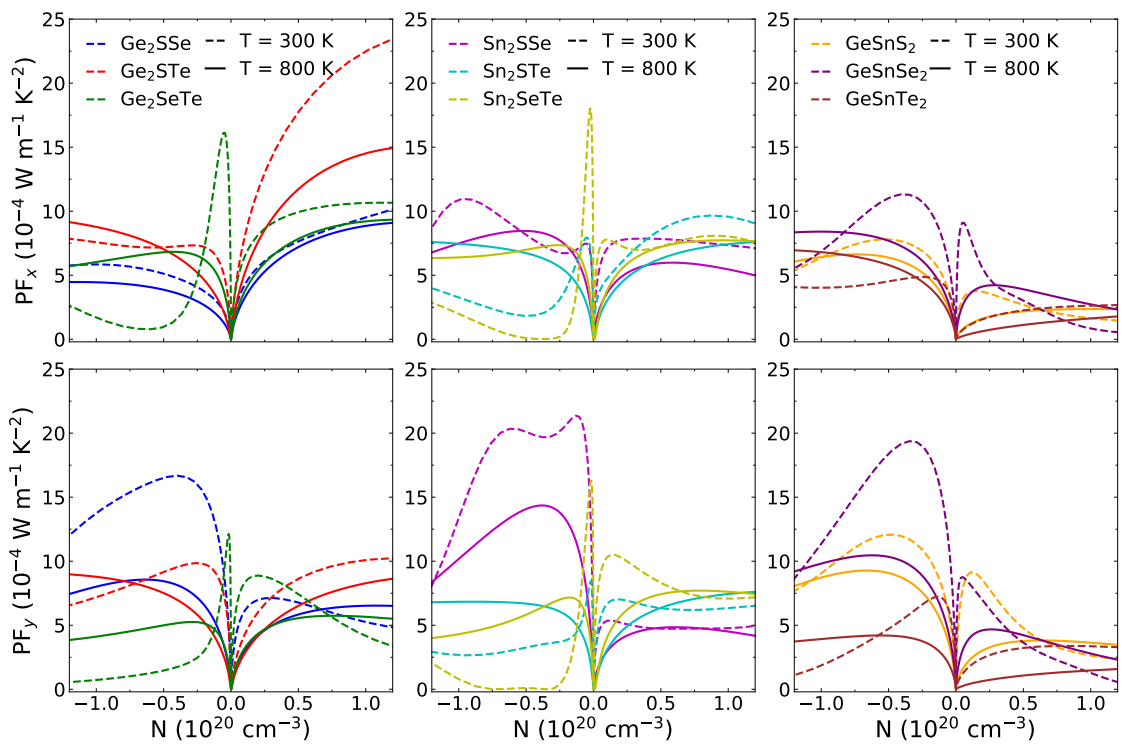

Figure 5.10: Power factor ($S^2\sigma$ (W/m.K^2)) of Janus monochalcogenides along x-direction (top-panel) and y-direction (bottom panel) as a function of carrier concentration for both n-type (N<0) and p-type (N>0) carriers.

The electronic band structures presented in Fig. 5.3 reveal features favorable for good thermoelectric performance. The presence of multiple extrema in the narrow energy window, each with different curvatures, leads to a strong dependence of electron carrier lifetime (τ_{ep}) on the carrier energy (E) in the vicinity of the Fermi-level. This dependence of τ_{ep} on E affects the transport coefficients significantly[220]. Therefore, we evaluate the transport coefficients by incorporating energy-dependent electron-phonon scattering, invoking the rigid band approximation(RBA).

In Fig. 5.10, we present the power factor (PF = $S^2\sigma$) as a function of carrier concentration (N) at 300 K and 800 K, along x- and y-directions, for all three series of Janus monochalcogenides. For all compounds, the PF decreases with increasing temperature. We find a significant anisotropy in the power factor across the series. Along x-direction, the maximum PF in Ge_2XY series is obtained for Ge_2SeTe (15×10^{-4} W m^{-1}K^{-2}) for n-type carrier, and for Ge_2STe (23×10^{-4} W m^{-1}K^{-2}) for p-type carrier. In Sn_2XY series, maximum PF along x-direction is obtained in case of Sn_2SeTe (18×10^{-4} W m^{-1}K^{-2}) for n-type carrier and in case of Sn_2STe (9×10^{-4} W m^{-1}K^{-2}) for p-type carrier. In $GeSnX_2$ series, $GeSnSe_2$ has maximum PF for both types

of carrier; 10.50×10^{-4} W m^{-1}K^{-2} for n-type and 8.65×10^{-4} W m^{-1}K^{-2} for p-type. Along the y-direction, the maximum PF values are as follows: in Ge_2XY series, Ge_2SSe has a maximum PF of 16×10^{-4} W m^{-1}K^{-2} for n-type carrier and Ge_2STe has a maximum PF of 10.05×10^{-4} W m^{-1}K^{-2} for p-type carrier. In Sn_2XY series, it is obtained for Sn_2SSe (20.25×10^{-4} W m^{-1}K^{-2}) and Sn_2SeTe (9.91×10^{-4} W m^{-1}K^{-2}) for n-type and p-type carriers, respectively. In $GeSnX_2$ series, maximum PF of 19×10^{-4} W m^{-1}K^{-2} for n-type carriers is obtained for $GeSnSe_2$ while it is 8×10^{-4} W m^{-1}K^{-2} for p-type carriers in $GeSnS_2$. These values are comparable to those of other well-studied thermoelectric compounds[221, 222, 223]. This anisotropy in the power factor originates from the anisotropic dispersion in electronic bands. Higher valley degeneracy near the band edges enhances the PF by either increasing the electrical conductivity (σ) without decreasing the Seebeck coefficient (S) and vice versa. The presence of flat-band edges increases the effective mass, leading to higher S, whereas the band convergence due to multivalley band edges may boost the S and σ. For the compounds under investigation, the variations in their S and σ with carrier concentration are shown in Figs. 5.11 and 5.12. These results imply two distinct trends. First, in the two series of M_2XY Janus, Ge_2STe (Ge_2SeTe) and Sn_2STe (Sn_2SeTe) have higher S (σ) among the members of their respective series. This can be traced back to their band structures. As we move along Ge_2SSe (Sn_2SSe)→ Ge_2STe (Sn_2STe) → Ge_2SeTe (Sn_2SeTe), the flatness of band edges reduces. This implies that S should reduce. On the other hand, band convergence with more valleys is found too. This means that S should increase. However, band convergence does not always promote the S. This is due to increased intra-band scattering of carriers. On top of this, with the increase in valleys, the carrier concentration increases too. This results in lower S as $S \propto 1/N$. Thus, a balance between band convergence, moderate band flatness, and reduced τ_{ep}^{-1}, can explain the trends of S and σ in M_2XY series. Second, in the remaining series, $GeSnTe_2$ ($GeSnSe_2$) with the most number of band valleys has the largest S (σ) compared to the rest. This is because here, the band-convergence is favorable for the enhancement of S. The reason could be a lower carrier scattering rate (τ_{ep}^{-1}).

For all compounds, we find that the inverse relationship between S and σ holds. The electronic thermal conductivity (κ_e) follows a similar trend, consistent with the Wiedemann-Franz law ($\sigma \propto \kappa_e$). The optimal PF is obtained at lower carrier concentrations, where κ_l dominates over κ_e. This suggests that κ_l will have a dominating effect on the maximum value of ZT.

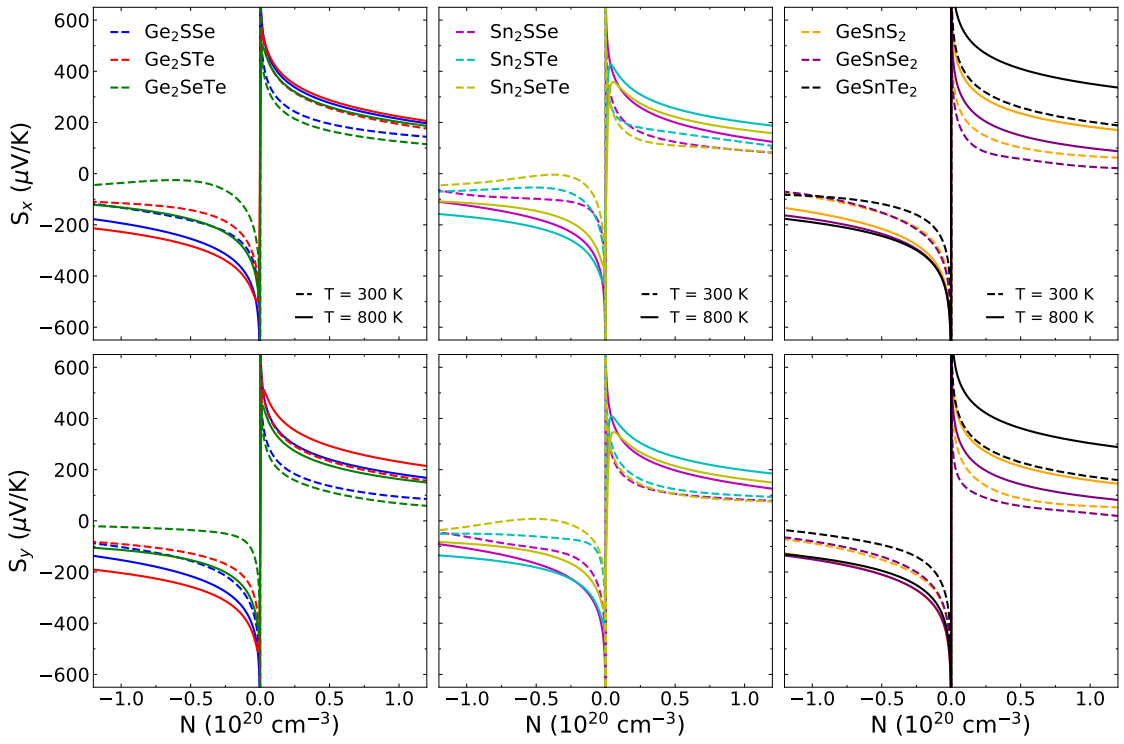

Figure 5.11: Seebeck coefficient (S $\mu V/K$) of Janus monochalcogenides along x-direction (top-panel) and y-direction (bottom panel) as a function of carrier concentration for both n-type (N<0) and p-type (N>0) carriers. Results are shown for 300 K (dashed line) and 800 K (solid line)

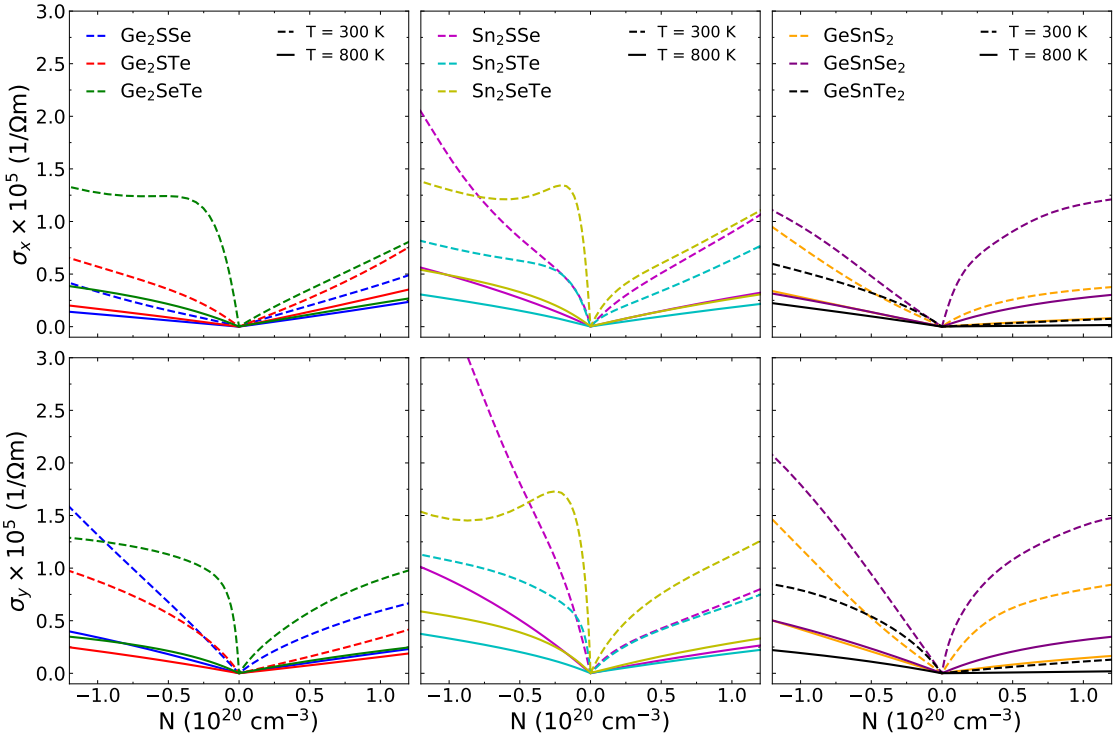

Figure 5.12: Electrical conductivity (σ $1/\Omega m$) of Janus monochalcogenides along x-direction (top-panel) and y-direction (bottom panel) as a function of carrier concentration for both n-type (N<0) and p-type (N>0) carriers. Results are shown for 300 K (dashed line) and 800 K (solid line).

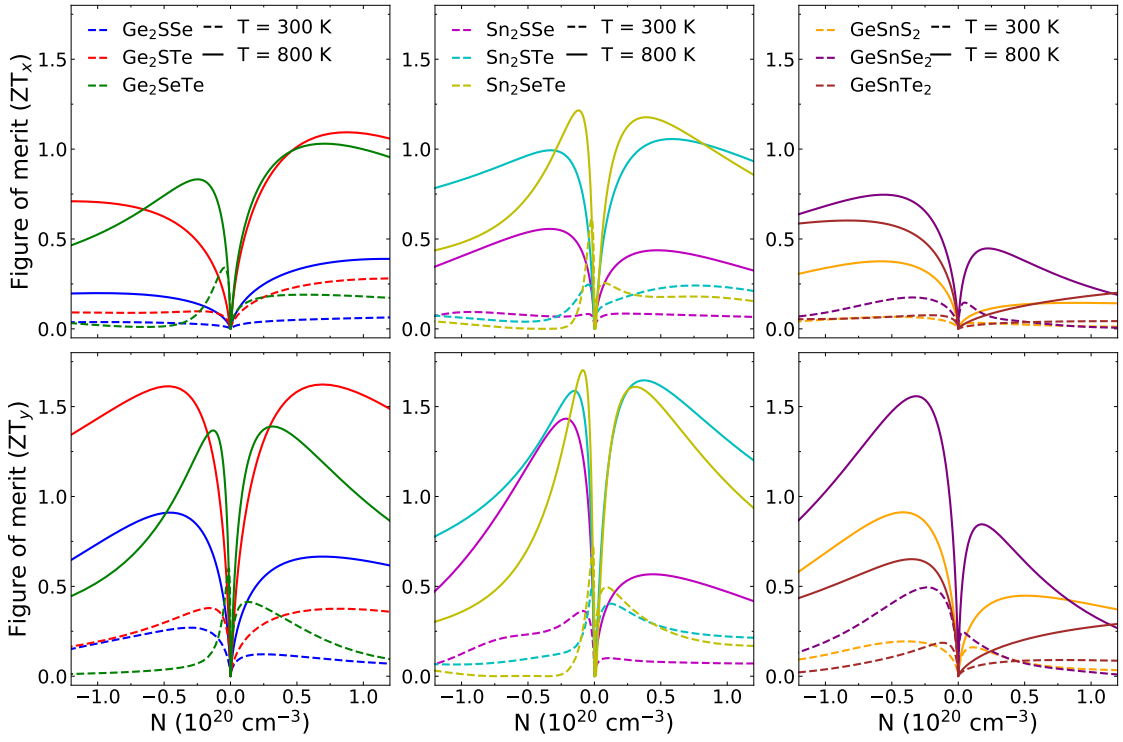

Figure 5.13: Figure of merit (ZT) for Janus monochalcogenides along x-direction (top-panel) and y-direction (bottom panel) as a function of carrier concentration (N) for both n-type (N<0) and p-type (N>0) carriers.

Fig. 5.13 shows the variation of ZT of all compounds as a function of carrier concentration at 300 K (dashed line) and 800 K (solid line) along the x- and y-directions. The ZT initially increases with N, reaches the maximum, and then decreases, exhibiting the typical "open book" shape feature. This trend suggests that the optimal thermoelectric performance is achieved with light n- and p-type doping within a narrow energy window near the Fermi level. It is clearly observed that for all Janus, (a) the ZT along the y-direction is more than the x-direction, and (b)ZT increases with temperature. The maximum ZT values at 800 K along the y-direction are 1.61 (1.62) for Ge_2STe, 1.70 (1.60) for Sn_2SeTe, and 1.55 (0.84) for $GeSnSe_2$, for the n-type (p-type) carrier, respectively. The primary reason for these high ZT values is the combination of a high PF and low κ_l.

Finally, for comparison, we have calculated the electronic transport parameters and ZT considering only the interaction of electrons and acoustic phonons. The carrier relaxation time τ is obtained from the deformation potential theory (DPT) [224] (discussed in Chapter 2). The results are shown in Table 5.3. As expected, we find the ZT, thus obtained, is substantially overestimated. We infer that, given the complexities in the electronic band structures of Janus monochalcogenides considered in this work, it becomes a necessity to consider the full electron-phonon interaction for the evaluation of the transport coefficients. Thus, the ZT obtained in this work is more realistic compared to the ones obtained in previous works [210, 212, 211].

System	Carrier	m_x^*/m_0	m_y^*/m_0	E_d^x (eV)	E_d^y (eV)	C_x (N/m)	C_y (N/m)	τ_x (fs)	τ_y (fs)	ZT_x	ZT_y
Ge_2SSe	e	0.604	0.526	2.60	0.30	45.06	15.59	35.64	926.65	1.84 (0.19)	4.77 (0.91)
	h	0.339	0.184	7.32	6.79			10.15	4.08	0.71 (0.39)	0.59 (0.67)
Ge_2STe	e	0.225	0.119	3.13	0.85	40.07	16.58	75.34	422.62	4.47 (0.71)	5.16 (1.61)
	h	0.298	0.232	8.74	4.78			6.01	8.31	1.09 (1.09)	2.09 (1.62)
Ge_2SeTe	e	0.105	0.051	6.64	1.47	46.56	22.72	43.49	433.03	4.57 (0.83)	5.88 (1.37)
	h	0.239	0.129	9.73	3.87			8.44	26.03	1.73 (1.03)	3.64 (1.39)
Sn_2SSe	e	0.163	0.290	0.27	1.52	36.11	13.81	6867.64	82.87	5.98 (0.55)	5.82 (1.43)
	h	0.180	0.310	8.25	4.97			6.77	7.13	0.62 (0.43)	0.74 (0.57)
Sn_2STe	e	0.164	0.063	5.73	1.24	32.46	19.02	29.32	366.70	3.99 (0.99)	5.49 (1.58)
	h	0.266	0.298	5.49	6.66			11.15	4.58	3.35 (1.06)	2.56 (1.64)
Sn_2SeTe	e	0.087	0.078	5.73	1.51	35.09	18.79	39.11	301.15	4.58 (1.21)	5.96 (1.70)
	h	0.241	0.127	8.49	4.64			8.38	15.03	1.65 (1.18)	3.29 (1.61)
$GeSnS_2$	e	3.490	2.600	4.28	1.61	34.56	10.42	1.88	4.02	0.12 (0.37)	0.57 (0.91)
	h	2.092	0.601	2.21	2.80			19.02	3.57	1.37 (0.14)	0.79 (0.45)
$GeSnSe_2$	e	0.238	0.088	2.59	0.16	35.00	11.92	108.66	969.69	4.12 (0.74)	4.65 (1.56)
	h	0.215	0.180	8.46	4.64			7.49	8.48	0.94 (0.45)	1.36 (0.85)
$GeSnTe_2$	e	0.048	0.105	4.98	0.52	33.97	16.46	58.15	2584.26	1.36 (0.60)	5.02 (0.65)
	h	0.133	0.206	9.27	3.23			7.19	28.72	0.40 (0.33)	1.43 (0.35)

Table 5.3: Effective mass (m^*), DP constant (E_d), In-plane stiffness (C), Relaxation times (τ) and figure of merit (ZT) of Janus monochalcogenides. Results presented are for electrons and holes along x- and y-direction. The values in parentheses are the ZT evaluated using EPA.

5.4 Conclusions

In this chapter, we have investigated the thermoelectric properties of three families of 2D Janus monochalcogenides: Ge_2XY, Sn_2XY and $GeSnX_2$ (X, Y = S, Se, Te), using first principles density functional theory in conjunction with Boltzmann transport theory. The electron-phonon approximation (EPA) is employed to evaluate the electron carrier lifetime, providing a more accurate quantitative assessment of transport parameters. Our analysis of the electronic band structures reveals the presence of pudding mold-shaped features near the band edges, which contribute to highly anisotropic transport parameters for both n-type and p-type doping. We find that the balance between flat band and valley degeneracy plays a crucial role in optimizing the power factor, particularly for Ge_2SeTe and Sn_2SeTe. The observed κ_l trends are attributed to both harmonic and anharmonic effects of lattice dynamics. The anisotropy in κ_l is explained using the results obtained for group velocity,three-phonon scattering strength of acoustic phonons, and mode-resolved Grüneisen parameters. Among the Janus compounds investigated, the highest figure of merit (ZT) is obtained at 800 K along the y-direction for n-type doping.Sn_2SeTe exhibits the highest ZT of 1.70, followed by Ge_2STe (ZT = 1.61), and $GeSnSe_2$ (ZT = 1.55). These high ZT values indicate that IV-VI Janus monochalcogenides are promising thermoelectric materials at elevated temperatures, benefiting from their optimized electronic and thermal transport properties. Our study lays the foundation for future experimental studies and optimization of materials for thermoelectric applications.

Chapter 6

Four-phonon scattering in h-NbN monolayer *

6.1 Introduction

Modeling κ_l using only three-phonon scattering processes is inadequate for 2D materials, especially when an acoustic-optical (A-O) phonon gap exists, flexural (ZA) modes are prominent, selection rules are strict, and acoustic phonon bunching arises from simplified lattice structures [225]. These features significantly enlarge the phase space for four-phonon interactions, opening additional scattering channels and leading to a substantial reduction in κ_l for materials such as graphene [74, 226], MoS_2 [227, 228], and other 2D systems [229, 230]. In graphene, theoretical predictions of high κ_l exceeding 3000 $W\,m^{-1}\,K^{-1}$ at 300 K arise from the long mean free paths of low-frequency ZA phonons, which dominate heat transport [76, 72, 74]. This is due to strict selection rules that limit three-phonon processes, especially for ZA modes, where in-plane reflection symmetry forbids interactions such as ZA + ZA $\leftrightarrow$ ZA [72]. However, inclusion of four-phonon scattering, driven by fourth-order anharmonicity, opens additional relaxation channels and significantly increases scattering rates, reducing κ_l closer to experimental measurements of 1000–1500 $W\,m^{-1}\,K^{-1}$ [74, 226, 231, 232]. It is important to note that heat conduction in graphene is highly sensitive to structural defects, sample size, substrate interactions, and isotope composition [233, 234, 235, 232, 236, 237] and is often associated with significant experimental uncertainties [236, 237, 238].

In the quest for novel 2D materials for next-generation devices, polymorphs of NbN, the rectangular s-NbN and honeycomb h-NbN monolayers, have gained significant attention [239]. While s-NbN retains superconducting behavior akin to its bulk rocksalt counterpart [240], h-NbN exhibits semiconducting properties along with an unusually large piezoelectric response, forbidden by symmetry in the bulk. Remarkably, h-NbN also hosts a Dirac semimetallic state that coexists with ferroelectricity, which couples strongly to both strain and external electric fields [241]. Owing to broken inversion symmetry and preserved time-reversal symmetry, h-NbN has been proposed as a promising valleytronic material [242]. The interplay between valley and spin degrees of freedom, mediated by Zeeman and Rashba-type spin splittings, further enhances its potential for device applications. Despite extensive interest in its semiconducting behavior, the lattice thermal and electronic transport properties of h-NbN remain largely unexplored.

In this chapter, we present a comprehensive investigation of the lattice thermal conductivity and electronic transport properties of the recently discovered honeycomb h-NbN using first-principles density functional theory combined with phonon Boltzmann transport formalism. Our study reveals that four-phonon scattering plays a critical role in suppressing κ_l, even in the absence of mirror symmetry. Under mechanical strain, κ_l shows a slight increase, primarily attributed to the changes in anharmonicity. Notably, κ_l of h-NbN remains significantly lower than that of prototypical 2D materials such as MoS_2. We further evaluate the electronic transport coefficients and thermoelectric figure of merit (zT) using an electron-phonon interaction-based approach. Our analysis reveals that four-phonon scattering plays a critical role in shaping zT, highlighting the necessity of its inclusion in predictive transport modeling. These findings indicate that h-NbN is a promising candidate for thermoelectric and nanoelectronic applications, where multi-phonon processes govern overall performance. The insights presented here contribute to the broader goal of understanding and engineering thermal transport in 2D materials, providing a foundation for future experimental and theoretical exploration.

*The contents of this chapter are published in 2025 Nanoscale, 17, 24301-24310

6.2 Computational Details

All total energy calculations were done by PAW formalism as implemented in VASP code (discussed in Chapter 2). Plane-wave energy cutoff of 550 eV and a $16 \times 16 \times 1$ Monkhorst-Pack **k**-point grid [243] were employed. Structural relaxations were performed until the total energy and forces converged below 10^{-7} eV and 10^{-3} eV/Å, respectively.

Harmonic second-order interatomic force constants (IFCs) were computed using a $10 \times 10 \times 1$ supercell with a $2 \times 2 \times 1$ **k**-mesh. Third- and fourth-order anharmonic IFCs were obtained using $8 \times 8 \times 1$ supercells with $2 \times 2 \times 1$ and $1 \times 1 \times 1$ **k**-meshes, capturing interactions up to the tenth and fourth nearest neighbors, respectively. The lattice thermal conductivity was calculated by iteratively solving the linearized phonon Boltzmann transport equation using the FourPhonon code [117], with a $60 \times 60 \times 1$ **q**-mesh.

While calculating electronic transport properties, the energy-dependent carrier relaxation time was computed using the electron-phonon averaged (EPA) approximation [112], within the plane-wave pseudopotential framework implemented in Quantum Espresso package [113], employing ultrasoft pseudopotentials [244]. A kinetic energy cutoff of 100 Ry was used, with $16 \times 16 \times 1$ **k**- and **q**-meshes. Electronic eigenvalues were interpolated onto a $64 \times 64 \times 1$ grid to ensure accurate transport property evaluation.

6.3 Results and Discussion

We begin with an analysis of the structural properties and phonon dispersion. We then examine the lattice thermal conductivity and its strain dependence, highlighting the essential role of four-phonon scattering in modeling heat transport. Finally, we explore the thermoelectric properties of the system.

6.3.1 Structural details

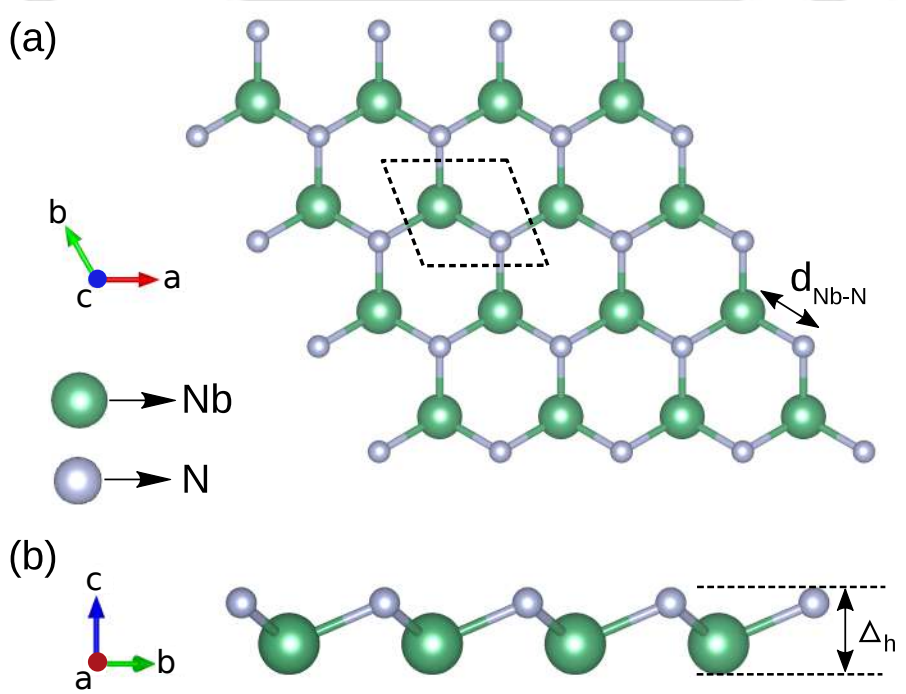

Figure 6.1: Crystal structure of h-NbN. (a) Top view shows a hexagonal lattice. (b) Side view reveals significant buckling that breaks reflection symmetry, likely influencing heat transport. The short Nb–N bond length indicates strong covalent bonding.

The h-NbN monolayer adopts a buckled hexagonal lattice (Figure 6.1) derived from the [111] planes of bulk rocksalt NbN. Unlike the planar honeycomb structures of graphene and h-BN, h-NbN features a pronounced buckling ($\Delta_h = d^z_{Nb} - d^z_N$) of 0.77 Å in the unstrained state, reflecting a vertical separation between Nb and N sublattices (Table 6.1). This buckling breaks in-plane reflection symmetry, thereby altering phonon

scattering and impacting κ_l. Similar symmetry-breaking effects have been reported in low-buckled 2D materials such as silicene, germanene, and stanene [230]. The optimized lattice constant of 3.15 Å and Nb−N bond length of 1.98 Å indicate strong covalent bonding, consistent with earlier predictions [241, 242]. Heat conduction can be tuned by in-plane strain ($\epsilon_{xx} = \epsilon_{yy} = \epsilon$) as tensile strain reduces buckling (Table 6.1). We investigate the effects of a tensile $\epsilon = 3\%$, remaining below the critical threshold at which the structure transitions to a planar configuration.

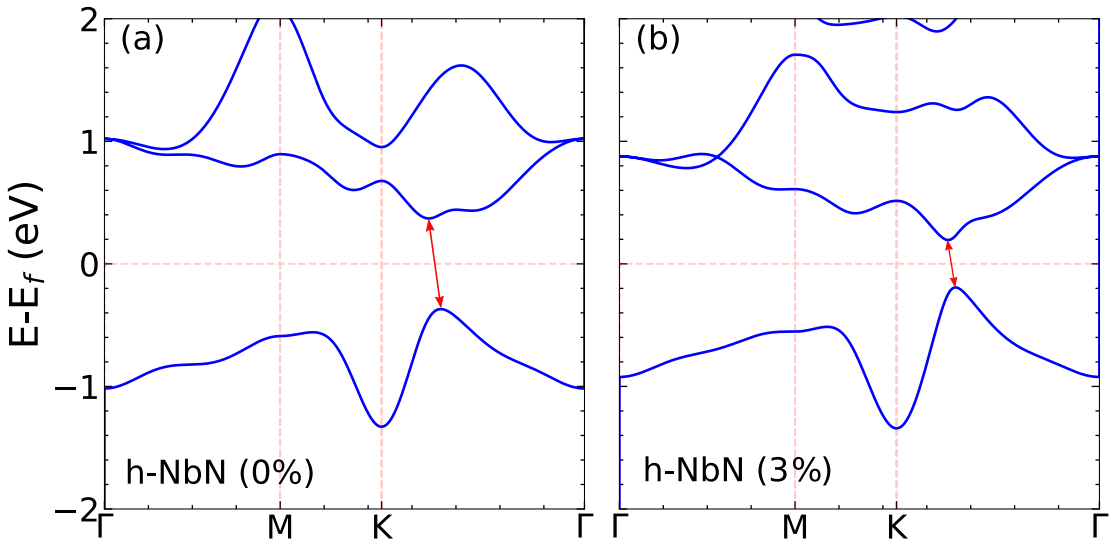

Figure 6.2: The electronic band structure reveals an indirect band gap along the $K-\Gamma$ path for both unstrained ($\epsilon = 0\%$) and strained ($\epsilon = 3\%$) h-NbN. The band gap decreases under strain. The Fermi level is set to 0 eV.

The electronic structure of the h-NbN monolayer reveals an indirect band gap of 0.75 eV along the $K-\Gamma$ path (Fig. 6.2). This moderate band gap confirms its semiconducting nature, suggesting that phonons dominate heat transport. Applying a tensile strain of $\epsilon = 3\%$ significantly narrows the band gap (Table 6.1) and reduces buckling. This is expected to influence κ_l by modifying phonon scattering mechanisms

Strain ϵ	a_0 (Å)	Δ_h (Å)	d_{Nb-N} (Å)	θ_{N-Nb-N} (°)	E_g (eV)
0%	3.16	0.77	1.98	105.65	0.75
3%	3.25	0.70	2.00	108.46	0.40

Table 6.1: Structural properties of unstrained and strained h-NbN monolayer. The lattice constant a_o, buckling height Δ_h, Nb−N bond length d_{Nb-N}, bond angle θ_{N-Nb-N}, and electronic band gap (E_g) are listed.

6.3.2 Lattice dynamics

Phonon dispersion confirms the dynamic stability of h-NbN monolayer, with no unstable modes [Figure 6.3(a)]. A wide A-O phonon gap of 9.5 THz arises from the significant mass difference between Nb and N. The phonon densities of states (PDOS) indicates that acoustic modes are associated with Nb vibrations, while optical modes stem primarily from N atoms. The flexural ZA mode exhibits the expected quadratic dispersion, $\omega \propto q^2$, near the Γ point, while the in-plane transverse (TA) and longitudinal (LA) acoustic modes follow a linear q dependence. Earlier, it was suggested that the quadratic ZA mode near Γ in 2D materials is influenced by structural buckling, contrasting planar graphene with buckled silicene [245]. However, it was later demonstrated that enforcing translational and rotational invariance in IFCs recovers the correct quadratic dispersion, independent of buckling [246]. By employing a larger supercell and enforcing the rotational sum rules, we ensure the quadratic ZA mode in h-NbN, achieving improved accuracy over prior reports [239, 242].

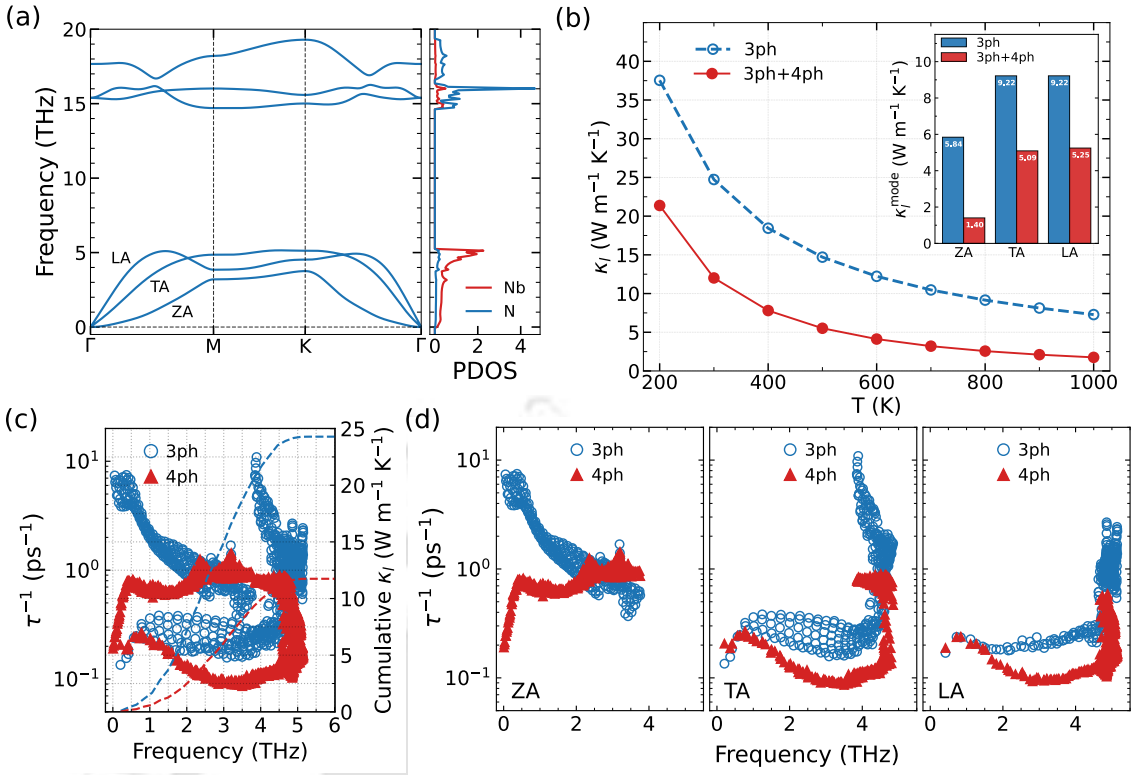

Figure 6.3: (a) The phonon dispersion of h-NbN confirms dynamic stability, featuring a quadratic ZA mode near Γ, a wide A-O gap, and nearly non-dispersive acoustic branches along $M - K$. PDOS analysis shows that acoustic modes are dominated by Nb vibrations, while N contributes mainly to optical modes. (b) The calculated lattice thermal conductivity (κ_l) shows a significant reduction when four-phonon scattering is included. The mode-resolved κ_l^{mode} at 300 K (inset) reveals that this suppression affects all acoustic branches, with the ZA mode being the most severely affected. (c) Scattering rates involving acoustic modes calculated at 300 K indicate that four-phonon processes are weaker at low frequencies, but become comparable to three-phonon scatterings in the intermediate frequency range. The cumulative κ_l corresponding to total scattering rates is also shown. (d) Mode-resolved acoustic scattering rates show that the ZA mode predominantly governs phonon scattering. Although TA and LA modes exhibit stronger scattering at higher frequencies, their contributions to κ_l remain limited.

The quadratic ZA mode and wide A-O phonon gap in h-NbN point to strong four-phonon scattering, consistent with observations in other 2D and bulk systems [74, 247, 248, 249]. This occurs because the large A-O gap suppresses many three-phonon scattering processes that cannot satisfy energy and momentum conservation. In contrast, four-phonon scattering processes are less restricted, as the involvement of an additional phonon offers greater flexibility in satisfying energy and momentum conservation laws. Moreover, the phonon dispersion of h-NbN reveals nearly non-dispersive acoustic branches along the $M - K$ path, reflected in a pronounced PDOS peak near the top of the acoustic band [Figure 6.3(a)]. Such flat dispersion further amplifies four-phonon scattering [250], reinforcing the need to account for higher-order anharmonicity in accurately evaluating the intrinsic lattice thermal conductivity.

6.3.3 Impact of four-phonon scattering on κ_l

Four-phonon interactions significantly reduce κ_l across all temperatures [Figure 6.3(b)]. At 300 K, the inclusion of both three- and four-phonon scatterings results in a 52% decrease in comparison to that obtained using only three-phonon scattering. This reduction becomes more pronounced at higher temperatures, reaching 72% at 800 K. This trend highlights the stronger temperature dependence of four-phonon scattering ($\tau_{4\text{ph}}^{-1} \sim T^2$) compared to the linear scaling of three-phonon scattering ($\tau_{3\text{ph}}^{-1} \sim T$). However, the impact of four-phonon processes varies across materials due to symmetry and phonon dispersion characteristics. At 300 K, the reduction in κ_l is substantial in graphene and MoS_2 (~75%) [74, 228], moderate in stanene and SnC (~50%) [230, 251], and modest in silicene and germanene (~35%) [230]. In h-NbN, acoustic phonons dominate heat transport, contributing about 98% to κ_l [Figure 6.3(b)], consistent with other 2D

materials. Mode-resolved κ_l^{mode} reveals that four-phonon scattering most strongly suppresses the ZA mode contribution [Figure 6.3(b)], highlighting its critical role in heat transport.

To further investigate the underlying mechanisms, we present the frequency-dependent scattering rates and cumulative κ_l in the acoustic region [Figure 6.3(c)]. Notably, four-phonon scattering is significant and comparable to three-phonon scattering in the intermediate frequency (2-4.5 THz) range. This trend persists at higher temperatures (Fig. 6.4), where four-phonon scattering becomes dominant above 1 THz, consistent with its stronger temperature dependence. However, three-phonon scattering remains dominant at low frequencies across all temperatures. This behavior is in contrast with prototypical 2D materials such as graphene [74], MoS_2 [228], and SnC [251], where in-plane mirror symmetry enforces reflection symmetry selection rules (RSSR). These rules forbid three-phonon processes involving an odd number of ZA phonons (e.g., TA/LA + ZA ↔ TA/LA and ZA + ZA ↔ ZA), thus suppressing effective three-phonon scattering [72, 252, 76]. In such cases, four-phonon processes become relevant, as they allow interactions involving two and four ZA phonons [74]. Combined with the large phonon population arising from the quadratic ZA dispersion at low frequencies, this explains the dominance of four-phonon scattering in 2D materials with mirror symmetry.

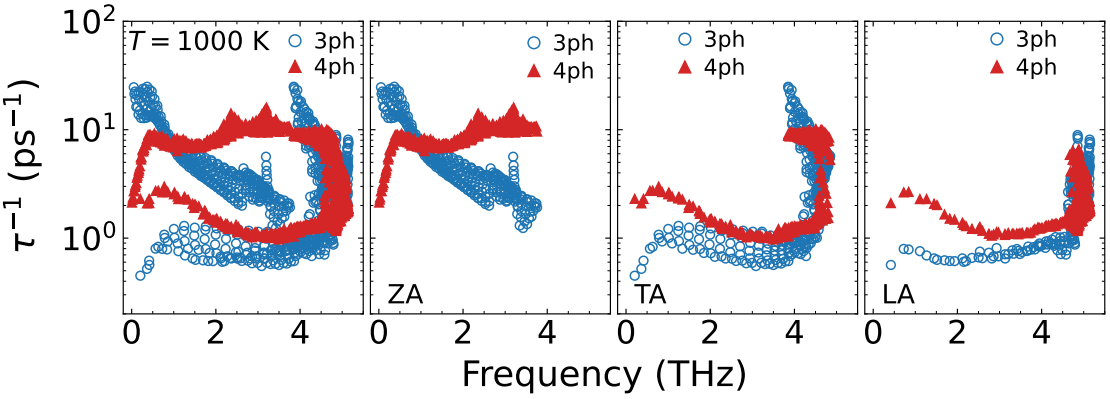

Figure 6.4: Comparison of three- and four-phonon scattering reveals that four-phonon processes increase more rapidly with temperature than three-phonon processes. Mode-resolved contributions further clarify this trend, showing that four-phonon scattering in the TA and LA modes surpasses their three-phonon counterparts.

In buckled 2D materials, the absence of mirror symmetry lifts the constraints imposed by RSSR, allowing both three- and four-phonon processes involving any number of ZA modes. Within the framework of perturbation theory, higher-order interactions are typically weaker; however, a large A-O phonon gap, flexural modes, and nearly non-dispersive acoustic branches [Figure 6.3(a)] together with enhanced four-phonon scattering in h-NbN [Figures 6.3(b) and 6.3(c)]. The A-O gap limits three-phonon processes involving optical modes due to restricted phase space for energy-momentum conservation, whereas four-phonon processes, with greater combinatorial flexibility, remain less restricted.

Mode-resolved scattering rates provide further insight into thermal transport in h-NbN [Figure 6.3(d)]. Since κ_l is dominated by acoustic modes, we focus on their τ^{-1}. While low-frequency phonons generally exhibit long lifetimes due to limited phase space, ZA modes involved in three-phonon processes display anomalously short lifetimes, indicative of strong scattering. This arises from the high population of low-energy ZA phonons, owing to their quadratic dispersion and absence of mirror symmetry, which lifts RSSR constraints and permits all ZA involved processes. Consequently, the three-phonon scattering is dominated by normal processes (Figure 6.5), which redistribute phonon momentum without disrupting heat flow, whereas Umklapp processes directly resist it by reversing momentum. A similar dominance of normal scattering has been reported in other low-buckled 2D materials like germanene and stanene [230]. However, in h-NbN, despite strong three-phonon scattering involving the ZA mode, its contribution to κ_l^{3ph} remains substantial, albeit lower than those of the TA and LA modes. This contrasts with other 2D materials [228, 74], where the ZA mode is the dominant contributor to κ_l when only three-phonon scattering is considered.

Four-phonon scattering of the ZA mode remain stronger than that of the TA and LA modes [Figure 6.3(d)], mainly via normal scattering [Figure 6.5(b)], reducing κ_l^{ZA} nearly fourfold, while the contributions from the TA and LA modes experience a smaller suppression. This trend in κ_l^{mode} now resembles that of graphene and other 2D materials [74]. Another key feature is the strong τ_{TA}^{-1} and τ_{LA}^{-1} in the 4-5

THz range [Figure 6.3(d)], driven by a high PDOS from non-dispersive acoustic branches in this region [Figure 6.3(a)]. However, this has minimal impact on κ_l, as the cumulative κ_l reveals that low-frequency acoustic phonons primarily govern thermal conductivity [Figure 6.3(c)].

The prominence of all-acoustic (AAA and AAAA) scattering in multi-phonon processes (Figure 6.5) arises from the quadratic ZA mode, large A-O phonon gap, and nearly flat acoustic branches. This behavior contrasts with bulk materials [248, 249], where mixed acoustic-optical AAOO interactions typically dominate, but aligns with graphene lacking a phonon gap [74] and $AgCrSe_2$ featuring flat dispersions [250].

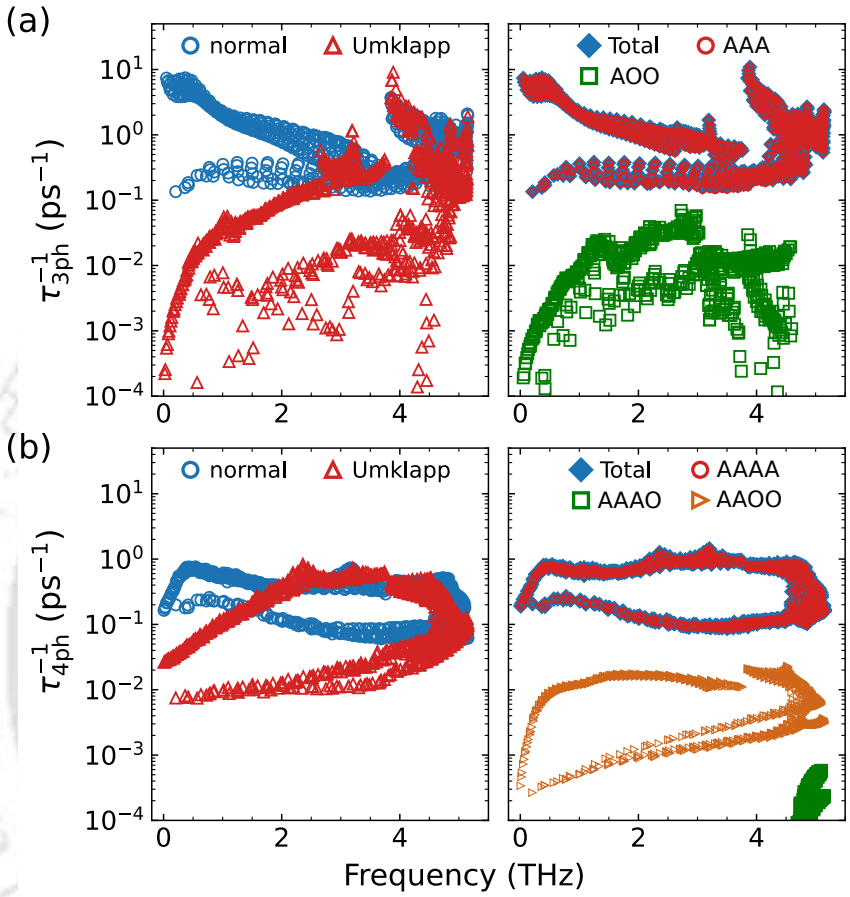

Figure 6.5: (a) Three-phonon (3ph) (b) four-phonon (4ph) scattering rates are presented. At 300 K, both three-phonon and four-phonon scattering in monolayer h-NbN are predominantly governed by normal processes rather than Umklapp scattering. Moreover, phonon scattering is primarily driven by all-acoustic processes, specifically the AAA and AAAA channels.

6.3.4 Effect of tensile strain on κ_l

A practical route to modulate ZA mode is through tensile strain, which can linearise its otherwise quadratic dispersion even at small values [76]. This transition significantly alters phonon populations and scattering dynamics, thereby impacting heat transport. To explore this effect, we apply a modest in-plane tensile strain of 3%, well below the threshold for inducing a planar structural transition [241].

The strained structure remains dynamically stable, with all phonon branches softening and shifting to lower frequencies [Figure 6.6(a)], leading to modified group velocities. Notably, the ZA mode transitions from a quadratic to a near-linear dispersion near the Γ point, consistent with observations in other 2D materials [251, 228]. Strain induces stronger softening of the optical branches, slightly narrowing the A-O gap (8.70 THz), which is unlikely to influence κ_l. Additionally, it slightly enhances acoustic phonon bunching, which can modify scattering rates.

Regardless of scattering order, the strained lattice exhibits a higher κ_l, with four-phonon processes being most significantly impacted [Figure 6.6(b)]. At 300 K, κ_l rises by 23% to 14.80 W m^{-1} K^{-1}, when accounting for scattering up to the fourth order; a notable increase compared to the result obtained by considering only three-phonon interactions.

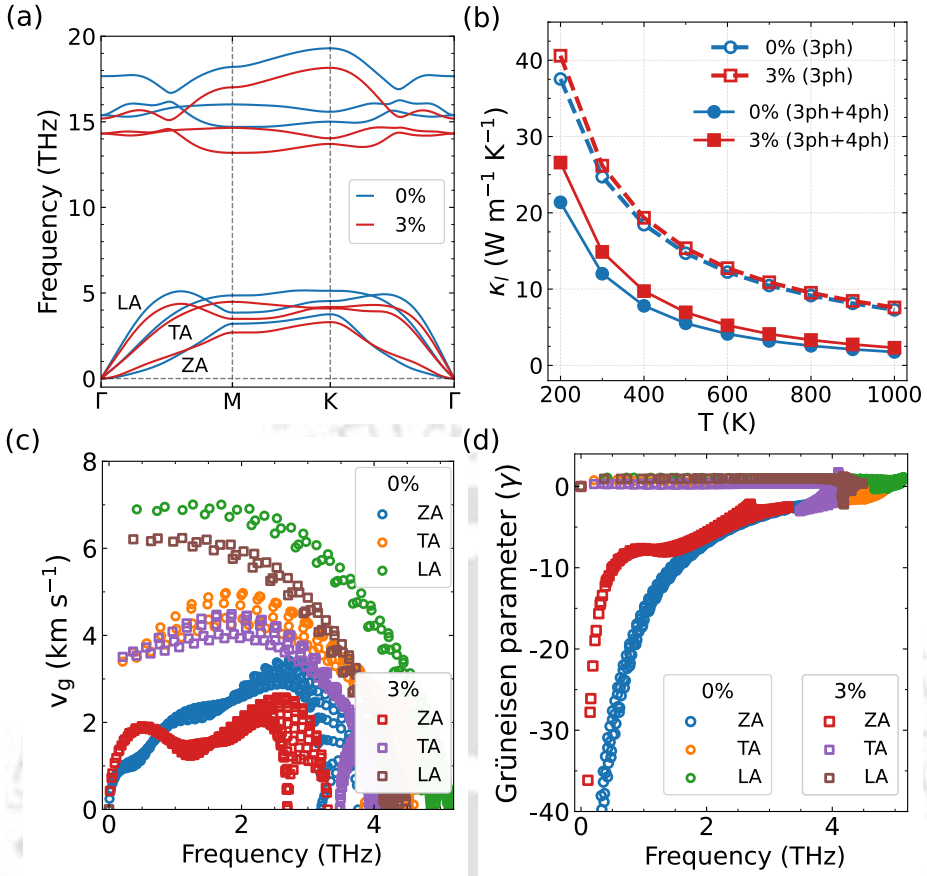

Figure 6.6: (a) The h-NbN monolayer remains dynamically stable under tensile strain $\epsilon = 3\%$, with phonon dispersion showing overall softening, a reduced A-O phonon gap, and a transition to nearly linear ZA dispersion near the Brillouin zone centre. (b) Lattice thermal conductivity (κ_l) as a function of temperature for both strained and unstrained h-NbN for multiphonon scattering considered. (c) The group velocity v_g, and (d) Mode-resolved Grüneisen parameter γ of all acoustic modes for unstrained and strained h-NbN monolayer .

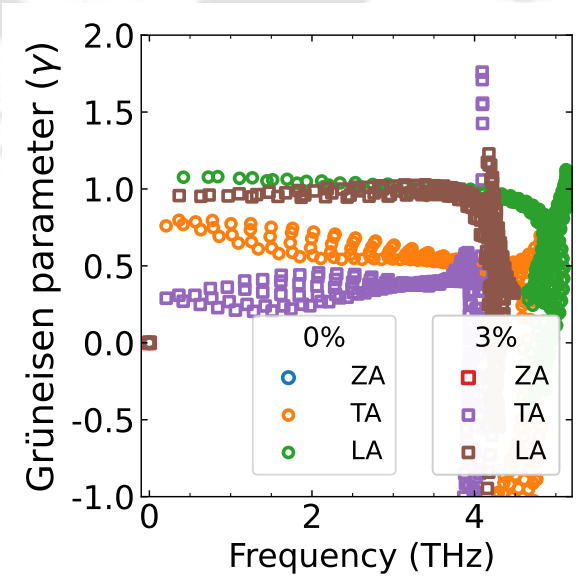

Figure 6.7: The Grüneisen parameter (γ) reflects the anharmonicity of the system and is primarily dominated by the ZA mode, which is significantly suppressed under tensile strain. Here, we highlight the suppression of γ for TA and LA modes under strain.

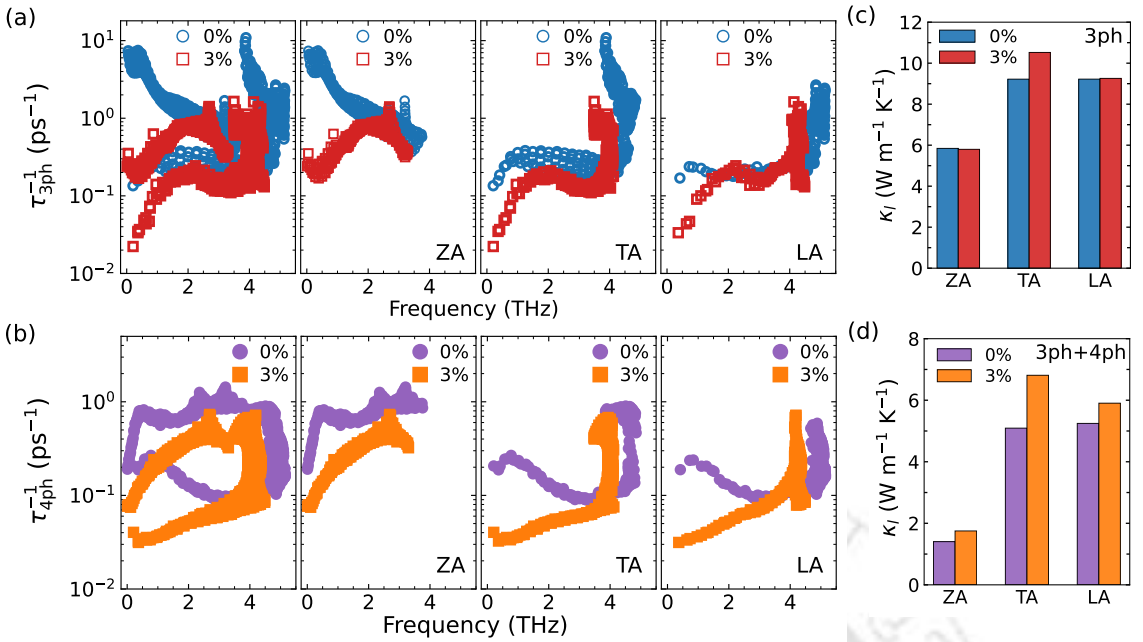

Figure 6.8: (a) Three-phonon τ_{3ph}^{-1} and (b) four-phonon τ_{4ph}^{-1} scattering rates and their mode-resolved contributions, in the strained monolayer, exhibit a pronounced reduction in the low frequency range, which plays a dominant role in heat conduction. Mode-resolved κ_l for (c) 3ph and (d) 3ph + 4ph processes shows that the modest enhancement is primarily driven by the weakening of four-phonon scattering under strain. All results presented are computed at 300 K.

We analyze the group velocity v_g, Grüneisen parameter, and phonon scattering rates to elucidate the mechanism driving thermal transport under strain. Tensile strain generally lowers v_g ($= d\omega/dq$) across all frequencies [Figure 6.6(c)], consistent with phonon softening and a narrower acoustic bandwidth [Figure 6.6(a)]. An exception arises near the Brillouin zone centre, where the ZA mode exhibits an increase in v_g below 1 THz as the dispersion becomes nearly linear, a regime that contributes negligibly to κ_l. Given that $\kappa_l \propto C v_g^2 \tau$ (with C as heat capacity), we compute the small-grain κ_l to isolate the influence of v_g, which drops from 2.2 to 1.8 W m^{-1} K^{-1} nm^{-1} under strain, consistent with reduced v_g. However, the overall increase in κ_l suggests that anharmonic phonon scattering plays the dominant role. To probe this, we calculate the Grüneisen parameter γ, a measure of anharmonicity. Mode-resolved γ reveals that ZA phonons exhibit the highest anharmonicity in unstrained h-NbN [Figure 6.6(d)], aligning with their strong scattering. Under strain, γ_{ZA} reduces by a factor of 2.2, indicating suppressed anharmonicity, and thus lower scattering rates, ultimately enhancing κ_l. Although the decrease in γ is less pronounced for LA and TA modes, they follow the same decreasing trend (Fig. 6.7). This trend aligns with graphene and SnC but differs from MoS_2 [76, 251, 228].

To further elucidate the scattering mechanism, we compute mode-resolved τ^{-1} for the strained lattice and compare it with the unstrained monolayer [Figure 6.8(a) and 6.8(b)]. Across all acoustic modes, tensile strain consistently reduces τ^{-1}, regardless of the scattering order, in line with the previously discussed reduction in anharmonicity. This decrease in scattering rates accounts for the enhanced κ_l observed in strained h-NbN [Figure 6.6(b)].

Mode-specific contributions to κ_l offer valuable insight. Although low-frequency scattering in τ_{3ph}^{-1} and τ_{4ph}^{-1} is significantly reduced under strain, this regime is primarily governed by normal scattering, which, as established for the unstrained monolayer [Figure 6.3(c) and Figure 6.5], does not directly impede heat transport. Consequently, κ_l under three-phonon scattering remains largely unaffected [Figure 6.8(c)]. An exception is the TA mode, where a reduction in τ_{3ph}^{-1} extends into the intermediate frequency range, leading to a modest increase in κ_l [Figure 6.6(b)]. A pronounced reduction in τ_{4ph}^{-1} across the intermediate frequency range, which governs heat transport, leads to an overall increase in mode-resolved κ_l for all acoustic modes [Figure 6.8(d)].

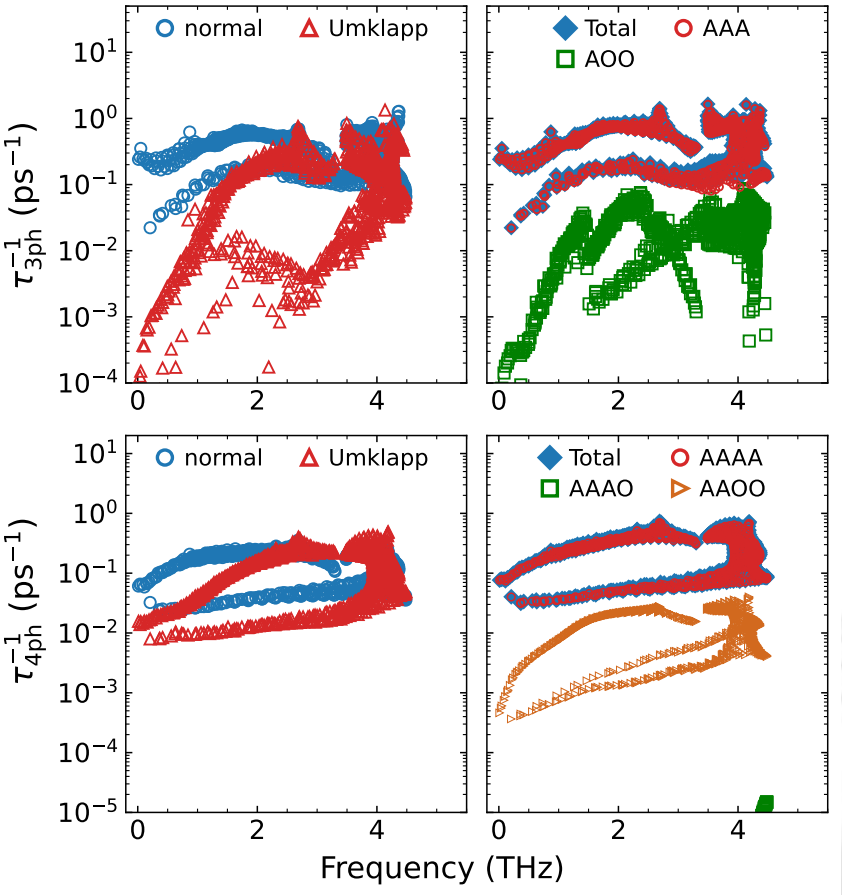

Figure 6.9: (a) Three-phonon (3ph) (b) four-phonon (4ph) scattering rates are presented. At 300 K, both three-phonon and four-phonon scattering in monolayer h-NbN are also predominantly governed by normal processes rather than Umklapp scattering under tensile strain 3%. Moreover, phonon scattering is primarily driven by all-acoustic processes, specifically the AAA and AAAA channels.

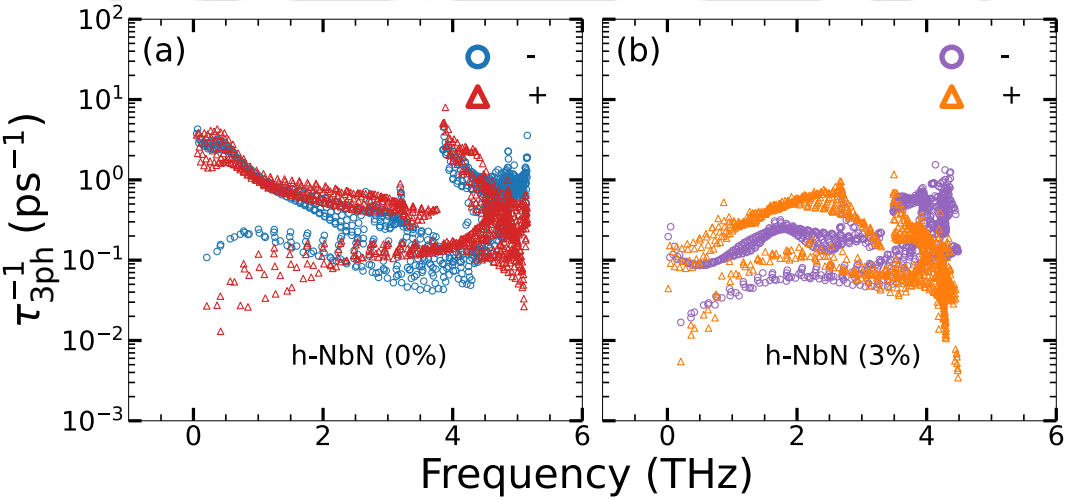

Figure 6.10: At 300 K, three-phonon scattering in h-NbN is dominated by absorption (+) processes rather than decay (−) events, under both unstrained and strained conditions.

Similar to the unstrained monolayer (Fig. 6.5), the multi-phonon scattering is predominantly driven by all acoustic modes (Fig. 6.9). For three-phonon scattering, decay ($\lambda_1 \rightarrow \lambda_2 + \lambda_3$) and absorption ($\lambda_1 + \lambda_2 \rightarrow \lambda_3$) processes contribute comparably in both unstrained and strained h-NbN (Fig. 6.10). In contrast, the four-phonon redistribution process ($\lambda_1 + \lambda_2 \leftrightarrow \lambda_3 + \lambda_4$) consistently overweights splitting ($\lambda_1 \rightarrow \lambda_2 + \lambda_3 +$

λ_4) and recombination ($\lambda_1 + \lambda_2 + \lambda_3 \rightarrow \lambda_4$), irrespective of strain (Fig. 6.11). The dominance of the redistribution process and AAAA scattering highlights ZA + ZA ↔ ZA + ZA as the leading scattering channel. The reduction in scattering rates under tensile strain arises from the contraction of the three- and four-phonon phase space (Fig. 6.12), leading to a modest increase in κ_l, albeit less pronounced than in other 2D materials [251]. These findings highlight the critical role of higher-order phonon interactions in accurately modeling thermal transport. Compared to other monolayers, the κ_l of h-NbN is lower than that of materials such as MoS_2 [228], Janus monolayers like PtSTe [253] and WSSe [254], and TiS_3 [255], yet remains higher than that of low-κ_l 2D energy materials such as SnSe [256] and SnS [257].

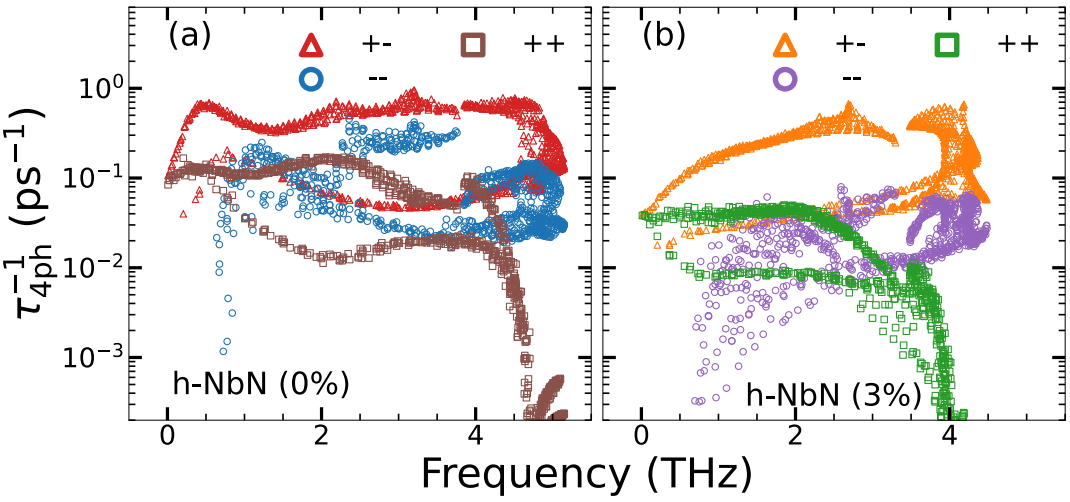

Figure 6.11: At 300 K, four-phonon scattering in h-NbN is predominantly governed by redistribution (+−) events over splitting (−−) and recombination (++) events, for both unstrained and strained conditions.

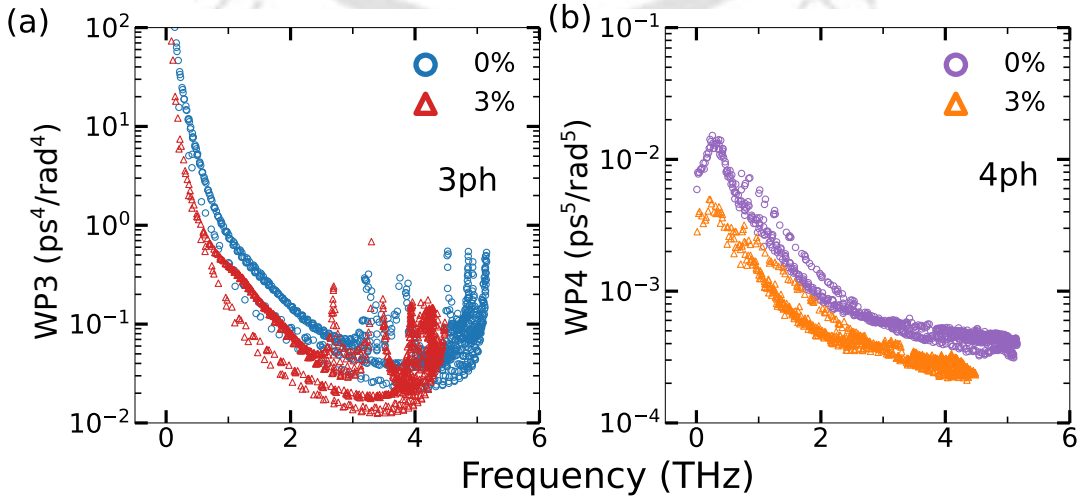

Figure 6.12: The weighted phase space for both three- and four-phonon processes decreases under strain, leading to reduced phonon scattering and an increase in lattice thermal conductivity at 300 K.

6.3.5 Thermoelectric properties

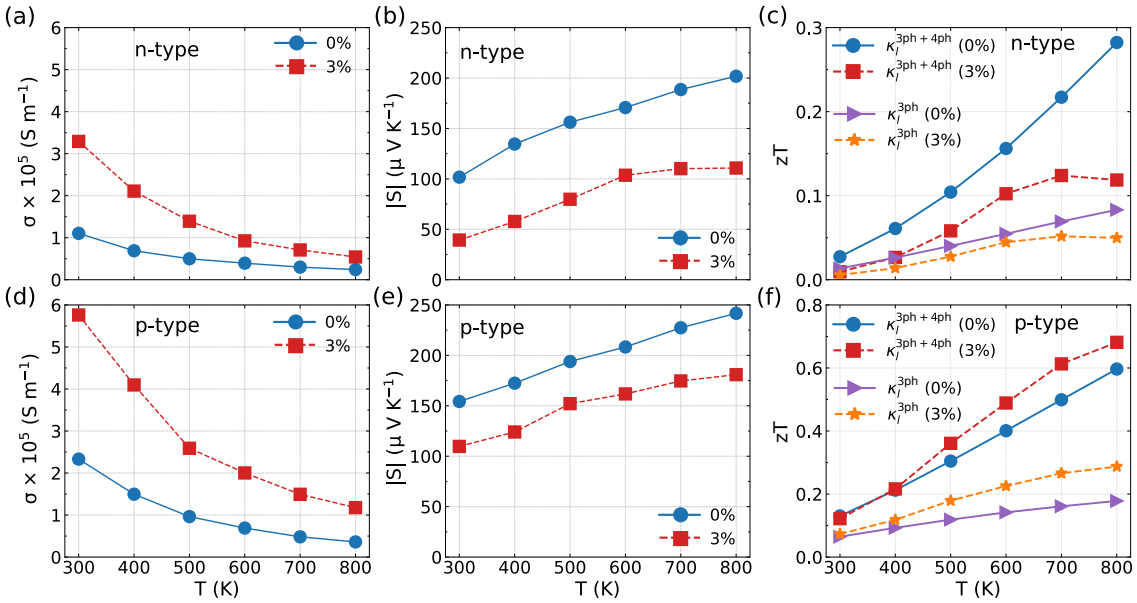

Figure 6.13: Electrical conductivity σ improves under tensile strain for both (a) n-type and (d) p-type carrier doping through a reduction in the electronic band gap. (b) and (e) As expected, the Seebeck coefficient S exhibits an inverse trend to σ under tensile strain. (c) and (f) The thermoelectric figure of merit zT, evaluated at a carrier concentration of $\sim 10^{20}$ cm^{-3}, exhibits distinct strain-dependent behavior for n-type and p-type doping. Calculations using both κ_l^{3ph} and $\kappa_l^{3ph+4ph}$ highlight the critical role of four-order phonon scattering in accurately predicting zT.

Owing to the intrinsically low lattice thermal conductivity of h-NbN, it is pertinent to evaluate its thermoelectric properties. We evaluate key parameters, including the electrical conductivity σ, Seebeck coefficient, and figure of merit zT (Figure 6.13), with particular emphasis on the influence of four-phonon scattering and strain. Incorporating energy-dependent electron-phonon interactions to calculate carrier relaxation times, even when averaged, is crucial for accurately computing electronic transport properties. This approach, combined with a comprehensive thermal transport modeling framework, outperforms conventional deformation potential methods, which often overestimate zT by oversimplifying relaxation times.

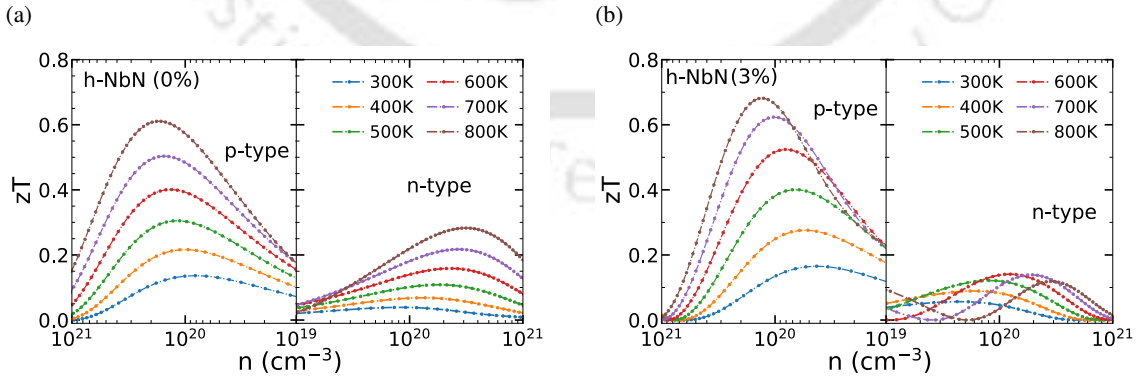

Figure 6.14: Variation of the figure of merit (zT) with carrier concentration (n) for both p- and n-type at different temperatures reveals the optimal doping levels required for enhanced thermoelectric performance. The zT values are evaluated using the lattice thermal conductivity considering both three- and four-phonon scattering ($\kappa_l^{3ph+4ph}$) for (a) unstrained (0%) and (b) tensile-strained (3%) h-NbN.

The narrowing of the electronic band gap under tensile strain (Table 6.1) results in an increase in σ, accompanied by a corresponding decrease in the Seebeck coefficient S (Figure 6.13). Although both car-

rier types follow a similar trend, the p-type system exhibits significantly higher σ, attributed to the more dispersive valence band, yielding a lighter effective mass near the band edge.

Accounting for four-phonon scattering is crucial, as it reduces κ_l, and prevents underestimation of zT if neglected [Figure 6.13(c) and (f)]. For n-type doping, zT decreases under tensile strain due to the rising κ_l. In contrast, p-type doping significantly enhances zT, even altering its strain dependence, as the enhancement in $S^2\sigma$ outweighs the increase in κ_l. Given that the optimal zT is determined at a carrier concentration near the Fermi level, high zT values can be attained through moderate carrier doping (Fig. 6.14a-6.14b). At higher temperatures, the calculated zT of h-NbN approaches 1, comparable to that of Janus monolayers [254, 253], highlighting its potential for high-temperature thermoelectric applications.

6.4 Summary

In this chapter, we present a comprehensive first-principles study of phonon and electronic transport in two-dimensional h-NbN, combining density functional theory with Boltzmann transport formalism. Our findings highlight the crucial role of multi-phonon scattering and strain in governing thermal and thermoelectric performance. Even in the absence of in-plane reflection symmetry selection rules due to lattice buckling, four-phonon scattering significantly limits lattice thermal conductivity. This arises predominantly from all-acoustic AAAA processes due to a large acoustic-optical phonon gap and is further amplified by the quadratic ZA mode and weakly dispersive acoustic branches.

Although the underlying scattering mechanisms remain unchanged under tensile strain, reduced bonding covalency softens the acoustic phonons, leading to lower group velocities and Grüneisen parameters. This diminished anharmonicity suppresses scattering rates, thereby enhancing the lattice thermal conductivity. Our results reveal that the thermoelectric response under tensile strain is governed by concurrent increases in thermal and electrical conductivity, driven by electronic band gap reduction. A high-temperature zT approaching 1 highlights the promising thermoelectric potential of h-NbN. These findings underscore the importance of comprehensive microscopic modeling, not only to accurately capture thermal transport but also to reliably predict thermoelectric performance.

Chapter 7

Conclusion

7.1 Summary and Outlook

In this dissertation, we have systematically investigated the thermoelectric properties of a wide range of two-dimensional materials. This is a rapidly growing field due to their unique electronic and phononic characteristics. The focus has been on understanding and tailoring transport properties through different design strategies, including structural arrangement, symmetry breaking, and strain engineering. These approaches collectively provide pathways to enhance the thermoelectric (TE) efficiency. The transport properties have been analyzed within the framework of the Boltzmann transport equation. For electronic transport, two distinct approaches were employed to evaluate the carrier relaxation time (τ). The deformation potential theory (DPT), which corresponds to a constant relaxation time approximation (CRTA), offers a qualitative estimate of τ, limited primarily to carrier–acoustic phonon scattering. In contrast, the electron–phonon averaged (EPA) method accounts for the full electron–phonon coupling matrix and yields an energy-dependent τ, thereby providing a more realistic description beyond CRTA, albeit with significantly higher computational cost. For phonon transport, the lattice thermal conductivity was determined by explicitly considering phonon lifetimes obtained from three-phonon and, when necessary, four-phonon scattering processes, ensuring a reliable treatment of anharmonicity. The summary of the chapters is as follows.

In **Chapter-3**, we investigated the thermoelectric properties of Si–X (X = N, P, As, Sb, Bi) monolayers, with a focus on the role of structural rearrangement. We explored an alternative atomic configuration, distinct from the conventional one, by reordering the inner and outer layer atoms. This rearrangement led to a significant enhancement in thermoelectric performance, with the SiP monolayer exhibiting a maximum theoretical efficiency of 27% in the optimized configuration. The figure of merit (ZT) was found to increase by a factor of 2–6, attributed to an improved electrical conductivity (σ) and a notably reduced lattice thermal conductivity (κ_l). These changes are linked to band edge modifications, such as increased flatness, and weaker bonding that amplifies phonon anharmonicity. Overall, this study demonstrates that the stacking arrangement in Si–X monolayers is a key parameter governing their thermoelectric behavior, offering a viable pathway for achieving high ZT values at elevated temperatures.

In **Chapter-4**, we introduced MXenes as a promising class of thermoelectric materials, which had remained largely unexplored in this context. Taking advantage of their inherent structural flexibility, we investigated two strategies to tune their thermoelectric performance: (i) surface engineering via the creation of Janus structures, and (ii) strain engineering applied to Janus MXenes. In the first part, we constructed Janus $MM'CO_2$ compounds by replacing one of the transition metal atoms ($M \neq M'$; M, M' = Ti, Zr, Hf, Mo) in M_2CO_2, thereby breaking inversion symmetry. This symmetry-breaking induced notable changes in the electronic structure. While Mo_2CO_2 is semi-metallic, its Janus derivatives, $TiMoCO_2$, $ZrMoCO_2$, and $HfMoCO_2$, exhibit narrow band gaps and semiconducting behavior. In particular, these Janus systems displayed flat bands near the Fermi level, leading to Van Hove singularities and enhanced Seebeck coefficients (S), especially in Mo-based compounds. For the phonon properties, we observed a discrepancy in the κ_l trends of parent M_2CO_2 systems, where conventional harmonic descriptors such as average atomic mass ($\bar{m}$), Debye temperature (Θ_D), and phonon group velocity (v_g) failed to explain the thermal transport behavior. The in-depth analysis of anharmonic features explains the origin of the anomaly in κ_l. However, in Janus MXenes, the emergence of acoustic bunching and enhanced anharmonicity, primarily rooted in weakening bonding strength, led to a systematic reduction in κ_l. The combined improvement in electronic and thermal transport properties resulted in an enhanced figure of merit (ZT), establishing surface engineering as a highly effective design strategy for MXenes. In the second part, we explored the influence of biaxial

strain on three Janus MXene variants: $ZrHfCO_2$, Zr_2COS, and ZrHfCOS. Application of tensile strain transformed the electronic structure by modulating the dispersive nature of band edges, shifting the compounds toward semiconducting behavior. In contrast, compressive strain induced more metallic characteristics. The opening of the band gap leads to the enhancement of the Seebeck coefficient (S). Tensile strain also promoted increased anharmonic phonon scattering and reduced phonon group velocity, further lowering κ_l. These results demonstrate that both symmetry breaking via surface engineering and strain modulation offer powerful levers to control and enhance the thermoelectric performance of MXenes. This work opens new pathways for designing efficient 2D thermoelectric materials through targeted structural manipulation.

In **Chapter-5**, we examined the thermoelectric properties of Janus monochalcogenides, motivated by the known efficiency of monochalcogenides in both bulk and low-dimensional forms. We studied three families of Janus compounds, Ge_2XY, Sn_2XY, and $GeSnX_2$ (X, Y = S, Se, Te), in which the lack of mirror symmetry leads to surface asymmetry. These systems exhibit highly anisotropic transport behavior, primarily due to their anisotropic crystal structure, where the in-plane lattice constants differ significantly. The electronic band structures exhibit characteristic pudding-mold shape features, which are flat near the band edges and dispersive elsewhere. Combined with the presence of multi-valley pockets, these features give rise to large power factors ($S^2\sigma$). Due to the complexity of the electronic band dispersion, the transport properties were evaluated using the electron-phonon averaged (EPA) method for improved quantitative accuracy. The surface asymmetry enhances phonon–phonon scattering and reduces lattice thermal conductivity (κ_l). As a result, several Janus compounds exhibit high thermoelectric performance, with ZT values ranging from 1.55 to 1.70 at 800 K. These findings underscore the effectiveness of surface asymmetry as a design strategy that not only amplifies the intrinsic anisotropy of monochalcogenides but also enables precise tuning of their transport properties. Overall, Janus monochalcogenides emerge as highly promising candidates for high-temperature thermoelectric applications.

In **Chapter-6**, we investigated the impact of four-phonon (4ph) scattering on the thermal and thermoelectric properties of the h-NbN monolayer. We found that inclusion of 4ph processes led to a significant reduction in lattice thermal conductivity (κ_l), decreasing by 52% at 300 K and 72% at 800 K compared to values obtained with only three-phonon (3ph) scattering. Unlike graphene or MoS_2, where the reflection symmetry selection rule (RSSR) governs the suppression of certain phonon scattering channels, h-NbN lacks mirror symmetry. Despite this, our results reveal that 4ph scattering remains strong, thereby challenging the common assumption that RSSR is a prerequisite for its significance in two-dimensional materials. The origin of this pronounced 4ph scattering lies in three key factors: (i) the quadratic dispersion of out-of-plane flexural (ZA) phonons, (ii) a large acoustic–optical (A–O) phonon gap, and (iii) flat acoustic branches, all of which collectively promote strong 4ph-scattering. A detailed process-wise scattering analysis showed that the dominant contributions to κ_l arise from acoustic–acoustic scattering events, AAA and AAAA processes for 3ph and 4ph interactions, respectively. Under +3% tensile strain, the ZA mode transitions from quadratic to nearly linear dispersion, reducing anharmonic scattering and increasing κ_l. Despite this increase, electronic transport analysis confirms that h-NbN maintains favorable thermoelectric performance, with ZT approaching 1 at elevated temperatures. This study establishes that four-phonon scattering can be substantial even in non-RSSR 2D systems, expanding the conventional understanding of anharmonicity in low-dimensional materials.

7.2 Scopes for Future Work

The present thesis opens several avenues for further investigation:

1. We found that four-phonon scattering can be prominent in 2D materials. Therefore, the inclusion of phonon-renormalization effects to obtain temperature-dependent force constants, thereby capturing the influence of phonon softening on scattering and anharmonicity can be attempted.

2. Development of machine-learned force fields (MLFF) to evaluate lattice thermal conductivity with high efficiency, accompanied by the creation of a dedicated database for two-dimensional materials is another direction.

3. Another direction is to extend surface engineering to include doping and solid solutions, which may provide further control over electronic and phonon transport in 2D materials.

4. Thermoelectric studies of heterostructures of newly synthesized two-dimensional materials is certainly worth doing. Such heterostructures can combine distinct electronic and phononic features from

different layers, potentially leading to synergistic effects such as enhanced Seebeck coefficient, interfacial phonon scattering, and reduced lattice thermal conductivity. Investigating their transport behavior will provide valuable insights into interface-driven thermoelectric mechanisms and open up new design routes for high-performance materials.

5. Recent studies have begun exploring the influence of magnetism on thermoelectric performance, particularly through the Anomalous Nernst Effect (ANE). Investigating such coupled phenomena, including magnetic effects and spin-caloritronics, can open new avenues for enhancing thermoelectric efficiency in two-dimensional materials.

Bibliography

[1] M. Allen, O. P. Dube, W. Solecki, F. Aragón-Durand, W. Cramer, S. Humphreys, M. Kainuma, *et al.*, Intergovernmental Panel on Climate Change (IPCC) **677**, 393 (2018).

[2] M. Igini, Earth. Org (2024).

[3] I. P. on Climate Change (IPCC), *Global Warming of 1.5°C: IPCC Special Report on Impacts of Global Warming of 1.5°C above Pre-industrial Levels in Context of Strengthening Response to Climate Change, Sustainable Development, and Efforts to Eradicate Poverty* (Cambridge University Press, 2022) p. 1–24.

[4] J. Ambrose, The Guardian (2024).

[5] L. E. Bell, science **321**, 1457 (2008).

[6] L. Miró, J. Gasia, and L. F. Cabeza, Applied energy **179**, 284 (2016).

[7] H. El Hage, M. Ramadan, H. Jaber, M. Khaled, and A. G. Olabi, Energy Sources, Part A: Recovery, Utilization, and Environmental Effects **42**, 3019 (2020).

[8] X. Yuan, J. Liu, S. Sun, X. Lin, X. Fan, W. Zhao, and R. Kosonen, Renewable and Sustainable Energy Reviews **219**, 115863 (2025).

[9] J. R. Sootsman, D. Y. Chung, and M. G. Kanatzidis, Angewandte Chemie International Edition **48**, 8616 (2009).

[10] G. J. Snyder and E. S. Toberer, Nature materials **7**, 105 (2008).

[11] B. Russ, A. Glaudell, J. J. Urban, M. L. Chabinyc, and R. A. Segalman, Nature Reviews Materials **1**, 1 (2016).

[12] F. J. DiSalvo, Science **285**, 703 (1999).

[13] A. F. Ioffe, L. Stil'Bans, E. Iordanishvili, T. Stavitskaya, A. Gelbtuch, and G. Vineyard, Physics Today **12**, 42 (1959).

[14] J. Ziman, *Electrons and Phonons: The Theory of Transport Phenomena in Solids* (Oxford University Press, 2001).

[15] R. L. Cataldo and G. L. Bennett, Radioisotopes-Applications in Physical Sciences , 473 (2011).

[16] D. Palaporn, S.-a. Tanusilp, Y. Sun, S. Pinitsoontorn, and K. Kurosaki, Materials Advances **5**, 5351 (2024).

[17] J. Yang and T. Caillat, MRS Bulletin **31**, 224–229 (2006).

[18] L. Yang, Z.-G. Chen, M. S. Dargusch, and J. Zou, Advanced Energy Materials **8**, 1701797 (2018).

[19] P. Baskaran and M. Rajasekar, Chemical Engineering Journal , 159929 (2025).

[20] Q. Zhang, A. Huang, X. Ai, J. Liao, Q. Song, H. Reith, X. Cao, Y. Fang, G. Schierning, K. Nielsch, *et al.*, Advanced energy materials **11**, 2101213 (2021).

[21] H. Moria, M. Ahmed, A. Alghanmi, T. I. Mohamad, and Y. Yaakob, Energy Procedia **158**, 198 (2019).

[22] C. Wang, Z. Xu, H. Wang, T. Cai, H. Tao, Y. Wang, and X. Tang, Energy Conversion and Management **297**, 117706 (2023).

[23] H. Ma, S. Pu, H. Wu, S. Jia, J. Zhou, H. Wang, W. Ma, Z. Wang, L. Yang, and Q. Sun, ACS Applied Materials & Interfaces **16**, 7453 (2024).

[24] D. Enescu, Energies **17**, 285 (2024).

[25] T. Cao, X.-L. Shi, and Z.-G. Chen, Progress in Materials Science **131**, 101003 (2023).

[26] N. Oueldna, N. Sabi, H. Aziam, V. Trabadelo, and H. B. Youcef, Materials Horizons **11**, 2323 (2024).

[27] H. Goldsmid, Proceedings of the Physical Society **71**, 633 (1958).

[28] A. D. LaLonde, Y. Pei, H. Wang, and G. J. Snyder, Materials today **14**, 526 (2011).

[29] L.-D. Zhao, S.-H. Lo, Y. Zhang, H. Sun, G. Tan, C. Uher, C. Wolverton, V. P. Dravid, and M. G. Kanatzidis, Nature **508**, 373 (2014).

[30] G. Rogl and P. Rogl, Current opinion in green and sustainable chemistry **4**, 50 (2017).

[31] W.-j. Tan, Y.-t. Liu, M. Zhu, T.-j. Zhu, X.-b. Zhao, X.-t. Tao, and S.-q. Xia, Inorganic chemistry **56**, 1646 (2017).

[32] R. Chetty, A. Bali, and R. C. Mallik, Journal of Materials Chemistry C **3**, 12364 (2015).

[33] J. A. Pérez-Taborda, O. Caballero-Calero, and M. Martín-González, *Silicon-germanium (SiGe) nanostructures for thermoelectric devices: recent advances and new approaches to high thermoelectric efficiency* (IntechOpen, 2017).

[34] H. Zhao, J. Sui, Z. Tang, Y. Lan, Q. Jie, D. Kraemer, K. McEnaney, A. Guloy, G. Chen, and Z. Ren, Nano Energy **7**, 97 (2014).

[35] W. Li, S. Ghosh, N. Liu, and B. Poudel, Joule **8**, 1274 (2024).

[36] J. Goldsmid, *The Physics of Thermoelectric Energy Conversion*, IOP Concise Physics (Morgan & Claypool Publishers, 2017).

[37] H. Goldsmid, *Thermoelectric refrigeration* (Springer New York, NY, 2013).

[38] Y. Pei, X. Shi, A. LaLonde, H. Wang, L. Chen, and G. J. Snyder, Nature **473**, 66 (2011).

[39] T. Zhu, Y. Liu, C. Fu, J. P. Heremans, J. G. Snyder, and X. Zhao, Adv. Mater. **29**, 1605884 (2017).

[40] N. Boukhris, H. Meradji, S. Ghemid, S. Drablia, and F. E. H. Hassan, Physica Scripta **83**, 065701 (2011).

[41] K. Hoang, S. Mahanti, and M. G. Kanatzidis, Physical Review B—Condensed Matter and Materials Physics **81**, 115106 (2010).

[42] J.-H. Bahk and A. Shakouri, Applied Physics Letters **105** (2014).

[43] S. Wang, J. Yang, T. Toll, J. Yang, W. Zhang, and X. Tang, Scientific reports **5**, 10136 (2015).

[44] Z. Liu, J. Mao, S. Peng, B. Zhou, W. Gao, J. Sui, Y. Pei, and Z. Ren, Materials Today Physics **2**, 54 (2017).

[45] J. Schmitt, Z. M. Gibbs, G. J. Snyder, and C. Felser, Materials Horizons **2**, 68 (2015).

[46] Y. Pei, X. Shi, A. LaLonde, H. Wang, L. Chen, and G. J. Snyder, Nature **473**, 66 (2011).

[47] K. H. Lee, S.-i. Kim, H.-S. Kim, and S. W. Kim, ACS Applied Energy Materials **3**, 2214 (2020).

[48] A. Banik and K. Biswas, Journal of Solid State Chemistry **242**, 43 (2016).

[49] Y. Feng, J. Li, Y. Li, T. Ding, C. Zhang, L. Hu, F. Liu, W. Ao, and C. Zhang, Journal of Materials Chemistry A **8**, 11370 (2020).

[50] J. W. Simonson, D. Wu, W. J. Xie, T. M. Tritt, and S. J. Poon, Phys. Rev. B **83**, 235211 (2011).

[51] J. P. Heremans, V. Jovovic, E. S. Toberer, A. Saramat, K. Kurosaki, A. Charoenphakdee, S. Yamanaka, and G. J. Snyder, Science **321**, 554 (2008).

[52] J. He and T. M. Tritt, Science **357**, eaak9997 (2017).

[53] J. Zhang, L. Song, S. H. Pedersen, H. Yin, L. T. Hung, and B. B. Iversen, Nature communications **8**, 13901 (2017).

[54] R. D'Souza, J. D. Querales-Flores, J. Cao, S. Fahy, and I. Savić, ACS Applied Energy Materials **5**, 7260 (2022).

[55] J. Parrott, Journal of Physics C: Solid State Physics **2**, 147 (1969).

[56] C. Chiritescu, C. Mortensen, D. G. Cahill, D. Johnson, and P. Zschack, Journal of Applied Physics **106** (2009).

[57] D. G. Cahill, S. K. Watson, and R. O. Pohl, Physical Review B **46**, 6131 (1992).

[58] B. Abeles, D. S. Beers, G. D. Cody, and J. P. Dismukes, Phys. Rev. **125**, 44 (1962).

[59] T. Knittel, *Thermal conductivity and other transport properties of lead telluride-tin telluride alloys* (University of New South Wales, 1978).

[60] W. Li, L. Lindsay, D. A. Broido, D. A. Stewart, and N. Mingo, Phys. Rev. B **86**, 174307 (2012).

[61] H. Zhu, R. He, J. Mao, Q. Zhu, C. Li, J. Sun, W. Ren, Y. Wang, Z. Liu, Z. Tang, *et al.*, Nature communications **9**, 2497 (2018).

[62] C. Gayner, L. T. Menezes, Y. Natanzon, Y. Kauffmann, H. Kleinke, and Y. Amouyal, ACS Applied Materials & Interfaces **15**, 13012 (2023).

[63] N. Satyala, A. Tahmasbi Rad, Z. Zamanipour, P. Norouzzadeh, J. S. Krasinski, L. Tayebi, and D. Vashaee, Journal of Applied Physics **115** (2014).

[64] S. Behera, S. Bose, P. Entel, and J. Schick**, Phase transitions **77**, 225 (2004).

[65] M. Dutta, A. Das, and K. Biswas, Inorganic Chemistry **63**, 20068 (2024).

[66] M. Christensen, A. B. Abrahamsen, N. B. Christensen, F. Juranyi, N. H. Andersen, K. Lefmann, J. Andreasson, C. R. Bahl, and B. B. Iversen, Nature materials **7**, 811 (2008).

[67] C. H. Lee, I. Hase, H. Sugawara, H. Yoshizawa, and H. Sato, Journal of the Physical Society of Japan **75**, 123602 (2006).

[68] X. Shi, J. Yang, J. R. Salvador, M. Chi, J. Y. Cho, H. Wang, S. Bai, J. Yang, W. Zhang, and L. Chen, Journal of the American Chemical Society **133**, 7837 (2011).

[69] L. D. Hicks and M. S. Dresselhaus, Physical Review B **47**, 12727 (1993).

[70] L. Hicks, T. Harman, X. Sun, and M. Dresselhaus, Physical Review B **53**, R10493 (1996).

[71] R. Venkatasubramanian, Physical Review B **61**, 3091 (2000).

[72] L. Lindsay, D. A. Broido, and N. Mingo, Phys. Rev. B **82**, 115427 (2010).

[73] B. Peng, H. Zhang, H. Shao, Y. Xu, G. Ni, R. Zhang, and H. Zhu, Physical Review B **94**, 245420 (2016).

[74] T. Feng and X. Ruan, Phys. Rev. B **97**, 045202 (2018).

[75] L. Lindsay, C. Hua, X. Ruan, and S. Lee, Materials Today Physics **7**, 106 (2018).

[76] L. Lindsay, W. Li, J. Carrete, N. Mingo, D. A. Broido, and T. L. Reinecke, Phys. Rev. B **89**, 155426 (2014).

[77] J. Hong, C. Lee, J. Park, and J. H. Shim, Phys. Rev. B **93**, 035445 (2016).

[78] M. Buscema, M. Barkelid, V. Zwiller, H. S. J. van der Zant, G. A. Steele, and A. Castellanos-Gomez, Nano Lett. **13**, 358 (2013).

[79] K. Hippalgaonkar, Y. Wang, Y. Ye, D. Y. Qiu, H. Zhu, Y. Wang, J. Moore, S. G. Louie, and X. Zhang, Phys. Rev. B **95**, 115407 (2017).

[80] E. Flores, J. R. Ares, A. Castellanos-Gomez, M. Barawi, I. J. Ferrer, and C. Sánchez, Appl. Phys. Lett. **106** (2015).

[81] Y. Saito, T. Iizuka, T. Koretsune, R. Arita, S. Shimizu, and Y. Iwasa, Nano lett. **16**, 4819 (2016).

[82] Z.-Y. Hu, K.-Y. Li, Y. Lu, Y. Huang, and X.-H. Shao, Nanoscale **9**, 16093 (2017).

[83] M. Khazaei, M. Arai, T. Sasaki, M. Estili, and Y. Sakka, Phys. Chem. Chem. Phys. **16**, 7841 (2014).

[84] S. Deng, L. Li, O. J. Guy, and Y. Zhang, Phys. Chem. Chem. Phys. **21**, 18161 (2019).

[85] X. Xue, S. Li, and M. Zhu, RSC advances **15**, 26919 (2025).

[86] Z. Mao, Z. Wang, T. Shi, P.-a. Zong, J. Liang, Z. Liu, P. Zhang, Y. Huang, Y. Han, K. Ahmad, *et al.*, Advanced Materials Interfaces **9**, 2200555 (2022).

[87] H. Sadeghi, S. Sangtarash, and C. J. Lambert, 2D Materials **4**, 015012 (2016).

[88] S. Bhattacharyya, T. Pandey, and A. K. Singh, Nanotechnology **25**, 465701 (2014).

[89] P. Hohenberg and W. Kohn, Physical review **136**, B864 (1964).

[90] W. Kohn and L. J. Sham, Physical review **140**, A1133 (1965).

[91] M. Born and R. Oppenheimer, Annalen der Physik **389**, 457 (1927).

[92] L. H. Thomas, in *Mathematical proceedings of the Cambridge philosophical society*, Vol. 23 (Cambridge University Press, 1927) pp. 542–548.

[93] E. Fermi, Rend. Accad. Naz. Lincei **6**, 5 (1927).

[94] D. R. Hartree, in *Mathematical Proceedings of the Cambridge Philosophical Society*, Vol. 24 (Cambridge university press, 1928) pp. 89–110.

[95] V. Fock, Zeitschrift für Physik **61**, 126 (1930).

[96] J. G. Lee, *Computational materials science: an introduction* (CRC press, 2016).

[97] R. M. Martin, *Electronic structure: basic theory and practical methods* (Cambridge university press, 2020).

[98] J. P. Perdew, K. Burke, and M. Ernzerhof, Physical review letters **77**, 3865 (1996).

[99] J. P. Perdew and W. Yue, Phys. Rev. B **33**, 8800 (1986).

[100] J. P. Perdew, K. Burke, and M. Ernzerhof, Phys. Rev. Lett. **77**, 3865 (1996).

[101] L. S. Pedroza, A. J. R. da Silva, and K. Capelle, Phys. Rev. B **79**, 201106 (2009).

[102] D. Vanderbilt, Physical review B **41**, 7892 (1990).

[103] K. Laasonen, R. Car, C. Lee, and D. Vanderbilt, Phys. Rev. B **43**, 6796 (1991).

[104] P. E. Blöchl, Physical review B **50**, 17953 (1994).

[105] D. J. Singh and L. Nordström, *Planewaves, pseudopotentials and the LAPW method* (Springer, 2006).

[106] J. C. Slater, Physical Review **51**, 846 (1937).

[107] J. Slater, in *Advances in quantum chemistry*, Vol. 1 (Elsevier, 1964) pp. 35–58.

[108] G. Kresse and J. Furthmüller, Physical review B **54**, 11169 (1996).

[109] G. K. Madsen, J. Carrete, and M. J. Verstraete, Computer Physics Communications **231**, 140 (2018).

[110] D. J. Singh and I. I. Mazin, Phys. Rev. B **56**, R1650 (1997).

[111] J. Bardeen and W. Shockley, Physical review **80**, 72 (1950).

[112] G. Samsonidze and B. Kozinsky, Adv. Energy Mater. **8**, 1800246 (2018).

[113] P. Giannozzi, S. Baroni, N. Bonini, M. Calandra, R. Car, C. Cavazzoni, D. Ceresoli, G. L. Chiarotti, M. Cococcioni, I. Dabo, A. Dal Corso, S. de Gironcoli, S. Fabris, G. Fratesi, R. Gebauer, U. Gerstmann, C. Gougoussis, A. Kokalj, M. Lazzeri, L. Martin-Samos, N. Marzari, F. Mauri, R. Mazzarello, S. Paolini, A. Pasquarello, L. Paulatto, C. Sbraccia, S. Scandolo, G. Sclauzero, A. P. Seitsonen, A. Smogunov, P. Umari, and R. M. Wentzcovitch, J. Phys.: Condens. Matter **21**, 395502 (19pp) (2009).

[114] G. P. Srivastava, *The physics of phonons* (CRC press, 2022).

[115] A. Togo and I. Tanaka, Scripta Materialia **108**, 1 (2015).

[116] W. Li, J. Carrete, N. A. Katcho, and N. Mingo, Computer Physics Communications **185**, 1747 (2014).

[117] Z. Han, X. Yang, W. Li, T. Feng, and X. Ruan, Comput. Phys. Commun. **270**, 108179 (2022).

[118] M. Born, in *Mathematical Proceedings of the Cambridge Philosophical Society*, Vol. 36 (Cambridge University Press, 1940) pp. 160–172.

[119] S. Nosé, J. Chem. Phys. **81**, 511 (1984).

[120] K. Momma and F. Izumi, Applied Crystallography **41**, 653 (2008).

[121] V. Wang, N. Xu, J.-C. Liu, G. Tang, and W.-T. Geng, Computer Physics Communications **267**, 108033 (2021).

[122] A. M. Ganose, A. J. Jackson, and D. O. Scanlon, J. Open Source Softw. **3**, 717 (2018).

[123] D. Wickramaratne, F. Zahid, and R. K. Lake, Journal of Applied Physics **140**, 124710 (2014).

[124] V. Zolyomi, N. D. Drummond, and V. I. Fal'ko, Physical Rev B **87**, 195403 (2013).

[125] V. Zolyomi, N. D. Drummond, and V. I. Fal'ko, Physical Rev B **89**, 205416 (2014).

[126] X. Zhou, J. Cheng, Y. Zhou, T. Cao, H. Homg, Z. Liao, S. Wu, H. Peng, K. Liu, and D. Yu, Journal of American Chemical Society **137**, 7994 (2015).

[127] D. Parker, X. Chen, and D. J. Singh, Physical Review Letters **110**, 146601 (2013).

[128] C. Barreteau, B. Michon, C. Besnard, and E. Giannini, Journal of Crystal Growth **443**, 75 (2016).

[129] L. Zhou, Y. Guo, and J. Zhao, Physica E: Low-dimensional Systems and Nanostructures **95**, 149 (2018).

[130] B. Huang, H. L. Zhuang, M. Yoon, B. G. Sumpter, and S. H. Wei, Physical Review B **91**, 121401 (2015).

[131] B. Özdamar, G. Özbal, M. N. Çınar, K. Sevim, G. Kurt, B. Kaya, and H. Sevinçli, Physical Review B **98**, 045431 (2018).

[132] R. N. Somaiya, Y. A. Sonvane, and S. K. Gupta, Physical Chemistry Chemical Physics **22**, 3990 (2020).

[133] H. H. Huang, X. Fan, D. J. Singh, and W. T. Zheng, Journal of Materials Chemistry C **7**, 10652 (2019).

[134] A. Majumdar, S. Chowdhury, and R. Ahuja, Nano Energy **88**, 106248 (2021).

[135] J. W. Furness, U. Ekström, T. Helgaker, and A. M. Teale, Molecular Physics **114**, 1415 (2016).

[136] J. Carrete, V. N. Tuoc, and G. K. Madsen, Physical Chemistry Chemical Physics **21**, 5215 (2019).

[137] Q. Cai, D. Scullion, W. Gan, A. Falin, S. Zhang, K. Watanabe, T. Taniguchi, Y. Chen, E. J. Santos, and L. H. Li, Science advances **5**, eaav0129 (2019).

[138] R. Yan, J. R. Simpson, S. Bertolazzi, J. Brivio, M. Watson, X. Wu, A. Kis, T. Luo, A. R. Hight Walker, and H. G. Xing, ACS nano **8**, 986 (2014).

[139] J. Chen, J. He, D. Pan, X. Wang, N. Yang, J. Zhu, S. A. Yang, and G. Zhang, Science China Physics, Mechanics & Astronomy **65**, 117002 (2022).

[140] M. Naguib, M. Kurtoglu, V. Presser, J. Lu, J. Niu, M. Heon, L. Hultman, Y. Gogotsi, and M. W. Barsoum, Adv. Mater. **23**, 4248 (2011).

[141] M. R. Lukatskaya, O. Mashtalir, C. E. Ren, Y. Dall'Agnese, P. Rozier, P. L. Taberna, M. Naguib, P. Simon, M. W. Barsoum, and Y. Gogotsi, Science **341**, 1502 (2013).

[142] X. Xie, S. Chen, W. Ding, Y. Nie, and Z. Wei, Chem. Commun. **49**, 10112 (2013).

[143] F. Shahzad, M. Alhabeb, C. B. Hatter, B. Anasori, S. M. Hong, C. M. Koo, and Y. Gogotsi, Science **353**, 1137 (2016).

[144] S. Kumar and U. Schwingenschlögl, Phys. Rev. B **94**, 035405 (2016).

[145] Z. Guo, N. Miao, J. Zhou, Y. Pan, and Z. Sun, Phys. Chem. Chem. Phys. **20**, 19689 (2018).

[146] A. N. Gandi, H. N. Alshareef, and U. Schwingenschlögl, Chem. Mater. **28**, 1647 (2016).

[147] S. Sarikurt, D. Çakır, M. Keçeli, and C. Sevik, Nanoscale **10**, 8859 (2018).

[148] D. Huang, H. Kim, G. Zou, X. Xu, Y. Zhu, K. Ahmad, Z. A. Almutairi, and H. N. Alshareef, Mater. Today Energy **29**, 101129 (2022).

[149] H. Kim, B. Anasori, Y. Gogotsi, and H. N. Alshareef, Chem. Mater. **29**, 6472 (2017).

[150] S. Karmakar and T. Saha-Dasgupta, Phys. Rev. Mater. **4**, 124007 (2020).

[151] Z. Jing, H. Wang, X. Feng, B. Xiao, Y. Ding, K. Wu, and Y. Cheng, J. Phys. Chem. Lett. **10**, 5721 (2019).

[152] A.-Y. Lu, H. Zhu, J. Xiao, C.-P. Chuu, Y. Han, M.-H. Chiu, C.-C. Cheng, C.-W. Yang, K.-H. Wei, Y. Yang, *et al.*, Nat. Nanotechnol. **12**, 744 (2017).

[153] S. Deng, L. Li, O. J. Guy, and Y. Zhang, Phys. Chem. Chem. Phys. **21**, 18161 (2019).

[154] H. Murari and S. Ghosh, Symmetry lowering through surface engineering and improved thermoelectric properties in mxenes (2024), arXiv:2401.06335 [cond-mat.mtrl-sci] .

[155] S. Lu, W. Ren, J. He, C. Yu, P. Jiang, and J. Chen, Phys. Rev. B **105**, 165301 (2022).

[156] X. Lou, S. Li, X. Chen, Q. Zhang, H. Deng, J. Zhang, D. Li, X. Zhang, Y. Zhang, H. Zeng, and G. Tang, ACS Nano **15**, 8204 (2021).

[157] T.-Y. Su, T.-H. Wang, D. P. Wong, Y.-C. Wang, A. Huang, Y.-C. Sheng, S.-Y. Tang, T.-C. Chou, T.-L. Chou, H.-T. Jeng, L.-C. Chen, K.-H. Chen, and Y.-L. Chueh, Chem. Mater. **33**, 3490 (2021).

[158] H. Y. Lv, W. J. Lu, D. F. Shao, H. Y. Lu, and Y. P. Sun, J. Mater. Chem. C **4**, 4538 (2016).

[159] S. Bhattacharyya, T. Pandey, and A. K. Singh, Nanotechnology **25**, 465701 (2014).

[160] C. Xu, P. A. Brown, and K. L. Shuford, RSC Adv. **5**, 83876 (2015).

[161] G. Zhang and Y.-W. Zhang, Mech. Mater. **91**, 382 (2015), mechanics of energy conversion and storage.

[162] S.-D. Guo, J. Mater. Chem. C **4**, 9366 (2016).

[163] H. Wang, Y.-S. Lan, B. Dai, X.-W. Zhang, Z.-G. Wang, and N.-N. Ge, ACS Omega **6**, 29820 (2021).

[164] M. Khazaei, M. Arai, T. Sasaki, M. Estili, and Y. Sakka, Phys. Chem. Chem. Phys. **16**, 7841 (2014).

[165] V. L. Deringer, A. L. Tchougréeff, and R. Dronskowski, J. Phys. Chem. A **115**, 5461 (2011).

[166] S. Maintz, V. L. Deringer, A. L. Tchougréeff, and R. Dronskowski, J. Comput. Chem. **37**, 1030 (2016).

[167] Z. M. Wong, T. Deng, W. Shi, G. Wu, T. L. Tan, and S.-W. Yang, Mater. Adv. **1**, 1176 (2020).

[168] Z. Shu, B. Wang, X. Cui, X. Yan, H. Yan, H. Jia, and Y. Cai, Chem. Eng. J. **454**, 140242 (2023).

[169] J. Yu, T. Li, G. Nie, B.-P. Zhang, and Q. Sun, Nanoscale **11**, 10306 (2019).

[170] G. Slack, J. Phys. Chem. Solids **34**, 321 (1973).

[171] B. Peng, H. Zhang, H. Shao, Y. Xu, X. Zhang, and H. Zhu, RSC Adv. **6**, 5767 (2016).

[172] D. A. Broido, A. Ward, and N. Mingo, Phys. Rev. B **72**, 014308 (2005).

[173] L. Lindsay and D. A. Broido, J. Phys.: Condens. Matter **20**, 165209 (2008).

[174] T. Pandey, C. A. Polanco, L. Lindsay, and D. S. Parker, Phys. Rev. B **95**, 224306 (2017).

[175] B. Liao, J. Zhou, B. Qiu, M. S. Dresselhaus, and G. Chen, Phys. Rev. B **91**, 235419 (2015).

[176] G. Sharma, V. K. Pandey, S. Datta, and P. Ghosh, Phys. Chem. Chem. Phys. **23**, 11663 (2021).

[177] Y. Wang, Y. Tao, Q. Zhang, R. Huang, B. Gao, Z. Li, G. Li, and N. Hu, Solid State Commun. **354**, 114893 (2022).

[178] M. Born, Math. Proc. Cambridge Philos. Soc. **36**, 160–172 (1940).

[179] M. Jonson and G. D. Mahan, Phys. Rev. B **21**, 4223 (1980).

[180] A. Hong, L. Li, R. He, J. Gong, Z. Yan, K. Wang, J.-M. Liu, and Z. Ren, Sci. Rep. **6**, 22778 (2016).

[181] D. Parker and D. J. Singh, Phys. Rev. B **85**, 125209 (2012).

[182] P. Shahi, D. J. Singh, J. P. Sun, L. X. Zhao, G. F. Chen, Y. Y. Lv, J. Li, J.-Q. Yan, D. G. Mandrus, and J.-G. Cheng, Phys. Rev. X **8**, 021055 (2018).

[183] L.-D. Zhao, S.-H. Lo, Y. Zhang, H. Sun, G. Tan, C. Uher, C. Wolverton, V. P. Dravid, and M. G. Kanatzidis, Nature **508**, 373 (2014).

[184] N. Wang, M. Li, H. Xiao, Z. Gao, Z. Liu, X. Zu, S. Li, and L. Qiao, npj Comput. Mater. **7**, 18 (2021).

[185] W.-L. Tao, Y.-Q. Zhao, Z.-Y. Zeng, X.-R. Chen, and H.-Y. Geng, ACS Appl. Mater. Interfaces **13**, 8700 (2021).

[186] S. Kumar and U. Schwingenschlögl, Chem. Mater. **27**, 1278 (2015).

[187] X. Gu and R. Yang, Appl. Phys. Lett. **105**, 131903 (2014).

[188] S. S. Naghavi, J. He, Y. Xia, and C. Wolverton, Chem. Mater. **30**, 5639 (2018).

[189] A. S. Sarkar and E. Stratakis, Adv. Sci. **7**, 2001655 (2020).

[190] A. K. Tołłoczko, S. J. Zelewski, J. Ziembicki, N. Olszowska, M. Rosmus, T. Woźniak, S. Tongay, and R. Kudrawiec, Adv. Optical Mater. **12**, 2302049 (2024).

[191] Z. Hu, Y. Ding, X. Hu, W. Zhou, X. Yu, and S. Zhang, Nanotechnology **30**, 252001 (2019).

[192] K. Chang, J. Liu, H. Lin, N. Wang, K. Zhao, A. Zhang, F. Jin, Y. Zhong, X. Hu, W. Duan, Q. Zhang, L. Fu, Q.-K. Xue, X. Chen, and S.-H. Ji, Science **353**, 274 (2016).

[193] Y. Bao, P. Song, Y. Liu, Z. Chen, M. Zhu, I. Abdelwahab, J. Su, W. Fu, X. Chi, W. Yu, W. Liu, X. Zhao, Q.-H. Xu, M. Yang, and K. P. Loh, Nano Lett. **19**, 5109 (2019).

[194] L.-D. Zhao, S.-H. Lo, Y. Zhang, H. Sun, G. Tan, C. Uher, C. Wolverton, V. P. Dravid, and M. G. Kanatzidis, nature **508**, 373 (2014).

[195] L.-D. Zhao, G. Tan, S. Hao, J. He, Y. Pei, H. Chi, H. Wang, S. Gong, H. Xu, V. P. Dravid, C. Uher, G. J. Snyder, C. Wolverton, and M. G. Kanatzidis, Science **351**, 141 (2016).

[196] D. Sarkar, S. Roychowdhury, R. Arora, T. Ghosh, A. Vasdev, B. Joseph, G. Sheet, U. V. Waghmare, and K. Biswas, Angew. Chem. Int. Ed. **60**, 10350 (2021).

[197] L. C. Gomes and A. Carvalho, Phys. Rev. B **92**, 085406 (2015).

[198] P. D. Antunez, J. J. Buckley, and R. L. Brutchey, Nanoscale **3**, 2399 (2011).

[199] K. Chang and S. S. P. Parkin, J. Appl. Phys. **127**, 220902 (2020).

[200] M. Xu, T. Liang, M. Shi, and H. Chen, Chem. Rev. **113**, 3766 (2013).

[201] M. Wu, S.-H. Wei, and L. Huang, Phys. Rev. B **96**, 205411 (2017).

[202] F. O. von Rohr, H. Ji, F. A. Cevallos, T. Gao, N. P. Ong, and R. J. Cava, J. Am. Chem. Soc. **139**, 2771 (2017).

[203] S. Lee, J.-E. Jung, H.-g. Kim, Y. Lee, J. M. Park, J. Jang, S. Yoon, A. Ghosh, M. Kim, J. Kim, W. Na, J. Kim, H. J. Choi, H. Cheong, and K. Kim, Nano Lett. **21**, 4305 (2021).

[204] Y. Zhou, M. Zhao, Z. W. Chen, X. M. Shi, and Q. Jiang, Phys. Chem. Chem. Phys. **20**, 30290 (2018).

[205] N. Luo, W. Duan, B. I. Yakobson, and X. Zou, Adv. Funct. Mater. **30**, 2000533 (2020).

[206] F. Q. Wang, S. Zhang, J. Yu, and Q. Wang, Nanoscale **7**, 15962 (2015).

[207] Z. Hu, Y. Ding, X. Hu, W. Zhou, X. Yu, and S. Zhang, Nanotechnology **30**, 252001 (2019).

[208] Y. Li, K. Ma, X. Fan, F. Liu, J. Li, and H. Xie, Appl. Surf. Sci. **521**, 146256 (2020).

[209] S.-D. Guo and Y.-H. Wang, J. Appl. Phys. **121**, 034302 (2017).

[210] H. Nautiyal and P. Scardi, Nanotechnology **33**, 325402 (2022).

[211] B. Kaur, Heena, S. A. Khandy, S. R. Ahmad, M. D. Albaqami, M. Srinivasan, L. Patra, S. Dhiman, and K. Kaur, Adv. Quantum Technol. **7**, 2300357 (2024).

[212] S. Saini, A. Shrivastava, and S. Singh, Eur. Phys. J. Plus **137**, 1 (2022).

[213] L. Seixas, J. Appl. Phys. **128**, 045115 (2020).

[214] X. Zhang, D. Wang, H. Wu, M. Yin, Y. Pei, S. Gong, L. Huang, S. J. Pennycook, J. He, and L.-D. Zhao, Energy Environ. Sci. **10**, 2420 (2017).

[215] H. Yu, S. Dai, and Y. Chen, Sci. Rep. **6**, 26193 (2016).

[216] X. Gu, Y. Wei, X. Yin, B. Li, and R. Yang, Rev. Mod. Phys. **90**, 041002 (2018).

[217] F. Eriksson, E. Fransson, and P. Erhart, Adv. Theor. Simul. **2**, 1800184 (2019).

[218] S. Chaudhuri, A. Bhattacharya, A. K. Das, G. P. Das, and B. N. Dev, Phys. Rev. B **109**, 235424 (2024).

[219] L. Lindsay, W. Li, J. Carrete, N. Mingo, D. A. Broido, and T. L. Reinecke, Phys. Rev. B **89**, 155426 (2014).

[220] N. S. Fedorova, A. Cepellotti, and B. Kozinsky, Adv. Funct. Mater. **32**, 2111354 (2022).

[221] M. Jakhar, R. Sharma, and A. Kumar, Nanoscale **15**, 5964 (2023).

[222] S. Huang, Z. Wang, R. Xiong, H. Yu, and J. Shi, Nano Energy **62**, 212 (2019).

[223] L. Pan, Z. Wang, J. Carrete, and G. K. H. Madsen, Phys. Rev. Mater. **6**, 084005 (2022).

[224] J. Bardeen and W. Shockley, Phys. Rev. **80**, 72 (1950).

[225] X. Gu, Y. Wei, X. Yin, B. Li, and R. Yang, Rev. Mod. Phys. **90**, 041002 (2018).

[226] Z. Han and X. Ruan, Phys. Rev. B **108**, L121412 (2023).

[227] A. G. Gokhale, D. Visaria, and A. Jain, Phys. Rev. B **104**, 115403 (2021).

[228] S. Chaudhuri, A. Bhattacharya, A. K. Das, G. P. Das, and B. N. Dev, Phys. Rev. B **109**, 235424 (2024).

[229] Z. Tang, X. Wang, J. Li, C. He, M. Chen, C. Tang, and T. Ouyang, Phys. Rev. B **108**, 214304 (2023).

[230] Y. Han, C. Yang, X. Cheng, D. Han, W. Ding, and X. Wang, ACS Appl. Energy Mater. **7**, 649 (2024).

[231] H. Xie, L. Chen, W. Yu, and B. Wang, Appl. Phys. Lett. **102**, 111911 (2013).

[232] X. Xu, L. F. C. Pereira, Y. Wang, J. Wu, K. Zhang, X. Zhao, S. Bae, C. Tinh Bui, R. Xie, J. T. L. Thong, B. H. Hong, K. P. Loh, D. Donadio, B. Li, and B. Özyilmaz, Nat. Commun. **5**, 3689 (2014).

[233] A. A. Balandin, S. Ghosh, W. Bao, I. Calizo, D. Teweldebrhan, F. Miao, and C. N. Lau, Nano Lett. **8**, 902 (2008).

[234] T. Ma, Z. Liu, J. Wen, Y. Gao, X. Ren, H. Chen, C. Jin, X.-L. Ma, N. Xu, H.-M. Cheng, and W. Ren, Nat. Commun. **8**, 14486 (2017).

[235] H. Malekpour, P. Ramnani, S. Srinivasan, G. Balasubramanian, D. L. Nika, A. Mulchandani, R. K. Lake, and A. A. Balandin, Nanoscale **8**, 14608 (2016).

[236] W. Cai, A. L. Moore, Y. Zhu, X. Li, S. Chen, L. Shi, and R. S. Ruoff, Nano Lett. **10**, 1645 (2010).

[237] S. Chen, Q. Wu, C. Mishra, J. Kang, H. Zhang, K. Cho, W. Cai, A. A. Balandin, and R. S. Ruoff, Nat. Mater. **11**, 203 (2012).

[238] S. Chen, A. L. Moore, W. Cai, J. W. Suk, J. An, C. Mishra, C. Amos, C. W. Magnuson, J. Kang, L. Shi, and R. S. Ruoff, ACS Nano **5**, 321 (2011).

[239] S. Anand, K. Thekkepat, and U. V. Waghmare, Nano Lett. **16**, 126 (2016).

[240] D. Hazra, N. Tsavdaris, S. Jebari, A. Grimm, F. Blanchet, F. Mercier, E. Blanquet, C. Chapelier, and M. Hofheinz, Supercond. Sci. Technol. **29**, 105011 (2016).

[241] A. Chanana and U. V. Waghmare, Phys. Rev. Lett. **123**, 037601 (2019).

[242] R. Ahammed and A. De Sarkar, Phys. Rev. B **105**, 045426 (2022).

[243] H. J. Monkhorst and J. D. Pack, Physical review B **13**, 5188 (1976).

[244] D. Vanderbilt, Phys. Rev. B **41**, 7892 (1990).

[245] X. Gu and R. Yang, J. Appl. Phys. **117**, 025102 (2015).

[246] J. Carrete, W. Li, L. Lindsay, D. A. Broido, L. J. Gallego, and N. Mingo, Mater. Res. Lett. **4**, 204 (2016).

[247] G. Zhang, S. Dong, C. Yang, D. Han, G. Xin, and X. Wang, Appl. Phys. Lett. **123**, 052205 (2023).

[248] T. Feng, L. Lindsay, and X. Ruan, Phys. Rev. B **96**, 161201 (2017).

[249] A. Kundu, X. Yang, J. Ma, T. Feng, J. Carrete, X. Ruan, G. K. H. Madsen, and W. Li, Phys. Rev. Lett. **126**, 115901 (2021).

[250] L. Xie, J. H. Feng, R. Li, and J. Q. He, Phys. Rev. Lett. **125**, 245901 (2020).

[251] L. Wei, X. Jin, Z. Zhou, X. Yang, G. Wang, and X. Zhou, Phys. Rev. B **110**, 045406 (2024).

[252] L. Lindsay, D. A. Broido, and N. Mingo, Phys. Rev. B **80**, 125407 (2009).

[253] L. Pan, Z. Wang, J. Carrete, and G. K. H. Madsen, Phys. Rev. Mater. **6**, 084005 (2022).

[254] A. Patel, D. Singh, Y. Sonvane, P. B. Thakor, and R. Ahuja, ACS Applied Materials & Interfaces **12**, 46212 (2020).

[255] J. Zhang, X. Liu, Y. Wen, L. Shi, R. Chen, H. Liu, and B. Shan, ACS Applied Materials & Interfaces **9**, 2509 (2017).

[256] M. Jin, Z. Chen, X. Tan, H. Shao, G. Liu, H. Hu, J. Xu, B. Yu, H. Shen, J. Xu, H. Jiang, Y. Pei, and J. Jiang, ACS Energy Letters **3**, 689 (2018).

[257] U. Aseginolaza, R. Bianco, L. Monacelli, L. Paulatto, M. Calandra, F. Mauri, A. Bergara, and I. Errea, Phys. Rev. B **100**, 214307 (2019).

List of Publications

1. **Himanshu Murari** and Subhradip Ghosh, *Structural arrangement and improved thermoelectric figure of merit in hexagonal SiX (X = N, P, As, Sb, Bi) monolayers: understanding from first-principles calculations*, J. Phys. D: Appl. Phys. 56 295501, (2023)*
2. Mandira Das, **Himanshu Murari**, Subhradip Ghosh and Biplab Sanyal, *Manipulation of electrochemical properties of MXene electrodes for supercapacitor applications by chemical and magnetic disorder*, Nanoscale, 16(3), 1352-1361, (2024)
3. **Himanshu Murari** and Subhradip Ghosh, *Symmetry lowering through surface engineering and improved thermoelectric properties in Janus MXenes*, Nanoscale, 16(23), 11336-11349, (2024)*
4. **Himanshu Murari**, Swati Shaw and Subhradip Ghosh, *Strain aided drastic reduction in lattice thermal conductivity and improved thermoelectric properties in Janus MXenes*, J. Phys.: Condens. Matter 36 445703, (2024)*
5. **Himanshu Murari** and Subhradip Ghosh, *Thermoelectric properties of 2D-Janus monochalcogenides: Anisotropic electronic and phonon transport*, Advanced Theory and Simulations (in press)*
6. **Himanshu Murari**, Subhradip Ghosh, Mukul Kabir, and Ashis Kundu, *Acoustic phonon-restricted four-phonon interactions: impact on thermal and thermoelectric transport in monolayer h-NbN*, Nanoscale, 2025,17, 24301-24310*
7. A book chapter published for ACS Symposium Series volume titled *Modeling and Simulation of Electrochemical, Thermoelectric, and Magnetic Properties of MXenes*, Age of MXenes, Volume 1. Fundamentals and Artificial Intelligence: Machine Learning Interventions. The authors are Mandira Das, Himangshu Sekhar Sarmah, **Himanshu Murari**, and Subhradip Ghosh.

Conferences attended

1. Delivered a talk titled *Structural modification driven lattice anharmonicity and improved thermoelectric properties in M_2CO_2 and $MM^{'}CO_2$ MXenes* at **International conference Emerging phenomena in Quantum materials**, December 11-15, 2023, organized jointly by Uppsala University and Savitribai Phule Pune University, at Bharatpur, India.
2. Presented a poster titled *"Effect of structural arrangements on thermoelectric properties of SiX (X = N, P, As, Sb, Bi) monolayers."* at the **International Conference on 60 Years of DFT: Advancements in Theory and Computation** held on July 21-26, 2024, at IIT Mandi.
3. Presented a poster titled *"Symmetry lowering through surface engineering and improved thermoelectric properties in Janus MXenes"* at **7^{th} Annual Conference on Quantum Condensed Matter (QMAT-2024)** held during December 20-23, 2024, at IIT Guwahati.
4. Presented a poster titled *"Acoustic phonon restricted four phonon interactions: Impact on lattice thermal conductivity in 2D h-NbN"* at **AAPALI PSI-K, International conference on DFT and applications** held during May 19-21, 2025, at IISER Pune.
5. Presented a poster title *"Acoustic phonon restricted four phonon interactions: Impact on lattice thermal conductivity in 2D h-NbN"* at **ICT/ACT 2025 – 41st/7th Asian International Conference on Thermoelectrics**, Sendai, Japan, June 2025.

Publications marked with * are included in the thesis